POWER FLOW AND ROTOR ANGLE STABILITY STUDIES OF HVAC-HVDC POWER SYSTEM INTERCONNECTIONS USING

DigSILENT

BY:

DAVID TEMITOPE OYEDOKUN
DEPARTMENT OF ELECTRICAL ENGINEERING
UNIVERSITY OF CAPE TOWN

This thesis was submitted to the University of Cape Town in fulfilment of the academic requirements for the Masters of Science degree in Electrical Engineering

Declaration

Although much literature was consulted during the preparation of this thesis, absolute caution has been taken within the bounds of human accuracy to ensure that all works have been properly referenced. I, therefore, declare that this thesis is my own work and it has not been submitted (prior to this submission) to any academic institution or body of academics for examination.

…………………………….
David Temitope Oyedokun, *BSc (Elec Eng) Cape Town, MIEEE*
5th February, 2010.

…………………………….
Prof Komla Folly (Supervisor)
5th February, 2010.

Acknowledgements

This MSc thesis serves as evidence that I have honed my ability and know-how in the area of power system stability and analysis. I can look back to my first day at UCT, as a BSc student, then to my graduating and becoming a member of convocation, an alumnus of this great institution - the best amongst equals, and, then more recently, to my taking up the challenge of Masters of Science Electrical Engineering degree and treading that path till this point of its completion. I would not have been able to arrive at this destination without the assistance and support of others, and must therefore acknowledge the following:

> the indisputable assistance and courage from God, the source of my inner strength and endurance who through his infinite mercy has never let me down;
>
> the constructive criticisms of my supervisor Prof Komla Folly whose contribution to this work I greatly appreciate. Through his knowledge acumen, experience and dedication to the academia, he has consistently worked with me and guided me through this degree right from its inception to its completion;
>
> Eskom's financial support of this research work and its providing me with a platform for engagements. For this I am very grateful;
>
> the support of my family whose presence and care was never lacking throughout my studies, and who gave me the encouragement I greatly needed and acted as a support structure which contributed to my stamina;
>
> all the members of the power systems group who made power system enjoyable by combining both social and academic events, and my friends around the globe whose friendship undoubtedly has contributed to my personal stability. To you all I owe many thanks; and
>
> Finally, the role of University of Cape Town and its community has been indispensable to my growth and my integration into the global order of intellectuals. It also provided me with the opportunities and resources needed to successfully engage in and complete my Masters degree, I shall always be grateful for this and will continually be a proud alumnus.

The Inspiration of

a Man's mind

comes from

within.

For the inner

is duly inspired

by the outer

expeditions.

© David Temitope Oyedokun

Synopsis

The backbone of all industrialised nations is the success of the power sector, which involves an efficient, reliable and secure means of power generation, transmission and distribution. Industrial growth and urbanisation have together endlessly stimulated electrical engineers to ensure that the electric power needs of the society are met. In pursuance of this quest and because of increasing demand, additional power plants and more transmission lines are built to deliver power to the load centres. Due to this increasing demand, the amount of power that needs to be generated and transmitted to the load centres has increased significantly.

Conventionally, High Voltage Alternating Current (HVAC) has been adequate for this purpose. In more recent times (since 1954), High Voltage Direct Current (HVDC) transmission has been used increasingly due to its advantages over HVAC for the long-distance transmission of bulk power. The debut of HVDC transmission has allowed for the connection of asynchronous power networks and underwater power transmission. Moreover, research has indicated that HVDC transmission lines increase the stability of power systems. The increase in the use of HVDC lines for transmission is also due to their reduced power loss and efficiency in power transmission as opposed to HVAC transmission.

One of the major concerns in respect of power systems that have been reported as early as 1912, however, is the issue of power system stability. This can be classified into voltage stability, frequency stability and rotor angle stability, the last of which will form the core of this thesis. Rotor angle stability can be divided into transient stability and small signal stability. However, load flow (power flow) analysis plays a significant role in, and is a primary level analysis of any power system. This is achieved by using advanced computational tools (software packages) to solve and determine the power flow in power systems. The use of advanced computational tools in the analysis of a power system is driven by complexity in power systems, the need for infrastructure expansion and planning which extends the use of such computational tools to stability analysis, contingency planning, distribution and protection. Several computational tools are available in the market for the analysis of power

systems. These include PSAT, Matlab, PSCAD/EMTDC and DigSILENT. Each of these computational tools has different strengths and weaknesses. This means that the choice of which software package to use in analysing a power system must be made carefully to ensure that correct results are obtained. In this thesis DigSILENT *powerfactory* is used for both the load flow and rotor angle stability analysis. Both transient stability and small signal stability will be considered. The reviewed literature has concluded that little work has been carried out in the area of parallel hybrid HVAC-HVDC transmission when compared with HVDC transmission. This thesis, thus, could contribute enormously to the available literature on hybrid parallel HVAC-HVDC power system interconnections. Also in this thesis, the modelling of an HVDC transmission line was explained, and an insight given, into the theory of HVAC and HVAC-HVDC load flow calculations using Newton-Raphson' algorithm.

To carry out the main objective of this thesis - power flow and rotor angle analysis of HVAC-HVDC interconnected power systems - two power system models were developed. These are the Single Machine Infinite Bus (SMIB) and the Two-Area Multi-Machine (TAMM) power system. In each of these models two transmission configurations are considered, namely, HVDC transmission and hybrid HVAC-HVDC transmission. In order to determine the rotor angle stability of the Single Machine Infinite Bus and the Two-Area Multi-Machine power systems, two types of fault were considered. The first was a DC system fault at both rectifier and inverter DC terminals of the HVDC line. Following this, a generator 3-phase to ground fault was considered. The fault in each case lasted for 50 ms. Furthermore, modal analysis was carried out to investigate the small signal stability of both power system models. While modelling the HVDC transmission scheme some challenges were faced. These included HVDC line modelling and the choice of the DC line parameters, converter control, reactive power compensation and load flow analysis. For the hybrid parallel HVAC-HVDC transmission scheme, the major challenge, in addition to the challenges inherited from the HVDC transmission line modelling, was the transmission scheduling between the HVAC and the HVDC transmission line.

The load flow analysis conducted on the SMIB power system indicated that the voltage drop across the HVDC transmission line for both transmission configurations was 0.03 pu. The reactive power demand by the converter stations was 3191 Mvar using HVDC transmission and 1824 Mvar with the hybrid HVAC-HVDC transmission. As a result, there was a 42.8 % decrease in the amount of reactive power demand by the converter stations. For both transmission schemes, the delivered real power to the distribution centre was the same at 1942 MW. Given that the transmission line losses in the two cases are different, the transmitted power in each case was different. The transmission loss in HVDC transmission line was found to be 54 MW while the loss in the hybrid HVAC-HVDC transmission line was found to be 82 MW. Therefore, the HVDC transmission scheme had the lowest transmission loss. Nevertheless, the hybrid HVAC-HVDC transmission scheme provided a solution for reducing the voltage angle difference between the terminating AC busbars on the HVAC and HVDC transmission line, while keeping the total amount of power transmitted constant. Consequently, the steady state stability margin is increased. This seems to be one of the major advantages of the hybrid HVAC-HVDC transmission line configuration.

The transient simulation results indicated that the SMIB power system regains stability faster with the use of HVDC transmission, after been subjected to AC and DC faults. This is explained by the reduced number of post fault rotor angle oscillations in the power system. These oscillations increased notably with the hybrid HVAC-HVDC transmission line. Some generators exceeded their maximum capacity due to reactive power generation during the transients, hence, there is a need for (dynamic) reactive compensation, or the generators which exceeded their maximum reactive power generation should be disconnected during the fault. Based on the findings in the section on small signal stability, it is concluded that the HVDC transmission scheme has less electromechanical modes when compared with the hybrid HVAC-HVDC transmission scheme. In the hybrid HVAC-HVDC transmission scheme, a new electromechanical mode was formed. Hence, the hybrid HVAC-HVDC scheme is less stable and more susceptible to small signal instability when compared to the HVDC scheme.
The load flow analysis conducted on the TAMM power system indicated that the voltage drop across the HVDC transmission line was 0.03 pu when HVDC transmission was used and

0.02 pu while using the hybrid HVAC-HVDC transmission line. The reactive power demand by the converter stations was 2466 Mvar using HVDC transmission and 1411 Mvar with the hybrid HVAC-HVDC transmission. As a result, there was a 57.2 % decrease in the amount of reactive power demand by the converter stations. The power loss in transmission using HVDC was found to be 56 MW, which is 29 MW lower than the power loss on the hybrid HVAC-HVDC transmission line.

The transient simulation results showed that the rotor angle responses of the generators in each area of the power system were found to be similar during the converter DC fault at G3. Nevertheless, the rectifier fault was found to be more severe on the rotor angle stability when compared to the inverter fault for the HVDC transmission scheme. For the hybrid HVAC-HVDC transmission scheme, the difference between the severity of the rectifier and the inverter fault on the rotor angle of G3 was not significant. The terminal voltage dip at G3 during the rectifier DC fault was larger than the terminal voltage dip at G3 during the inverter fault across both transmission schemes. This dip however, was found to be reduced with the hybrid HVAC-HVDC transmission scheme. The reactive power increase at G3 during the inverter fault was 800 Mvar lower than the reactive power increase during the inverter fault with the hybrid HVAC-HVDC transmission line. The inverter DC fault was more severe as compared to the rectifier DC fault on the rotor angle of G2 across both transmission schemes. The inverter DC fault however, was more severe with the HVDC transmission scheme when compared to the hybrid HVAC-HVDC transmission scheme. The terminal voltage shoot during both inverter and rectifier DC fault was found to be reduced with the hybrid HVAC-HVDC transmission scheme. During the converter DC fault, the terminal voltage at G2 had more post fault oscillations when the hybrid HVAC-HVDC transmission line was used. The active power increase during both converter faults was reduced with the hybrid HVAC-HVDC transmission line. Similarly, the reactive power drawn at G2 during the converter faults was reduced by using the hybrid-HVAC-HVDC transmission line. Only G3 exceeded its capacity during the converter fault due to the additional active and reactive power it had to provide. To prevent this, there is a need for (dynamic) reactive power compensation, or G3 would be disconnected during the converter fault.

In the TAMM power system model, the response of G2 to the 3-phase to ground fault at G4 was found to be somewhat similar when compared to its response to the converter DC fault with both transmission schemes. At G3 however, the active power during the 3-phase to ground fault decreased before increasing to steady state with the HVDC transmission line, which is different to its response to the converter DC fault. During the converter DC fault, the active power increased first before decreasing. With the hybrid transmission line, the 3-phase to ground fault at G4 was more severe on the rotor angle of G3, although the impact it had on the reactive power and the active power generation at G3 was the same with that of the HVDC transmission scheme. From the results obtained on the small signal stability analysis, it can be concluded that the HVDC transmission scheme has less inter-area oscillations when compared to the hybrid HVAC-HVDC transmission scheme. In the hybrid HVAC-HVDC transmission scheme, a new electromechanical mode was formed. Hence, the hybrid HVAC-HVDC scheme is relatively less stable and more susceptible to small signal instability, when compared to the HVDC scheme. For the Hybrid HVAC-HVDC transmission scheme, the only state that contributed to oscillatory mode is the speed. The excitation flux contributed to one of the modes for the HVDC transmission scheme.

Table of Contents

List of Figures

List of Tables

CHAPTER 1

INTRODUCTION

During the last three years South Africa has experienced power outages due to the strain on the existing generating capacity and the increasing load demand. Existing High voltage AC (HVAC) transmission lines are not efficient in transmitting bulk power over long distances. This paved the way for recent discussions about the building of new power stations and upgrading existing transmission infrastructures to alleviate the situation. With regards to the transmission of bulk power over long distance, the use of HVDC is the preferred means. However, HVDC transmission lines are used in conjunction with HVAC transmission lines. Therefore there is a need to investigate the effect of the interaction of HVDC transmission lines with existing HVAC transmission lines.

This thesis deals with power flow (load flow) and rotor angle stability studies of HVAC-HVDC power system interconnections using DigSILENT (developed by DigSILENT GmbH in Germany). This software package is used in industry and in the educational sector for network optimisation, protection, distribution planning and the analysis of steady state and fault conditions. Two network models are used in this thesis; the Single Machine Infinite Bus (SMIB) and the Two-Area Multi-Machine (TAMM) power system models. In each of these models, power flow studies are conducted using the HVDC transmission and the hybrid HVAC-HVDC transmission schemes. Furthermore, transient and small signal analyses are conducted on the two power system models each with the two different transmission configurations.

1.1 BACKGROUND TO THESIS

The continuous need to increase generation and transmission capacity which is driven by industrialisation and growth across the globe, in addition to the debut of HVDC transmission which has seen increasing global acceptance since the 1950s led to the initiation of this thesis research work [1, 2, 3]. The first HVDC transmission scheme in South Africa was the Cahora-Bassa Hydro-electric scheme between Mozambique and South Africa with a capacity of 1920 MW. This increased the amount of power available to Eskom for distribution to its customers. To increase South Africa's generating capacity, Eskom accelerated the building of new power stations across the country, returning old power stations back into service, and upgrading others [4]. Since the capacity expansion programme started in 2005 with a budget of R385 billion, an additional 4, 453.5 MW has been commissioned as of March 2009. By 2017, an additional 16, 204 MW is planned to be added to South Africa generating capacity [5].

Examples of HVDC schemes include the HVDC Pacific Intertie in the USA which has a total of 3100 MW over a distance of 1360 km [7], the Hydro Quebec New England link which exchanges 2250 MW via HVDC transmission, Itaipu HVDC scheme in Brazil with a capacity of 6300 MW [7, 8], the cross channel UK-France scheme with a capacity of 2000 MW and Wybord in Russia with a capacity of 1050 MW [7]. The scheme between the North and South Islands of New Zealand is of 1240 MW capacity. In China, the first HVDC transmission scheme known as the GESHA scheme has a capacity of 1200 MW which interconnects central China and eastern China over a distance of 1045 km [9]. As of 2005, the worldwide installed HVDC capacity was 55GW which is 1.4% of the worldwide installed generation capacity [10, 11]. Moreover, the literature review also indicated that few published works are available in the field of hybrid HVAC-HVDC parallel transmission. The issue of power system stability which has been documented as early as 1912 plays a significant role in the expansion of transmission infrastructure. These stability issues include rotor angle stability, frequency stability and voltage stability [1, 2, 7, 12]. Therefore, as the power utility in South Africa, Eskom plans to build additional transmission infrastructure to support its existing infrastructure, it has become increasingly important to investigate the effect that introducing HVDC transmission lines will have on the entire system in areas of load flow and rotor angle stability. In the SMIB and TAMM power system models, HVDC transmission and hybrid parallel HVAC-HVDC is been adopted. Under the analysis of the rotor angle stability, both transients and small signals will be considered.

1.2 OBJECTIVES

The objectives of this thesis were to:

- Investigate the interaction between HVAC and HVDC transmission lines during steady-state and fault conditions. This was achieved by analysing the load flow and rotor angle stability of power system models which are interconnected by HVDC and hybrid HVAC-HVDC transmission lines; and
- Compare the performance of the power system with HVDC line alone and hybrid HVAC-HVDC.

1.3 METHODOLOGY

A literature review was conducted to enhance the researcher's knowledge around the topic of the thesis. Following the literature review, it was decided that two major types of power system would be considered. These are the Single Machine Infinite Bus (SMIB) and the Multi-Machine Power System model. For the latter, only a Two-Area power system model is considered.

The load flow calculation tool in DigSILENT was used for the load flow analysis. Parameters such as bus voltage angle, bus voltage magnitude, active power flow, reactive power flow and power loss in transmission were observed to check and ensure that the system was operating under normal conditions. In addition to this, the reactive power demand by the rectifier and the inverter was also analysed in relation to the reactive power supplied by the generating stations, to determine the amount of reactive power compensation by capacitor banks.

The stability analysis tool in DigSILENT was used to conduct the transient and small signal stability analysis. In the section on transient stability, relatively large disturbances such as DC faults at the rectifier and inverter DC terminal and 3-phase to ground fault at one generating station were simulated. Each of these fault lasted for 50 ms. The pre-fault and post-fault operation conditions of the generators were observed. This was carried out by analysing the behaviour of the rotor angle, terminal voltage, active and reactive power at the generating stations before, during and after the fault. Modal analysis tools in DigSILENT were used to conduct the small signal analysis on the SMIB and the TAMM power system.

Figure 1.1 illustrates the system models and the analyses that were conducted on the system models using both HVDC and hybrid HVAC-HVDC transmission schemes.

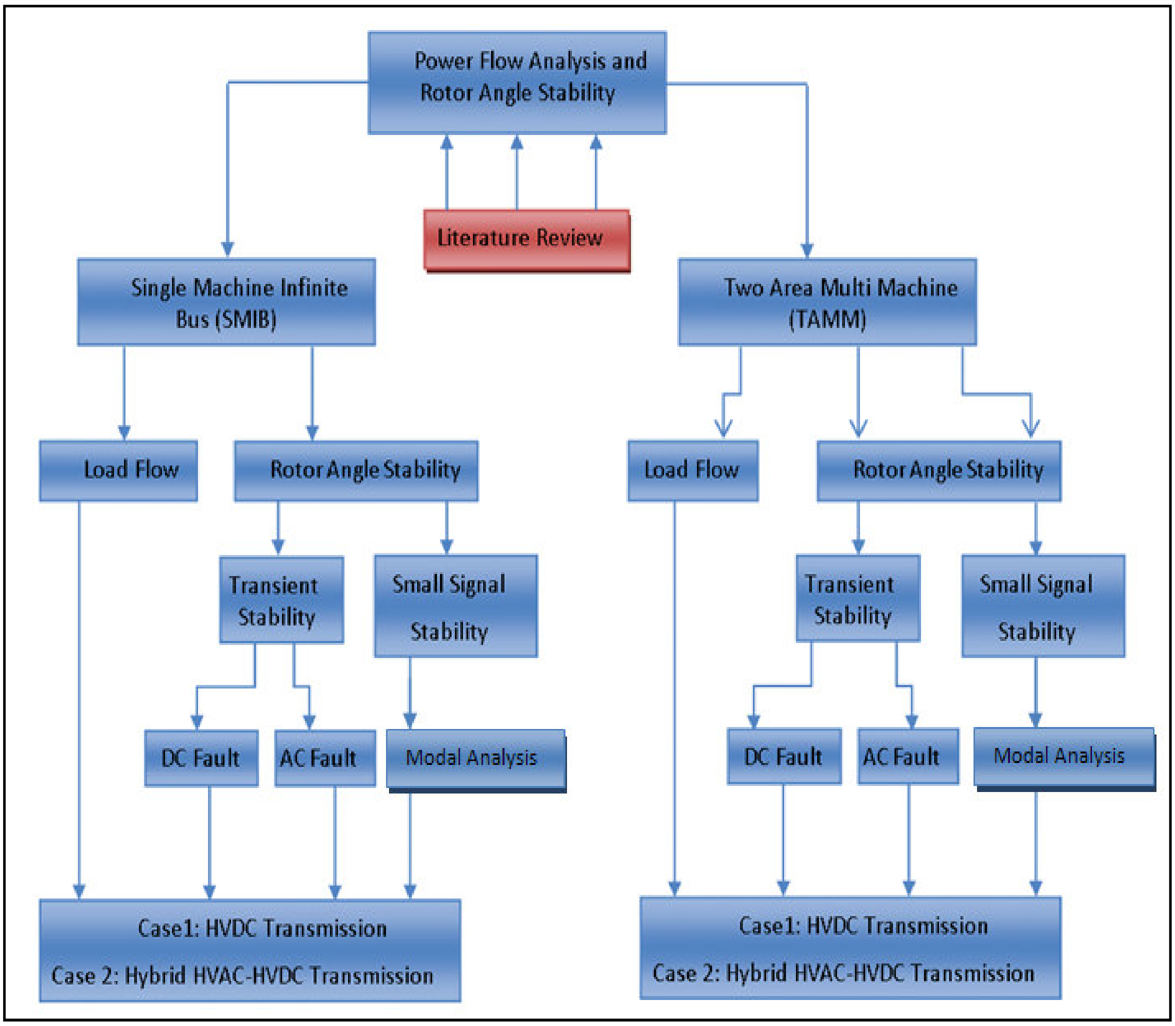

Figure 1.1 Thesis Development Diagram

For each of the models, load flow and rotor angle stability analysis were conducted under two cases. In the first case, HVDC was used for transmission while in the second case, hybrid HVAC-HVDC was used for transmission. In the transient stability section, rectifier and inverter DC faults were simulated to represent the DC fault. For the AC fault, a generator 3-phase to ground fault was simulated. In all the fault scenarios, the fault lasted for 50 ms.

1.4 LIMITATIONS AND SCOPE

Analysis and simulation are limited to two power system models built in DigSILENT. In the simulation it was assumed that the load demand was 2440 MW, which is twice the Surge Impedance Loading (SIL) of a HVAC transmission line at 500 kV with an additional 440 MW. Hence in case 1, two HVDC transmission lines were used to deliver 2000 MW to the distribution centre over 500 km instead of using HVAC. One of the HVDC transmission line was replaced in case 2 with a HVAC transmission line to form hybrid HVAC-HVDC transmission.

1.5 CONTRIBUTIONS OF THIS THESIS

On account of the simulations carried out in this thesis, certain results have been considered as contributions to the existing body of knowledge regarding the interconnection of HVAC and HVDC transmission lines, as well as parallel hybrid HVAC-HVDC transmission. These contributions include the following:

- The use of hybrid-HVAC-HVDC transmission significantly reduces the power angle at the terminating AC busbars as compared to the case where only HVAC is used. The decrease in power angle is achieved by controlling the power that is transmitted via the HVDC line. This is beneficial to the steady state stability of the power system; and
- An additional inter-area mode is introduced to the power system when hybrid HVAC-HVDC transmission is used. This is as a result of the AC link between the two areas.

1.6 STRUCTURE OF THE THESIS

This section aims to provide insight into the content of the rest of this thesis, from chapter two which introduces HVDC transmission, to chapter nine which concludes this thesis.

Chapter two introduces HVDC transmission. It discusses the advantages of HVDC transmission, the main configurations of HVDC schemes and transmission line types.

Chapter three discusses the theory of AC to DC conversion, harmonic filters and reactive power compensation which forms a critical part of HVDC transmission.

Chapter four deals with load flow analysis of HVAC interconnected systems and HVDC interconnected power systems.

Chapter five focuses on the control of HVDC transmission schemes. It covers the real and ideal V-I characteristics of HVDC control.

Chapter six looks into rotor angle stability and deals with the behaviour of synchronous machines under fault conditions.

Chapter seven presents the simulation results from the Single Machine Infinite Bus power system model using DigSILENT. This includes load flow analysis, transient stability and small signal stability studies. In each of these sections; the two transmission configurations namely HVDC and hybrid HVAC-HVDC are used.

Chapter eight presents the simulation results from the Two-Area Multi-Machine power system model using DigSILENT. It also includes load flow analysis, transient stability and small signal stability studies. In each of these sections; the two transmission configurations namely, HVDC and hybrid HVAC-HVDC are used.

And finally, conclusions and recommendations are given in chapter nine.

CHAPTER 2

HVDC TRANSMISSION SYSTEMS

The first HVDC transmission line was put into service in 1954 between the Swedish mainland and the island of Gotland. This system was an underwater link spanning 90 km with a capacity of 90 MW. The development in the use of thyristor valve converters has led to the growth in the use of HVDC for transmission, especially for long distance bulk transmission, underwater transmission and asynchronous connections with larger schemes now in operation across the globe [13].

For example, the HVDC Pacific Intertie in the USA has a total of 3100 MW over a distance of 1360 km, the Hydro Quebec New England link exchanges 2250 MW via HVDC transmission, the Itaipu HVDC scheme in Brazil has a capacity of 6300 MW, the cross channel UK-France scheme has a capacity of 2000 MW and the Wybord in Russia has a capacity of 1050 MW [7]. The scheme between the North and the South Island of New Zealand is 1240 MW and the Cahora-Bassa Hydro-electric scheme between Mozambique and South Africa has a capacity of 1920 MW [14]. In China, the first HVDC transmission scheme known as the GESHA scheme has a capacity of 1200 MW which interconnects central and eastern China over a distance of 1045 km [9]. As of 2005, the worldwide installed HVDC capacity was 55 GW which is 1.4% of the worldwide installed generation capacity [10].

HVDC is obtained directly from High Voltage Alternating Current (HVAC) through the use of HVDC converters and their associated devices like filters, reactors and capacitor banks which provide reactive power support for the HVDC converters. In most HVDC schemes around the world, the twelve-pulse thyristor converter configuration has been adopted to reduce the requirements for smoothing the DC waveform [12]. With regards to power system stability, it has been shown that the use of HVDC transmission lines in parallel with HVAC transmission lines increases the strength and the stability of the system. An example of such an interconnection is the Pacific HVDC Intertie in between California and Oregon [15].

Three major types of transmission lines are used in High Voltage Direct Current Transmission lines (HVDC). These are overhead transmission lines, underground cables and sub-marine cables. Each of these HVDC transmission lines can be designed using different link configurations. The most common link configurations are the monopolar and bipolar configurations.

2.1 ADVANTAGES OF HVDC TRANSMISSION

2.1.1 Bulk Power Transmission

HVDC transmission provides a more economical mode of power transmission for long distances as opposed to HVAC transmission. Research has shown that once the length of a transmission line exceeds a certain distance known as the breakeven distance, HVDC transmission lines become more economical than HVAC transmission lines. The breakeven distance, as shown in figure 2.1, is approximately 500 – 800 km for overhead lines and 40-50 km for underground cables. As a result, it is more affordable to use HVDC for very long distance transmission of bulk power [16].

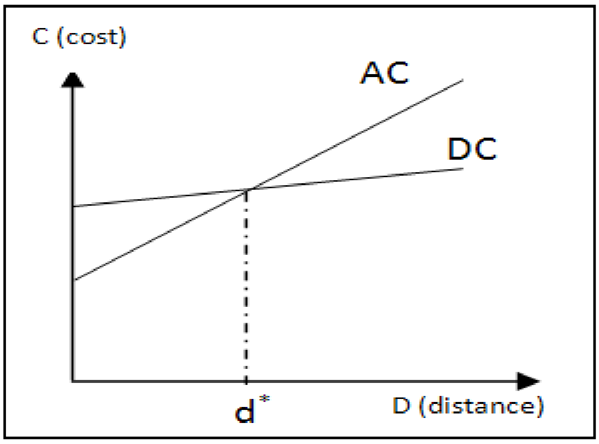

Figure 2.1 HVDC versus HVAC Transmission Cost Variation with Distance [4]

2.1.2 Reduced Transmission Losses

HVDC transmission lines (i.e. submarine, underground and overhead transmission lines) do not make use of the three phase cables as in HVAC transmission therefore; the I^2R losses incurred in the DC lines are lower than that of the AC line. This is explained in [17] as follows:

For a given cable conductor area, the line losses with HVDC cables can be about half those of AC cables. This is due to AC cables requiring more conductors (three phases) to carrying the reactive component of current, the skin-effect, and the induced currents in the cable sheath and armour. Since HVDC allows the use of fewer conductors, these losses are reduced.

2.1.3 Asynchronous Ties

Another advantage of HVDC transmission is the interconnection of asynchronous systems, which allows for a more economical operation. This kind of interconnection often uses a back-to-back converter and in some cases, both AC-to-DC and DC-to-AC converters are at the same site [14]. Asynchronous ties act as a 'fire wall', preventing the propagation of cascading system faults. Examples of such connections exist in North America, between Mexico and the south-west power pool (SPP), also between Quebec and its neighbours (New England and the Maritimes) [17].

2.1.4 Power Transfer and Stability Limits

Research has shown that the power transfer capability of HVAC lines decreases as the distance increases due to line reactance and stability issues. That is, the power transfer in AC transmission lines depends on the angle difference between the voltage phases at the sending and receiving ends. For a lossless line, the theoretical steady-state maximum power transfer is reached when the power angle $\delta = 90^0$ as given in equation 2.1 [18]. The stability of the system cannot be maintained beyond this angle, [16, 19].

$$P = \frac{V_s V_R}{X} \sin \delta \qquad (2.1)$$

Where

P: Active power

V_S and V_R : Sending-end voltage and Receiving-end voltage

X : Line reactance

2.2 MAIN CONFIGURATION OF HVDC TRANSMISSION SYSTEMS

2.2.1 Monopolar

This link uses one conductor for transmission and utilises the ground, sea or a metallic conductor for return. The ground currents when the earth is used as a return path in a monopolar setup needs careful consideration and analysis to prevent high levels of interference with other utilities such as communication networks. The use of earth as return could impact negatively on the environment and the wellbeing of animals. Moreover, the reliability of ship navigation equipments and undersea systems could be compromised. The use of a metallic conductor as return is normally adopted in areas where the resistivity of the soil is too high [15, 20]. Figure 2.2 shows a monopolar HVDC link using the earth as a return path.

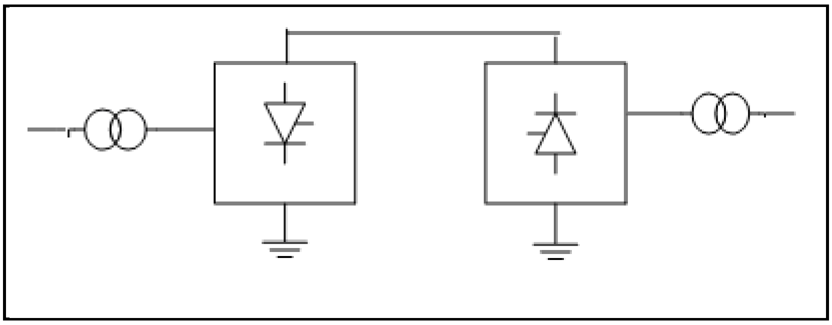

Figure 2.2 Monopolar DC Link Configuration [20]

2.2.2 Bipolar

The bipolar link has two conductors of negative and positive polarities. Each terminal in this configuration has two sets of converters whose ratings are identical. The junction between a set on each terminal is grounded as seen in figure 2.3. This type of HVDC link is more reliable than the monopolar link as one set of converters can still be in operation in the event of a disturbance, such as faults on the other set of converters [20].

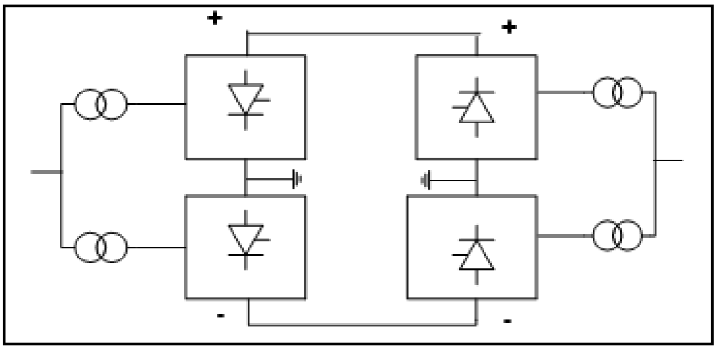

Figure 2.3 Bipolar DC Link Configuration [20]

In bipolar systems, ground wires are used to counter the effect of harmonic currents flowing through the ground, thereby reducing interference with communication networks [15, 20].

2.2.3 Back-to-Back

The existence of the back-to-back link is one of the major benefits of using HVDC transmission. This link can either be monopolar or bipolar and is used mainly to connect two asynchronous AC networks, i.e. networks which adopt different operating frequencies. From a global perspective, the whole of America, excluding Paraguay and Argentina, uses 60 Hz as its operating frequency. The rest of the world adopts the 50 Hz standard, with the exception of Japan which uses both frequencies.

2.2.4 Multi Terminal HVDC Links

This consists of several two-terminal HVDC systems. The first Multi-Terminal HVDC (MTDC) system was the Sardinia-Corsica-Italy scheme which was completed in 1991. MTDC schemes could be designed using two major configurations, namely, constant voltage parallel scheme and the constant current series scheme. In the parallel configuration, the converters are connected in parallel. This means that all the converters will operate at the same voltage. This configuration can either be a radial or a meshed connection. In the series configuration, the converters are connected in series, thereby allowing the same direct current to flow through them [19].

2.3 HVDC TRANSMISSION LINE TYPES

2.3.1 Overhead Lines

Overhead HVDC transmission lines offer a more economic solution to long distance bulk power transmission as opposed to HVAC. One of the reasons for this is that fewer conductors are used in it as compared with HVAC, especially in the monopolar HVDC transmission line configuration. Overhead transmission lines can be used for short, long and very long distances.

2.3.2 Underground and Submarine Cable

A cable is an assembly of one or more electrical conductors with a sheath covering the assembly. Between the conductors and the sheath are different layers of insulation. The type of insulation and the number of insulative layers used depends on the cable application. HV cables (i.e. AC or DC) usually have two or more insulative layers between the conductor and the sheath. Breakdowns in HVDC cables occur mainly due to the punctures within the insulative layers of the HVDC cable.

Due to the absence or very much reduced ionic motion (i.e. the movement of electrons in a conducting material) and large kinetic energy caused by the alternating nature of HVAC, the working stress of oil-impregnated paper-insulated cables used in HVDC transmission lines can be as high as 30-40 kV/mm. This is about three to four times higher than the 10 kV/mm in AC cables of the same insulation. Another advantage, in addition to the absence of high ionic motion in DC cables, is the reduction in the heat level of the cables which inherently reduces the power loss [20]. An example of submarine HVDC cable application is the 600 MW, 450 kV, monopole, 250 km HVDC transmission cable buried under the Baltic sea between Germany and Sweden. The submarine cable was chosen largely due to the unavailability of the right of way for overhead transmission [10].

2.4 HVDC TRANSMISSION LINE MODELLING

HVDC transmission lines can be modelled as a T or π model [21]. T or π models may not be adequate for a very long line where both precision and accuracy in models are important (i.e., for fast transient studies were travelling waves are of importance). In this case, distributed parameters line model should be used. The difference between HVDC and HVAC transmission lines is that HVAC transmission lines have a higher value of susceptance and reactance as opposed to HVDC transmission lines. Typical HVDC transmission line parameters are given in table 2.1.

Table 2-1 HVDC Transmission Line Impedances [15, 22, 23, 24, 25]

HVDC Line Impedance				
S/No	**R(Ω/Km)**	**L(mH/Km)**	**C(nF/Km)**	**Line voltage**
1	0.015	0.792	14.4	500
2	0.0281	2.249	10.06	500
3	0.0625	22.9	*	500
4	0.01	1	13	500
5	0.0029	12.5	260	500

2.4.1 Pie Model

Figure 2.4 shows the nominal π -model of a HVDC transmission line.

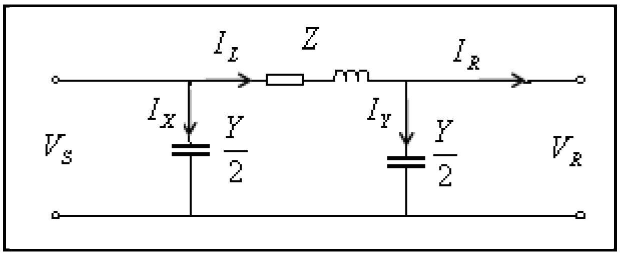

Figure 2.4 Nominal Pie (π) Circuit Model for HVDC Transmission Line

The equivalent impedance calculations are similar to the T-circuit equivalent. The sending end voltage and current for the nominal π-circuit model of the transmission line are derived in equations 2.3 to 2.9 [26].

$$I_L = I_R + I_Y \tag{2.3}$$

$$I_L = I_R + \frac{V_R Y}{2} \tag{2.4}$$

$$V_S = ZI_L + V_R \tag{2.5}$$

$$V_S = \left(1 + \frac{YZ}{2}\right)V_R + ZI_R \tag{2.6}$$

$$I_X = \frac{V_S Y}{2} \tag{2.7}$$

$$I_S = I_L + I_X \tag{2.8}$$

$$I_S = Y\left(1 + \frac{YZ}{4}\right)V_R + \left(1 + \frac{YZ}{2}\right)I_R \tag{2.9}$$

Where V_S : DC Voltage at the sending end of the HVDC transmission line

V_R: DC Voltage at the receiving end of the HVDC transmission line

I_S: DC Current at the sending end of the HVDC transmission line

I_R: DC Current at the receiving end of the HVDC transmission line

$Y/2$: Half of the total shunt admittance

I_X =Current through the shunt admittance at the sending end

I_Y =Current through the shunt admittance at the receiving end

Z = Impedance of the HVDC Transmission Line

2.4.2 T-Model

Figure 2.5 shows the T circuit equivalent of a HVDC transmission line.

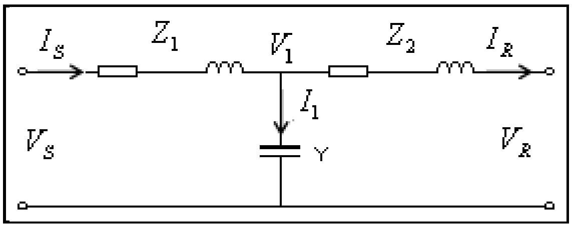

Figure 2.5 T-Circuit Model for HVDC Transmission Line

The sending end voltage and current for the T-circuit model of the transmission line are derived in equations 2.10 to 2.15 [26].

$$I_R = \frac{V_1 - V_R}{Z_2} \tag{2.10}$$

$$V_1 = V_R + Z_2 I_R \tag{2.11}$$

$$I_S = V_1 Y + \frac{V_1 - V_R}{Z_2} \tag{2.12}$$

From equations 2.11 and 2.12,

$$I_S = V_R Y + I_R (1 + Z_2 Y) \tag{2.13}$$

$$V_S = V_1 + Z_1 I_S \tag{2.14}$$

Substituting equations 2.11 and 2.13 into 2.14,

$$V_S = V_R(1 + Z_1 Y) + I_R(Z_1 + Z_2 + Z_1 Z_2 Y) \qquad (2.15)$$

Therefore, the sending end current and voltage are given by equations 2.13 and 2.15 respectively.

2.4.3 HVDC Transmission Line Frequency

The HVDC transmission line model comprises of passive components which are arranged in different forms depending on the model in question. These passive components include resistors, inductors and capacitors. Thus, modelling the transmission line correctly is largely dependent on the frequency used for calculating the line reactance. The HVDC transmission line operates in two major conditions, in steady state and also in the presence of transients. An investigation into the frequency range used for calculating the line parameters under both conditions (i.e. steady state condition and under transient conditions) indicated that, 5 Hz is used under steady state conditions and 90 Hz for the transients [20, 27]. Table 2.2 shows a range of frequencies used by different authors for this calculation.

Table 2-2 Typical Frequency Values for a HVDC Line

DC line Frequency			
S/No	**Steady state**	**High Frequency transients**	**References**
1	5 Hz	90 Hz	[13]
2	-	100 Hz	[22]
3	5 Hz	90 Hz	[20, 27]
4	5 Hz	90 Hz	[28]
5	2.5 Hz - 3.1 Hz	-	[29]

CHAPTER 3

AC To DC CONVERSION

Figure 3.1 shows the AC to DC conversion and DC to AC conversion. AC Power is generated at bus 1, it is converted to DC using a twelve-pulse rectifier and is transmitted over a HVDC transmission line to the inverter where the DC to AC conversion process takes place.

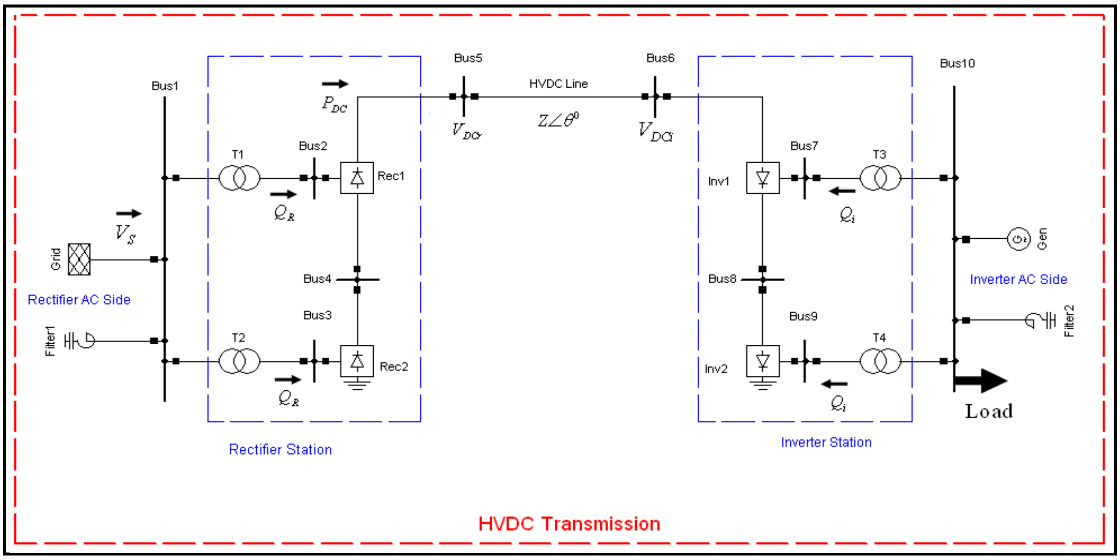

Figure 3.1 AC to DC Conversion and Transmission

Assuming the magnitude of the input line-to-neutral RMS AC voltage is V_S and V_A, V_B, V_C are the phase voltages,

$$\begin{cases} V_A = V_S \cos(\theta + 60^0) \\ V_B = V_S \cos(\theta - 60^0) \\ V_C = V_S \cos(\theta - 180^0) \end{cases} \tag{3.1}$$

Then, the line-to-line voltage between phase A and C is:

$$V_{AC} = V_A - V_C = \sqrt{3} V_S \cos(\theta + 30^0) \tag{3.2}$$

V_{BA} and V_{CB} can be derived similarly.

Since the conversion is a full wave three-phase rectification, a full cycle of 360^0 has six pulses separated by 60^0 each [21]. By integrating V_{AC} over a 60^0 period, the average DC voltage, V_{DC} is obtained taking the delay angle α into consideration at the rectifier [21].

$$V_{DC} = \frac{3}{\pi} \int_{-(60^0 - \alpha)}^{\alpha} V_{AC}\, d\theta \tag{3.3}$$

After integrating and neglecting commutation overlap,

$$V_{DC} = \frac{3\sqrt{2}}{\pi} V_S B.a.\cos\alpha \tag{3.4}$$

Where: B = Number of converter bridges

a = Transformer turns ratio

$$V_{DC(R)} = \frac{3\sqrt{2}}{\pi} V_{SR} B.a.\cos\alpha \tag{3.5}$$

$$V_{DC(I)} = \frac{3\sqrt{2}}{\pi} V_{SI} B.a.\cos\gamma \tag{3.6}$$

$$I_{DC}=\frac{V_{DC(R)}-V_{DC(I)}}{R_R+R_L+R_I} \tag{3.7}$$

Where: $V_{DC(R)}$ = Rectifier DC voltage

V_{SR} = Rectifier AC Voltage

$V_{DC(I)}$ = Inverter DC voltage

V_{SI} = Inverter AC Voltage

R_R = Resistance of the Rectifier

R_I = Resistance of the Inverter

R_L = Resistance of the HVDC Line

I_{DC} = DC line current

γ =Inverter extinction angle

α = firing angle

Hence from (3.5) and (3.7), the DC power output from the rectifier is given as follows:

$$P_{DC}=V_{DC(R)}*I_{DC} \tag{3.8}$$

3.1 HARMONICS AND REACTIVE POWER COMPENSATION

In HVDC transmission, harmonics are observed to be induced in the AC and DC sides of the converter stations. When these harmonics are present, they affect the Quality of Supply (QoS) and also may affect neighbouring telecommunication equipment that is close to the

HVDC transmission line. Other problems associated with harmonics are overvoltage due to resonances, instability of converter controls, overheating and power loss [21]. Although the twelve-pulse-phase shifted transformer converter bridge configuration seeks to reduce the harmonics, it is still important to use filters to further reduce the harmonics. Harmonics in AC and DC systems could either be characteristic or non-characteristic harmonics.

The AC characteristic harmonics are in the order of

$$h = np \pm 1$$

where p is the pulse number and n is any integer.

The DC characteristic harmonics are

$$h = np$$

In general, harmonics that are not of the order of the characteristic harmonics are non-characteristic harmonics [20].

3.2 AC AND DC FILTERS

AC and DC filters are used to mitigate the effects of harmonics in power systems. These filters are normally tuned or double tuned filters [21]. The series smoothing reactor, a DC element which will be discussed in section 3.4, also acts as a DC filter which is in series with the HVDC transmission line. For the AC side, figures 3.2 and 3.3 show some filter configurations that could be used for the 3rd, 5th and 7th AC harmonics. These filters are connected to the AC bus of the rectifier and inverter stations.

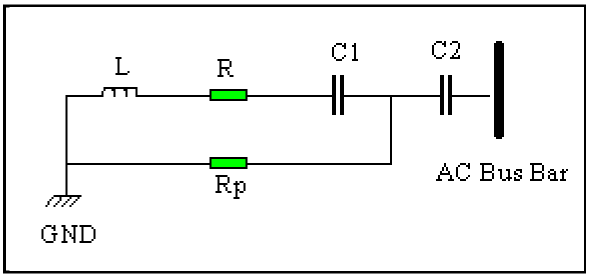

Figure 3.2 AC Filter

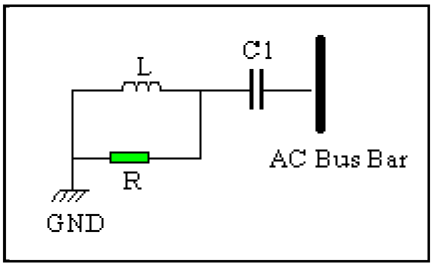

Figure 3.3 Tuned filter for one harmonic

3.3 REACTIVE POWER COMPENSATION

AC filters serve as a source of reactive power to the system, in addition to playing a major role in harmonic reduction and mitigation.

Furthermore, capacitor banks are used to increase the reactive power compensation as required by the load and the converter stations. According to Kundur [19], under steady state conditions the reactive power consumed is about 50% of the active power transferred and under transient conditions; the reactive power consumption is much higher.

It is important that high emphasis be placed on reactive power compensation. When this is not properly considered during system design, generating plants could be forced to supply more reactive power to the extent that the reactive power supply is far more than the active power supply leading to a scenario where the power factor becomes very small. A reasonable range of power factor operation should be between 0.8 and 0.95.

3.4 SMOOTHING REACTORS

Smoothing reactors, in addition to limiting the discharge during faults on HVDC transmission lines, are used to improve the DC current waveform. Two series reactors are normally used in series with the HVDC line, one at the rectifier DC side and the other at the DC end of the inverter. Another application of smoothing reactors can be seen on the AC side of each of the converter stations where they are used to limit the impact of converter to ground faults

[13]. Normally, the DC line short circuit current and the [1]Short Circuit Ratio (SCR) [16] are used to determine the size of the series reactor. In practice, this is limited to a range of 0.5 H to 1.0 H [20].

While the current waveform improves with increasing inductance (i.e. size of the reactor), [20], there have been some reports suggesting that increasing the inductance of the reactor slows down the control response and reduces the resonance frequency which makes current control a more difficult task [20].

Tests conducted in 1989 and 1990 on a weak inverter station indicated that increasing the size of the series reactor increased the fault detection time from 16 ms to 25 ms [30]. From these results, and in terms of the stability of the HVDC link, an increase in fault detection time is not desirable. Nevertheless, a reduction in the fault detection time can be achieved using fast signal processors [30]. Table 3.1 shows the typical values of HVDC transmission line series reactors.

Table 3.1 Typical Values of HVDC Line Series Reactors

Series Reactors				
S/No	**SCR**	**Rectifier side (H)**	**Inverter side (H)**	**Reference**
1	3.5	0.3 - 0.8	-	[30]
2	3.5	-	0.3 - 0.4	[30]
3	1.5 - 2.7	-	0.6 - 2.2	[30]
4	-	0.75	0.75	[25]
5	-	0.5 - 1.0	0.5 - 1.0	[20]
6	3.5 - 14.5	0.75	0.75	[28]
7	3.2 - 10	0.04 - 0.08	0.04 - 0.08	[31]
8	3.5	0.6 - 0.8	0.4 - 2.2	[29]

---

[1] SCR is the ratio of the Short Circuit Level (MVA) of the AC system at the converter bus to the Rated DC power (MW)

CHAPTER 4

LOAD FLOW ANALYSIS

Load flow (power flow) analysis can be defined as a process which is aimed at ascertaining the voltage magnitude, voltage angle, active power and reactive power at various nodes in a power system operating under steady state conditions. This analysis assists system engineers to determine the stress on the power system in terms of its loading and its operation with respect to normal conditions. Furthermore, load flow analysis gives an indication of areas in the power system that may need capacity expansion due to increase in load demand. Several methods have been developed to analyse the load flow condition on power systems which includes Gauss-Seidel, Newton-Raphson, decoupled and the fast decoupled load flow method. These methods are mainly deployed on HVAC systems. Moreover, for systems with HVDC transmission lines the Newton-Raphson method has been adapted to include the DC parameters that originate from the HVDC transmission scheme [6, 32]. The advantages and limitations of the above methods can be found in [6, 16, 32]. There are three fundamental bus type classifications in load flow analysis. The first bus type is the swing bus which is also referred to as the reference or slack bus. At this bus, the voltage magnitude and the phase angle are specified. The second bus type is the PV bus, also known as the generator or voltage controlled bus. Here the voltage magnitude and the active power are specified. The third bus type is the PQ bus, also known as the load bus. At this bus the active and reactive powers are specified [6].

4.1 HVAC LOAD FLOW

In this section, the Newton-Raphson load flow method will be used to determine the HVAC load flow. This method, which is also adopted by DigSILENT, uses an iterative technique for solving a set of simultaneous nonlinear equations. In doing this, rectangular or polar coordinates can be used in defining the bus voltages and line admittances. In this thesis, the polar coordinates will be used.

Assuming a power system with bus 1, 2, 3……n

The net complex power injected at bus k is given as

$$S_k^* = P_k - jQ_k = V_k^* I_k = |V_k|\angle - \delta_k \sum_{i=1}^{N} |Y_{ki} V_i| \angle(\theta_{ki} + \delta_i) \qquad (4.1)$$

where θ_{ki} is the angle of the admittance Y_{ki}.

δ_i and δ_k are the phase angles of the bus voltages V_i and V_k respectively

When separating the real and imaginary parts of equation 4.1, we get

$$P_k = \sum_{i=1}^{N} |Y_{ki} V_i V_k| cos(\theta_{ki} + \delta_i - \delta_k) \qquad (4.2)$$

$$= |V_k^2 Y_{kk}| \cos(\theta_{kk}) + \sum_{i \neq k}^{N} |Y_{ki} V_i V_k| cos(\theta_{ki} + \delta_i - \delta_k) \; k = 2, 3, \ldots., N \qquad (4.3)$$

$$Q_k = -\sum_{i=1}^{N} |Y_{ki} V_i V_k| sin(\theta_{ki} + \delta_i - \delta_k) \qquad (4.4)$$

$$= -|V_k^2 Y_{kk}| \sin(\theta_{kk}) - \sum_{i \neq k}^{N} |Y_{ki} V_i V_k| sin(\theta_{ki} + \delta_i - \delta_k) \; k = 2, 3, \ldots., N \qquad (4.5)$$

Equations 4.3 and 4.5 give a set of non-linear algebraic equations in terms of the voltage magnitude in pu and phase angle in radians which are all independent variables.

Assuming that all system busbars are PQ bus except the slack bus, the active and reactive power at each bus is specified. This means that each of the other buses with the exception of the slack bus has two variables δ_k and $|V|_k$ to be calculated in the load flow solution.

Therefore, the power mismatches $\Delta P_k^{(i)}$ and $\Delta Q_k^{(i)}$ are the difference between the scheduled and calculated values of the active and reactive power respectively at bus k in the i^{th} iteration. This is given by equation 4.6.

$$\left.\begin{aligned} \Delta P_k^{(i)} &= P_k^{sch} - P_k^{(i)} \\ \Delta Q_k^{(i)} &= Q_k^{sch} - Q_k^{(i)} \end{aligned}\right\} \qquad (4.6)$$

For the load bus:

$$\left.\begin{array}{c} P_k^{sch} < 0 \\ \text{and} \\ Q_k^{sch} < 0 \end{array}\right\} \text{if the load is inductive.}$$

While

$$\left.\begin{array}{c} P_k^{sch} < 0 \\ \text{and} \\ Q_k^{sch} > 0 \end{array}\right\} \text{if the load is capacitive.}$$

For each load bus we have two of these equations given by (4.3) and (4.5), and one equation given by (4.3) for each PV bus. Expanding equations (4.3) and (4.5) in Taylor's series about the initial estimate and neglecting all higher order terms will result in equation 4.7.

$$\begin{bmatrix} \Delta P_2^{(i)} \\ \cdots \\ \Delta P_N^{(i)} \\ \Delta Q_2^{(i)} \\ \cdots \\ \Delta Q_N^{(i)} \end{bmatrix} = \begin{bmatrix} \frac{\partial P_2^{(i)}}{\partial \delta_2} & \cdots & \frac{\partial P_2^{(i)}}{\partial \delta_N} & \frac{\partial P_2^{(i)}}{\partial |V_2|} & \frac{\partial P_2^{(i)}}{\partial |V_N|} \\ \cdots & \cdots & \cdots & \cdots & \cdots \\ \frac{\partial P_N^{(i)}}{\partial \delta_2} & \cdots & \frac{\partial P_N^{(i)}}{\partial \delta_N} & \frac{\partial P_N^{(i)}}{\partial |V_2|} & \frac{\partial P_N^{(i)}}{\partial |V_N|} \\ \frac{\partial Q_2^{(i)}}{\partial \delta_2} & \cdots & \frac{\partial Q_2^{(i)}}{\partial \delta_N} & \frac{\partial Q_2^{(i)}}{\partial |V_2|} & \frac{\partial Q_2^{(i)}}{\partial |V_2|} \\ \cdots & \cdots & \cdots & \cdots & \cdots \\ \frac{\partial Q_N^{(i)}}{\partial \delta_2} & \cdots & \frac{\partial Q_N^{(i)}}{\partial \delta_N} & \frac{\partial Q_N^{(i)}}{\partial |V_2|} & \frac{\partial Q_N^{(i)}}{\partial |V_N|} \end{bmatrix} \begin{bmatrix} \Delta \delta_2^{(i)} \\ \cdots \\ \Delta \delta_N^{(i)} \\ \Delta |V_2^{(i)}| \\ \cdots \\ \Delta |V_N^{(i)}| \end{bmatrix} \tag{4.7}$$

In equation 4.7, bus 1 is excluded in the matrix because it is assumed to be the swing bus.

We can summarise equation 4.7 above, as written in equation 4.8.

$$\begin{bmatrix}\Delta \boldsymbol{P}\\ \Delta \boldsymbol{Q}\end{bmatrix} = \overbrace{\begin{bmatrix}\mathbf{J_1} & \mathbf{J_2}\\ \mathbf{J_3} & \mathbf{J_4}\end{bmatrix}}^{\mathrm{J}}\begin{bmatrix}\Delta \boldsymbol{\delta}\\ \Delta|\boldsymbol{V}|\end{bmatrix} \tag{4.8}$$

Matrix **J** is called the Jacobian matrix whose elements are partial derivatives of equations 4.3 and 4.5 with respect to $\delta_k^{(i)}$ and $|V_k^{(i)}|$. The Jacobian matrix gives the linearised relationship between changes in voltage angle and voltage magnitude with the small changes in the real and reactive power [6, 19].

For voltage controlled (PV) bus, the voltage magnitudes are known. Therefore, if *m* buses of the system are voltage-controlled, *m* equations involving $\Delta \boldsymbol{Q}$ and $\Delta \boldsymbol{V}$ and corresponding columns of the Jacobian matrix are eliminated. Accordingly, there are *n*-1 real power constraints and n-1-m reactive power constraints and the Jacobian matrix is of order (2*n*-2-*m*) x (2*n*-2-*m*).

The diagonal and off-diagonal elements if **J₁** are

$$\frac{\partial P_k}{\partial \delta_k} = \sum_{j=1, j\neq k}^{N} |Y_{kj}V_k V_j| \sin(\theta_{kj} + \delta_j - \delta_k) \tag{4.9}$$

$$\frac{\partial P_k}{\partial \delta_j} = -|Y_{kj}V_kV_j| \sin(\theta_{kj} + \delta_j - \delta_k) \qquad j \neq k \tag{4.10}$$

The diagonal and off-diagonal elements if **J₂** are

$$\frac{\partial P_k}{\partial |V_k|} = 2|V_kY_{kk}|\cos(\theta_{kk}) + \sum_{j=1, j\neq k}^{N} |Y_{kj}V_j| \sin(\theta_{kj} + \delta_j - \delta_k) \tag{4.11}$$

$$\frac{\partial P_k}{\partial |V_j|} = \left|Y_{kj}V_k\right| \cos(\theta_{kj} + \delta_j - \delta_k) \qquad j \neq k \tag{4.12}$$

The diagonal and off-diagonal elements if **J₃** are

$$\frac{\partial Q_k}{\partial \delta_k} = \sum_{j=1, j\neq k}^{N} |Y_{kj} V_k V_j| \cos\,(\theta_{kj} + \delta_j - \delta_k) \tag{4.13}$$

$$\frac{\partial Q_k}{\partial \delta_j} = -\left|Y_{kj} V_k V_j\right| \cos\left(\theta_{kj} + \delta_j - \delta_k\right) \qquad j \neq k \tag{4.14}$$

The diagonal and off-diagonal elements if **J₄** are

$$\frac{\partial Q_k}{\partial |V_k|} = -2|V_k Y_{kk}| \sin(\theta_{kk}) - \sum_{j=1, j\neq k}^{N} |Y_{kj}\, V_j| \sin\,(\theta_{kj} + \delta_j - \delta_k) \tag{4.15}$$

$$\frac{\partial Q_k}{\partial |V_j|} = -\left|Y_{kj} V_k\right| \sin\,(\theta_{kj} + \delta_j - \delta_k) \qquad j \neq k \tag{4.16}$$

Once the Jacobian Matrix J has been calculated, the new estimates for bus voltage magnitude and angle are given by:

$$\left.\begin{aligned} \delta_k^{(i+1)} &= \delta_k^{(i)} + \Delta\delta_k^{(i)} \\ |V_k^{(i+1)}| &= |V_k^{(i)}| + \Delta|V_k^{(i)}| \end{aligned}\right\} \tag{4.17}$$

In case of PV bus there are some limits imposed on the reactive power

The next step will be to re-evaluate equations 4.3 to 4.17 using the new values obtained in equation 4.17 as the initial condition for the next iteration. This will be repeated until the power mismatches given in equation 4.6 are less than the specified tolerance which is usually $\varepsilon \cong 10^{-5}$.

4.2 HVAC-HVDC LOAD FLOW

Conventional iterative techniques for load flow calculations are used mainly for AC systems which include Gauss Seidel, Newton-Raphson and the fast decoupled techniques. Correspondence with DigSILENT shows that the algorithm used for HVAC-HVDC load flow calculation is similar to the one given in section 4.1. In this section, the decoupled Newton's load flow method will be used for the HVAC and HVDC load flow in HVAC- HVDC power systems [32, 33]. However, this algorithm still needs to be tested using software like matlab.

4.2.1 AC – DC System Bus interrelation

In general, AC power systems can be defined in terms of a set of independent variables as seen in equation 4.18.

$$[\overline{V},\overline{\delta}]^T \tag{4.18}$$

where $\vec{V}$ is a vector of all the AC system bus voltage magnitudes

$\overline{\delta}$ is a vector of all the AC system busbar voltage angles.

Assuming that there is a power system with bus k, the active and reactive power at bus k is given by equations 4.2 to 4.5, but for convenience it has been reproduced in equations 4.19 to 4.22

$$P_k = \sum_{i=1}^{N} |Y_{ki}\, V_i V_k| cos(\theta_{ki} + \delta_i - \delta_k) \tag{4.19}$$

$$= |V_k^2 Y_{kk}| \cos\, (\theta_{kk)} + \sum_{i \neq k}^{N}\, |Y_{ki}\, V_i V_k| cos(\theta_{ki} + \delta_i - \delta_k)\ k =\ 2, 3, \dots., N \tag{4.20}$$

$$Q_k = -\sum_{i=1}^{N} |Y_{ki}\, V_i V_k| sin(\theta_{ki} + \delta_i - \delta_k) \tag{4.21}$$

$$= -|V_k^2 Y_{kk}|\sin(\theta_{kk}) - \sum_{i\neq k}^{N} |Y_{ki} V_i V_k| sin(\theta_{ki} + \delta_i - \delta_k) \; k = 2, 3, \ldots., N \qquad (4.22)$$

To accommodate the HVDC system in the conventional Newton-Raphson's load flow method for an AC power system, certain modifications need to be made. New equations with variables have to be included in the conventional algorithm. The new variables for an HVAC-HVDC system are defined as

$$[\vec{V}, \vec{\delta}, \vec{X}]^T \qquad (4.23)$$

$\overline{X}$ is a vector of all the DC variables.

At the converter terminals, the real and reactive power is given by equations 4.24 and 4.25.

$$P_T{}^L - P_{T(AC)} = P_{T(DC)} \qquad (4.24)$$

$$Q_T{}^L - Q_{T(AC)} = Q_{T(DC)} \qquad (4.25)$$

Where:

$P_{T(AC)}$ is the injected real power at the terminal busbar as a function of AC system variables

$Q_{T(AC)}$ is the injected reactive power at the terminal busbar as a function of AC system variables

$P_{T(DC)}$ is the injected real power at the terminal busbar as a function of the DC system variables

$Q_{T(DC)}$ is the injected reactive power at the terminal busbar as a function of the DC system variables

P_T^L is the real power absorbed by the system load

Q_T^L is the reactive power absorbed by the system load .

The injected DC power $P_{T(DC)}$ and $Q_{T(DC)}$ can be written as functions of DC system variables and the converter AC terminal busbar voltage in equation 4.26 and 4.27.

$$P_{T(DC)} = f(V_T, \overline{X}) \tag{4.26}$$

$$Q_{T(DC)} = f(V_T, \overline{X}) \tag{4.27}$$

Where V_T represents the AC terminal busbar voltage

The equation derived from the AC-system condition is summarised as

$$\begin{bmatrix} \Delta\vec{P}(\vec{V},\overline{\theta}) \\ \Delta\vec{P}_T(\vec{V},\overline{\theta},\overline{X}) \\ \Delta\vec{Q}(\vec{V},\overline{\theta}) \\ \Delta\vec{Q}_T(\vec{V},\overline{\theta},\overline{X}) \\ \end{bmatrix} = 0 \tag{4.28}$$

Where the mismatches at the converter terminal buses are indicated by equation 4.29 as:

$$\vec{R} = (V_T, \overline{X})_K = 0 \tag{4.29}$$

k =1,... m, where m is the number of converters present in the system.

To improve the performance of the calculation algorithm and decoupling of the AC and DC system variables, the angle reference for the DC system variables are chosen separately from that of the AC system variables [32].

Therefore, the general solution of the AC–DC power flow problem can be written in equation 4.30 [16, 20] as:

$$\begin{bmatrix} \Delta\vec{P}(\vec{V},\overline{\theta}) \\ \Delta\vec{P}_T(\vec{V},\overline{\theta},\overline{X}) \\ \Delta\vec{Q}(\vec{V},\overline{\theta}) \\ \Delta\vec{Q}_T(\vec{V},\overline{\theta},\overline{X}) \\ \vec{R}(\vec{V}_T,\overline{\theta},\overline{X}) \end{bmatrix} = 0 \qquad (4.30)$$

4.2.2 Identifying the Matrix of DC Variable, $[\overline{X}]$

In order to identify the matrix of DC variables we shall consider figure 4.1 which details the AC side to the rectifier station of a HVDC scheme. The angles are with reference to the DC system.

To determine $\vec{X}$, the vector of DC variables, several basic assumptions which are generally accepted in the analysis of steady-state AC-DC converter operations are required. Such assumptions include that the AC system voltages and converter operation are balanced and the DC side voltage and current have no component of the AC voltage and current respectively. Furthermore, the HVDC converter transformer is assumed to be lossless.

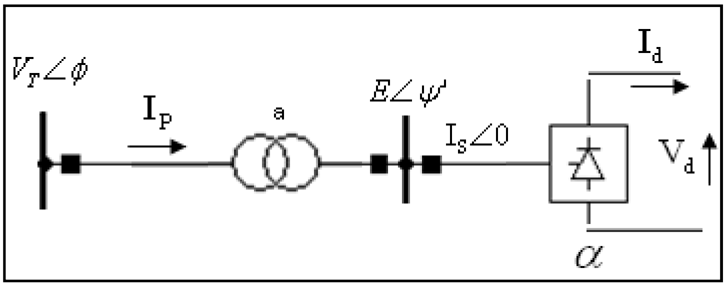

Figure 4.1 HVAC- HVDC Converter Terminal [32]

In figure 4.1,

I_d and V_d are converter DC current and voltage respectively

a is the transformer off – nominal tap ratio

α is the converter firing angle

I_P and I_S are the converter transformer's AC current on the primary and secondary sides, respectively.

$E\angle\psi$ is the secondary voltage of the converter transformer

$V_T\angle\phi$ is the AC terminal voltage (with phase angle referred to the DC system reference).

All the aforementioned variables are possible candidates for the matrix of DC variables. It should be noted that the real and reactive power are not included because they are both dependant on the variables listed above [32].

It should be noted that only two independent variables are sufficient to model a HVDC converter which is operating under balanced conditions from a known terminal voltage source. However, the control specifications of HVDC converters are such that a range of variables are used. Since the control specifications (e.g., constant power) in HVDC converters are usually a function of independent variables, the matrix of DC variables must be chosen such that it contains all the necessary independent variables that will also satisfy the control requirements [19, 32].

Examples of HVDC control specifications are given in equation 4.31.

$$\left.\begin{aligned} &a-a^{sp}=0\\ &I_d-I_d^{\;sp}=0\\ &cos\alpha-\cos\alpha_{\min}=0\\ &V_d*I_d-P_{DC}^{\;sp}=0 \end{aligned}\right\} \qquad (4.31)$$

Where P_{DC}^{sp} is the specified DC power

α is the converter firing angle

I_d and I_d^{sp} are the actual and the rated converter DC current , respectively.

a and a^{sp} are the actual and the specified converter transformer off-nominal tap ratio respectively

Therefore, the derived matrix of DC variables is given in equation 4.32.

$$[\bar{X}] = [V_d\ , I_d, a, cos\alpha\ ] \tag{4.32}$$

4.2.3 Further Definitions towards $P_{T(DC)}$ and $Q_{T(DC)}$

To avoid per unit to actual value conversion and to unify convergence tolerance for both AC and DC system quantities, a per unit system is adopted for the DC quantities.

To do this the same power and voltage base parameters are used on both AC and DC sides of the converter. As a result the direct current base obtained directly from (MVA_B/V_B) has to be multiplied by the AC current base.

For a smooth DC and neglecting commutation overlap, the r.m.s fundamental component of the phase current is related to I_d by equation 4.33.

$$I_s = \frac{\sqrt{6}}{\pi} I_d \tag{4.33}$$

When the commutation overlap and per unit are taken into consideration, equation 4.33 can be written as equation 4.34.

$$I_{s(p.u)} = k\frac{3\sqrt{2}}{\pi} I_{d(p.u)} \tag{4.34}$$

Therefore, the per unit relationship for the variables in figure 4.1 can be defined as follows in equation 4.35 and 4.36.

$$I_s = k\frac{3\sqrt{2}}{\pi} I_d \tag{4.35}$$

$$I_p = a\, I_s \tag{4.36}$$

Equation 4.35 gives the relationship between the converter AC side current magnitude and the direct current. Equation 4.36 relates the current magnitude on both sides of the converter transformer through the off-nominal tap ratio.

The DC voltage can be written in terms of the AC source voltage referred to the transformer secondary side in equation 4.37.

$$V_d = \left[\frac{3\sqrt{2}}{\pi} aV_T cos\alpha\right] - \left[\frac{3}{\pi} I_d X_c\right] \tag{4.37}$$

Where V_T is the AC source voltage.

The DC power is related to the transformer secondary power in terms of fundamental components, as given in equation 4.38.

$$V_d I_d = EI_s cos\psi \tag{4.38}$$

The primary real power for a lossless transformer is equal to the DC power as given in equation 4.39

$$V_d I_d = V_T I_p cos\phi \tag{4.39}$$

So far, equations 4.33 to 4.39 have been derived in terms of the converter variables.

The equations for $P_{DC}\ and\ Q_{DC}$ can be written as;

$$Q_{T(DC)} = V_T I_p sin\phi \tag{4.40}$$

$$P_{T(DC)} = V_T I_p cos\phi \qquad (4.41)$$

Substitution equations 4.35 and 4.36 in equation 4.40;

$$Q_{T(DC)} = V_T \frac{\sqrt[3]{2}}{\pi} k a I_d sin\phi \qquad (4.42)$$

Substitution equations 4.35 and 4.36 in equation 4.41;

$$P_{T(DC)} = V_T \frac{\sqrt[3]{2}}{\pi} k a I_d cos\phi \qquad (4.43)$$

4.2.4 Combined AC-DC solution and Simplification

The combined AC-DC solution takes into account the interdependence of AC and DC system equations to solve the complete AC-DC system. Hence equation 4.31 can be re-written as equation 4.44 where J is the Jacobian (the matrix of partial derivatives) [16, 32].

$$\begin{bmatrix} \Delta\vec{P}(\vec{V},\overline{\theta}) \\ \Delta\vec{P}_T(\vec{V},\overline{\theta},\overline{X}) \\ \Delta\vec{Q}(\vec{V},\overline{\theta}) \\ \Delta\vec{Q}_T(\vec{V},\overline{\theta},\overline{X}) \\ \vec{R}(\vec{V}_T,\overline{\theta},\overline{X}) \end{bmatrix} = \left[\vec{J}\right] \begin{bmatrix} \Delta\overline{\theta} \\ \Delta\overline{\theta}_T \\ \Delta\vec{V} \\ \Delta\vec{V}_T \\ \Delta\overline{X} \end{bmatrix} \qquad (4.44)$$

By applying the fast decoupled assumptions to all elements of the Jacobian matrix which are related to the AC system, we get the following:

$$\begin{bmatrix} \Delta\vec{P}/\vec{V} \\ \Delta\vec{P}_T/\vec{V}_T \\ \Delta\vec{Q}/\vec{V} \\ \Delta\vec{Q}_T/\vec{V} \\ \vec{R} \end{bmatrix} = \begin{bmatrix} \mathrm{B'} & \mathrm{B'} & 0 & 0 & 0 \\ \mathrm{B'} & \mathrm{B'} & 0 & 0 & \mathrm{AA'} \\ 0 & 0 & \mathrm{B''} & \mathrm{B''} & 0 \\ 0 & 0 & \mathrm{B''} & \mathrm{B''}_{\mathrm{ii}} & \mathrm{AA''} \\ 0 & 0 & 0 & \mathrm{BB''} & \mathrm{A} \end{bmatrix} . \begin{bmatrix} \Delta\bar{\theta} \\ \Delta\bar{\theta}_T \\ \Delta\vec{V} \\ \Delta\vec{V}_T \\ \Delta\bar{X} \end{bmatrix} \tag{4.45}$$

Where:

$$B'_{km} = -\frac{1}{X_{km}} \text{ for m} \neq \text{k} \tag{4.46}$$

$$B'_{kk} = \sum_{mwk} \frac{1}{X_{km}} \tag{4.47}$$

$$B''_{km} = -B_{km} \quad \text{for m} \neq \text{k} \tag{4.48}$$

$$B''_{kk} = \sum_{mwk} B_{km} \tag{4.49}$$

$$BB'' = \partial\bar{R}/\partial V_T \tag{4.50}$$

[B’] and [B’’] are kept constant

$$[AA'] = \frac{1}{V_T}[\partial\Delta P_T/\partial\bar{X}] \tag{4.51}$$

$$= \frac{1}{V_T}[\partial P_{T(AC)} / \partial \overline{X}] + \frac{1}{V_T}[\partial P_{T(DC)} / \partial \overline{X}] \tag{4.52}$$

hence,

$$[AA'] = 0 + \frac{1}{V_T}[\partial P_{T(DC)} / \partial \overline{X}] \tag{4.53}$$

Similarly,

$$[AA''] = \frac{1}{V_T}[\partial \Delta Q_T / \partial \overline{X}] \tag{4.54}$$

$$= \frac{1}{V_T}[\partial Q_{T(DC)} / \partial \overline{X}] \tag{4.55}$$

$$[A] = \partial \overline{R} / \partial \overline{X} \tag{4.56}$$

$$B''_{ii} = \frac{1}{V_T}[\partial \Delta Q_T / \partial V_T] \tag{4.57}$$

$$= \frac{1}{V_T}\partial Q_{T(AC)} / \partial V_T + \frac{1}{V_T}[\partial Q_{T(DC)} / \partial V_T] \tag{4.58}$$

This method proposed by [32] from equation 4.18 to 4.58 should be coded in Mathlab and tested on the hybrid HVAC-HVDC system model that is developed in this thesis.

CHAPTER 5

HVDC TRANSMISSION AND CONTROL

In order to fully maximize the benefits of HVDC transmission, adequate control measures must be adopted to coordinate the behaviour and performance of the rectifier and the inverter. This will prevent system collapse or damage to network components.

Moreover, HVDC control also prevents large fluctuations in the direct current due to possible variation in the AC system voltage. Other benefits of adequate HVDC control include reduced system unplanned downtimes, maintaining the DC voltage close to 1.0 per unit values as may be required by industry regulations, and the prevention of commutation failures.

In [19] it was stated that under the normal operation of a HVDC transmission link, the AC systems should operate at a high power factor. Moreover, the HVDC converters should operate under a low firing angle and an extinction angle. According to [19, 20], the minimum firing angle allowed for the rectifier is $5^{0,}$ but ideally the minimum firing angle ranges from 15^{0} to 20^{0} with a maximum of about 75^{0} while for the inverter, the typical operating extinction angle is 15^{0} for 50 Hz systems [19, 20]. All these can only be achieved through adequate control measures.

Furthermore, current and voltage controls which are normally separated and handled by separate converters allows for a complete control over the whole system which includes reactive power, active power, DC voltage and current. Under normal operation, the rectifier controls the flow of DC current using a control mode called Constant Current (CC) control mode while the inverter controls the DC voltage using a control mode called the Constant Extinction Angle (CEA) control mode [19].

5.1 IDEAL STEADY STATE V-I CHARACTERISTICS OF HVDC CONTROL

The converter control voltage and current characteristics are illustrated in figure 5.1 which is called the V-I characteristics curve. The current is shown on the horizontal axis while the voltage is shown on the vertical axis.

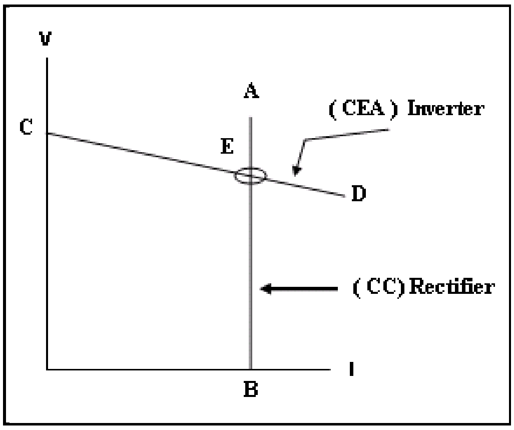

Figure 5.1 Ideal Steady State V-I Characteristics

Normally, a converter is designed to function as a rectifier or inverter and hence, its operating condition is defined by the point E shown in figure 5.1. This satisfies both the rectifier and the inverter functions [17, 19]. To control the DC current (I_d) on the HVDC transmission line, the current order I_{ord} (i.e. the desired current set point) can be adjusted, thus changing the rectifier characteristics.

The direct current I_d on the HVDC transmission line is defined as a function of the converter resistance, the AC voltage and firing angle of the rectifier, the AC voltage and extinction angle of the inverter and the resistance of the HVDC line as given in equation 5.1.

$$I_d = \frac{V_{dor}\cos\alpha - V_{doi}\cos\gamma}{R_{cr} + R_L - R_{ci}} \qquad (5.1)$$

Where:

V_{dor} is the ideal no-load direct voltage at the rectifier

V_{doi} is the ideal no-load direct voltage at the inverter

α is the ignition delay (firing) angle

γ is the extinction advance angle

R_{cr} reactance of the rectifier

R_{ci} reactance of the inverter

R_L resistance of the HVDC transmission line.

When the measured current I_d on the HVDC line is less than the current order I_{ord} (i.e. the desired current set point), the current regulator decreases the firing angle of the rectifier which leads to an increase in the DC current on the HVDC line. For the inverter, the tapping of the inverter transformer can either be lowered or raised. It should be mentioned here that during the process of transformer tap adjustment the extinction angle of the inverter alters, but the Constant Extinction Angle (CEA) regulator immediately resorts to the required extinction advance angle (γ).

In actual systems, the rectifier current control may not be a perfect straight line as depicted in figure 5.1, but has a negative slope as indicated in figure 5.2. This is especially the case with current regulators that uses proportional controllers. These regulators are built with an infinite gain and hence contribute to the negative slope as reflected in figure 5.2 [19, 34].

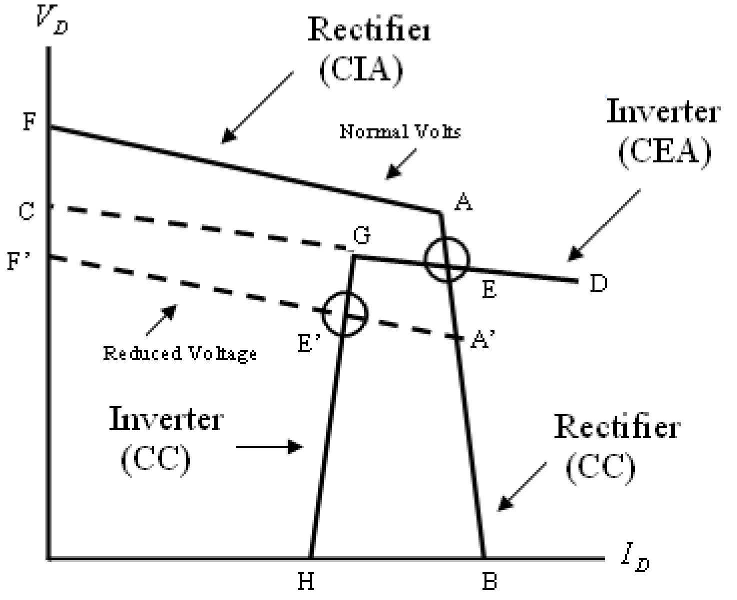

Figure 5.2 Actual V-I Characteristics of HVDC Converters

5.2 ACTUAL V-I CHARACTERISTICS OF HVDC CONTROL

The rectifier uses Constant Current (CC) control to maintain the DC power on the HVDC link. The DC voltage is set by the inverter and the rectifier adjusts to maintain the current flowing in the HVDC line. Moreover, there is a minimum firing angle allowed for rectifier operation which is about 5^0 [19]. This means that Constant Current control cannot be fully adopted to control the power on the HVDC link when the rectifier is in a state where the firing angle needs to be reduced below 5^0 [13, 19]. In actual HVDC schemes the rectifier is equipped with the capability to operate under the two modes, namely, Constant Current and Constant Ignition Angle. In figure 5.2, the Constant Current control region is shown by line AB and the Constant Ignition Angle by line FA.

When there is a reduced voltage at the inverter side as represented by F'A'B in figure 5.2, the current and the power reduces to zero for a short time. To avoid this, the inverter operation is modified to DGH as seen in figure 5.2.

In figure 5.2, H represents the current order of the inverter $I_{ord(I)}$ and B represents the current order of the rectifier $I_{ord(R)}$. The difference between the two points is the current margin (I_M) as given in equation 5.2. The current margin is normally set to a value that lies within 10% to 15% of the rated current. Equation 5.3 shows the current margin as a fraction of the rated current. This is done to avoid overlapping the inverter and rectifier characteristics.

$$I_M = I_{ord(R)} - I_{ord(I)} \tag{5.2}$$

$$I_M = AI_S \tag{5.3}$$

$$I_{ord(I)} = I_{ord(R)} - AI_S \tag{5.4}$$

Where I_S = Rated current

A = Positive real number between 0.1 and 0.15.

Under steady-state operation, the rectifier is set to control the current while the voltage is controlled by the inverter which is represented by E in figure 5.2.

During large transients conditions such as a large reduction in voltage, the rectifier switches to the CIA while the inverter switches to the CC which represents E’ in figure 5.2. This process is called the mode shift [13, 19].

5.3 DUAL CHARACTERISTICS OF HVDC CONVERTERS

Since there is a possibility of power flow reversal on HVDC transmission lines by reversing the polarity of the voltage, each converter is equipped with both rectifier and inverter characteristics. This characteristic is represented by figure 5.3.

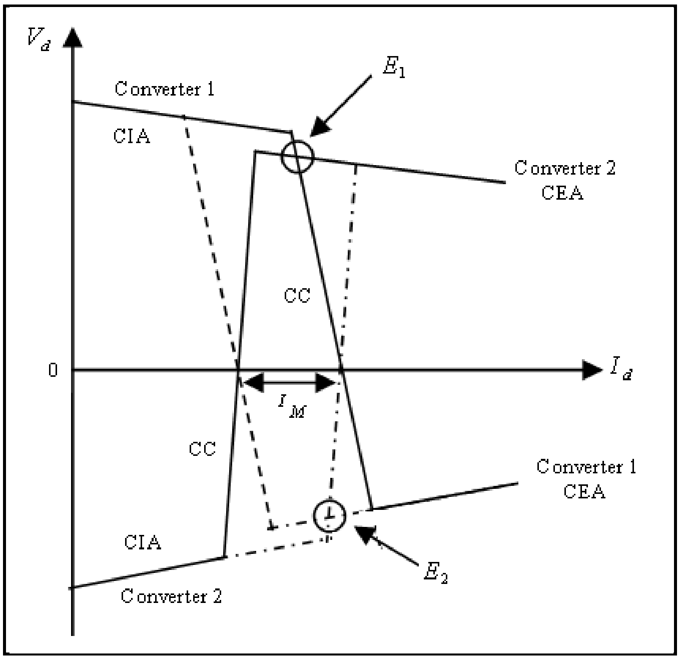

Figure 5.3 Dual Characteristics of HVDC Converters

Each of the converter characteristics is in three segments, namely, CC, CEA and CIA, which correspond to an operating condition when the minimum firing angle is reached [16, 27]. The dotted line in figure 5.3 shows the transfer of power from converter 2 to converter 1, where converter 1 is the rectifier and converter 2 is the inverter. This operating condition is indicated by E_2. When the margin is reversed by making the current order setting of converter 1 exceed that of converter 2, the flow of power is from converter 1 to converter 2 where converter 1 is the rectifier and converter 2 is the inverter. This operating condition is defined by E_1. The current remains the same under the two operating conditions but it is the voltage polarity that changes.

5.3.1 Current and Voltage Limits

During the operation of HVDC links the AC and DC voltage as well as the current may change due to faults or because of changes in the operating conditions. As a result, the converters may not be able to function at its rated capacity (i.e., voltage, current and power). Hence, it is important to consider the following limits, these being the maximum and minimum current limit as well as the maximum and the minimum voltage limits. Control of the current order limit is commonly referred to as the voltage-dependent current-order limit (VDCOL) [19, 21, 27].

5.3.1.1 Maximum Current Limit

When excessive current (greater than 1.3 times the full load current) is allowed to flow through the converter valves, the thermal level of the valve increases beyond the rated thermal level and may damage the valve. According to [19], to prevent this, the maximum allowable current flowing through the valve is normally set to a maximum of 1.2 to 1.3 times the full load current, i.e. 20% to 30% more than the full load current.

5.3.1.2 Minimum Current Limit

When the alternating current supplied to the valve is at a very low value, for example, about 0.2 per unit of the full load current value, ripples in the current may give rise to an intermittent supply of current which becomes very significant in a twelve-pulse operation. This intermittency causes high voltages in the transformer windings and the DC reactors [19].

Furthermore, the low DC current observed will give rise to small overlap angles in the converter which is not a favourable operating condition. When the overlap angles are too small, the sudden shoot of the DC voltage leads to an increase in the stress levels of the converter valves. When the maximum stress level is exceeded, the converter breaks down. Another consequence of the sudden shoot of DC voltage across the converter due to very small DC current is the flashovers across the terminals of each converter bridge [18].

5.3.1.3 Voltage-dependent Current-order Limit (VDCOL)

In the event of the voltage at the rectifier decreasing to about 30% of the rated voltage the reactive power at the inverter increases to accommodate the sudden decrease in the rectifier voltage. This increase in inverter voltage increases the reactive power absorbed by the inverter which may reduce the power factor of the inverter end AC system. In addition to this, the increase in gamma (extinction angle) at the inverter increases the reactive power absorption by the inverter leading to possible voltage instabilities. To prevent these problems associated with low voltages, the VDCOL is used. The VDCOL operates by reducing the maximum allowable current depending on the DC voltage level. Hence, the maximum current is a function of the DC voltage. When the DC voltage goes below a pre-determined value, the maximum allowable current is reduced to prevent voltage instabilities [11, 35]. Other methods of HVDC control include DC voltage and DC power control. For the DC voltage control scheme, other converter station parameters are moderated to keep the DC voltage at the set point. Similarly for the DC power control, the rest converter station parameters are moderated to keep the transmitted DC power constant [19, 20, 50].

5.4 HVDC CONTROL RESPONSES TO DC AND AC FAULTS

Power systems with HVDC transmission schemes are not completely infallible to faults. The stability of such power systems are affected by DC line faults and converter faults. In AC systems, relays and circuit breakers are used for fault detection and clearance. In fact, most of the faults in DC systems are self-clearing or are cleared through the action of converter controls [19]. In some cases, though, it may become necessary to take a bridge or an entire pole out of service.

5.4.1 Responses to DC Line Faults

The most common type of fault on DC lines is the pole-to-ground fault. This fault blocks power transfer on the affected pole with the rest poles remaining intact. During this fault the short circuit causes the rectifier current to increase while the inverter current decreases. The rectifier current control acts to reduce the direct voltage and also to reduce the current back to the current set point (normal operation current level). At the inverter side of the scheme, the current level reduces below its current reference value $(I_{ord} - I_m)$. This causes the inverter to change from CEA control to CC control. As a result, the voltage of the inverter reduces to zero and then reverses its polarity as shown by line B in figure 5.4 [17, 19, 30, 42, 47].

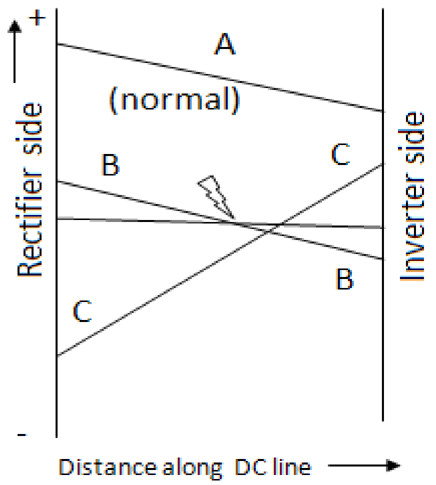

Figure 5.4 Voltage Profile on a DC line

After the fault under normal control action the fault arc is not extinguished while limiting the fault current to the current margin [19, 48]. The fault is detected with a fast-acting line protection by the drop in DC voltage and current at the rectifier and the inverter respectively. After the fault has been detected, the angle beta of the inverter is changed to a maximum limit of 80^0 to allow the inverter voltage reduce to zero but not to reverse polarity as explained under normal control action. At the rectifier side, the rectifier firing angle is changed above 90^0. This is shown by line C in figure 5.4. Although the current in the pole may attempt to change polarity, this will not be done successfully as a result of the unidirectional current characteristics of converter valves. Consequently, the current is reduced to zero in a very rapid manner. This process is called 'forced retard'. Following this, the DC line is restarted with time for de-ionisation taken into consideration. Typically, the total time it takes for fault clearance and return to service is between 200 to 300 ms [19, 42, 48].

5.4.2 Responses to DC Converter Faults

Most of the converter DC faults lead to a complete shutdown of a valve group or a pole. During this time, a fast reduction in the DC current to zero is required while the firing angle at the rectifier is shifted to at least 90^0 or higher into the inverter region. The time taken to reduce the current to zero can be as small as 30 ms [19].

5.4.3 Responses to AC System Faults

The DC system response to an AC fault is faster than that of the AC system. The DC system is capable of self sustenance through the AC system fault or in severe cases, there will be a reduction in power or a complete shutdown till the AC system recovers from the fault [19].

5.4.3.1 Rectifier Side AC System Faults

When the AC fault is a distant 3-phase fault at the rectifier AC side there will be a reduction in the rectifier commutation voltage. This will lead to a reduction in the DC voltage and current. The current regulator will decrease the firing angle to restore the current by increasing the voltage. However, if the firing angle reaches its minimum value, the control measure will switch the rectifier from CC mode to CIA mode while the inverter changes to CC mode. The VDCOL regulates the transfer of current and power depending on how low the voltage at the rectifier drops during the rectifier side AC fault. Although in theory DC power may be transmitted via the HVDC transmission line when the rectifier voltage is very low, the resulting increase in reactive power consumption may be damaging to the generator of the AC system. This is mainly because the inverter would have to change from CEA to CC mode by lowering its voltage and increasing β [19, 48].

5.4.3.2 Inverter Side AC System Faults

When the AC fault is a distant three-phase fault at the inverter AC side there will be a reduction in the inverter commutation voltage while the direct current increases. In this case the CC at the rectifier and the CEA at the inverter stays in control. In the event when the low AC voltage persists, tap changers will mediate in restoring the converter firing angle and the DC voltage. If the reduction in AC voltage is significant, this may lead to a temporary commutation failure at the inverter without adequate control, It takes about 1 to 2 cycles to clear the commutation failure [19] if the inverter were operating at a gamma angle of 18^0. The power that is transmitted via the HVDC line during the low voltage operation will lead to an increase in the reactive power consumption which may lead to the reduction in the direct current with the aid of the VDCOL. During low voltage operations, several commutation failures may occur and, therefore, valves may be blocked and bypassed until the AC voltage recovers. The restoration of the system post fault depends on the strength of the AC system and the AC/DC interconnection.

CHAPTER 6

ROTOR ANGLE STABILITY

Power system stability can be defined as

> the ability of an electric power system, for a given operating condition, to regain a state of operating equilibrium after being subjected to a physical disturbance, with most system variables bounded so that practically the entire system remains intact [3, 19].

Power System Stability can be classified into three broad streams which are; Voltage stability, Frequency Stability and Rotor Angle Stability, the last of which is the main focus of this thesis. Figure 6.1 shows the classification of power system stability.

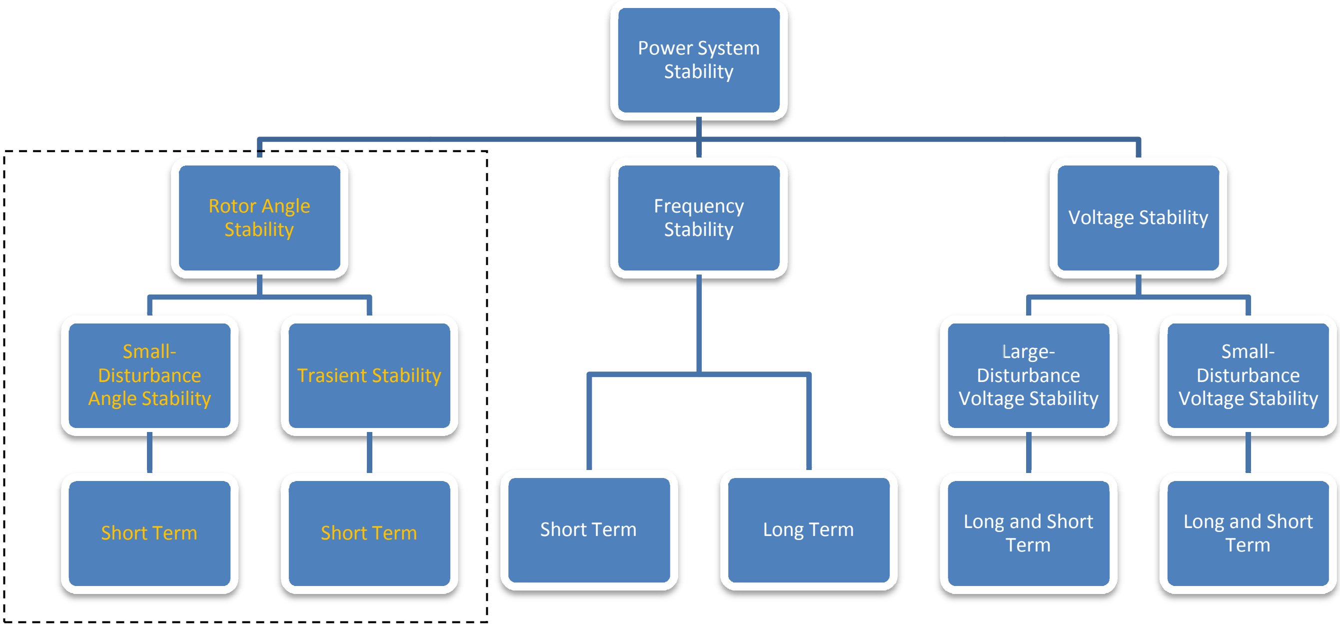

Figure 6.1 Classification of Power System Stability

According to [1], voltage stability is the ability of a power system to maintain steady voltages as all busbars in the system after been subjected to a disturbance. Frequency stability refers to the ability of a power system to maintain steady frequency following a severe system disturbance which results in a significant imbalance between load and generation. The highlighted part in the classification of the power system stability diagram in figure 6.1 is the rotor angle stability which is the core focus of this thesis.

Rotor angle stability is, therefore, the ability of synchronous machines in a power system to remain in synchronism after being subjected to a disturbance. Frequency stability is a separate branch of power system stability. This is done to cater for large load-generation imbalance post a system disturbance. To achieve synchronism in a power system with interconnected synchronous machines, the stator voltage and current of all the machines must have the same frequency [19]. Also, the rotor mechanical speed of each of the machines must be synchronised to this frequency. This stability also depends on the ability of the machines to maintain equilibrium between the electromagnetic torque and the mechanical torque [21]. The movement of the rotor is governed by the Newton's second law of motion given in equation 6.1 [1, 42].

$$J\alpha_m(t) = T_m(t) - T_e(t) = T_a(t) \qquad (6.1)$$

Where:

J =total moment of inertia of the rotating mass, kg m^2

α_m= rotor angular acceleration, rad/s^2

T_m = mechanical torque, Nm

T_e= electrical torque, Nm

T_a = net accelerating torque, Nm

The rotor angular acceleration is given by equation 6.2.

$$\alpha_m(t) = \frac{d^2\theta_m(t)}{dt^2} \qquad (6.2)$$

Where θ_m is the rotor angular position.

After substituting equation 6.2 into equation 6.1, converting from toque to power, the swing equation can be given in per unit as:

$$2H\omega_{p.u}(t)\frac{d^2\delta(t)}{dt^2} = P_{m\,p.u}(t) - P_{e\,p.u}(t) = P_{a\,p.u}(t) \qquad (6.3)$$

Where:

H= normalized inertia constant

P_a= accelerating power

P_m and P_e = mechanical and electrical power.

Under equilibrium conditions the relationship between the exchange of power and the rotor angles of interconnected synchronous machines in a power system is called the power versus angle relationship [19]. To illustrate this non-linear relationship, a power system with one motor connected to a generator is considered in figure 6.2.

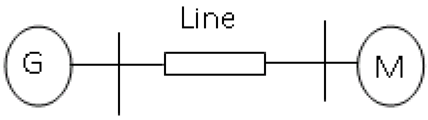

Figure 6.2 Power System Single Line Diagram

In figure 6.2 the power transferred from the generator to the motor is a function of the rotor angular separation (δ) between the generator and the motor. This separation is caused by three factors namely, the generator internal angle (δ_G); the angular difference between the terminal voltages of the generator and the motor; and the internal angle of the motor. The model presented in figure 6.2 can be expanded as shown in figure 6.3. For steady state analysis, the synchronous reactance is used with the assumption that the internal voltage is equal to the excitation voltage [19].

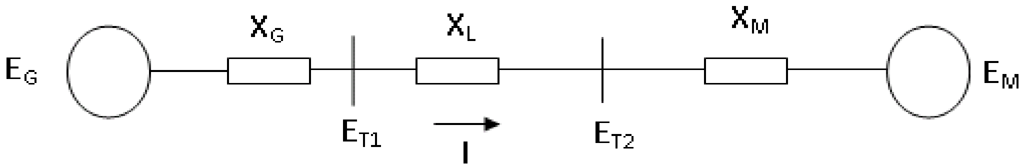

Figure 6.3 Linearised Model of the Power System

The power transferred from the generator to the motor is given by equation 6.4

$$P = \frac{E_G\, E_M}{X_T} \sin \delta \qquad (6.4)$$

where: $X_T = X_G + X_L + X_M$

X_T is the total reactance, X_G is the reactance of the generator, X_L is the transmission line inductive reactance and X_M is the reactance of the machine.

The phasor diagram showing the relationship between the generator and the motor voltages is given in figure 6.4.

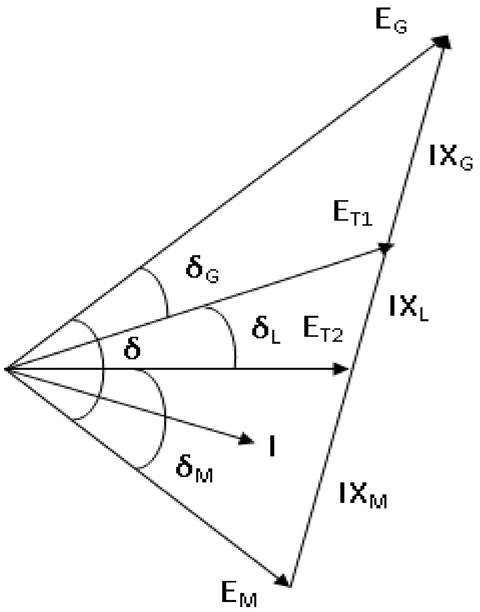

Figure 6.4 Phasor Diagram of Generator and Motor Voltages

δ_G is the generator internal angle (angle by which the generator rotor angle leads the stator angle)

δ_M is the motor internal angle (angle by which the motor rotor angle leads the stator angle)

δ_L is the angular separation between voltage at E_{T1} and E_{T2}

δ is the angular separation between the rotor angle of the generator and the rotor angle of the motor

E_{T1} is the voltage at terminal, T_1 and E_{T2} is the voltage at terminal, T_2

E_M is the motor internal voltage and E_G is the generator internal voltage

I is the current .

The corresponding power-angle relationship is shown in figure 6.5. The representation in figure 6.5 is that of an idealised model. The power transfer varies as the sine of the angle. When the effects of controllers such as Automatic Voltage Regulators (AVRs) and Power System Stabilizers (PSS) are taken into account, the shape of the curve in figure 6.5 will vary slightly.

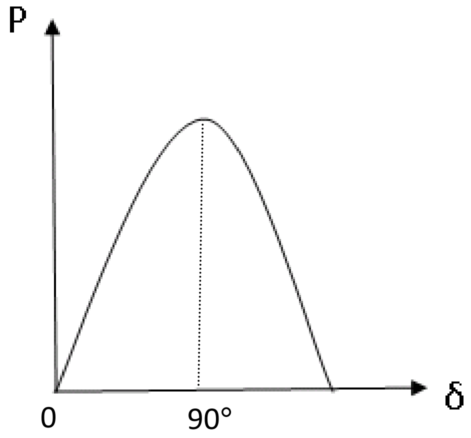

Figure 6.5 Power-angle Curve

When the angle is zero, there is no power transferred. As the angle increases from zero to 90^0, the amount of power transferred reaches its maximum. Any further increase in it will lead to a decrease in the amount of power transmitted. Similarly, in a multi-machine power system, the relative rotor angular displacement affects the interchange of power as well as the complex relationship between the load distribution and the power generation [19].

6.1 SMALL SIGNAL STABILITY

6.1.1 Introductory Concepts to Small Signal Stability

Small signal stability refers to the ability of a power system which is subject to small disturbances to maintain synchronism. Such disturbances include continuous and small variations in load and generation. As a result of these disturbances, instability in the system can arise due to lack of either synchronising torque, which manifests as a steady increase in generator rotor angle, or the lack of sufficient damping torque which manifests as rotor angle oscillations with increasing amplitudes [19].

When a generator without an AVR is connected to a power system the instability experienced is normally due to the lack of sufficient synchronising torque. This manifests as an oscillatory mode as shown in figure 6.6. Figure 6.7 shows the stable system with positive damping and synchronising torque.

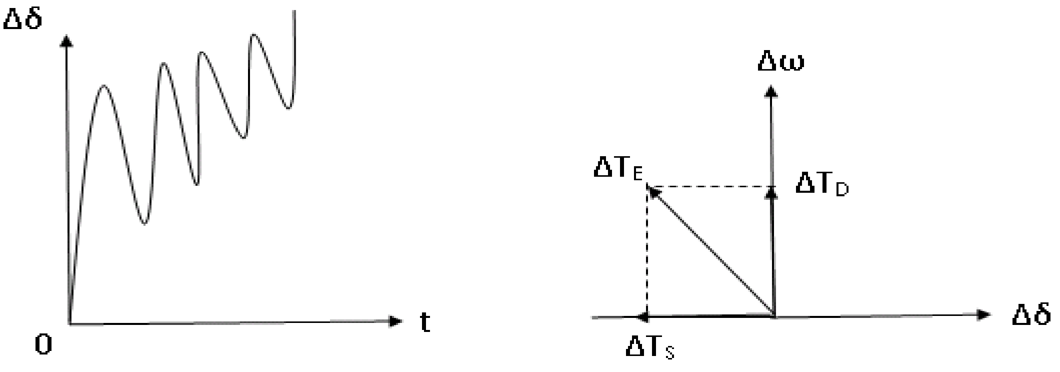

(a) **(b)**

Figure 6.6 Oscillatory Instability with Positive T_D and Negative T_S

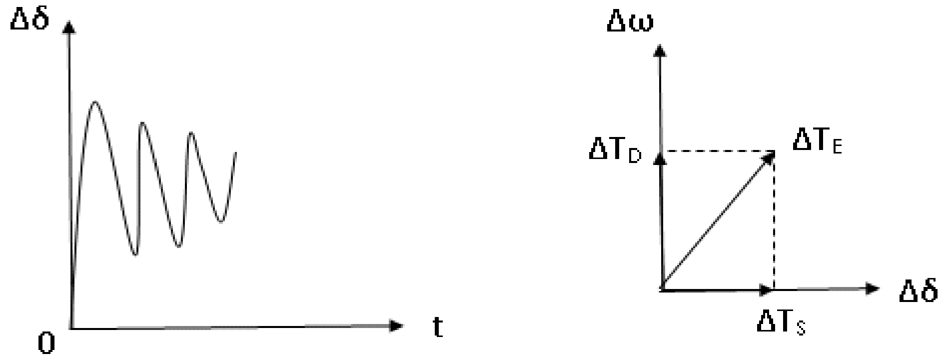

(a) **(b)**

Figure 6.7 Stable System with Positive T_D and T_S

With the addition of AVRs the problem of small signal stability becomes that of sufficient damping. The instability in the presence of AVRs manifests as oscillations with increasing amplitudes. This is shown in figure 6.8.

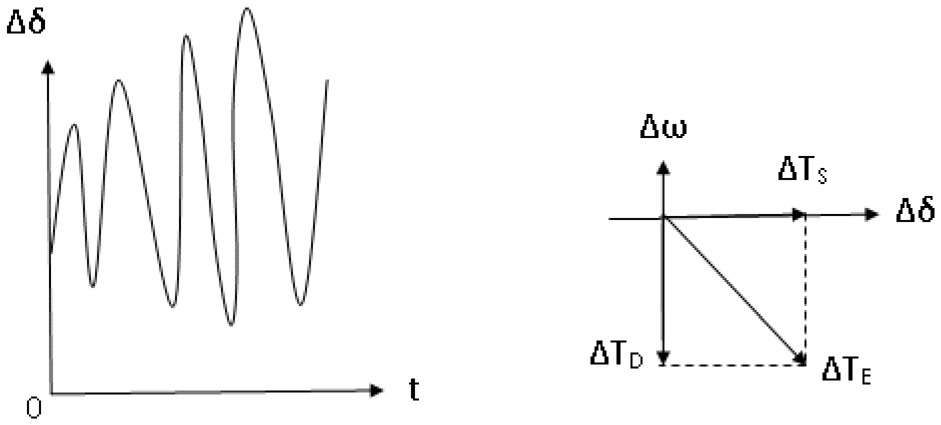

Figure 6.8 Oscillatory Instability with Positive T_S and Negative T_D

Power system oscillations can be classified into the following categories: local modes, inter-area modes; control modes; and torsional modes.

- Local modes or machine modes: these modes are linked with the swinging of the units at a generating station with respect to the rest of the entire power system
- Inter-area modes: these modes are linked with the swinging of several machines in one part of the power system against machines in other parts of the power system. This mode is caused by a weak tie with connecting areas of a power system.
- Control modes: these modes are linked to generating units and controllers. Poorly tuned exciters, speed governors and HVDC converters and SVCs are possible sources of control modes.
- Torsional modes: these are linked to turbine-generator shaft system rotational components. This may be caused by interactions with excitation controls, speed governors and HVDC controls [19].

6.1.2 State-space Representation

The behaviour of a power system can be described by a set of n first order nonlinear differential equations as shown in equation 6.5.

$$\dot{x_i} = f_i(x_1, x_2, \ldots., x_n,: u_1, u_2, \ldots., u_r; t \qquad i = 1,2, \ldots., n \qquad (6.5)$$

Where n is the order of the system and r is the number of inputs.

Equation 6.5 can be written in the vector-matrix notation as shown in equation 6.6.

$$\dot{\boldsymbol{x}} = \boldsymbol{f}(\boldsymbol{x}, \boldsymbol{u}, t) \tag{6.6}$$

In equation 6.6, *u* is a column vector of inputs to the system, *x* is the state vector and time is denoted by t. The derivative of the state variable with respect to time is denoted by $\dot{x}$. For an autonomous system, the derivatives of the state variables are not explicitly functions with respect to time. Hence, equation 6.6 simplifies to equation 6.7.

$$\dot{\boldsymbol{x}} = \boldsymbol{f}(\boldsymbol{x}, \boldsymbol{u}) \tag{6.7}$$

To get the output variables of the system, vector *y* can be written in terms of the state variables and the input variables in the form [19]:

$$y = \boldsymbol{g}(\boldsymbol{x}, \boldsymbol{u}) \tag{6.8}$$

Where

$$y = \begin{bmatrix} y_1 \\ y_2 \\ \cdot \\ \cdot \\ \cdot \\ y_m \end{bmatrix} \quad \text{and} \quad g = \begin{bmatrix} g_1 \\ g_2 \\ \cdot \\ \cdot \\ \cdot \\ g_m \end{bmatrix}$$

6.1.3 Linearisation

In this section, equation 6.7 is linearised. Assuming x_0 is the initial state vector and u_0 is the input vector corresponding to the point of equilibrium about which the analysis of small-signal stability is to be carried out, then x_0 and u_0 satisfies equation 6.7 and can be written in equation 6.9 as;

$$\dot{\boldsymbol{x_0}} = \boldsymbol{f}(\boldsymbol{x_0}, \boldsymbol{u_0}) = 0 \tag{6.9}$$

By assuming $x = \boldsymbol{x_0} + \boldsymbol{\Delta x}$ and $\boldsymbol{u} = \boldsymbol{u_0} + \boldsymbol{\Delta u}$ to perturb the system in equation 6.9, where Δ represents a small deviation, then

$$\dot{\boldsymbol{x}} = \boldsymbol{f}[(\boldsymbol{x_0} + \boldsymbol{\Delta x}), (\boldsymbol{u_0} + \boldsymbol{\Delta u})] \qquad (6.10)$$

Based on the assumption that the perturbation is small, the nonlinear function $f(x, u)$ can be expressed in terms of the Taylor's series expansion. A further assumption used in the Taylor's series is that the terms involving higher order powers of $\Delta x \; and \; \Delta u$ are neglected [19]. Hence,

$$\dot{x}_i = \dot{x_{io}} + \Delta \dot{x}_i = f_i[(x_o + \Delta x), (u_0 + \Delta u)] \qquad (6.11)$$

The complete linearization of the system is given in Kundur [19].

6.1.4 Eigenvalue Analysis of Small Signal Stability

In this thesis, the analysis of small signal stability will be carried out using eigenvalues and modal analysis.

Assuming a matrix A of dimension n x n represents the state matrix of a synchronous generator, the values of *s (the Laplace operator)* which forms the solution set to equation 6.12 are the eigenvalues of the matrix A, where equation 6.12 is called the characteristic equation of A. The number of solutions in the solution set determines the number of modes that the generator operates in.

$$\det(sI - A) = 0 \qquad (6.12)$$

An examination of the solution will give an insight into the stability, speed, damping and frequency of oscillation of the generator. The time it takes for the synchronous generator to reach its final value or set point can also be determined from the eigenvalues. Eigenvalues can be drawn on the s-plane to determine the small signal stability of a mode [19].

According to Kundur [19], Lyapunnov's first method of eigenvalue analysis in the s-plane is as follows:

i. When the eigenvalues have negative real parts, the original system is asymptotically stable; and
ii. When at least one of the eigenvalues has a positive real part, the original system is unstable.

When the real part of an eigenvalue is zero, it is not possible on the basis of the first approximation to say anything about the stability [19].

For a complex pair of eigenvalues λ, as represented by equation 6.13, the real part gives the damping while the imaginary part gives the frequency of oscillation. The frequency of oscillation (*f*) in Hz is given by equation 6.14. Figure 6.9 shows a complex pole drawn on the s-plane.

$$\lambda = \alpha \pm j\omega \qquad (6.13)$$

$$f = \frac{\omega}{2\pi} \qquad (6.14)$$

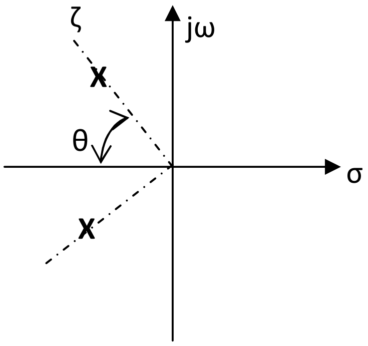

Figure 6.9 Complex eigenvalue on the s-Plane

θ is the damping angle.

The decay rate of the amplitude of an eigenvalue is called the damping ratio and is also represented by equation 6.15.

$$\zeta = \frac{-\alpha}{\sqrt{\alpha^2 + \omega^2}} \qquad (6.15)$$

6.2 TRANSIENT STABILITY

This refers to the ability of a system to maintain stability and return to its normal operating condition after it has been subjected to large disturbances. The location and magnitude of the disturbance, therefore, are important in the analysis of transient stability. Possible causes of disturbances could be three-phase faults, line to ground faults, loss of network elements such as generators, etc. [16]. These large disturbances normally upset the rotor angle of generators from their state of equilibrium.

Under steady state equilibrium conditions the mechanical power and the electrical power of the generator in equation 6.3 are the same while the speed of the generator remains constant [26]. There is thus no accelerating power, which means the rotor angle of the synchronous machines in the interconnected power system will be stable at a fixed angular position. When a power system experiences a disturbance, such as a three-phase fault or the loss of a generating unit, the equilibrium between P_e and P_m is lost and the speed of the generator changes. In a case where the mechanical power, P_m , is greater than the electrical power P_e at a certain instant in time, the generator accelerates from an old rotor angle value δ_1, to a new value corresponding to δ_2 such that $\delta_2 > \delta_1$. Furthermore, if P_e is greater that P_m, the generator decelerates. This process is continued until a new equilibrium position is reached if the system is stable, or the system will loose its stability.

When an interconnected power system is perturbed or is under a certain defined disturbance, the speed of the generator differs according to the location and size of the both the disturbance and the generator. If the speed of one of the generators is faster than the others in the interconnected system at any moment in time t_0, the angular position of its rotor relative to that of the slower machine will advance. This will lead to the transfer of the load from the slower generator to the faster generator [1, 26, 36].

CHAPTER 7

SIMULATION RESULTS FOR THE SINGLE MACHINE INFINITE BUS (SMIB)

Figure 7.1 and figure 7.2 show the single line diagram of the power system that was used in case 1 and case 2. Area 1 has one generator (G1) which is connected to bus 1 (the infinite bus). Area 2 has one generator (G2) which is connected to bus 4 (the PV bus). The only distribution station is connected to area 2 at bus 4. The AC side of the rectifier and inverter are connected to bus 1 and bus 4, respectively. The HVDC line is connected between the DC side of the rectifier and the DC side of the inverter via 0.86 H series rectors at bus 2a and bus 3a, respectively as shown in figure 7.1. Series reactors are used to smooth the DC current waveform on the HVDC transmission line and to reduce the impact of line faults on the converter station [38, 40]. The HVAC transmission line is between bus 2 and bus 3 as shown in figure 7.2. The transformer reactance and other system parameters are given in Appendix B.

Load flow convergence problems were encountered when modelling the tap changers in the built-in transformer of the converter model. To solve this problem, the converter model was used with an external transformer which did not have a tap changer.

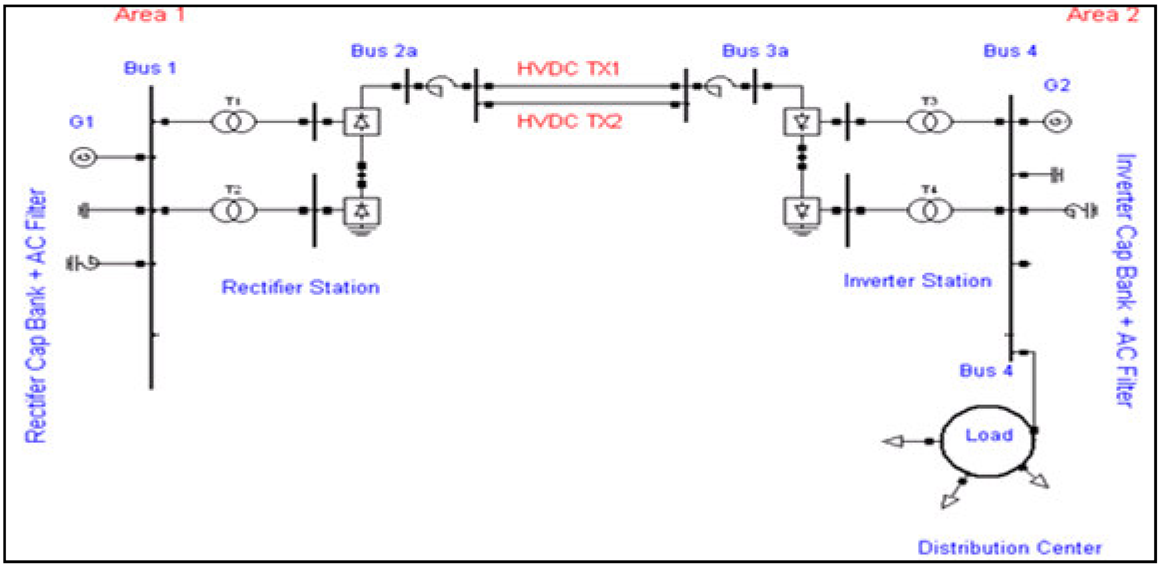

Figure 7.1 Single Machine Infinite Bus Power System Model

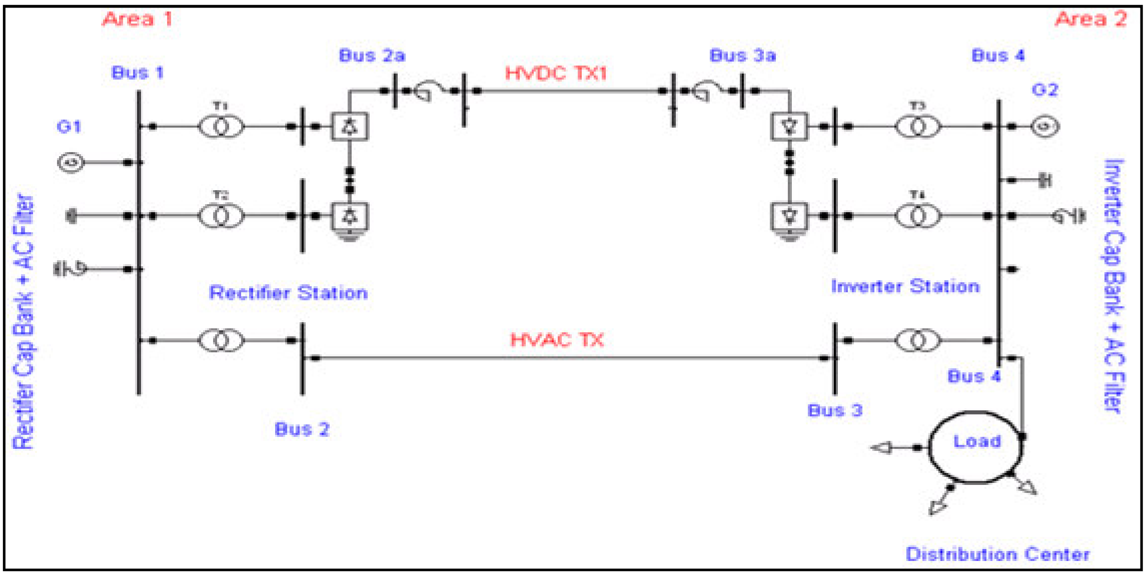

Figure 7.2 Single Machine Infinite Bus Power System Model

The simulations in this section are divided into three parts; load flow, transient stability and small signal stability. In each of these parts double circuit HVDC transmission and Hybrid HVDC-HVAC transmission are be considered in separate cases for power transmission.

7.1 LOAD FLOW

7.1.1 Case 1: HVDC Transmission

In this case study, a double circuit HVDC transmission line is used for power transmission. Tables 7.1 and 7.2 show the voltages and powers at all the system busbars. The distribution centre connected to bus four supplies a load of 2442 MW at a power factor of 0.9. Current control is adopted at the rectifier to control the flow of the DC current, while the inverter is operating under the extinction angle control. The DC current order is set to 3.86 kA, which at 500 kV will allow the transmission of about 2000 MW via the HVDC transmission line.

Table 7-1 Bus Voltage Magnitude and Angles (Case 1)

Element	Rated Voltage (kV)	Actual Voltage (kV)	Voltage (p.u)	Voltage angle (°)
Bus 1	345	362.25	1.05	0
Bus 2a	500	523.4	1.05	*N/A
Bus3a	500	509.15	1.02	*N/A
Bus 4	230	230	1	0

*N/A: Not applicable

Table 7-2 Active and Reactive Power (Case 1)

Element	Bus	Active Power [MW]	Reactive Power [Mvar]
G1	1	1995	791
G2	4	502	384
HVDC TX 1	2a	997	0
	3a	970	0
HVDC TX 2	2a	997	0
	3a	970	0
Rectifier AC Filters	1	0	6.6
Inverter AC Filters	4	-0.09	210
Rectifier Cap Bank	1	0	881
Inverter Cap Bank	4	0	2100
Rectifier	1	1995	1680
	2a	-1995	0
Inverter	3a	1940	0
	4	-1940	1511
Distribution Centre	4	2442	1183

The negative sign at the inverter AC filter means that the inverter absorbs 0.09 MW which adds to the total system losses in MW. The DC power injected through the series reactor to the HVDC transmission line from the rectifier is indicated by the negative 1995 MW at bus 2a. Also, the negative sign at the inverter on bus four indicates that 1940 MW of AC power was inverted to AC power by the inverter. The per unit voltage at the rectifier DC bus is 1.05 pu corresponding to 523.40 kV as indicated in table 7.1, which results in 1940 MW being transmitted to the distribution centre as can be seen in table 7.2. The rest of the 502 MW is supplied by G2. From Table 7.2, the losses in both HVDC transmission lines TX1 and TX2 can be found to be 54 MW. Major sources of reactive power demand in this case are the rectifier and the inverter. The reactive power needed was supplied by G1, G2, the AC filters and the capacitor banks.

7.1.2 Case 2: Hybrid HVAC- HVDC Transmission

In case 2, a hybrid combination of a single HVAC line in parallel with a single HVDC transmission line is used to transmit power from area one to area two. This means that HVDC TX1 and HVAC are used in Figure 7.1. The distribution centre supplying a load of 2442 MW at 0.9 pf is connected to bus four in area two. Current control is adopted by the rectifier to control the flow of DC current on the DC transmission line while the inverter is operating under the extinction angle control.

The DC current order is set to 1.98 kA which at 500 kV will theoretically allow about 1050 MW to be transmitted via the HVDC transmission line and the rest of the power will be transmitted via the HVAC transmission line. The flow of power in the HVDC line is controlled by adjusting the current order at the rectifier. The current order was chosen to be 1.98 kA so as to split the amount of power transmitted between the HVDC and the HVAC transmission lines almost equally. Table 7.3 and table 7.4 show the voltages and powers at all the system buses.

Table 7-3 Bus Voltage Magnitude and Angles (Case 2)

Element	Rated Voltage(kV)	Actual Voltage (kV)	Voltage (p.u)	Voltage Angle (^{0})
Bus 1	345	362.25	1.05	0
Bus 2	500	525.06	1.05	-0.1
Bus3	500	500	1	-28.57
Bus 2a	500	511.91	1.02	N/A
Bus3a	500	496.16	0.99	N/A
Bus4	230	230	1	-28.68

The maximum bus voltage is 1.05 pu at bus one and bus two and the lowest voltage was observed at bus 3a as 0.99 pu as indicated in table 7.3. Since the power transmitted (949 MW) via the HVAC transmission line is close to the SIL of the line (1000 MW), the amount of reactive supplied by HVAC transmission line is low. This means that the reactive power absorbed by the inductive reactance of the HVAC transmission line is slightly lower than the reactive power generated by the capacitive reactance of the transmission line [16]. The exact amount of power that flows through the two transmission lines, the active power supplied by G1 and G2, and the reactive power compensation are given in table 7.4.

Table 7-4 Active and Reactive power flow (Case 2)

Element	Bus	Active Power [MW]	Reactive Power [Mvar]
G1	1	2024	554
G2	4	500	407
HVDC TX line	2a	1075	0
	3a	-1042	0
HVAC TX line	2	949	-65
	3	-900	-35
Rectifier AC Filters	1	0	6.6
Inverter AC Filters	4	-0.09	210
Rectifier Cap Bank	1	0	330
Inverter Cap Bank	4	0	1400
Rectifier	1	1076	956
	2a	-1076	0
Inverter	3a	1045	0
	4	-1045	868
Distribution Centre	4	2442	1183

As in case 1, the negative sign at the inverter AC filter means that the inverter absorbs 0.09 MW which adds to the total system losses in MW. The DC power injected through the series reactor to the HVDC transmission line from the rectifier is indicated by the negative 1076 MW at bus 2a. Also, the negative sign at the inverter on bus four indicates that 1045 MW of AC power was inverted to AC power by the inverter.

Table 7.4 shows the active and reactive power at several busbar. It can be seen from Table 7.4 that the reactive power supplied by G2 is about 81.4% of the real power. This is particularly high under normal operating conditions, while the power factor of G2 is 0.78. The maximum amount of reactive power that G2 can generate is 842 Mvar. To reduce the reactive power supplied by generator G2 (i.e., increasing its power factor), additional capacitor banks will be needed.

7.1.3 Effect of DC line Loading on Load Flow

The table 7.5, below, shows the effect of HVDC line loading on the voltage angle across bus one and bus four which are the terminating AC buses for both HVAC and HVDC transmission.

Table 7-5 HVAC and HVDC Transmission Line Current Loading for the Transmission of 2000 MW

Line Parameter	**Level 1**	**Level 2**	**Level 3**	**level 4**	**Level 5**	**Level 6**
DC line Current (kA)	3	2.5	2.1	1.8	1.4	1
Active Power-HVDC (MW)	1582	1297	1074	911	698	491
Active Power-HVAC (MW)	418	703	926	1089	1302	1509
Total Transmitted Power (MW)	2000	2000	2000	2000	2000	2000
Voltage Angle Diff between Bus 1 and 4 (deg)	14.81	25.43	34.26	41.28	51.66	64.59

Level 1 to level 6 in table 7.5 represent the various current control settings of the HVDC converter station from 3 kA to 1 kA. At each of these levels the total amount of power transmitted by the HVAC and HVDC line is 2000 MW. For instance, when the current control was set to 2.5 kA in level 2, the amount of power that was transmitted via the HVDC line was 1297 MW, and 703 MW via the HVAC transmission line. Under this setting, the voltage angle difference between bus one and bus four is 25.43^0.

Figure 7.3 illustrates the results in Table 7.5. It can be argued that in cases where there is a need to reduce the voltage angle difference between bus one and bus four, the HVDC line current can be increased to increase the amount of power that flows via the HVDC transmission line. This seems to be one of the major advantages of the Hybrid HVAC-HVDC transmission line configuration.

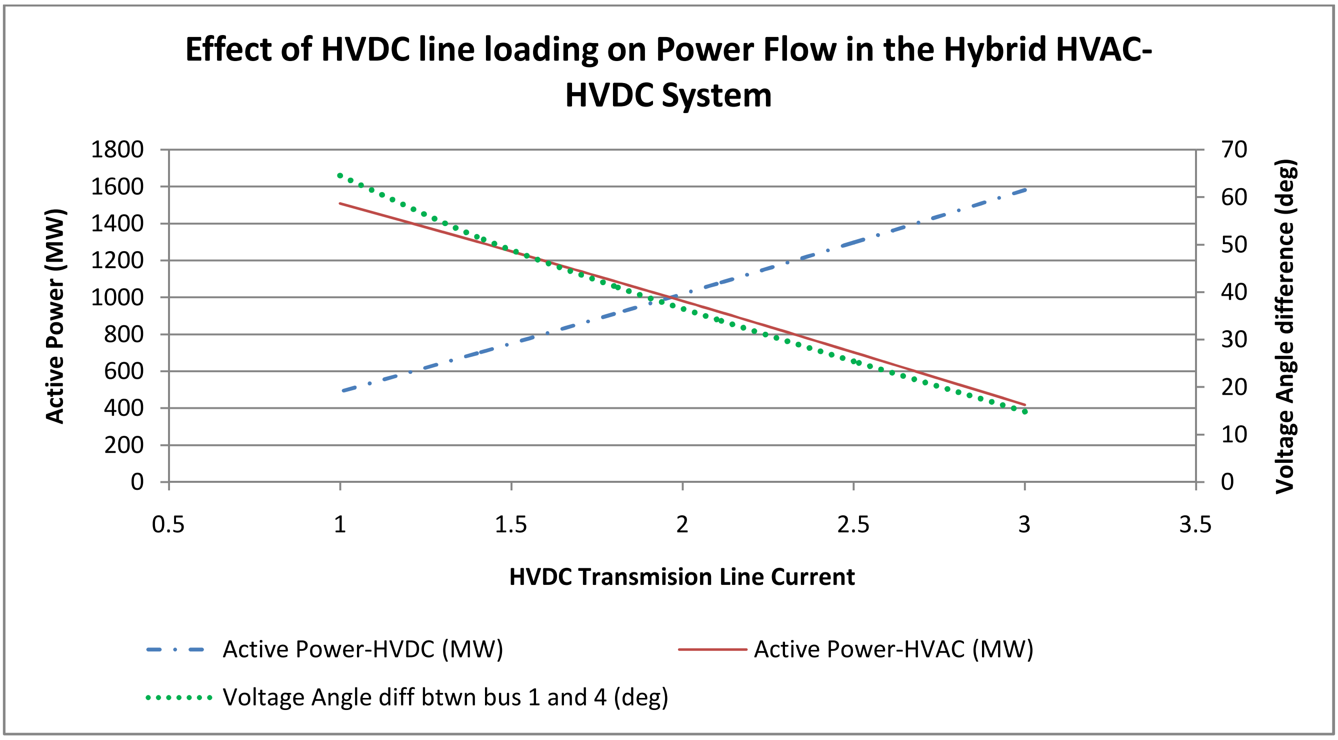

Figure 7.3 Effect of HVDC Line Loading on Power Flow in a Hybrid HVAC-HVDC Transmission Scheme

7.1.4 Comparison of HVDC and HVAC-HVDC

Major sources of reactive power demand in case one and case two are from the converter stations. Reducing this demand will, in turn, reduce the total reactive power demand.

In case one, the reactive power demand by the converter stations was 3191 Mvar, and 1824 Mvar in case two. The reactive power required by the converter stations was reduced in case two because half of the real power transmitted was via the HVAC transmission line.

In both cases the delivered real power to the distribution centre is the same at 1942 MW. Since the transmission line losses in the two cases are different, the transmitted power in each case is different. From the results presented in tables 7.1 to 7.4, it can be concluded that case one, where HVDC only was used for transmission, has the lowest transmission line losses. The transmission loss in case one was found to be 54 MW as calculated from the values in table 7.2. In case two, the loss in the HVAC line was 49 MW while the loss in the HVDC transmission line was 33 MW. The total loss in transmission in case two is 82 MW, as calculated from the values in table 7.4.

The transient stability in section 7.2 and the small signal stability in section 7.3 are based on the load flow results presented in section 7.1.

7.2 TRANSIENT STABILITY

Transient stability, which is a subset of rotor angle stability, is considered in this section. The transient stability of the SMIB power system under different transmission configurations and different faults is considered [8, 36, 41, 42]. The configurations used are the same as discussed in section 7.1. That is, HVDC transmission and hybrid HVAC-HVDC. The faults considered are DC faults at the rectifier (bus 2a), the inverter (bus 3a) of the HVDC line and a three-phase AC fault to ground at the generator G1 terminal. In each of these fault conditions, two transmission configuration cases are considered.

In case one, which uses HVDC transmission, the HVDC transmission line was scheduled to deliver about 2000 MW over 500 km to area two, with current control at the rectifier and extinction angle control at the inverter. The current order of the rectifier was set at 3.84 kA.

In case two, hybrid HVAC-HVDC transmission lines were used. The HVDC transmission line was scheduled to deliver about 1000 MW over 500 km to area two, with current control at the rectifier and extinction angle control at the inverter. The current order of the rectifier was set at 1.98 kA. The HVAC line transmitted 1000 MW.

The results obtained were exported from DigSILENT into MS Excel and then interfaced with Matlab for plotting.

7.2.1 Effects of DC Converter Faults on Transient Stability

At one second into the simulation, a 50 ms DC fault was applied at the DC terminal of the rectifier (bus 2a). Following that, another simulation was run and at one second, a 50 ms DC fault was applied at the DC terminal of the inverter (bus 3a). The effects of both rectifier and inverter DC faults on the transient stability as well as the recovery of the voltage level at the generating stations in area one and area two are investigated.

7.2.1.1 Case 1: HVDC Transmission Line

Only the HVDC transmission section in figure 7.1 was used in case one. The simulation results obtained in this case are shown in figures 7.4 to 7.11.

The pre-fault value of the rotor angle of G1 is around -75º. When the fault was initiated at one second into the simulation for both the rectifier and the inverter fault, the rotor angle of G1 increased from -75º to 170º momentarily and decreased to -170º. At four seconds into the simulation, the rotor angle increased steadily till it reached a steady state after 60 seconds. The final steady state value of the rotor angle for G1 after the rectifier DC fault was found to be 50º more than the final value of the rotor angle for G1, after the inverter DC fault. Figure 7.5 shows the terminal voltage of G1. It can be seen that the terminal voltage at G1 during the rectifier DC fault is 0.1 pu less than the terminal voltage at G1 during the inverter DC fault as seen in figure 7.5. This is because G1 is closer to the rectifier station. The impact of both the rectifier and the inverter fault on the settling time for the terminal voltage at G1 is the same. At 4.3 seconds into the simulation, the terminal voltage settled at 1.05 pu.

The results shown in figures 7.4 to 7.7 are obtained from G1 in area one.

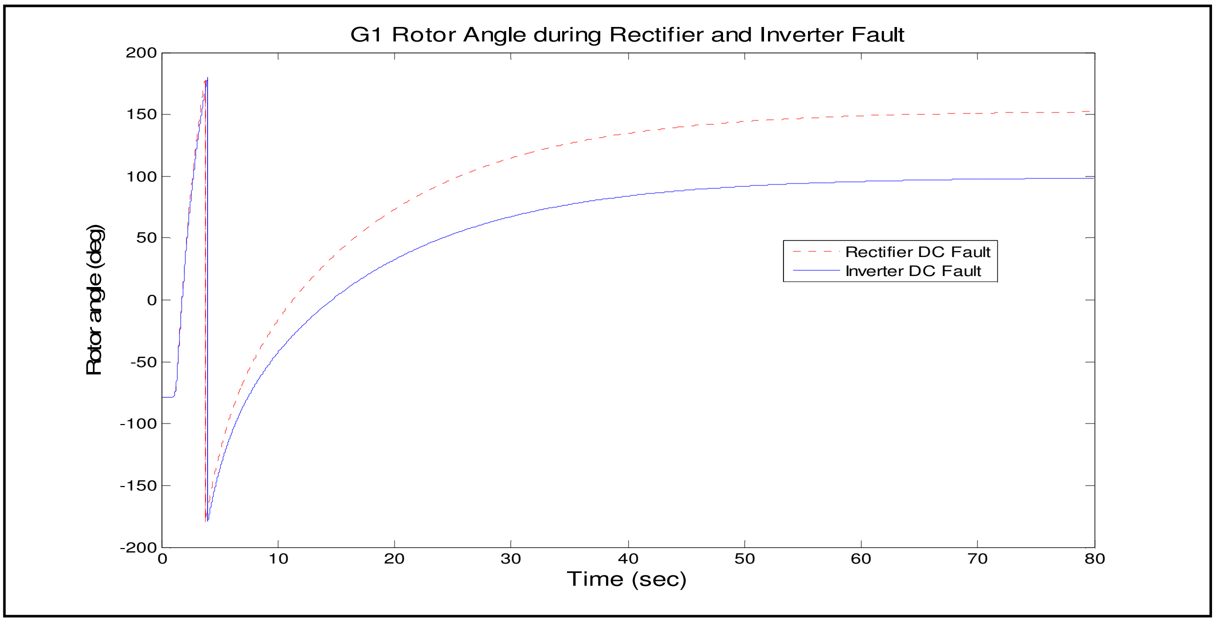

Figure 7.4 Case 1: Effects of Converter Fault on the Rotor Angle of G1

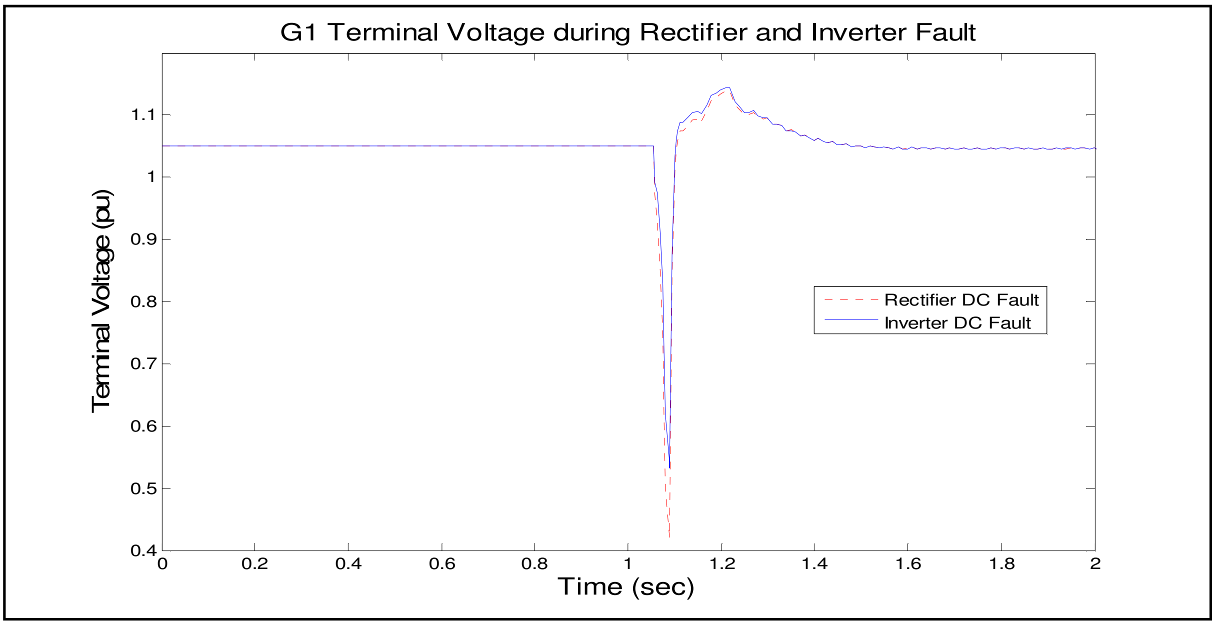

Figure 7.5 Case1: Effects of Converter Fault on the Terminal voltage of G1

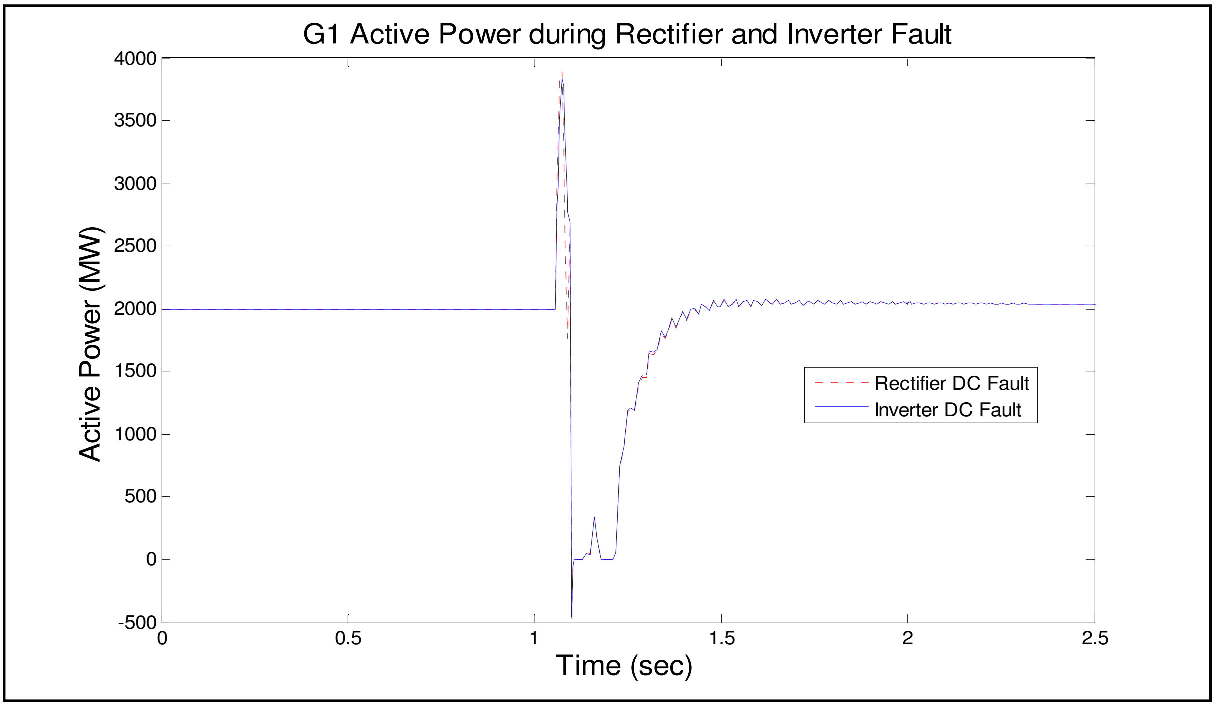

Figure 7.6 Case 1: Effects of Converter Fault on the Active Power at G1

It can be observed from figure 7.6 that the effect of both the inverter and the rectifier fault on the active power generation at G1 is fairly the same as the two curves overlap. Of critical importance is the active power shoot at the time of the fault. At the time of the fault the active power at G1 increased first from 1995 MW to 3800 MW and then decreased to -500 MW. After about four seconds the active power returned to its pre-fault value of 1995 MW. Furthermore, as seen from figure 7.7, the reactive power at G1 increased from 791 Mvar to about 4500 Mvar (469 %) during the inverter fault and to 4600 Mvar (482 %) during the rectifier fault. This is because the rectifier had a greater proximity to G1 as opposed to the inverter which is 500 km away from G1. At four seconds into the simulation, the reactive power returned to its pre-fault value of 791 Mvar.

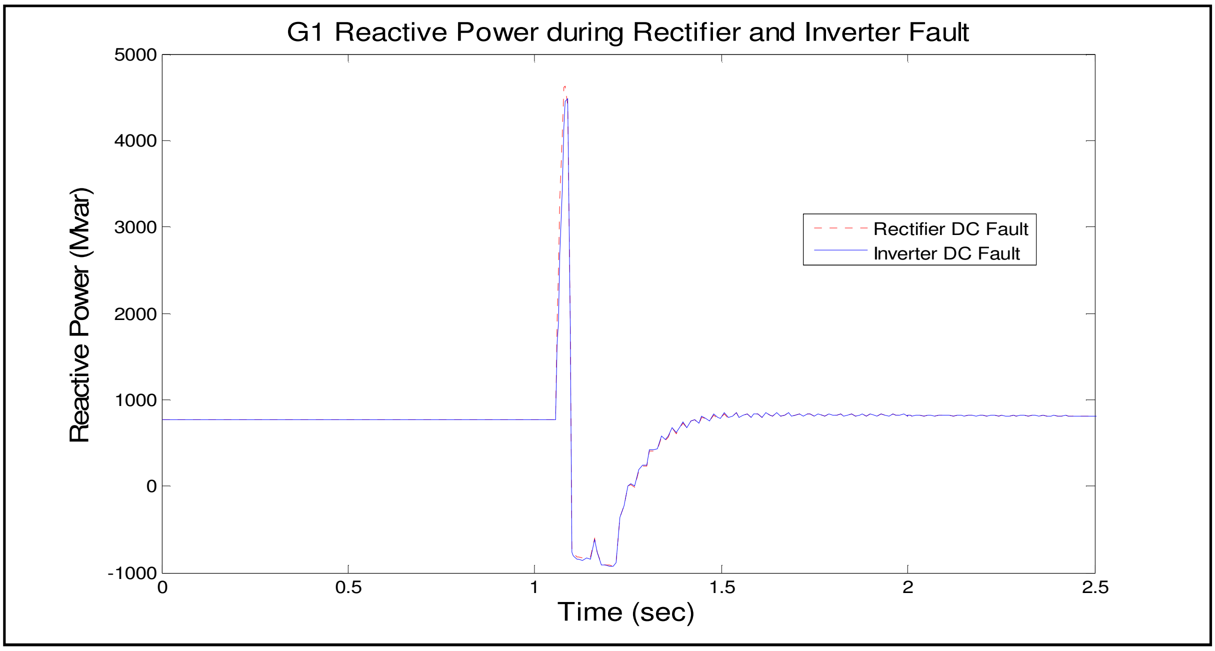

Figure 7.7 Case 1: Effects of Converter Fault on the Reactive Power at G1

The results shown in figure 7.8 and figure 7.11 were obtained from G2 in area 2.

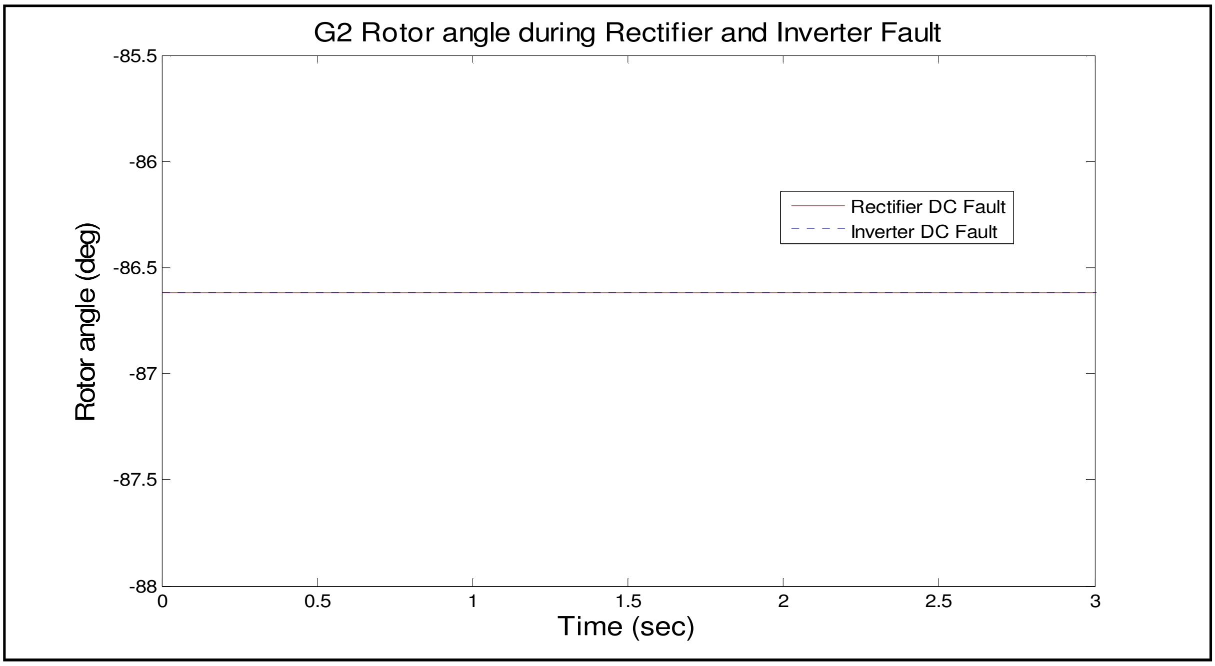

Figure 7.8 Case 1: Effects of Converter Fault on the Rotor Angle of G2

On the other side of the power system, the rotor angle of G2 remained at -87^0 during both rectifier and inverter faults under the HVDC transmission configuration as seen in figure 7.8.

The scheduled active power generation at G2 is 500 MW which is added to the 1900 MW delivered by the HVDC transmission line to the distribution centre. During both faults G2 increased its current output from 0.18 pu to 0.72 pu to increase its active power generation to meet the load demand as seen in figure 7.9. It took eight seconds for the active power generation to stabilise at 502 MW. Due to the HVDC line between area one and area two, G2 had to generate 502 MW to maintain the balance of power.

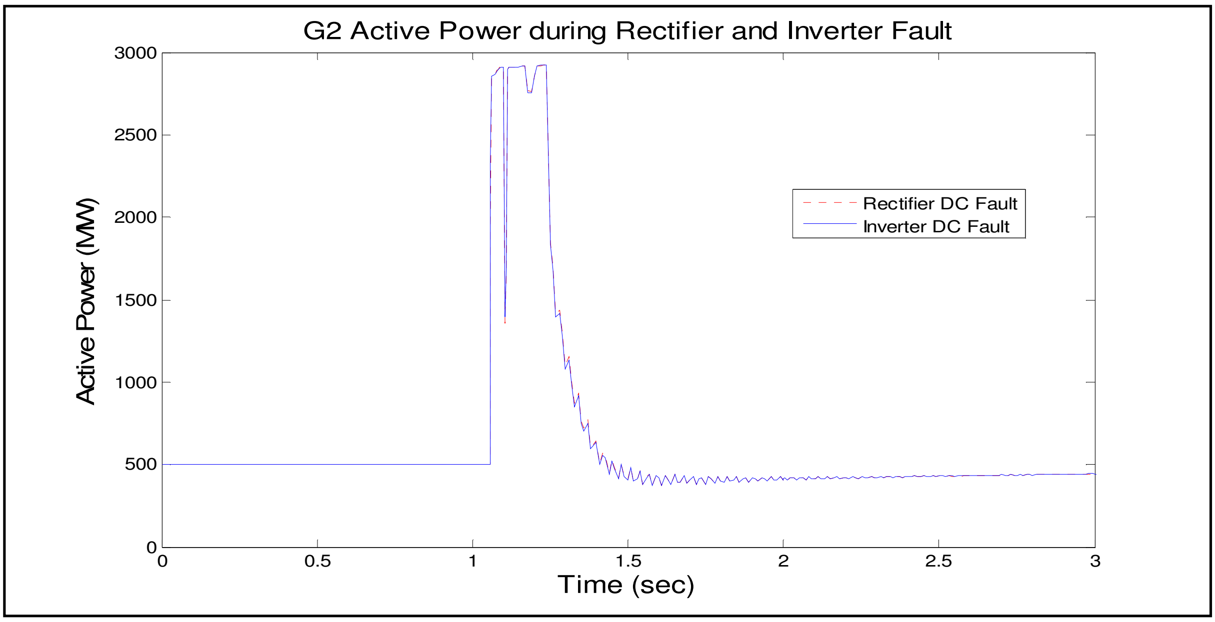

Figure 7.9 Case 1: Effects of Converter Fault on the Active Power at G2

As opposed to G1 in area one where the reactive power increased, in this case the reactive power at G2 decreased from 384 Mvar to -950 Mvar as seen in figure 7.10. This is because G2 absorbed -950 Mvar out of the 2310 Mvar in the inverter side of the network. G2 absorbed so much reactive power because, the amount of reactive power needed by the inverter decreased with the decrease in active power transmitted during the fault.

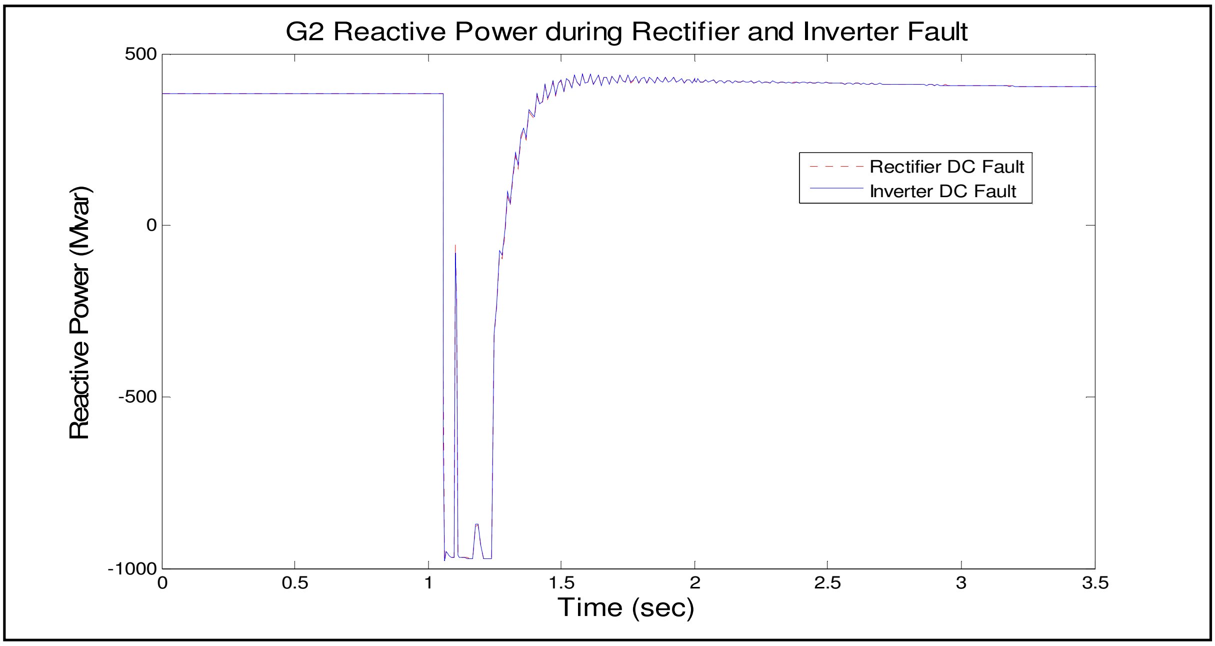

Figure 7.10 Case 1: Effects of Converter Fault on the Reactive Power at G2

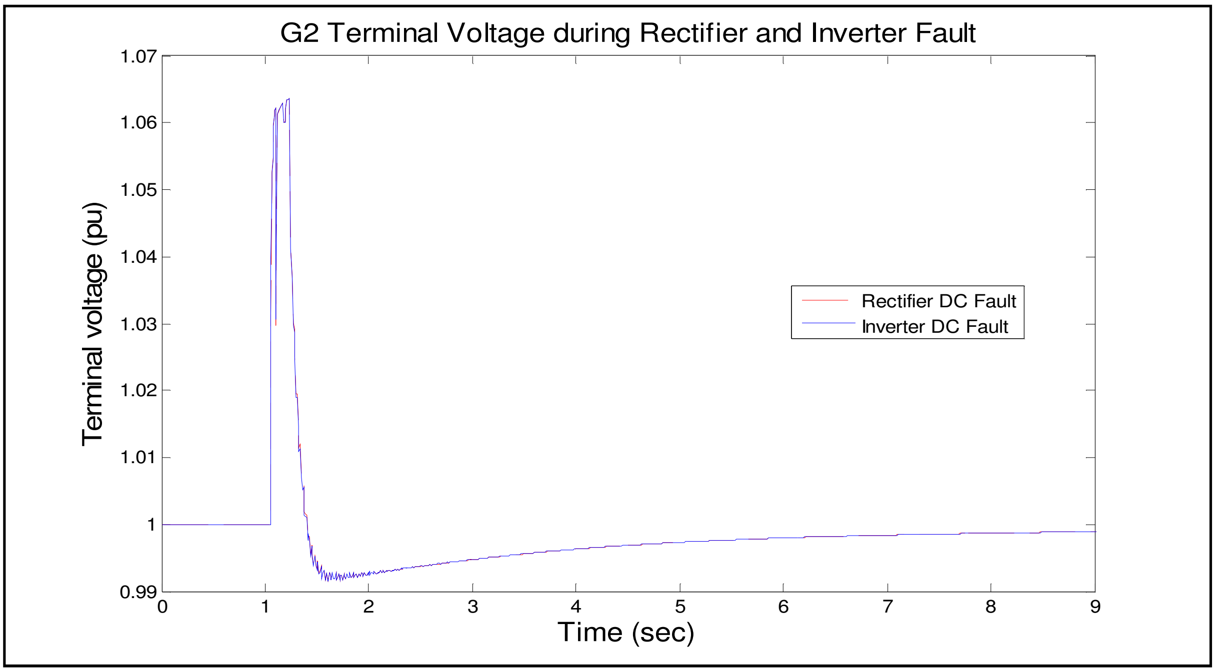

Figure 7.11 Case 1: Effects of Converter Fault on the Terminal Voltage of G2

At G1, the voltage decreased for both converter faults. In area two, the terminal voltage of G2 increased to 1.065 pu from 1.0 pu as shown in figure 7.11. It took about 12.3 seconds for the terminal voltage to return to its pre-fault value of 1.0 pu.

7.2.1.2 Case 2: Hybrid HVAC- HVDC Transmission

The simulation results obtained in this case are given in figures 7.12 to 7.19. The results shown from figure 7.12 to figure 7.15 are obtained from G1 in area one. The rotor angle of G1 remained unchanged during both the rectifier and the inverter faults. In case two both the rectifier and the inverter fault did not affect the rotor angle of generator G1 shown in figure 7.12.

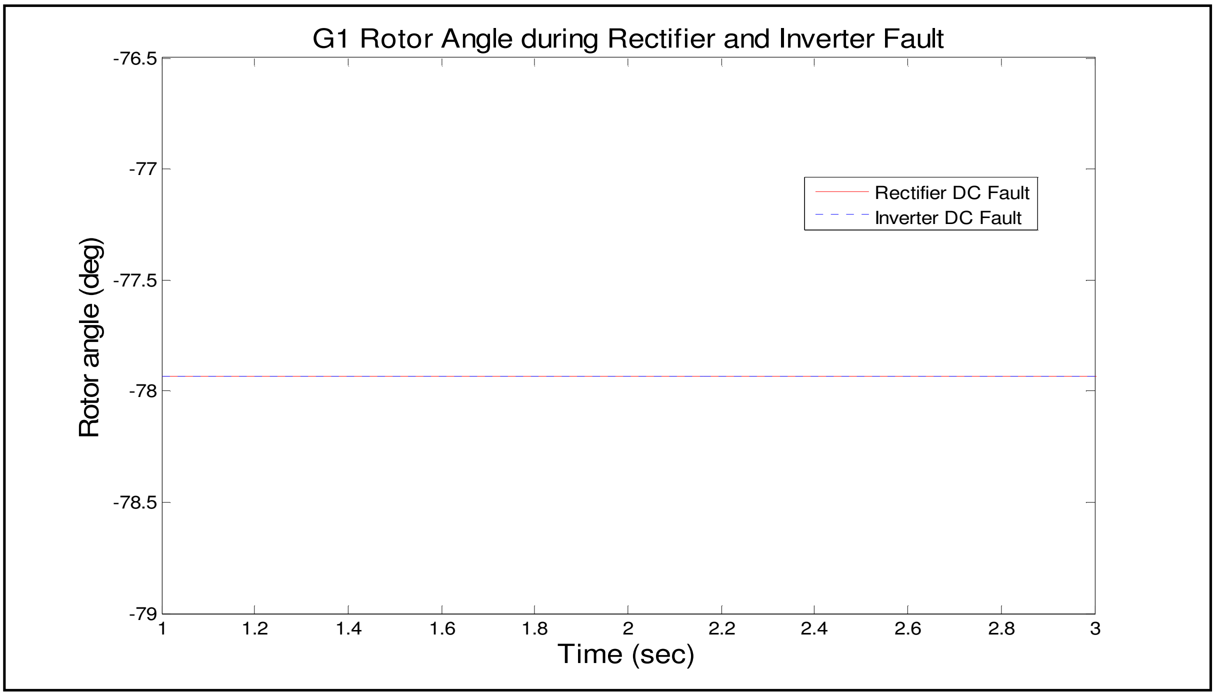

Figure 7.12 Case 2: Effects of Converter Fault on the Rotor Angle of G1

The rectifier and the inverter faults caused the active power at G1 to shoot to 4000 MW and then it dropped to 1000 MW. After the fault the active power at G1 oscillated for about eighteen seconds before settling down at 2000 MW as shown in figure 7.13. This led to the transmission lines being overloaded. Also, the rectifier fault had less impact on the active power generation at G1, as is seen by the difference in the oscillations of the active power in figure 7.13.

In respect of the hybrid transmission the rectifier DC fault caused the terminal voltage at G1 to drop to 0.47 pu, while it dropped to 0.67 pu during the inverter fault, as shown in figure

7.14. This is different from the result in case one, where the voltage at G1 dropped to 0.45 pu and 0.55 pu during the rectifier and the inverter fault respectively.

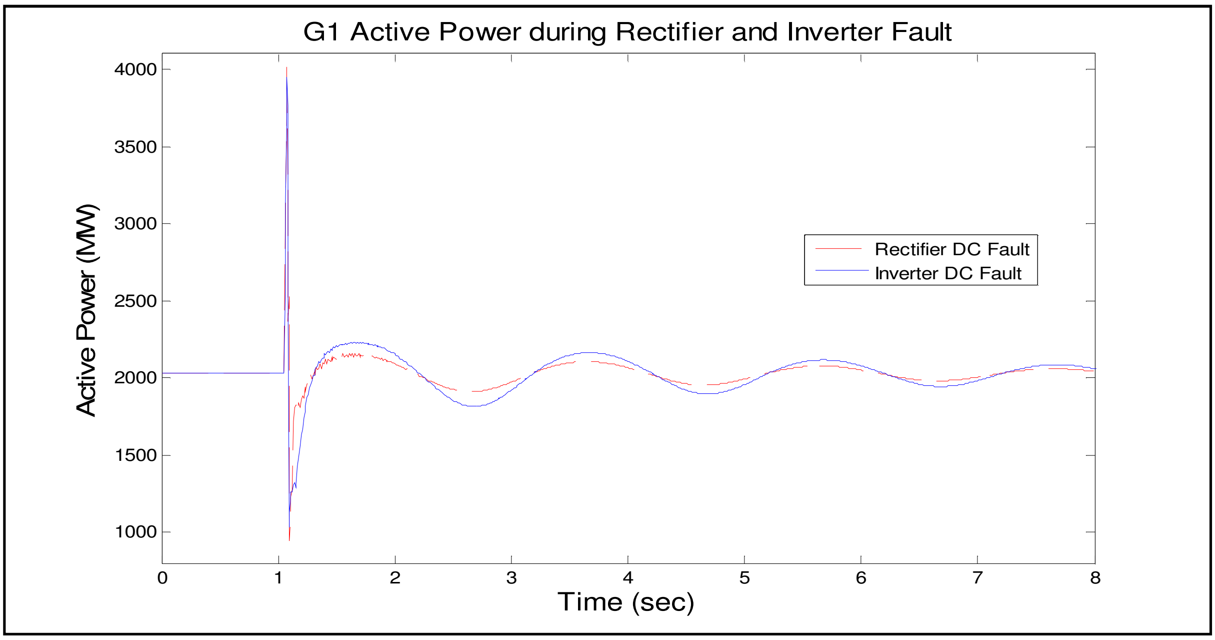

Figure 7.13 Case 2: Effects of Converter Fault on the Active Power at G1

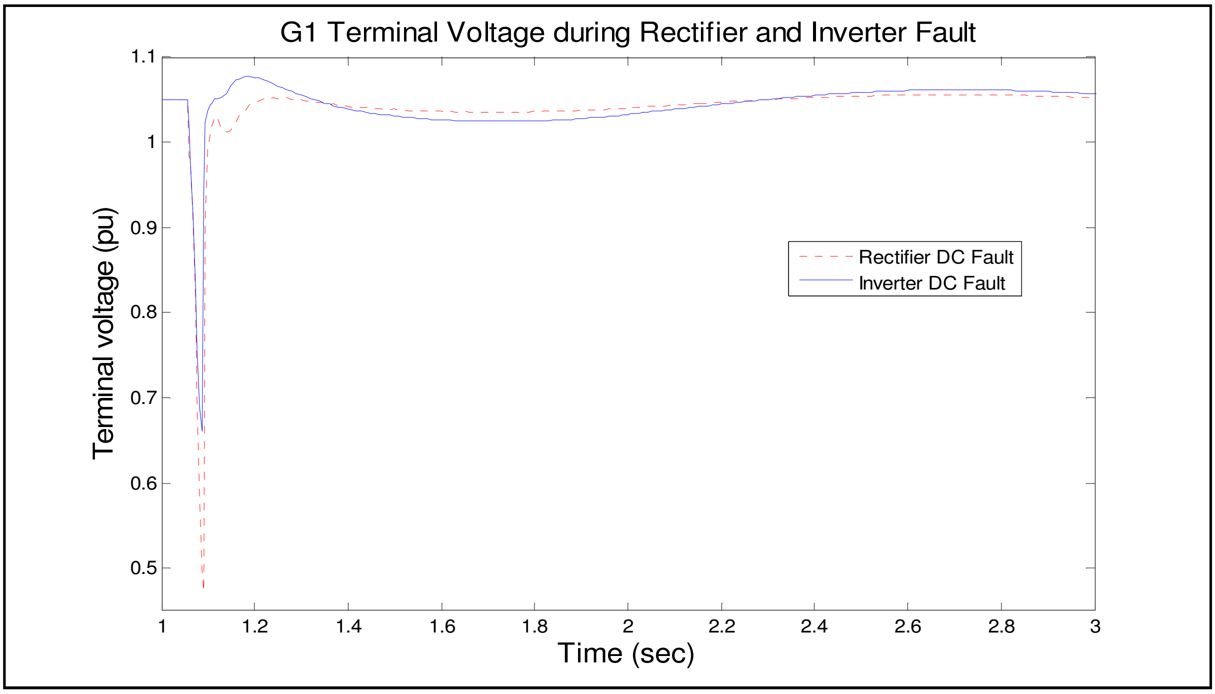

Figure 7.14 Case 2: Effects of Converter Fault on the Terminal Voltage at G1

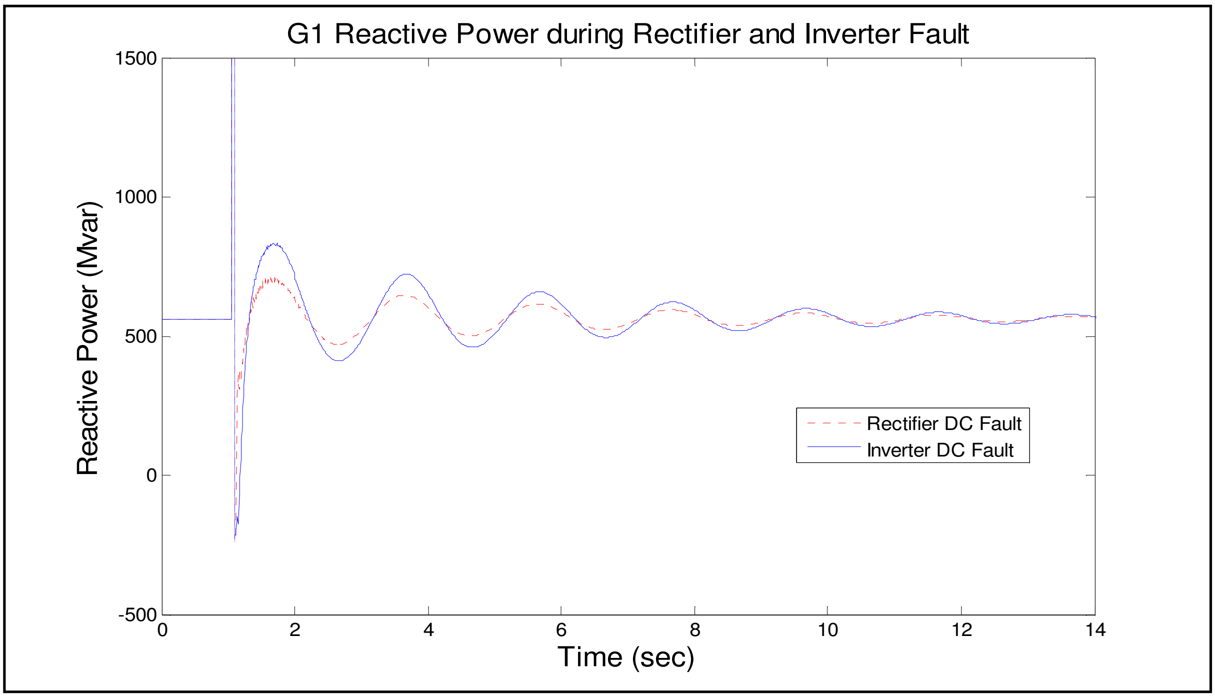

Figure 7.15 Case 2: Effects of Converter Fault on the Reactive Power at G1

In figure 7.15, the reactive power increase at G1 during both the inverter and the rectifier faults is lower than what is seen in case one. In this case (case two), the HVAC line transmitted about 800 Mvar towards bus two from bus three during the fault, as more power was transmitted via the HVAC transmission line. The results shown in figures 7.16 to 7.19 are obtained from G2 in area two.

The inverter DC fault had a greater effect on the rotor angle of G2, as shown in figure 7.16. It can be seen that the difference between the peak of the first swing for the rotor angle during the inverter fault is about 8° more than the peak of the first swing for the rotor angle of G2 during the rectifier fault. The rotor angle stabilised for both rectifier and inverter faults in about twenty seconds.

As in the case of the rotor angle of G2, the inverter DC fault also has a bigger impact on the active power generation as seen in figure 7.17. The amount of active power generated by G2 in figure 7.17 during both the rectifier and inverter faults in this case is about 500 MW less than the active power generation by G2 in case 1 (see figure 7.9).

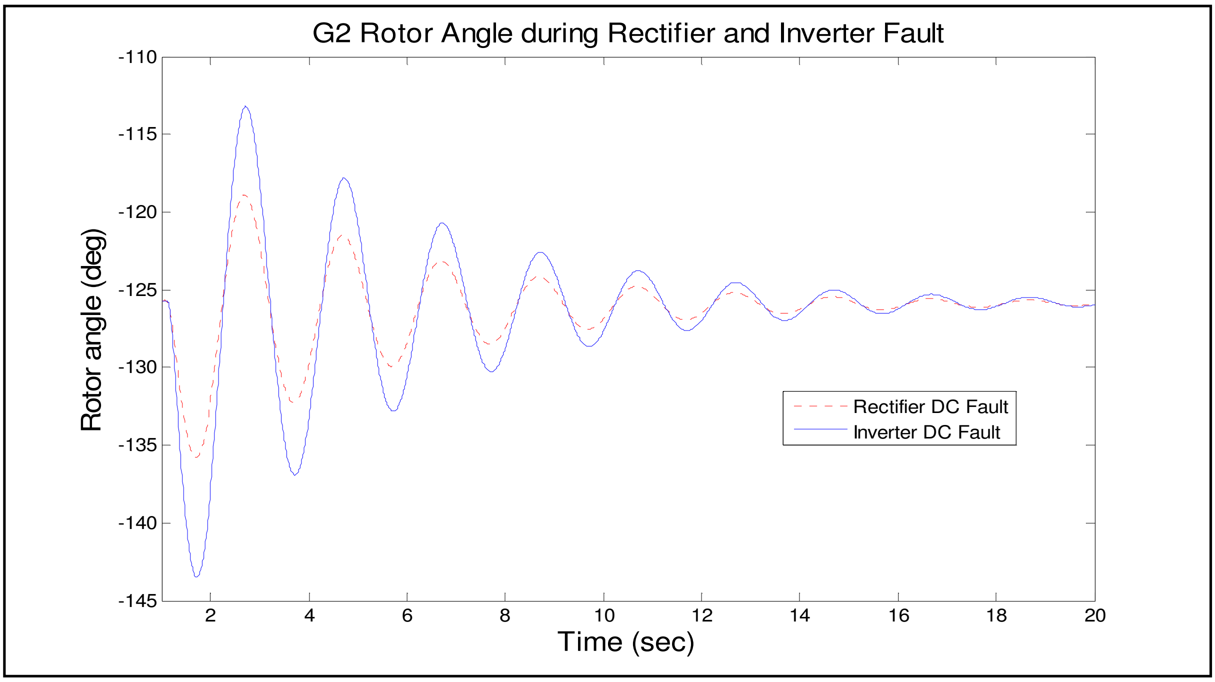

Figure 7.16 Case 2: Effects of Converter Fault on the Rotor Angle at G2

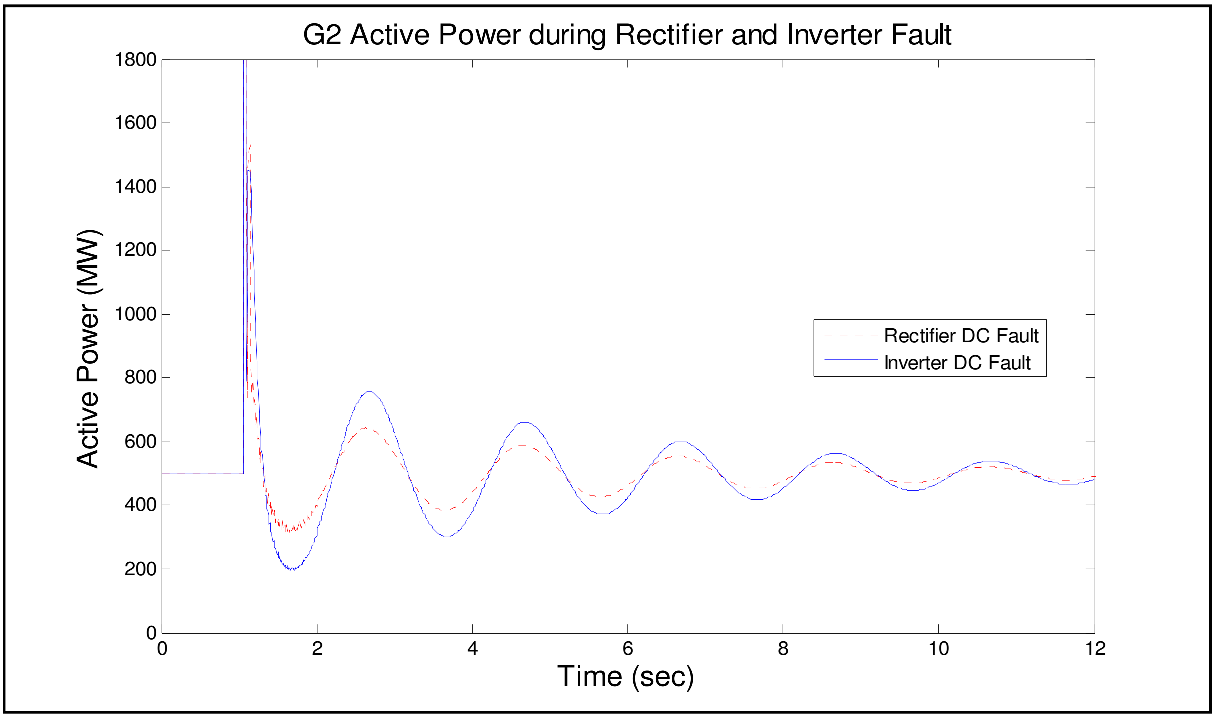

Figure 7.17 Case 2: Effects of Converter Fault on the Active Power at G2

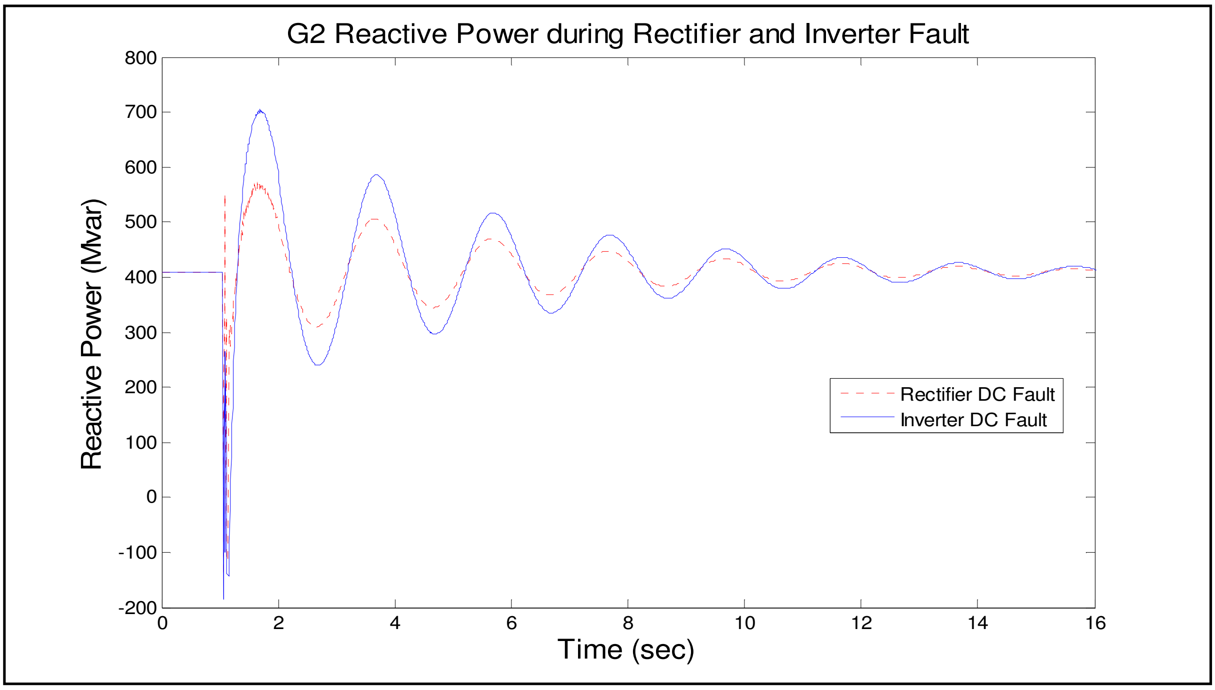

Figure 7.18 Case 2: Effects of Converter Fault on the Reactive Power at G2

Figure 7.18 shows the reactive power generated at G2. It can be seen that generator G2 absorbed less reactive power (200 Mvar) under both rectifier and inverter DC faults as compared with case one (figure 7.10). Although the settling time for the reactive power at G2 in case one was about ten seconds faster when compared with that in case two, the reactive power absorbed during the fault in case two is too high. The effect of the inverter DC fault is higher than the effect of the rectifier DC fault, as seen in figure 7.17 and figure 7.18. Figure 7.19 shows the terminal voltage at G2. It can be seen that the terminal voltage at G2 in this case had more oscillations and took about nine seconds more than in case one to settle to the pre-fault value of 1.0 pu. Also the terminal voltage increases to 1.025 pu as compared with 1.065 pu, as in case one. Since the amount of active power that was transmitted via the HVDC lien dropped during the fault, the amount of reactive power needed by the converters dropped. Hence there was a temporary excess of reactive power between the generators and the converters. Hence, it is assumed at this stage that this is why the terminal voltage at the time of the faults increased first before decreasing.

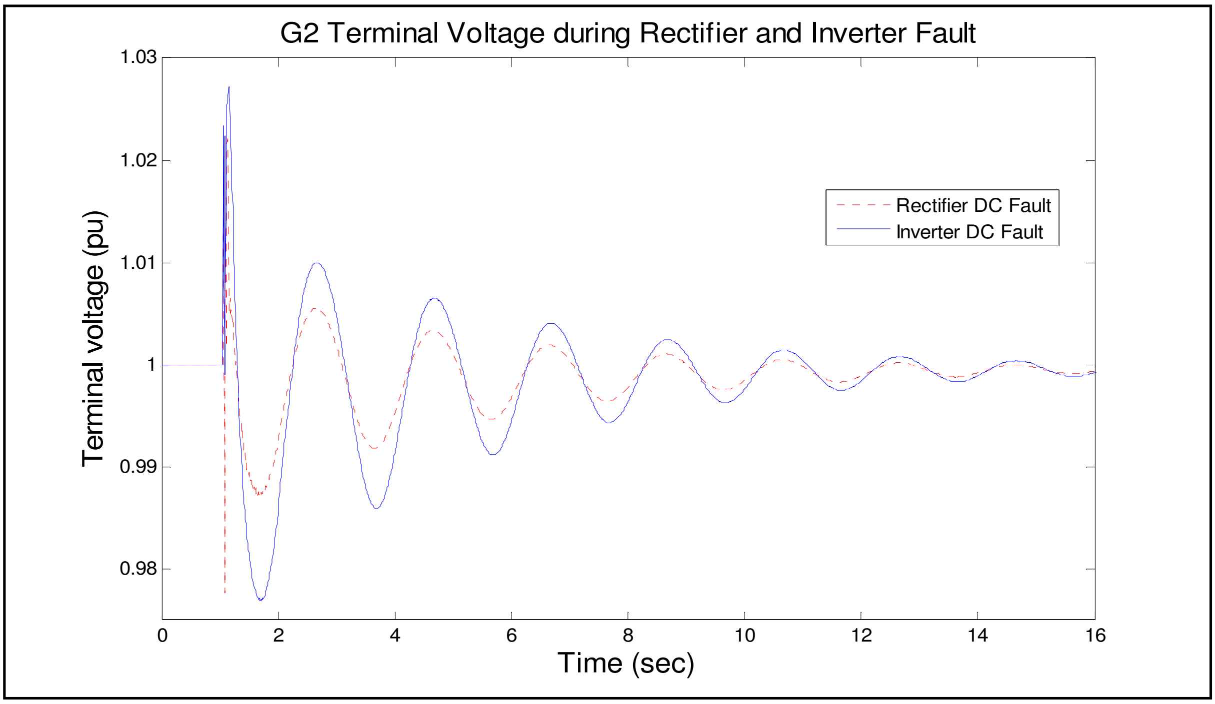

Figure 7.19 Case 2: Effects of Converter Fault on the Terminal Voltage at G2

7.2.2 Effects of Generator 3-phase Fault on the Transient Stability

At one second into the simulation a three-phase fault was applied at the terminal of generator G1 for 50 ms. The effect of the three-phase to ground fault on both generators, G1 and G2 are investigated.

7.2.2.1 Case 1: HVDC Transmission

The simulation results obtained in this case are given in figures 7.20 to 7.27. The results shown in figure 7.20 to figure 7.23 are obtained from G1 in area one. The pre-fault value of the rotor angle of G1 in figure 7.20 is around -75º. When the fault was initiated at one second into the simulation, the rotor angle of the G1 oscillated between -170º to 170º for about twenty seconds and slowly settled down to -18º after 90 seconds into the simulation.

During the fault the terminal voltage of G1 dropped to 0 pu as seen in figure 7.21, which corresponds to the decrease in active power to 0 MW as shown in figure 7.22.

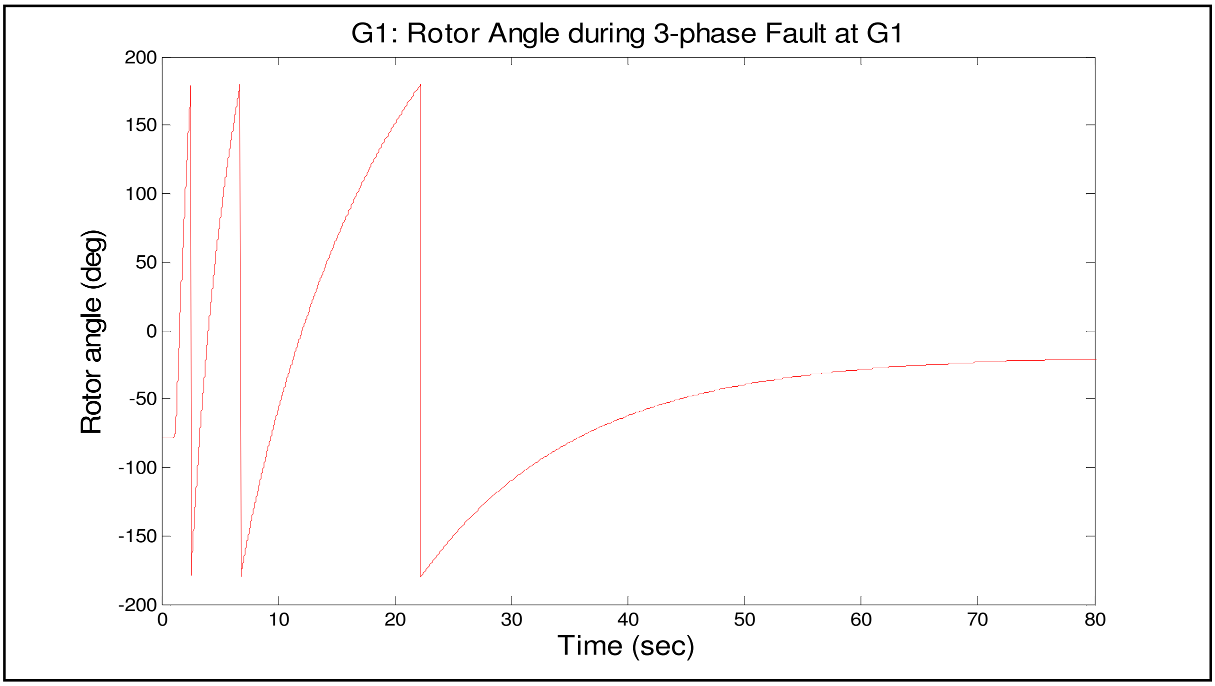

Figure 7.20 Case 1: Effect of G1 3-Phase Fault on the Rotor Angle of G1

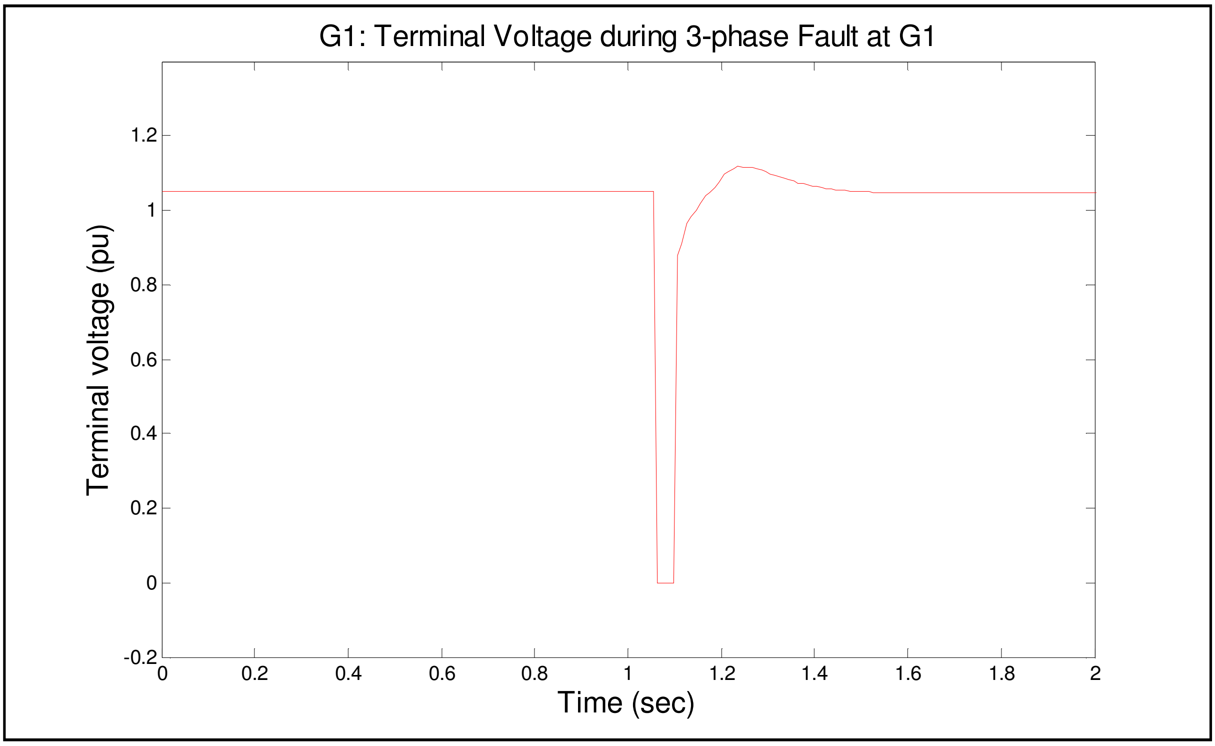

Figure 7.21 Case 1: Effect of G1 3-Phase Fault on the Terminal Voltage of G1

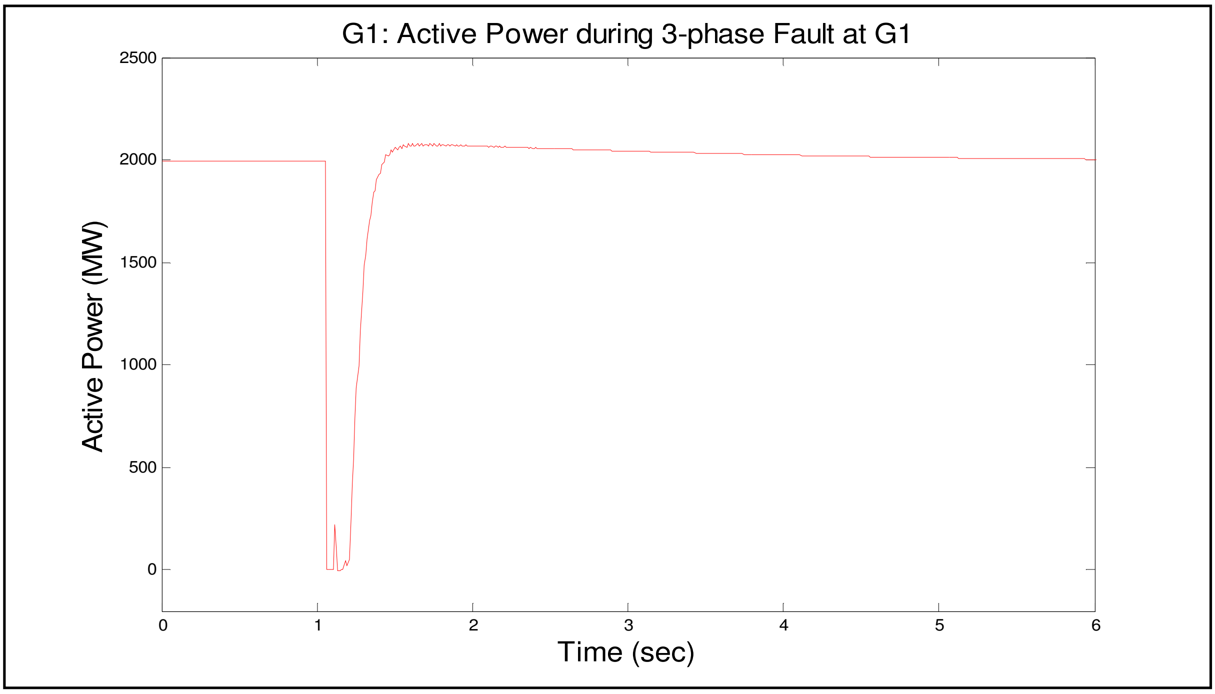

Figure 7.22 Case 1: Effect of G1 3-Phase Fault on the Active Power at G1

Because the capacitor banks and AC filter, which provide reactive power compensation at the rectifier side of the HVDC transmission line in area one, are fixed they were still providing reactive power while the converter was not operating (i.e., was not transmitting power to area one during the fault). As a result, G1 absorbed about 800 Mvar of the excess reactive power that was generated.

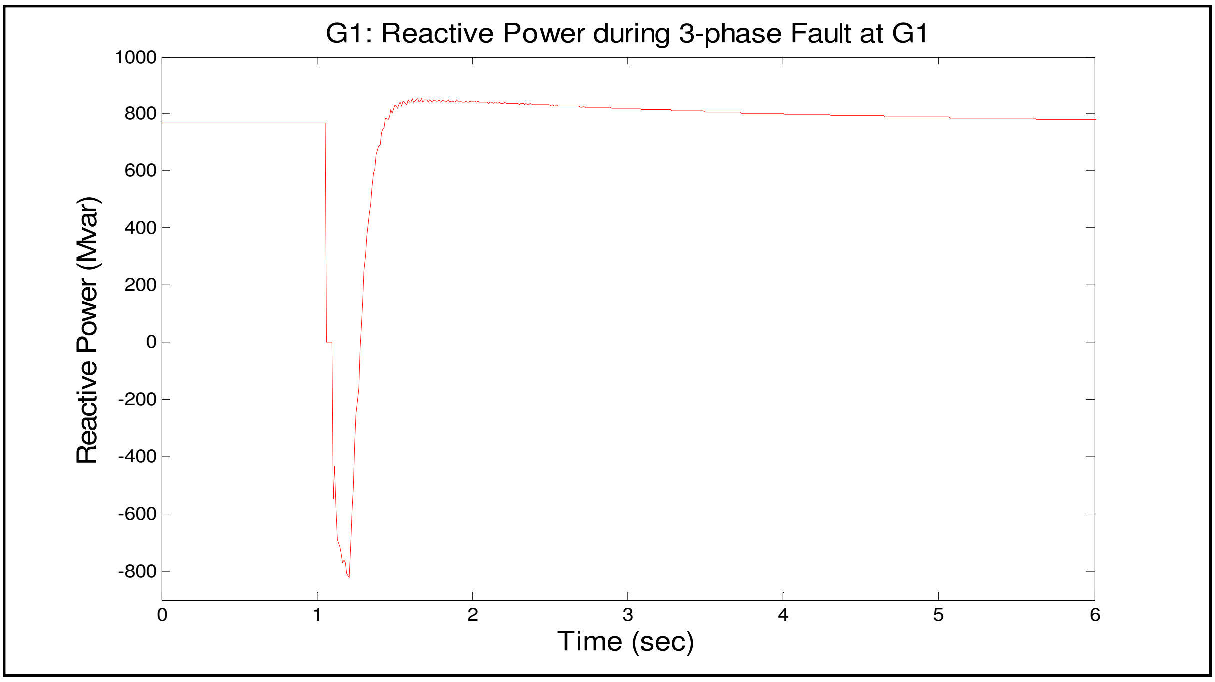

Figure 7.23 Case 1: Effect of G1 3-Phase Fault on the Reactive Power at G1

The results shown from figures 7.24 to 7.27 were obtained from G2 in area 2. In figure 7.24 the rotor angle of generator G2 in area two is constant at -86° throughout the simulation. As mentioned in section 7.2.1, the HVDC transmission line serves as a 'wall' between area one and area one, thus the oscillations in area one has a minimal affect on area two.

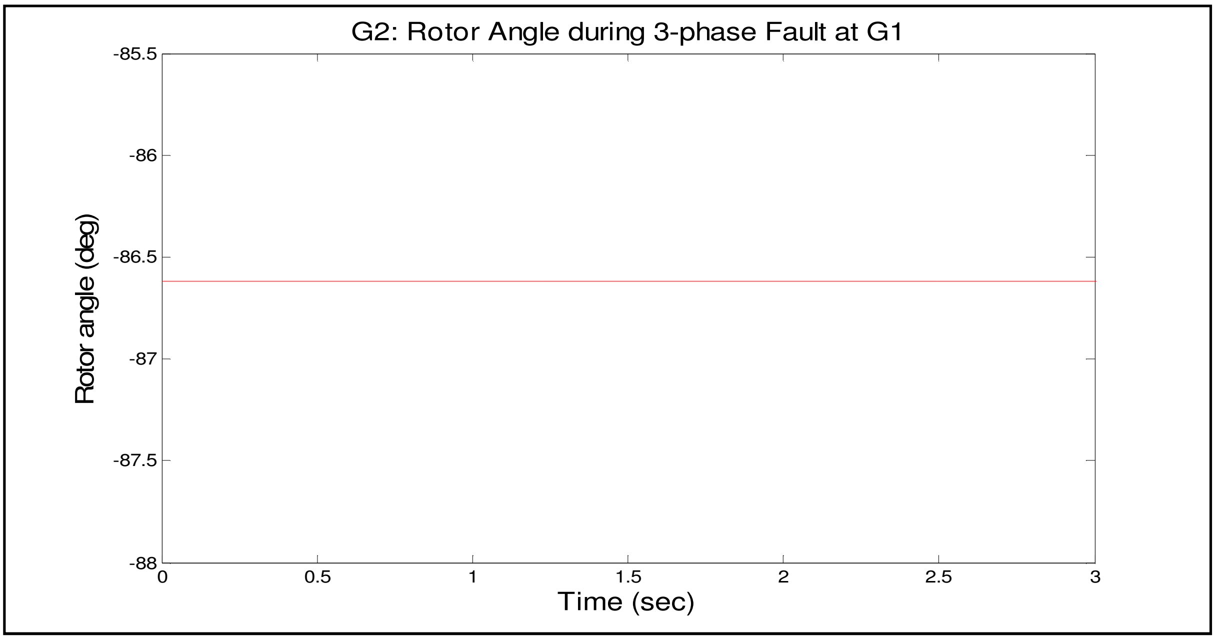

Figure 7.24 Case 1: Effect of G1 3-Phase Fault on the Rotor Angle of G2

Since power was not delivered to area two through the HVDC transmission line during the fault, the terminal voltage at G2 increased from 1.0 pu to 1.06 pu in order to meet the distribution centre load requirements in area two, as shown in figure 7.25. The active power supply from G2 increased from 500 MW to 2700 MW as shown in figure 7.26.

Both the terminal voltage and the active power at G2 returned to pre-fault values at 17 seconds and 6.5 seconds respectively once the fault was cleared.

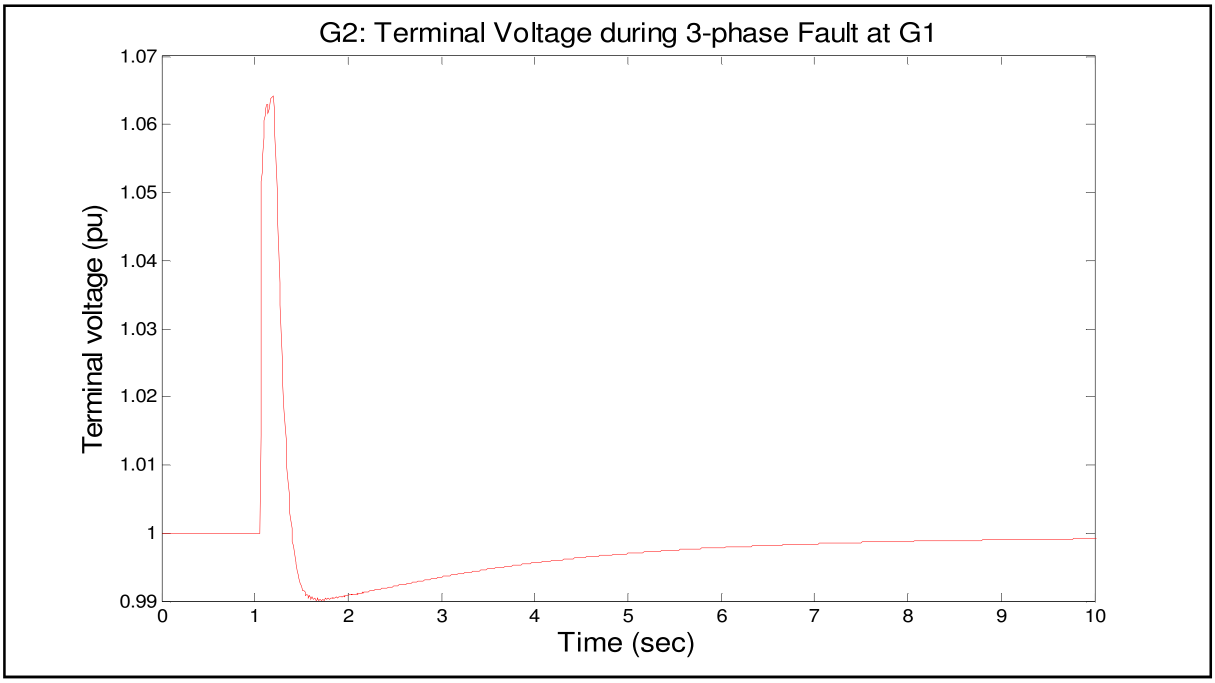

Figure 7.25 Case 1: Effect of G1 3-Phase Fault on the Terminal Voltage at G2

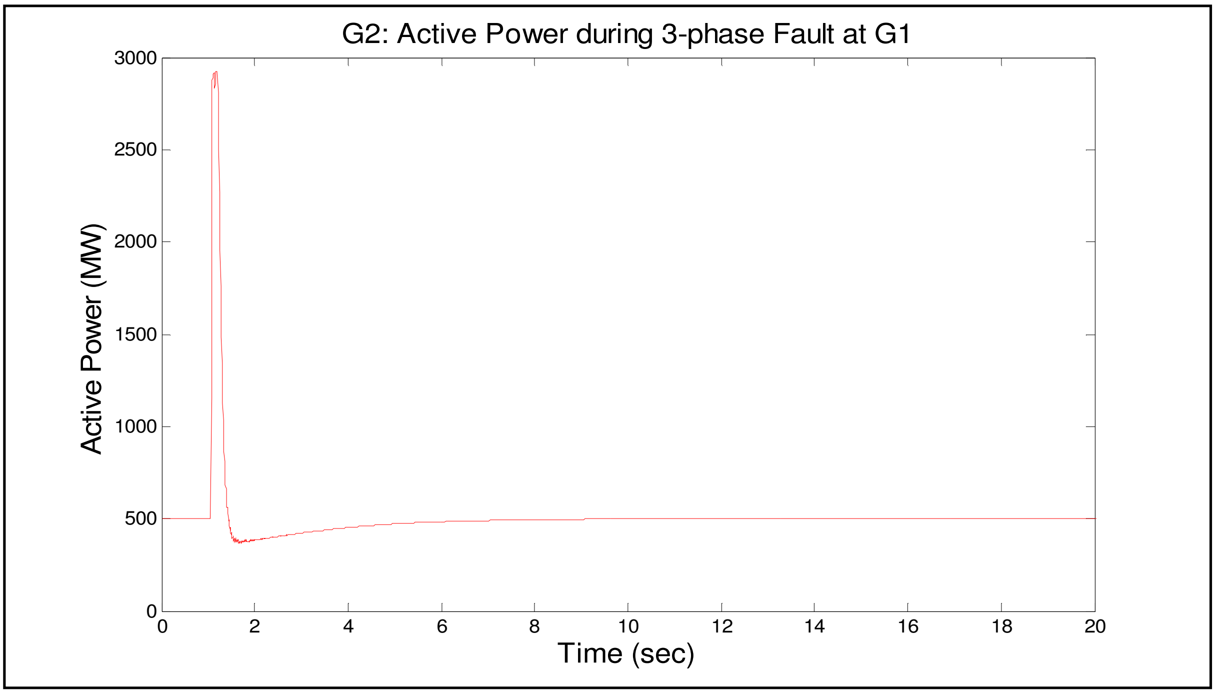

Figure 7.26 Case 1: Effect of G1 3-Phase Fault on the Active Power at G2

It can be seen from Figure 7.27 that during the fault G2 absorbed about 900 Mvar. Under steady state conditions G2 generates about 400 Mvar. This is because the inverter reactive power demand dropped during the fault as no power was transmitted through the HVDC transmission line to area two. After the fault was cleared and the HVDC transmission was restored, the reactive power demand by the inverter returned to its pre-fault value and hence the reactive power that was absorbed by G2 was reduced. At 6.5 seconds G2 reactive power generation reached its pre-fault value of about 390 Mvar.

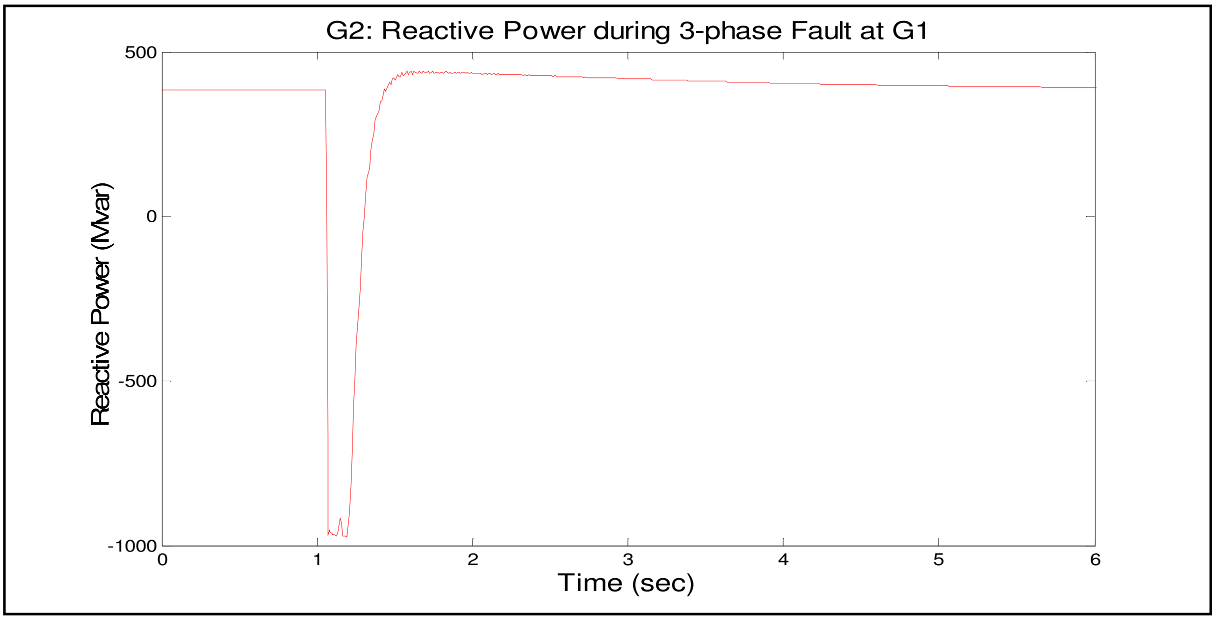

Figure 7.27 Case 1: Effect of G1 3-Phase Fault on the Reactive Power at G2

7.2.2.2 Case 2: Hybrid HVAC-HVDC Transmission

The simulation results obtained in this case are shown in figures 7.28 to 7.35. The results shown from figures 7.28 to 7.31 are obtained from G1 in area one. The effect of the converter DC fault on the rotor angle of G1 (in figure 7.12 during the DC fault on the hybrid system) resembled that on the rotor angle of G1 in figure 7.28 and thus remained unchanged.

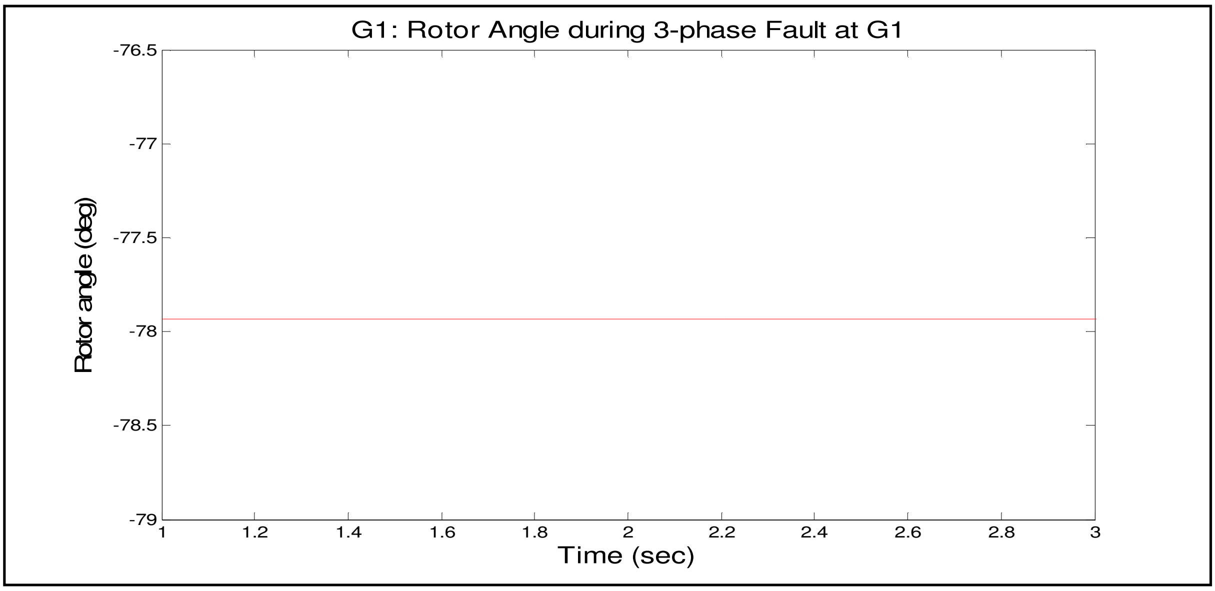

Figure 7.28 Case 2: Effect of G1 3-Phase Fault on the Rotor Angle of G1

During the fault the terminal voltage of G1 dropped to 0 pu as seen in figure 7.29, which corresponds to the decrease in active power to 0 MW in figure 7.30. Thus both the HVAC and the HVDC transmission lines were not transmitting active power. After the fault was cleared the active power generation at G1 returned to its pre-fault value of 2024 MW (see load flow results in section 7.1).

Figure 7.31 shows the change in reactive power during the fault and after it was cleared. It can be seen that during the fault G1 absorbed about 200 Mvar. Once the fault was cleared the reactive power generated by G1 oscillated between -200 Mvar and 1200 Mvar, with decaying oscillations, and reached its pre-fault operating condition of 555 Mvar in twenty seconds.

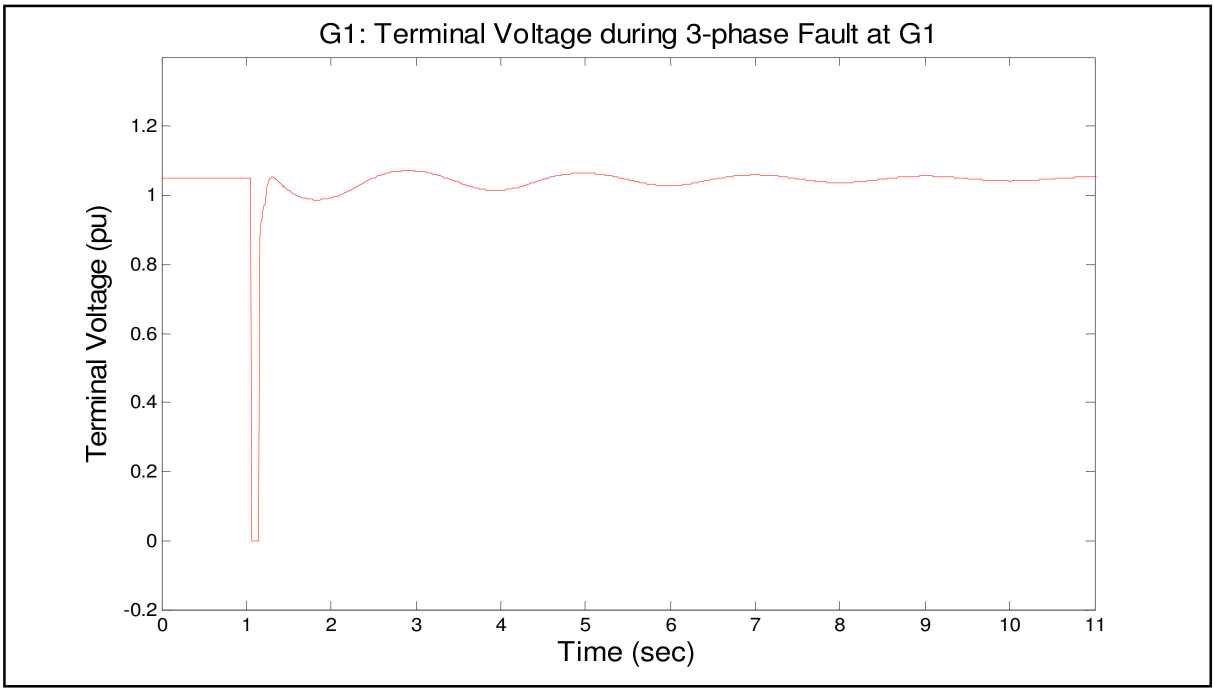

Figure 7.29 Case 2: Effect of G1 3-Phase Fault on the Terminal Voltage of G1

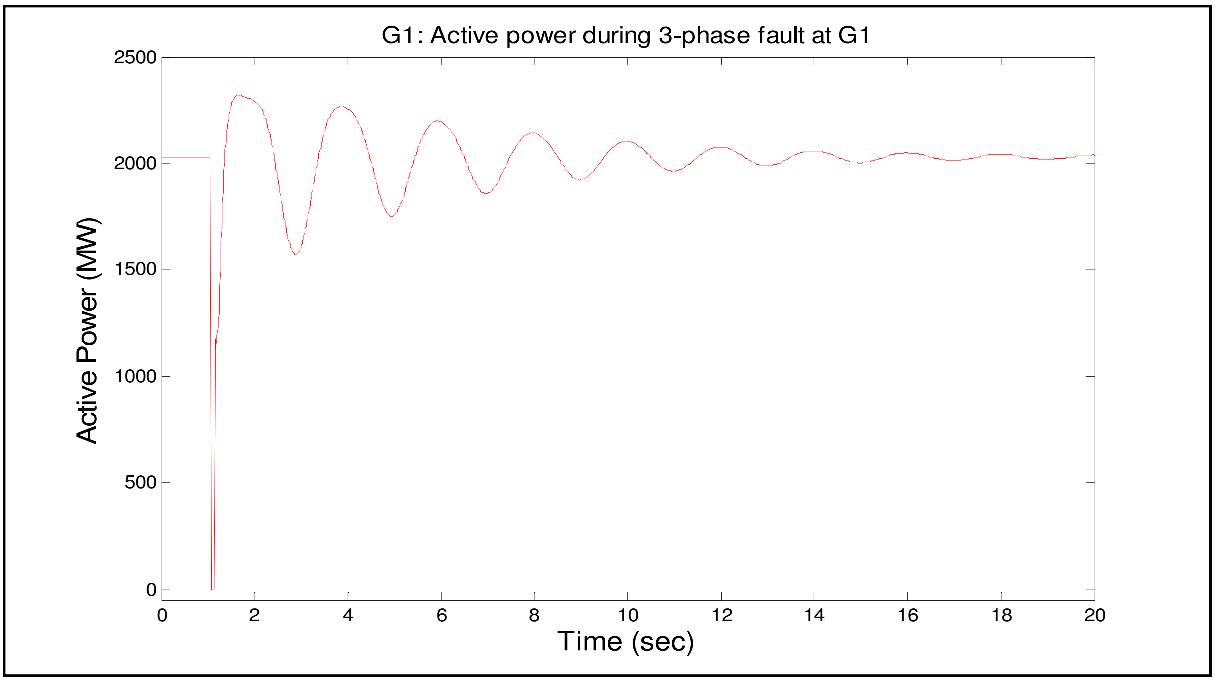

Figure 7.30 Case 2: Effect of G1 3-Phase Fault on the Active Power at G1

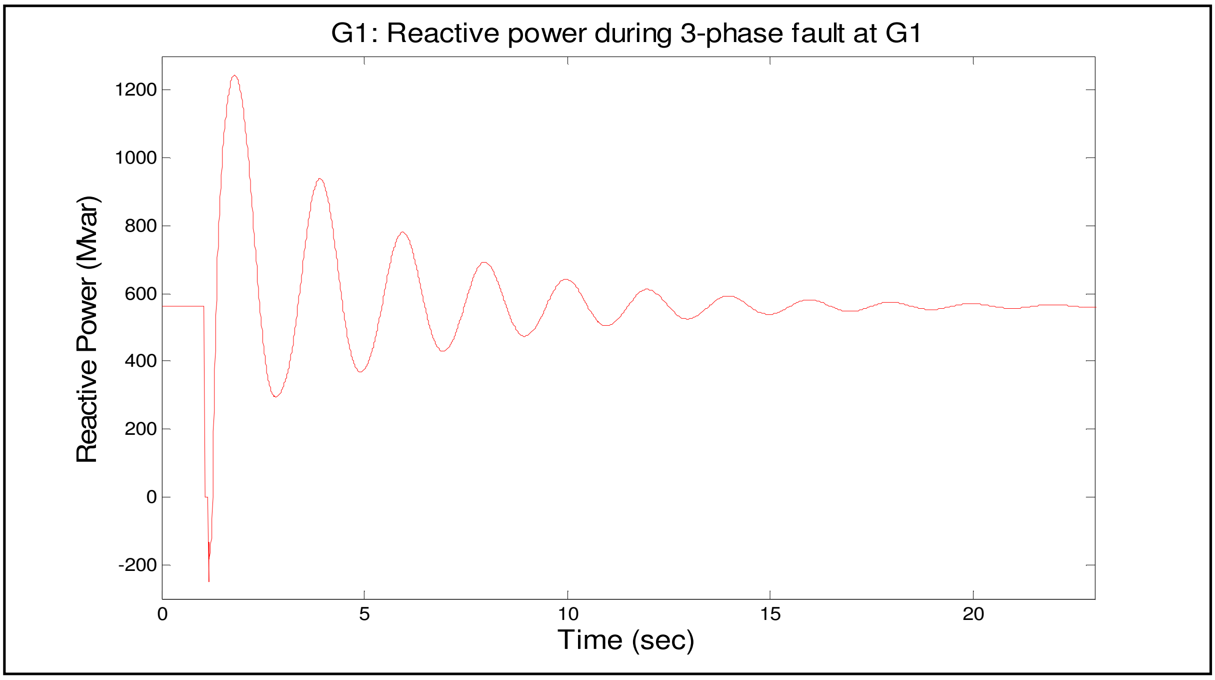

Figure 7.31 Case 2: Effect of G1 3-Phase Fault on the Reactive Power at G1

The results shown from figures 7.32 to 7.35 were obtained from G2 in area two.

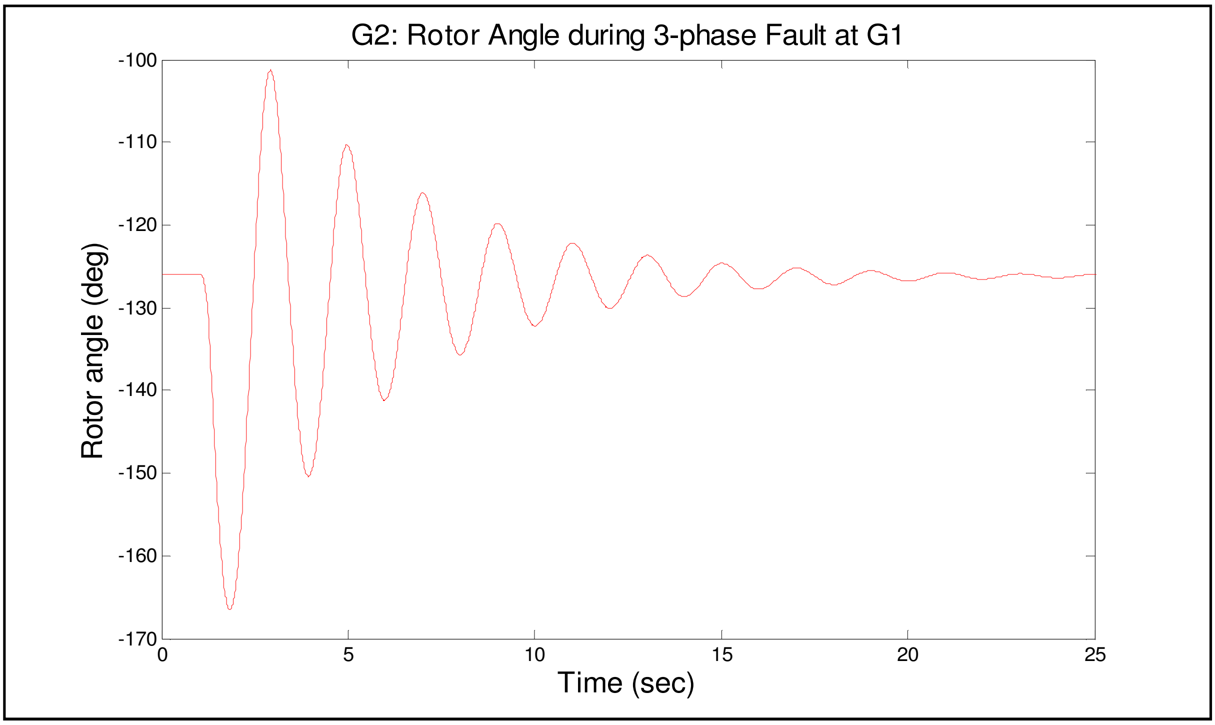

Figure 7.32 Case 2: Effect of G1 3-Phase Fault on the Rotor Angle of G2

During the fault the rotor angle of G2 reduced from -127^0 to -168^0. After the fault was cleared the rotor angle oscillated between -168^0 and -105^0 before it settled at its pre-fault value of -127^0 in twenty seconds.

In order to meet the distribution centre load requirements in area two during the fault, the active power supply from G2 increased from 500 MW to 2400 MW, as shown in figure 7.33. Once the fault was cleared the active power at G2 returned to pre-fault value in nineteen seconds.

Contrary to case one (figure 7.25), the terminal voltage at G2 decreased during the fault from 1.0 pu to 0.95 pu and oscillates, as seen in figure 7.34. The terminal voltage stabilised after nineteen seconds into the simulation.

The reactive power at G2 during the fault increased from 407 Mvar to 1250 Mvar and oscillated for about eighteen seconds after the fault was cleared. It then settled down at about twenty seconds, as shown in figure 7.35. This increase is aimed at supplying the loads which are connected to bus two. Otherwise the load demand will not be met.

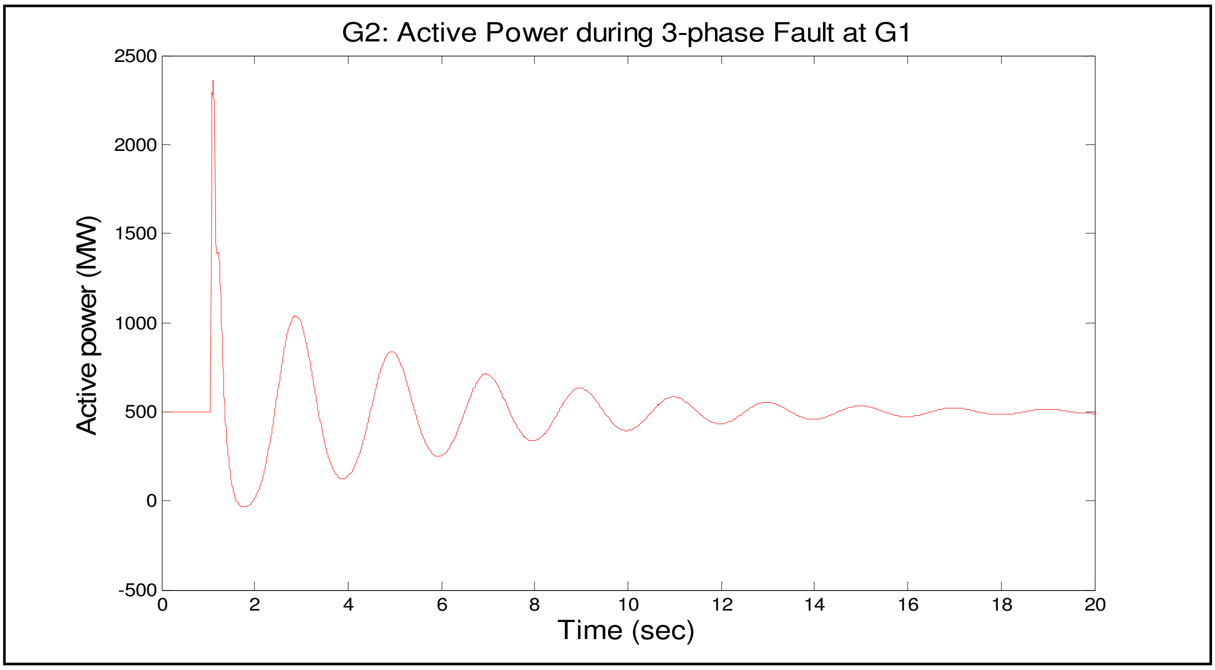

Figure 7.33 Case 2: Effect of G1 3-Phase Fault on the Active Power at G2

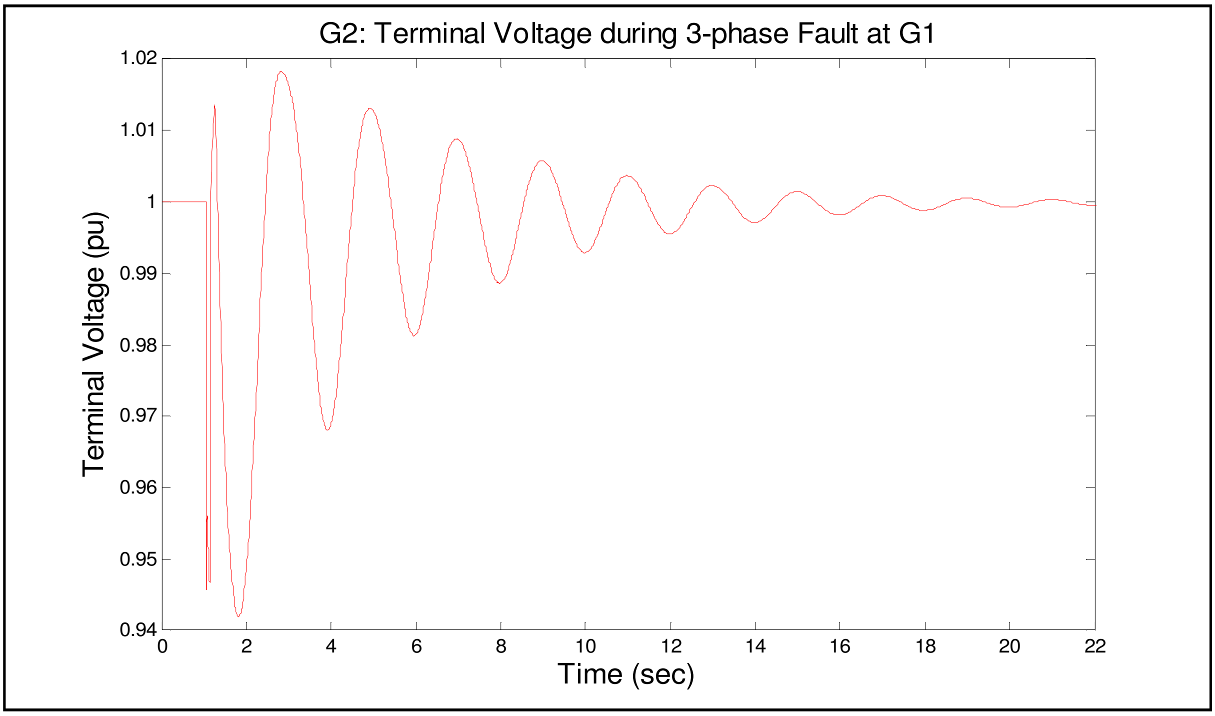

Figure 7.34 Case 2: Effect of G1 3-Phase Fault on the Terminal Voltage at G2

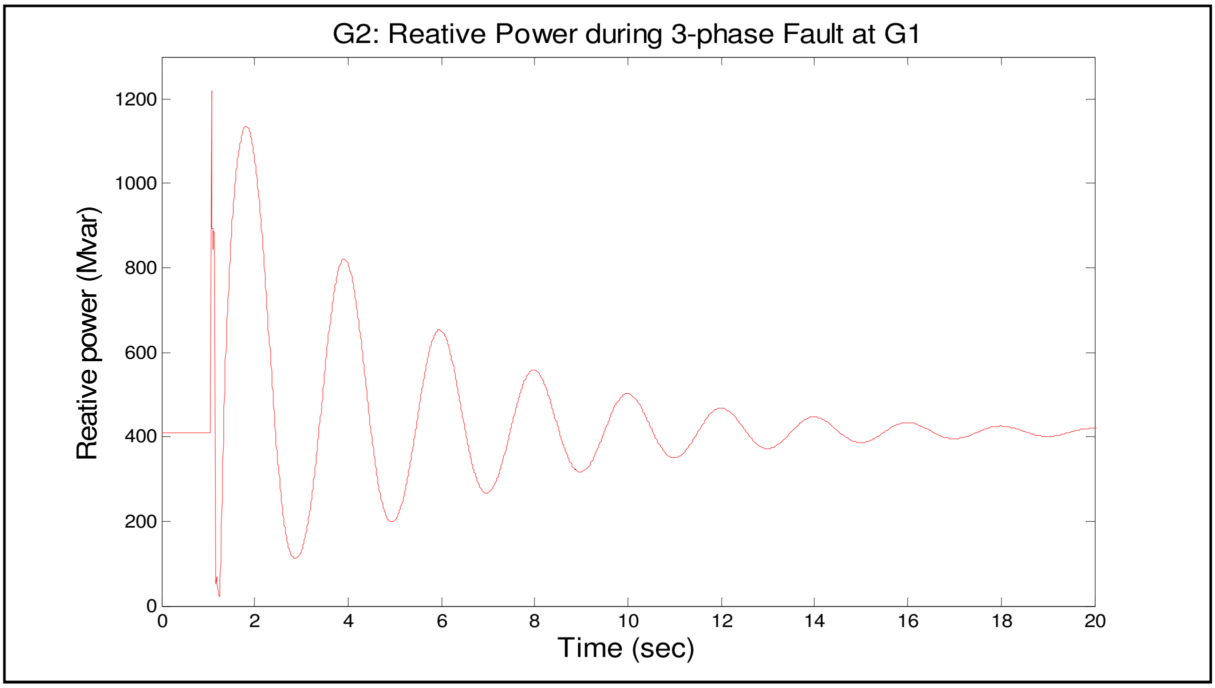

Figure 7.35 Case 2: Effect of G1 3-Phase Fault on the Reactive Power at G2

7.2.3 Conclusions on the effect of Converter DC fault and 3-Phase AC Fault on the Transient Stability of the SMIB Power System

The results presented in section 7.2.1 and 7.2.2, above, showed the impact of converter DC fault and a three-phase fault on the transient stability of the SMIB power system, using the two different transmission schemes. From these results, the following conclusions are made.

Converter DC faults:-

When hybrid HVAC-HVDC was used for transmission, the amount of rotor angle, terminal voltage and active and reactive power oscillations were increased when compared with the use of HVDC transmission. This means that the Hybrid HVAC-HVDC system is more unstable in terms of the number of oscillations. Nevertheless when using the hybrid HVAC-HVDC system, the lower peak of G1's first active power swing reduced by 1500 MW (i.e., from -500 MW to 1000 MW), while the upper peak of G2's first active power swing reduced by 500 MW (i.e., from 2800 MW to 2300 MW). As the generators recovered from the fault, the reactive power absorbed at G1 reduced from -900 Mvar to -250 Mvar and from -950 Mvar to 180 Mvar at G2. The terminal voltage at G1 improved by an average of 0.07 pu and G2 by an average of 0.0075 pu as the generators recovered from the fault. The rotor angle of G1 did not change while the rotor angle of G2 had large and decaying oscillations.

For both transmission schemes, the active and reactive power overshoot exceeded the generating capacity of G1 and G2.

Generator three-phase fault:-

The use of Hybrid HVAC-HVDC transmission introduced more rotor angle, terminal voltage, and active and reactive power oscillations as the generators (G1 and G2) recovered from the converter DC fault. Nevertheless, the lower peak of G1’s first reactive power swing reduced from -800 Mvar to -210 Mvar, while the upper peak was at 1250 Mvar. The lower peak of G2’s first reactive power swing reduced from -900 Mvar to 40 Mvar, while the upper peak was as 1200 Mvar. At G2 the terminal voltage overshoot during the fault reduced from 1.06 pu to 1.01 pu, while the active power overshoot reduced from 2800 MW to 2300 MW.

For both transmission schemes the active power at G1 reduced from 2000 MW to 0 MW during the fault while the terminal voltage reduced from 1.05 pu to 0 pu. As in the case of the DC converter fault, the generating capacities of G1 and G2 were exceeded.

In order to prevent the generators from exceeding their capacities during the fault they must be disconnected by fast control and protection action. Otherwise, to prevent total blackout, load shedding can be carried out at the distribution centre to disconnect non-essential customers in order to meet the local generating capacity at G2, pending the restoration of power import from G1.

7.3 SMALL SIGNAL STABILITY

The DigSILENT round rotor synchronous generator model was used in the simulation. This generator is modelled as a fifth order generator [37]. Hence, five modes are expected from each of the generators in the result of the modal analysis of the small signal stability. The IEEET1 AVR and IEEEST PSS controllers were added to the model of generator G2. The function of the PSS is to add damping to the generator oscillations by controlling its excitation using stabilising signal(s). The AVR has four state variables in its model which yielded four modes, while the PSS has eight state variables in its model, which give eight modes. The block diagram and the parameters of the PSS and the AVR are given in Appendix D. Therefore the total number of modes expected from the modal analysis simulation result is 22.

Tables 7.6 and 7.7 show the modes in case 1 (HVDC transmission) and in case two (hybrid HVAC-HVDC transmission) respectively.

Table 7-6 Eigenvalues from Case 1: HVDC Transmission

Modes	Real Part	Imaginary Part	Magnitude	Damped Frequency	Damping Ratio
	1/s	rad/s	1/s	Hz	
Mode 01 & 02 & 03	0	0	0	0	0
Mode 04	-999.9999	0	999.9999	0	1
Mode 05	-50.00787	0	50.00787	0	1
Mode 06	-33.19344	0	33.19344	0	1
Mode 07	-24.80938	0	24.80938	0	1
Mode 08	-22.33808	0	22.33808	0	1
Mode 09	-8.438625	0	8.438625	0	1
Mode 10	-8.0364	0	8.0364	0	1
Mode 11	-5.014393	0	5.014393	0	1
Mode 12	-3.322664	0	3.322664	0	1
Mode 13 & 14	-0.2546854	±0.962995	0.996104	0.1532653	0.2556816
Mode 15 & 16	-1	0	1	0	1
Mode 17	-0.6475613	0	0.6475613	0	1
Mode 18	-0.555615	0	0.555615	0	1
Mode 19	-0.1240529	0	0.1240529	0	1
Mode 20 & 21	-0.06963148	±0.003122	0.06970143	0.00049687	0.9989964
Mode 22	-0.0000001	0	0.0000001	0	1

The eigenvalues of the modes in table 7.6 show that all the 22 modes are stable. This is because of the positive damping ratio and the negative real part of their eigenvalues. Modes 13 & 14 are oscillatory modes with a damping ratio of 0.26. The damping frequency of modes 13 and 14 indicates that they are inter-area modes. The rest of the modes are critically damped including the control mode (20 & 21). For a SMIB power system, local modes are expected with a frequency within the range, [0.9 2.0] Hz. However, the infinite bus may not be modeled as a large generator. While this is mandatory for small signal stability, in load flow analysis, it is not mandatory as the amount of power that the machines dispatch is what is used for load flow calculations. In SMIB model used for the simulation, the rating of the two machines where the same, although the G1 (slack bus) dispatched about 2000 MW while the G2 (PV bus) dispatched about 500 MW. Therefore, the frequency of the electromechanical mode represented an inter-area mode.

Figure 7.36 to 7.39 shows the only two states and their participation factor to the electromechanical modes (13 & 14) and (20 & 21). These states are speed and excitation flux.

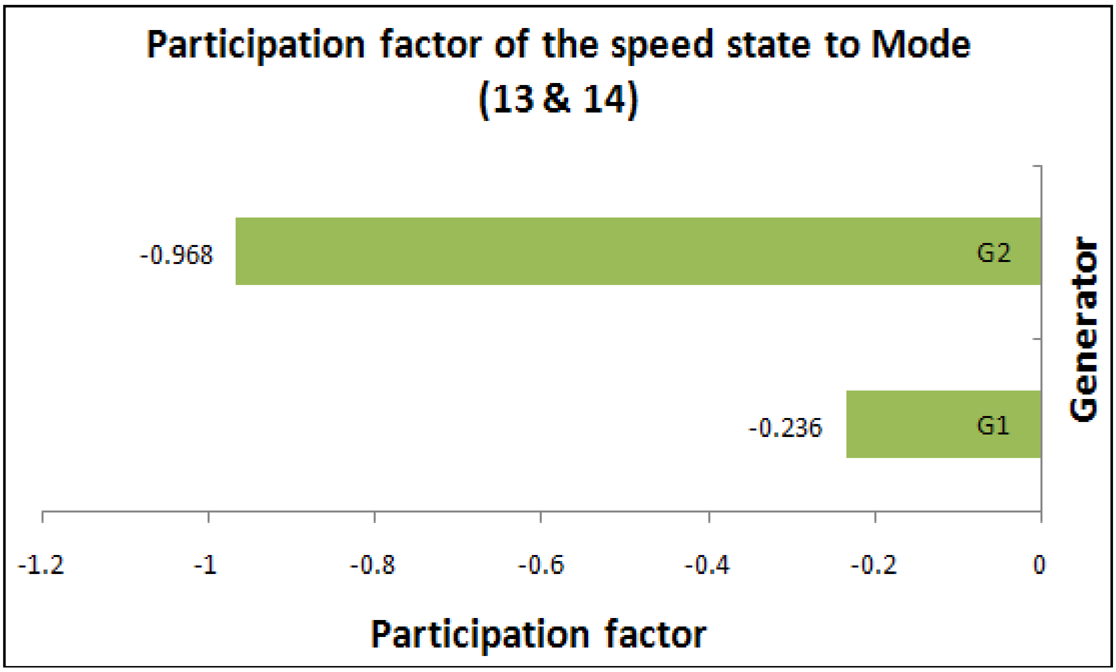

Figure 7.36 Speed participation factor to mode 13 & 14

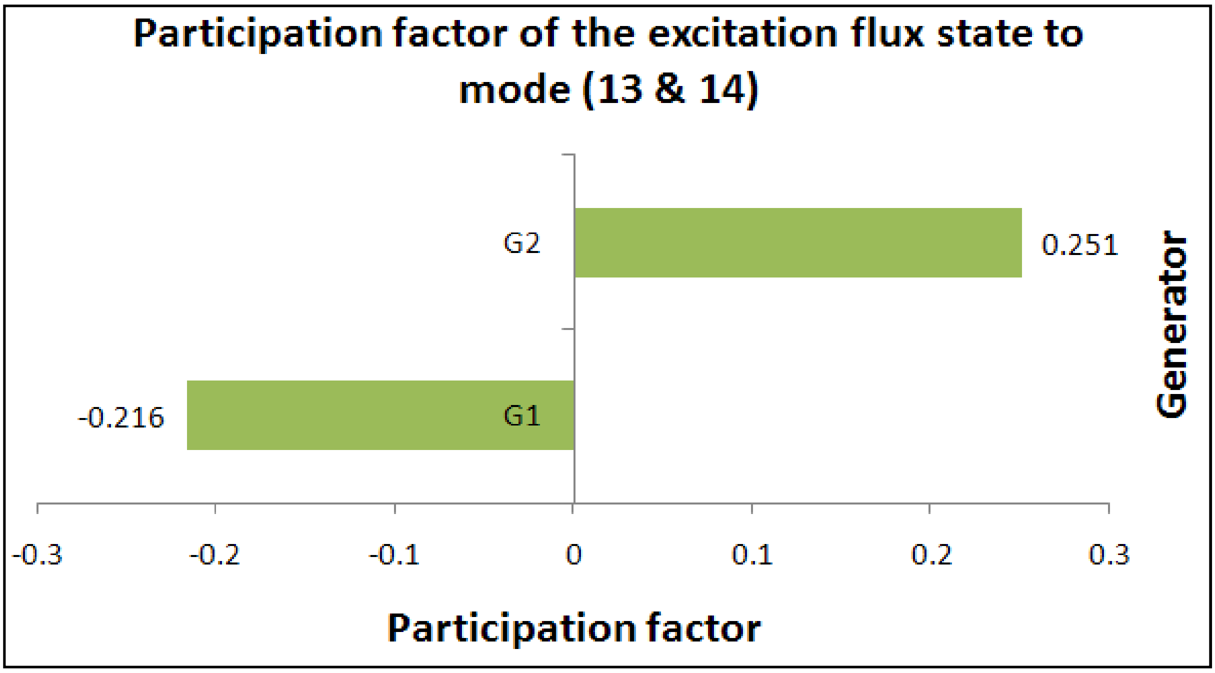

Figure 7.37 Excitation flux participation factor to mode 13 & 14

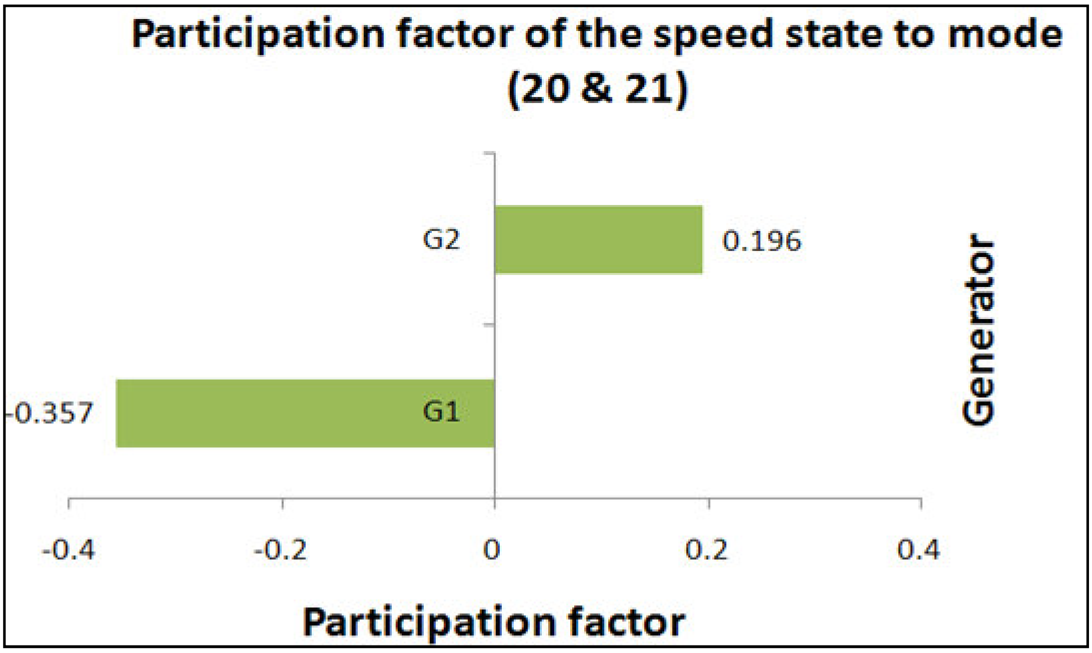

Figure 7.38 Speed participation factor to mode 20 & 21

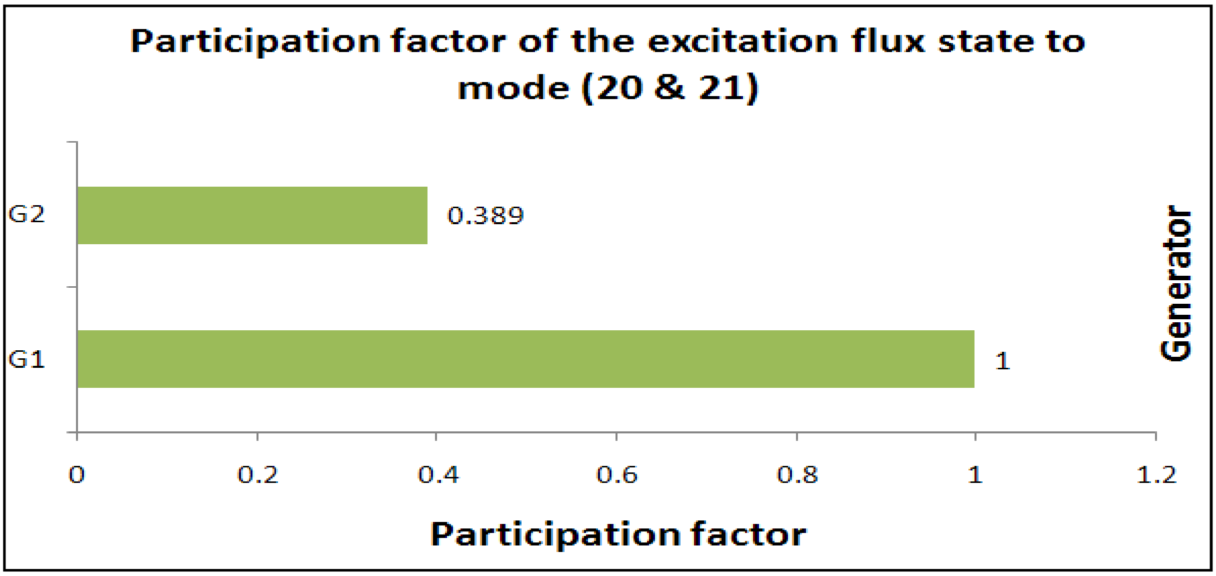

Figure 7.39 Excitation flux participation factor to mode 20 & 21

From the participation factors, it can be concluded that generator speed had a greater influence on mode (13 & 14) while the excitation flux had a greater influence on mode (20 & 21). There was no participation of the rotor angle to these states. For case two, with the hybrid HVAC-HVDC transmission line, the eigenvalues obtained from the system are presented in table 7.7.

Table 7-7 Eigenvalues from Case 2: Hybrid HVAC-HVDC Transmission

Mode	Real Part	Imaginary Part	Magnitude	Damped Frequency	Damping Ratio
	1/s	rad/s	1/s	Hz	
Mode 01 & 02 & 03	0	0	0	0	0
Mode 04	-999.9999	0	999.9999	0	1
Mode 05	-50.0075	0	50.0075	0	1
Mode 06	-33.19306	0	33.19306	0	1
Mode 07	-24.71876	0	24.71876	0	1
Mode 08	-22.10347	0	22.10347	0	1
Mode 09 & 10	-8.830152	0	8.830152	0	1
Mode 11	-5.041496	0	5.041496	0	1
Mode 12 & 13	-0.2106676	±3.106716	3.113851	0.4944492	0.06765501
Mode 14	-3.329756	0	3.329756	0	1
Mode 15 & 16	-0.2507619	±0.9680661	1.000017	0.1540725	0.2507577
Mode 17 & 18	-1	0	1	0	1
Mode 19	-0.6528545	0	0.6528545	0	1
Mode 20	-0.1437174	0	0.1437174	0	1
Mode 21 & 22	-0.07121907	±0.00296276	0.07128067	0.00047154	0.9991358

Three sets of oscillatory modes exist in table 7.7. These are modes 12 & 13, 15 & 16 and 21 & 22. Among these oscillatory modes, only modes 21 & 22 are critically damped with a damping ratio of 0.99. Modes 15 and 16 are well damped while modes 12 & 13 are poorly damped. Furthermore, mode 21 & 22 are slightly oscillatory with a vey low frequency of 0.00047 Hz and a damping ratio of approximately 1. All the modes excluding modes 01, 02 and 03 are stable as their eigenvalues have negative real parts. Figure 7.40 to 7.44 shows the only two states and their participation factor to the electromechanical modes (12 & 13), (15 & 16) and (21 &22). These states are speed and excitation flux.

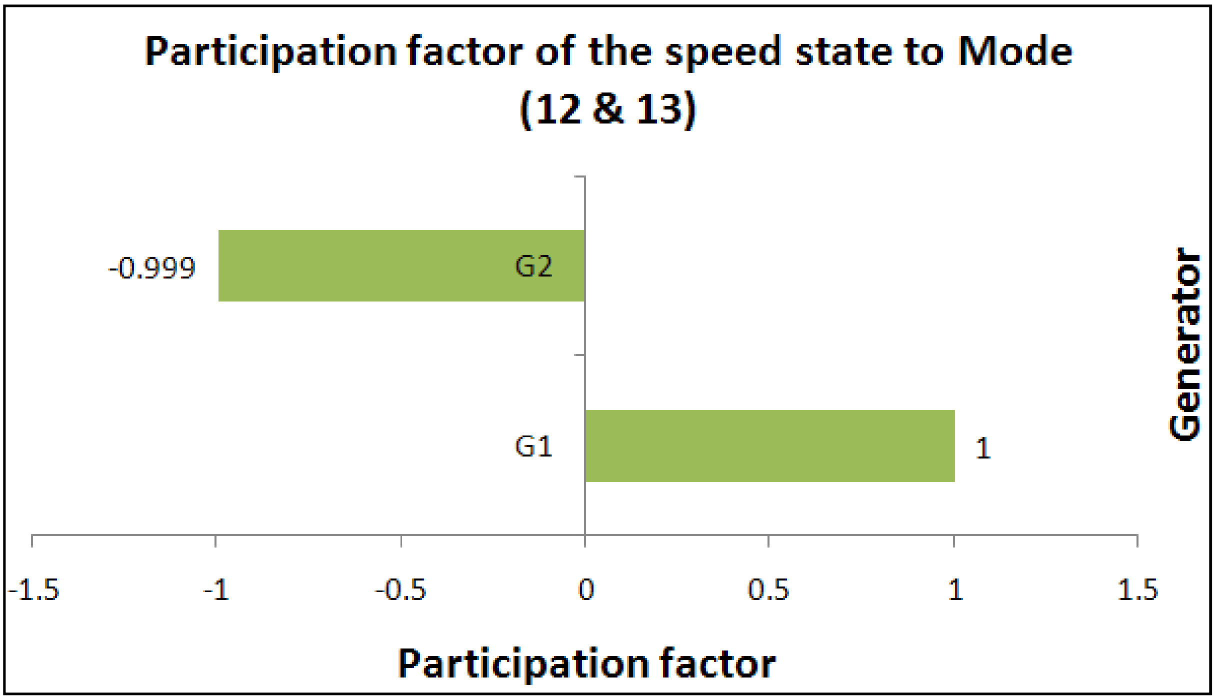

Figure 7.40 Speed participation factor to mode (12 & 13)

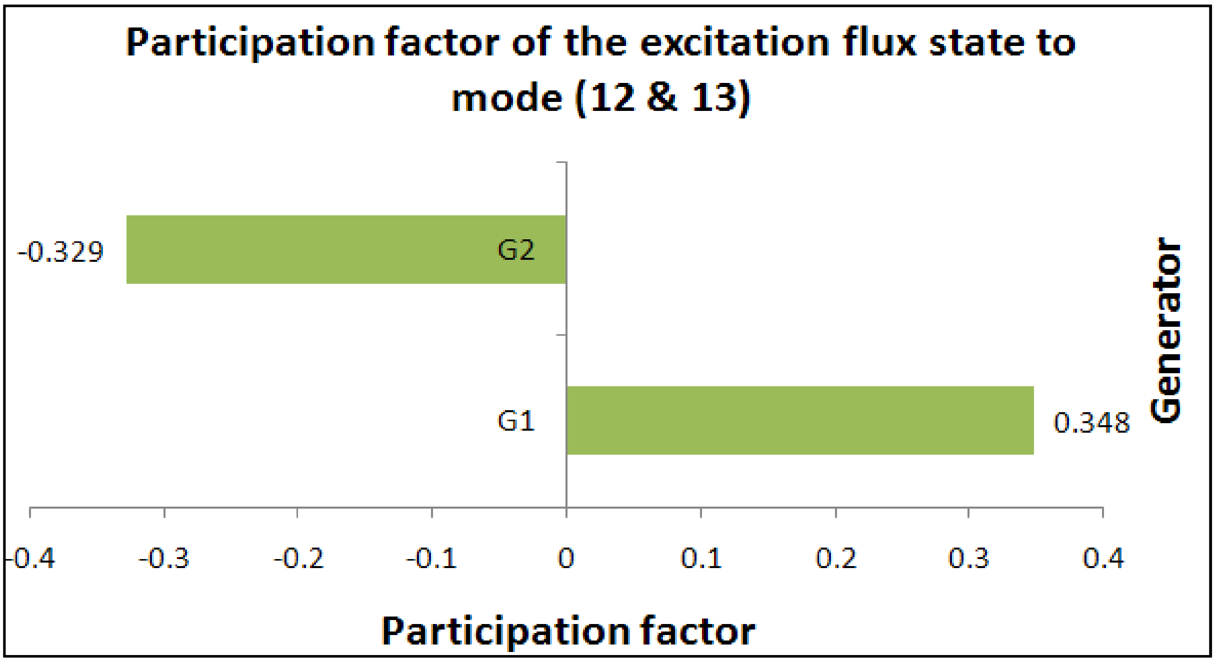

Figure 7.41 Excitation flux participation factor to mode 12 & 13

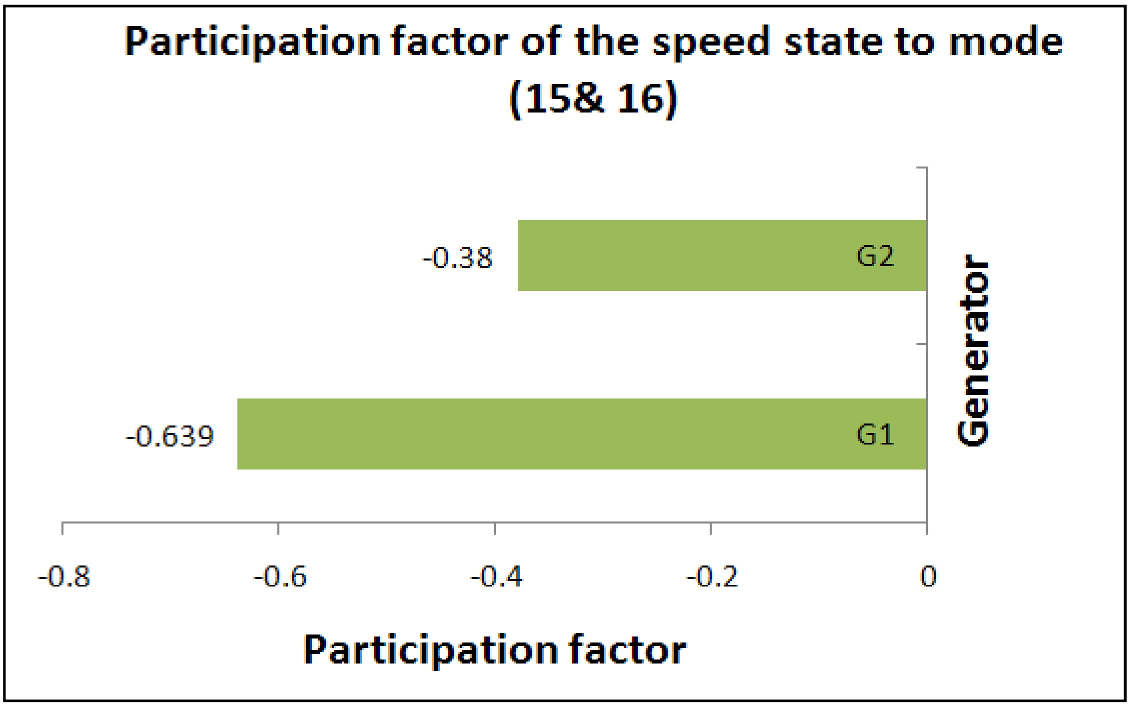

Figure 7.42 Speed participation factor to mode 15 & 16

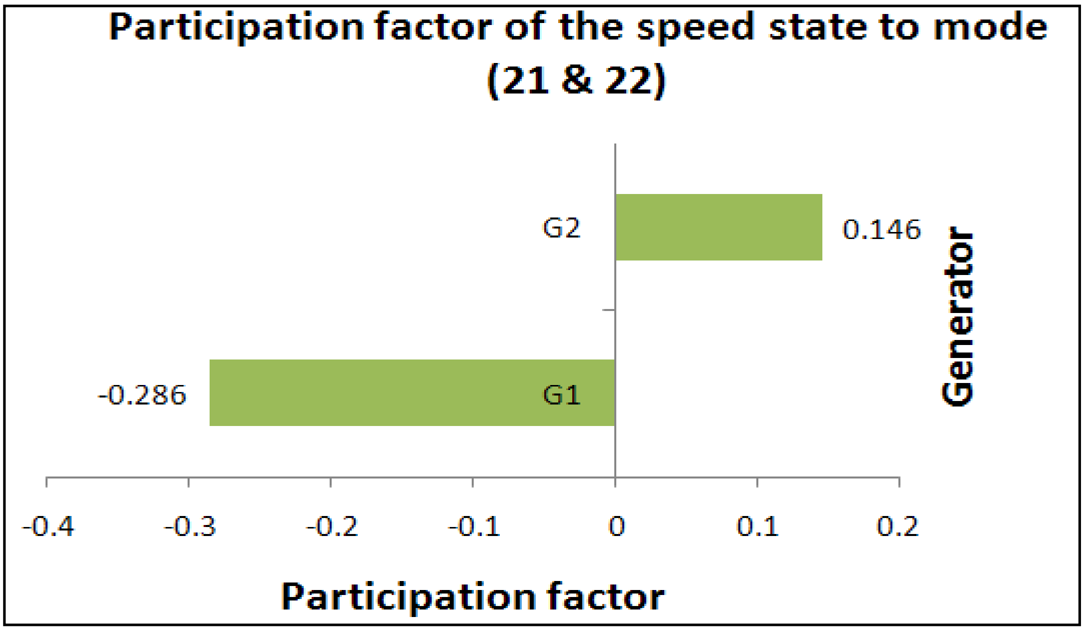

Figure 7.43 Speed participation factor to mode 21 & 22

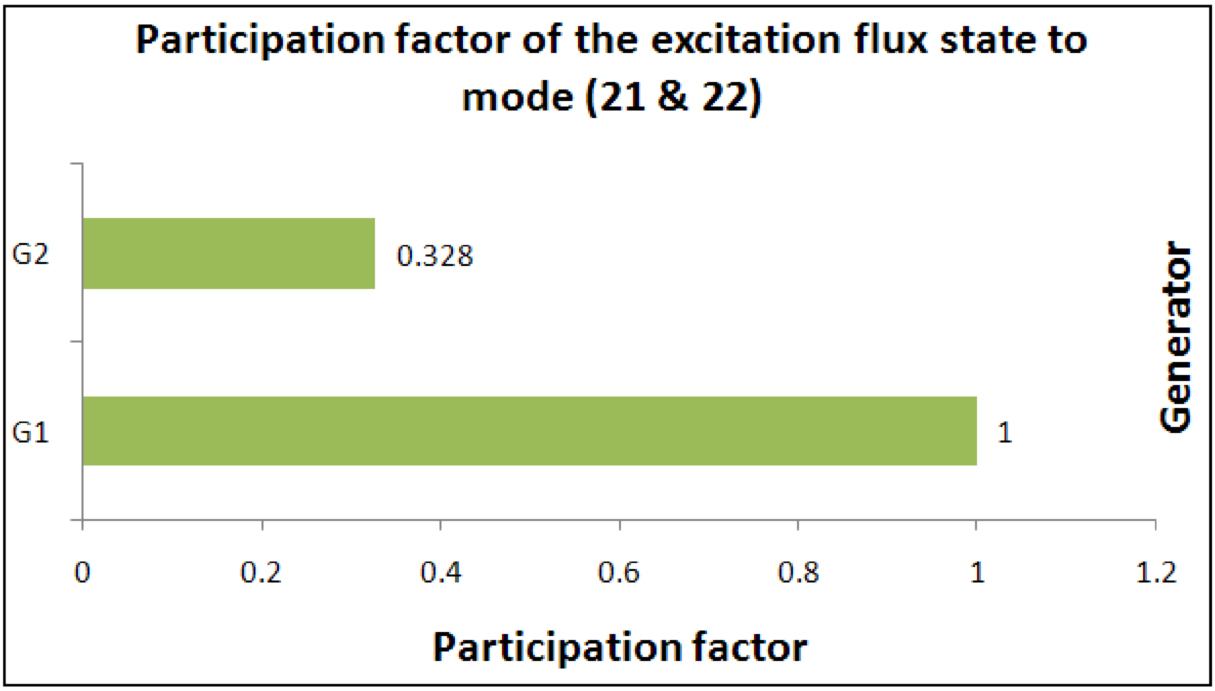

Figure 7.44 Excitation flux participation factor to mode 21 & 22

From the result of the participation factors, it can be concluded that generator speed had a greater influence on the electromechanical mode (12 & 13); the excitation flux had no influence on mode (15 & 16) and the excitation flux had a greater influence on mode (21 &

22) when compared to the speed. Figure 7.45 shows the combined eigenvalue plot from both case one and case two. From figure 7.45, it can be concluded that the hybrid system has one more electromechanical mode (15 & 16), which is only influenced by the speed, when compared to the HVDC transmission system. Each of the two cases has a mode with an eigenvalue, whose real part is at -1000 and imaginary part is at zero. This eigenvalue is far from the region of instability. Most of the eigenvalues from case one and case two are clustered around the origin of the X-Y axis in figure 7.45.

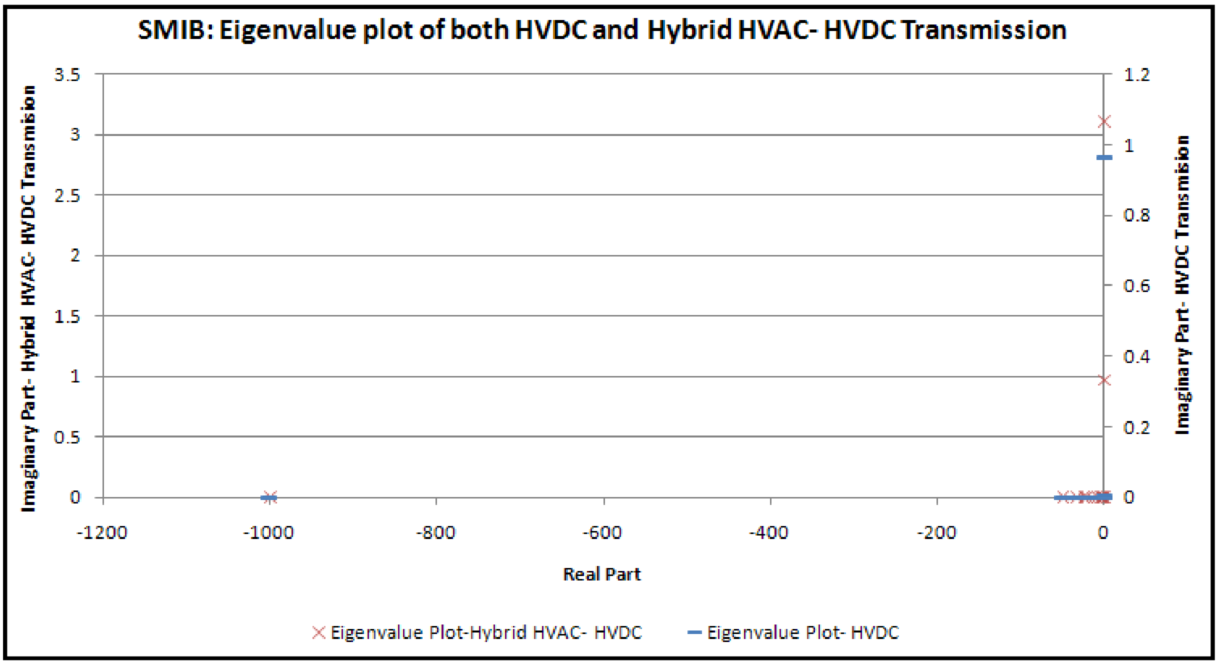

Figure 7.45 SMIB eigenvalue plot of HVDC Transmission and Hybrid HVAC-HVDC Transmission

Based on the findings above, it can be concluded that the HVDC transmission scheme has less electromechanical modes when compared with the hybrid HVAC-HVDC transmission scheme. The hybrid HVAC-HVDC transmission scheme introduced an additional electromechanical. Hence, the hybrid HVAC-HVDC scheme is less stable and more susceptible to small signal instability when compared to the HVDC scheme.

CHAPTER 8

TWO-AREA MULTI-MACHINE (TAMM): SIMULATION RESULTS

Figures 8.1 and 8.2 show the one-line diagrams of the power system for the hybrid HVAC-HVDC and the double circuits HVDC respectively. In figure 8.1, area 2 is on the right with two generating stations G1 and G2 connected to bus one and bus one respectively. Area one is on the left side of the network in figure 8.1. This also has two generating stations, namely G3 and G4. The two distribution centres in area two are connected to buses seven and eight. The AC sides of the inverter and rectifier are connected to bus five and bus six respectively. The HVDC line is connected between the DC side of the rectifier and the DC side of the inverter, via a series rector at bus 6a and at bus 5a respectively, as shown in figure 8.2. The HVAC transmission line is between bus six and bus five.

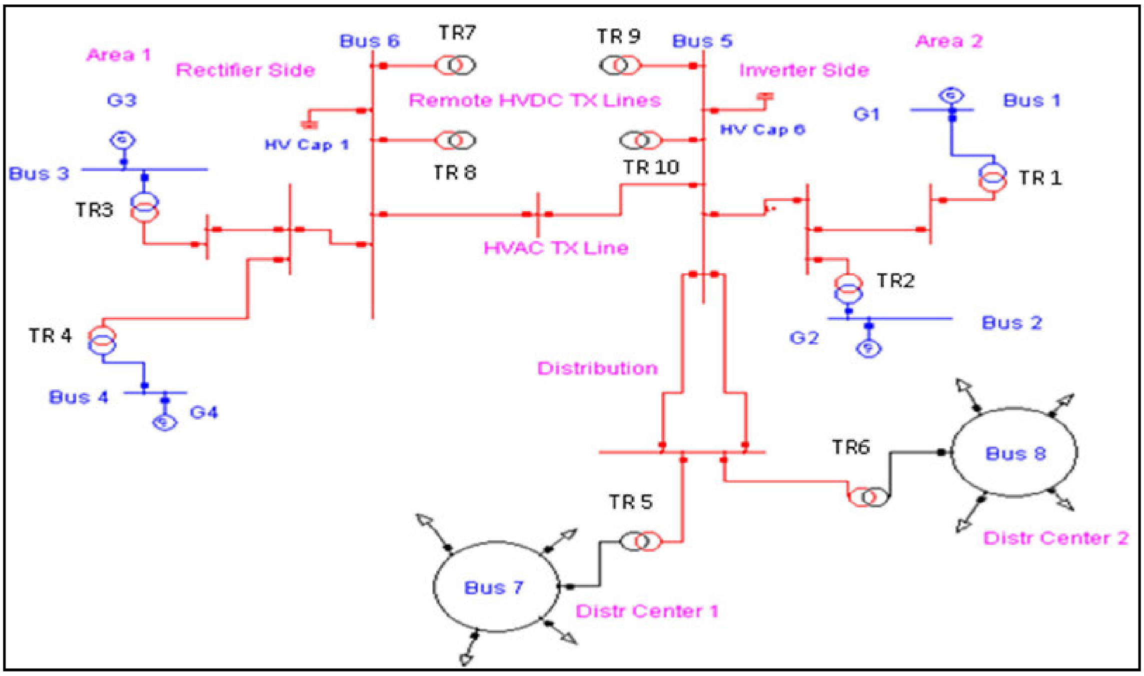

Figure 8.1 The Entire Power Network Excluding the HVDC Scheme

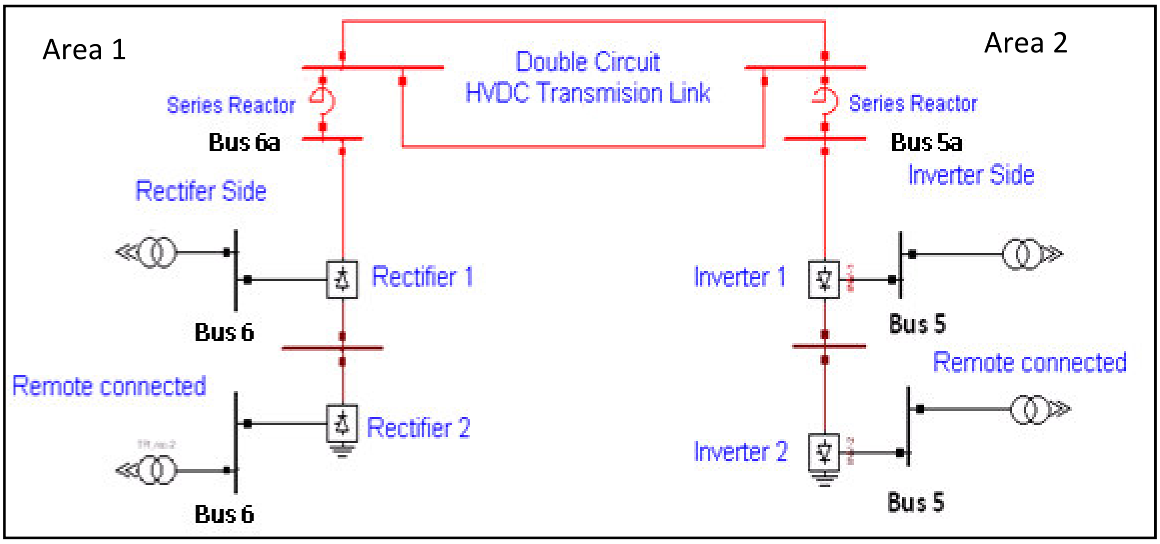

Figure 8.2 The Remote HVDC Scheme between Area 1 and Area 2

The simulation results are divided into three parts: the load flow, transient stability and small signal stability. In each of these parts, both the HVDC transmission and the hybrid HVDC-HVAC transmission schemes are considered.

8.1 LOAD FLOW

8.1.1 Case 1: HVDC Transmission

The first transmission considered for the Two Area Multi-Machine (TAMM) system is the double circuit HVDC transmission line, as shown in Figure 8.2. Table 8.1 and table 8.2 show the voltages and powers at selected system buses. Current control is adopted by the rectifier to control the flow of the DC current, while the inverter is operating under the extinction angle control (voltage control). The DC current order is set to 3.84 kA on the HVDC transmission line.

Table 8-1 Bus Voltage Magnitude and Angles (TAMM, Case 1)

Element	Rated Voltage	Actual Voltage	Voltage (pu)	Voltage angle (^{0})
Bus 1	22.00	22.00	1.00	0.00
Bus 2	22.00	22.00	1.00	0.35
Bus 3	22.00	22.00	1.00	0.11
Bus 4	22.00	22.00	1.00	0.00
Bus 5	500.00	494.80	0.99	-0.15
Bus 5a	500.00	506.88	1.01	N/A
Bus 6	500.00	494.65	0.99	-1.31
Bus 6a	500.00	521.28	1.04	N/A
Bus 7	11.00	10.86	0.99	-1.41
Bus 8	11.00	10.82	0.98	-1.76

In this case there is no AC link between area one and area two, as such, the two areas are almost isolated by the HVDC transmission line. Based on this, the two areas both need individual voltage references. Since there are multiple machines in each of these two areas, bus one is the slack (reference) bus for area two and bus four is the slack (reference) bus for area one. The AC voltage as bus 6 is stepped down by the converter transformers before conversion to DC. Similarly, the inverter DC voltage is stepped up to 500 kV by the inverter transformer at bus 5. The total load connected to both distribution centres is 2443 MW. The active power generated in area one of the power system is 2002 MW, while the active power generated in area one is 497 MW as seen in table 8.2.

The active power on the HVDC line flows from the rectifier bus to the inverter bus. This corresponds to the theory of DC power flow which states that, DC power flows from higher bus voltage magnitude to lower bus voltage magnitudes. As seen in table 8.1, the rectifier DC bus (bus 6a) voltage (1.04pu) is higher than the inverter DC bus (bus 5a) voltage (1.01 pu). The transmission line experienced a slight drop in transmission line voltage of 0.03pu between the inverter and the rectifier which is 3% of the nominal voltage. High voltage transmission lines ideally have a voltage drop less than 10% [19]. Regarding the flow of reactive power, the total reactive power generated by all the generators in areas one and one is 1804 Mvar. The total reactive power compensation in area one and in area two are 617 Mvar and 392 Mvar respectively. The total reactive power generated in the system, thus, is 2813 Mvar which was utilised by the loads and the converter stations.

Furthermore, the voltage angles become more lagging as power flows away from the generating stations toward the double-circuit HVDC transmission line as indicated in table 8.1. In area one, the voltage angles became more lagging from 0^0 at bus 1 (G1) to -0.15^0 at bus five and in area one it became more lagging from 0^0 at bus four (G4) to -1.31^0 at bus six. However, as active power flows from bus six to bus five through the HVDC line via two intermediate buses (6a and 5a), the flow now depends on the magnitude of the voltage on the two intermediate DC buses. Although the voltage angle at bus five is leading with respect to bus six, the DC power flows from bus six to bus five. Table 8.1 indicates that the voltage magnitude at the DC rectifier bus (bus 6a) is 1.04 pu and that of the DC inverter bus (bus 5a) is 1.01 pu. That is why power is flowing from bus 6a to bus 5a.

Table 8-2 Active and Reactive Power (TAMM, Case 1)

Element	Bus	Active Power (MW)	Reactive Power (Mvar)
G 1	1	97	431
G 2	2	400	461
G 3	3	1000	435
G 4	4	1002	477
HVDC TX 1	6a	1001	0
	5a	-973	0
HVDC TX 2	6a	1001	0
	5a	-973	0
Rectifier		2002	1190
Inverter		-1946	1276
Distr Center 1	7	1064	74
Distr Center 2	8	1379	274
HV CAP 1	6	0	392
HV CAP 2	5		617

The amount of active power transmitted via the HVDC transmission lines was found to be 2002 MW, of which 56 MW was lost in the transmission lines. In other words, 2002 MW is sent from bus 6a (rectifier), but only 1946 MW is received at bus 5a (inverter). Since the load demand at bus five is 2443 MW, the rest of the power demand (497 MW) is supplied by G1 and G2. There was no real power loss in the HVDC converters.

8.1.2 Case 2: Hybrid HVAC-HVDC Transmission

Table 8.3 and table 8.4 show the voltages and powers at all the system buses. Current control is adopted by the rectifier to control the flow of DC current on the DC transmission line, while the inverter is operating under the extinction angle control. The current order was chosen to be 1.98 kA so as to split the amount of power transmitted between the two types of transmission lines almost equally. In this case the flow of power on the HVAC transmission line is controlled by controlling the current order at the rectifier station.

Table 8-3 Bus Voltage Magnitude and Angles (TAMM, Case 2)

Element	Rated Voltage	Actual Voltage	Voltage (pu)	Voltage angle (^{0})
Bus 1	22.00	22.00	1.00	0.00
Bus 2	22.00	22.00	1.00	0.30
Bus 3	22.00	22.00	1.00	38.60
Bus 4	22.00	22.00	1.00	38.49
Bus 6	500.00	498.11	1.00	37.19
Bus 5	500.00	497.69	1.00	-0.19
Bus 6a	500.00	507.43	1.01	0.00
Bus 5a	500.00	492.58	0.99	0.00
Bus 7	11.00	10.89	0.99	-1.79
Bus 8	11.00	10.93	0.99	-1.44

From table 8.3 it can be seen that all the bus voltage magnitudes are within the set acceptable range between 0.95 pu and 1.10 pu. The slack bus in area one is set to be bus one (G1) and since there is a HVAC transmission line between area one and area two, the voltage reference in area one is also taken with respect to G1 in area 2. With regards to AC power flow between bus 6 and bus 5, bus 6 angle is leading with respect to bus five. Hence, AC power flowed from bus six to bus five. Between these two busbars is also the HVDC transmission line with the rectifier DC bus (bus 6a) and the inverter DC bus (bus 5a). Because the determinant of DC power flow is the voltage magnitude, DC power flows from rectifier DC bus (area one) to inverter DC bus (area two).

Table 8-4 Active and Reactive Power (TAMM, Case 2)

Element	Bus	Active Power (MW)	Reactive Power (Mvar)
G 1	1	128	190
G 2	2	400	204
G 3	3	1000	156
G 4	4	1000	170
HVDC TX	6a	1005	0
	5a	-975	0
HVAC TX	6	995	-26
	5	-940	128
Rectifier		1005	686
Inverter		-975	725
Distr Center 1	7	1064	67
Distr Center 2	8	1379	267
HV CAP 1	6	0	398
HV CAP 2	5	0	872

As in case one, the voltage angle becomes more lagging as power flows away from the generating stations towards the Hybrid HVAC-HVDC transmission line. The power loss on both the HVAC and the HVDC transmission lines between bus six and bus five is 85 MW (i.e. losses on HVDC 1005-975=30 MW, losses on HVAC= 995-940=55MW) and it is higher than the loss in case one (56MW).

8.2 TRANSIENT STABILITY

Transient stability is considered in this section. The two-area power system of figures 8.1 and 8.2 are examined to determine the transient stability of the power system in each of the transmission configurations. Two-fault conditions are considered, namely, converter DC fault and the three-phase to ground fault at the terminal of generator G4. The system configuration is similar to that used for the load flow calculation in section 8.1. In each of these fault conditions, two transmission configuration cases are considered. In case one which uses HVDC transmission, the HVDC transmission line was scheduled to deliver about 2000 MW over 500 km to area one with current control at the rectifier and extinction angle control at the inverter. The current order of the rectifier was set at 3.84 kA.

In case two hybrid HVAC-HVDC transmission lines were used. The HVDC transmission line was scheduled to deliver about 1000 MW over 500 km to area one with current control at the rectifier and extinction angle control at the inverter. The current order of the rectifier was set at 1.98 kA. The HVAC line transmitted 1000 MW.

8.2.1 Effects of DC Converter Faults on Transient Stability

At one second into the simulation, a 50 ms DC fault was applied at the DC terminal of the rectifier. Following that, another simulation was run and at one second, a 50 ms DC fault was applied at the DC terminal of the inverter. The effects of both rectifier and inverter DC faults on the transient stability as well as the recovery of the voltage level at the generating stations in area one and area two are investigated.

8.2.1.1 Case 1: HVDC Transmission Line

The simulation results obtained in this case are given in figures 8.3 to 8.10. The results shown from figure 8.4 to figure 8.7 are obtained from G3. Figure 8.3 shows the rotor angle of G3. It can be observed that during the 50 ms rectifier and inverter DC faults, the rotor angle of G3 increased from -87° to about -70°. After the fault was cleared, the rotor angle oscillated between 180° and -180^0 before it reached a steady rotor angle of -110^0 and -145^0 for the inverter and rectifier DC faults, respectively. Also, the rectifier DC fault had a greater impact on the rotor angle of G3. It took about ten seconds longer for the rotor angle of G3 to drop from 180^0 to -180^0 during the rectifier fault as compared to the inverter fault. Also, the final rotor angle of G3 after the rectifier fault is 30^0 larger than the final rotor angle of G3 after the inverter fault.

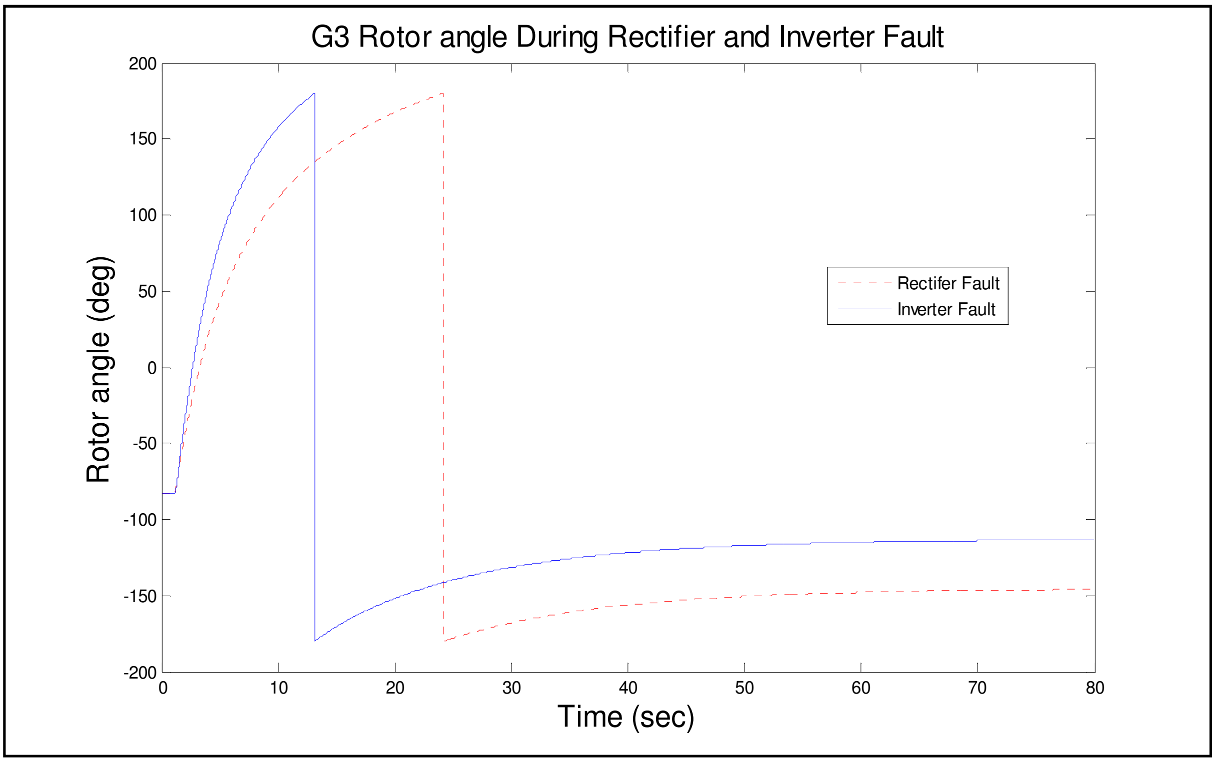

Figure 8.3 Case 1: Effects of Converter Fault on the Rotor Angle of G3

The effect of the rectifier fault is also larger than the effect of the inverter fault at the terminal voltage of G3. During the inverter fault, the terminal voltage of G3 dropped to 0.73 pu while it dropped to 0.63 during the rectifier fault as seen in figure 8.4. After 7.5 seconds, the terminal voltage at G3 stabilised for both rectifier and inverter DC faults, respectively.

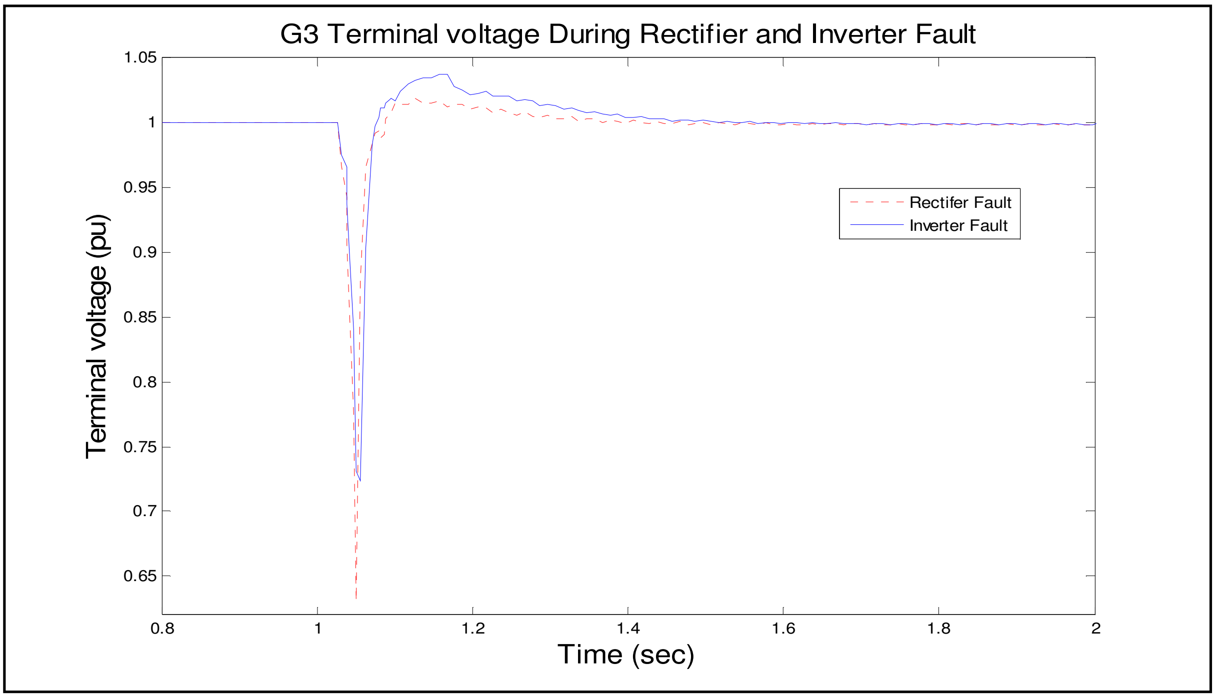

Figure 8.4 Case 1: Effects of Converter Fault on the Terminal Voltage of G3

During both rectifier and inverter faults, the active power generation increased momentarily to a high of 3050 MW from 1000 MW (this is about the normal value), as shown in figure 8.5. After this increase, the active power dropped to -100 MW and increased till it reached its pre-fault value of 1000 MW. This was reached in 4.5 seconds as reflected in figure 8.5. Figure F.3 in Appendix F shows the current waveform of G3. The current increased from 0.6 pu to 3.1 pu during the rectifier fault and from 0.6 pu to 2.8 pu during the inverter fault. This indicates that the capacity of G2 was exceeded during the both rectifier and inverter DC faults while using the HVDC transmission line. Hence, in practice, this increase in active power generation is not acceptable.

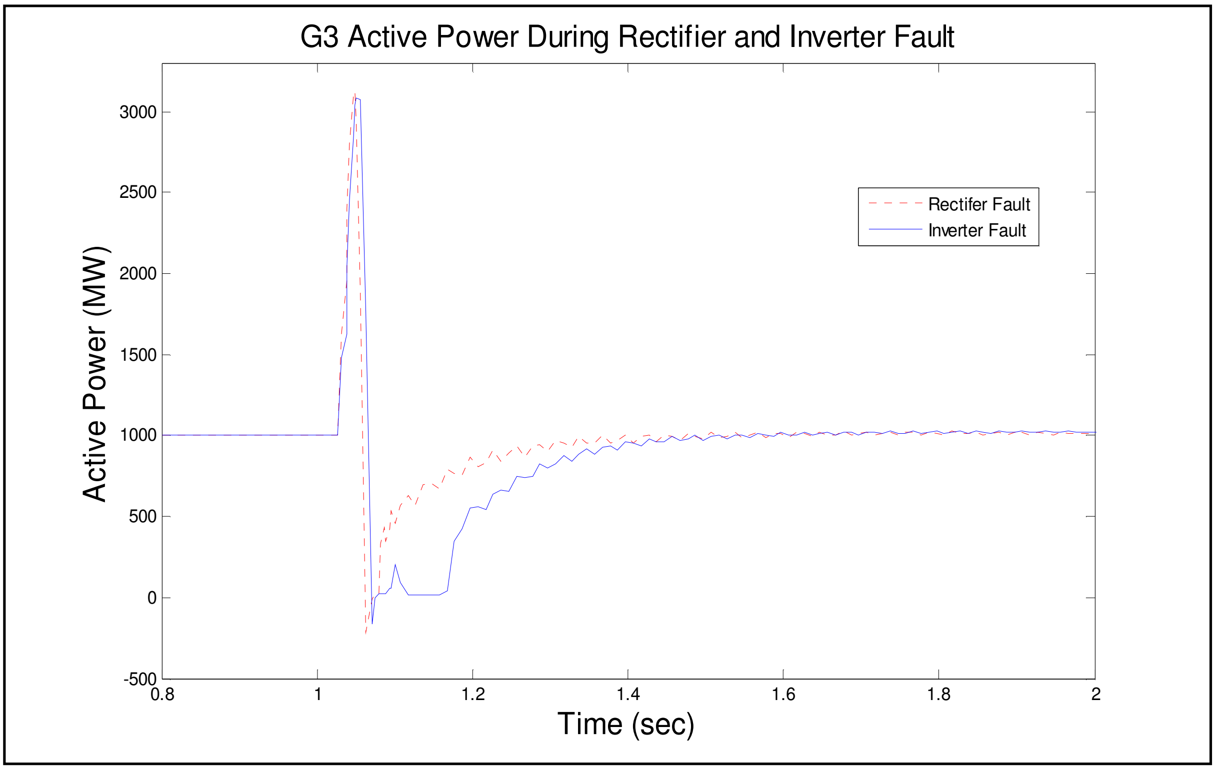

Figure 8.5 Case 1: Effects of Converter Fault on the Active Power of G3

As shown in figure 8.6, the reactive power generated by G3 increased from 497 Mvar to 3600 Mvar during the rectifier fault and from 497 Mvar to 3100 Mvar during the inverter fault. This is mainly because the recovery of the rectifier during both inverter and rectifier faults requires reactive power and as such, the generator has to supply it. At two seconds into the simulation, the reactive power generation by G3 is restored to its pre-fault value of 435 Mvar.

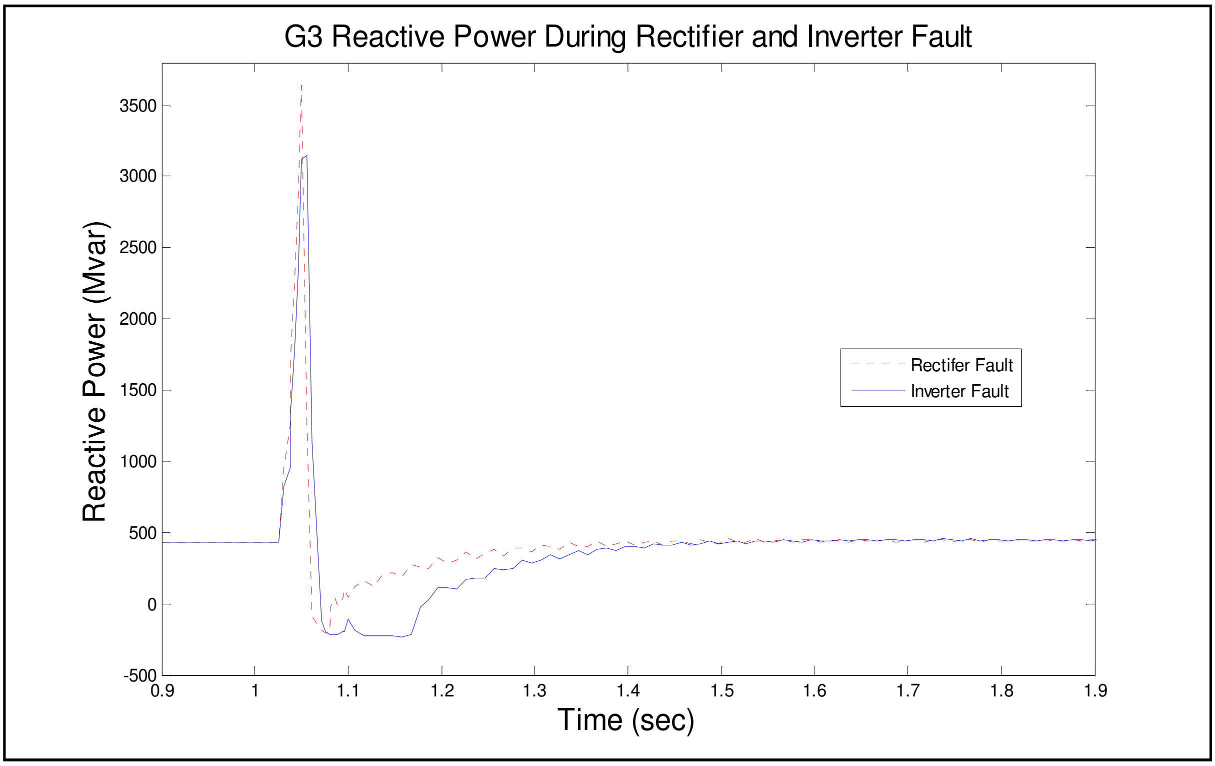

Figure 8.6 Case 1: Effects of Converter Fault on the Reactive Power of G3

From figure 8.7, it can be seen that the rotor angle of G2 oscillated between -86.9^0 and -87.2^0 (which damped out in eight seconds), in order to balance the load demand of 2442 MW with the aid of active power supply by G1 during both rectifier and inverter faults. Because G2 is closer to the inverter side, the effect of the inverter DC fault on the rotor angle of G2 is greater than that of the rectifier DC fault.

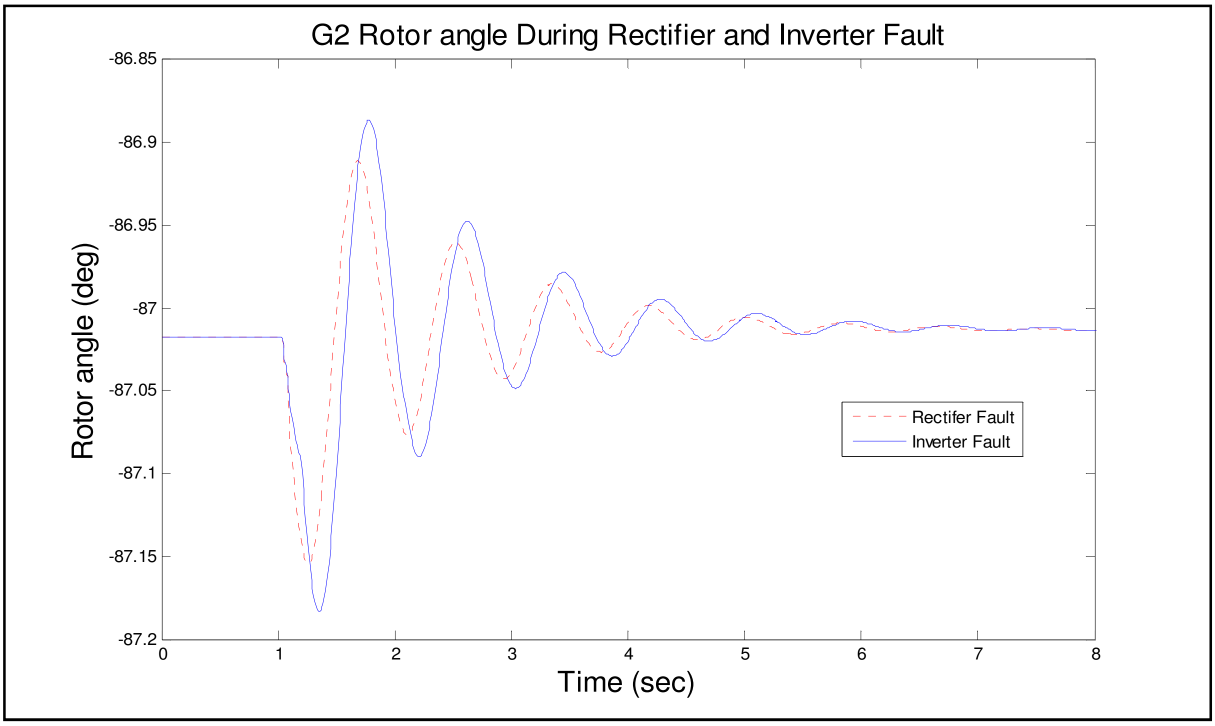

Figure 8.7 Case 1: Effects of Converter Fault on the Rotor Angle of G2

Figure 8.8 shows the terminal voltage at G2. The terminal voltage at G2 increased during the faults. This is because, during the rectifier and inverter DC faults, the reactive power required by the converters dropped due to the drop in active power transmitted via the HVDC line. Figure 8.9 shows that the active power generation at G2 increased from 400 MW to 1500 MW during the fault. The rest of the power needed by the distribution centres during the fault was supplied by G1. Figure F.2 in Appendix F shows the current waveform of G2. The current increased from 0.25 pu to 0.85 pu for both rectifier and inverter faults. As a result, the capacity of G2 was not exceeded while using the hybrid HVAC-HVDC transmission line.

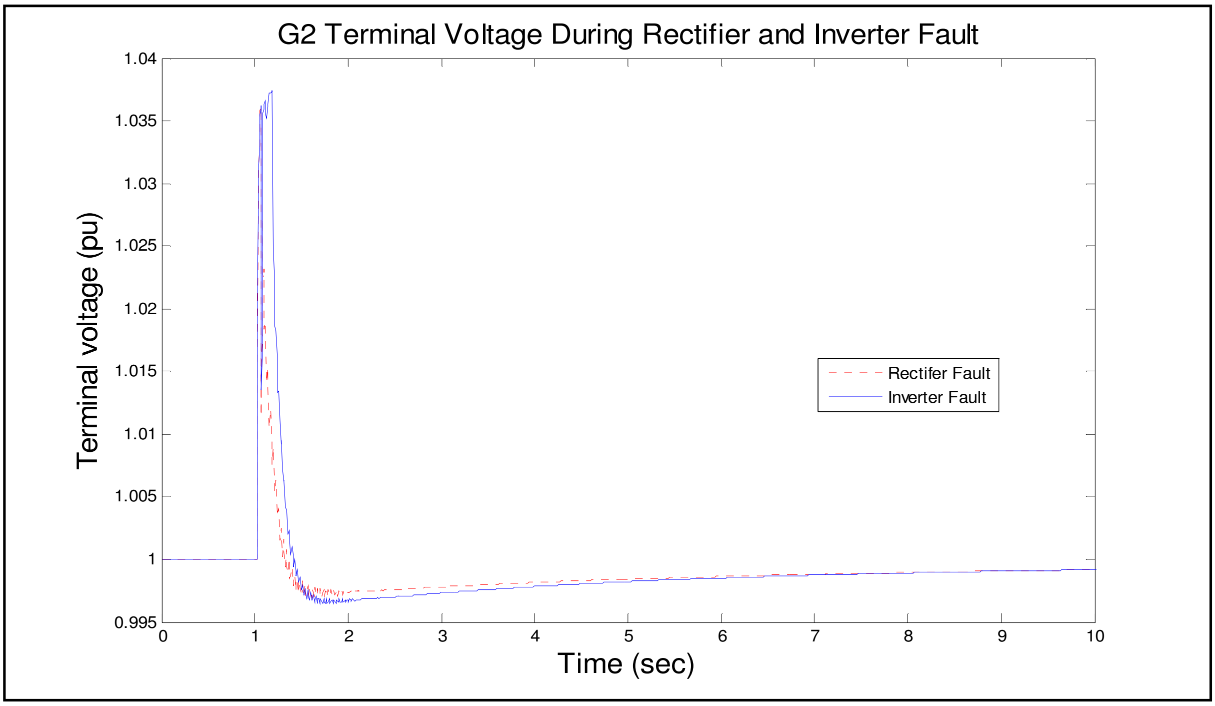

Figure 8.8 Case 1: Effects of Converter Fault on the Terminal Voltage at G2

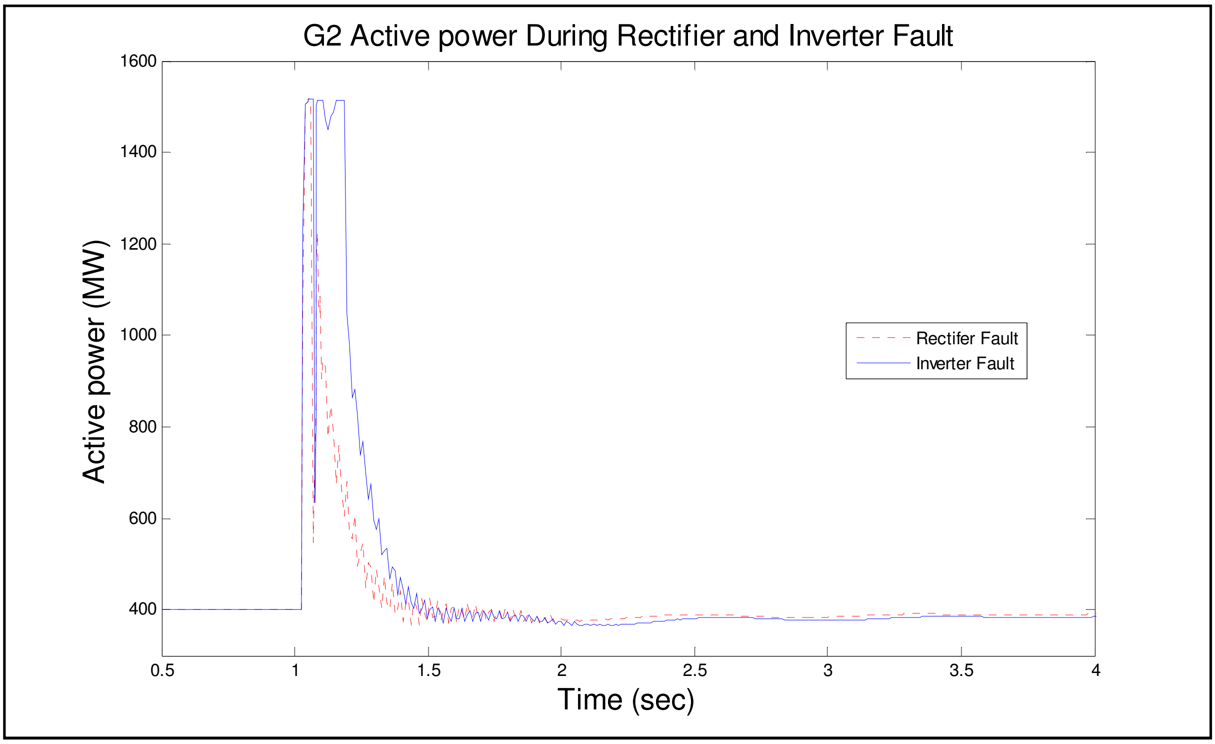

Figure 8.9 Case 1: Effects of Converter Fault on the Active Power of G2

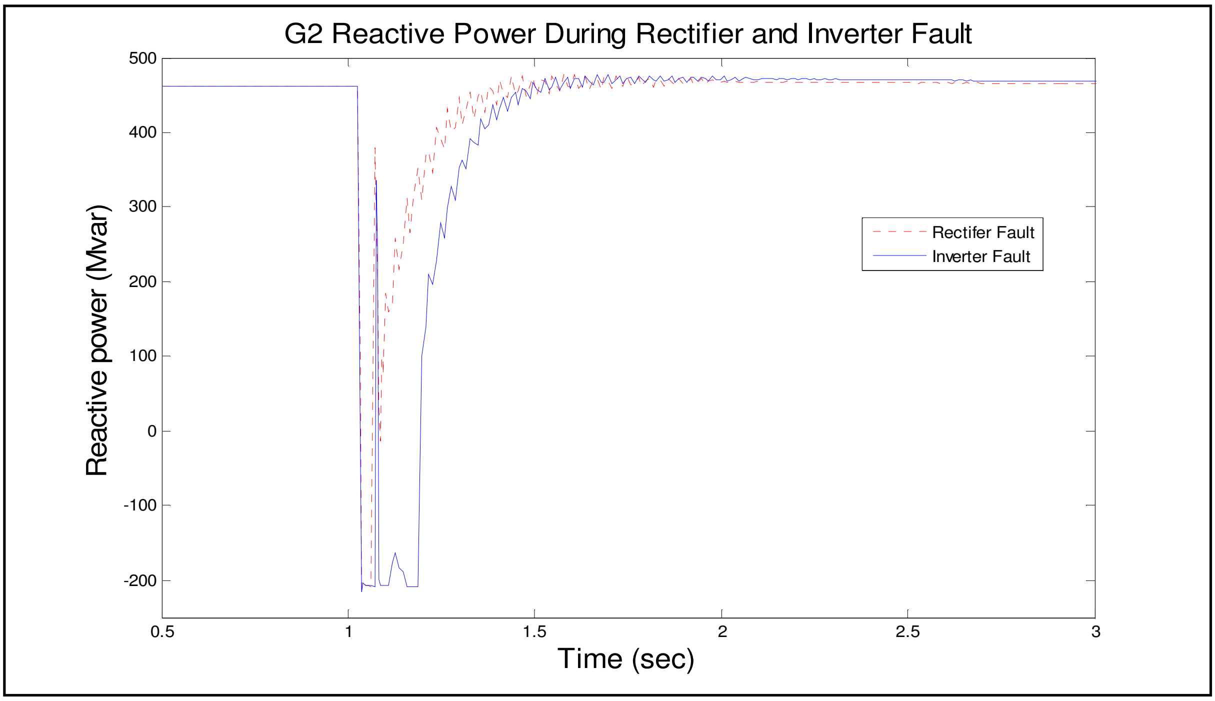

Figure 8.10 Case 1: Effects of Converter Fault on the Reactive Power at G2

From figure 8.10 it can be seen that the reactive power at G2 decreased. This is because there was excess reactive power supplied during the converter faults, and this was absorbed by G1 and G2 as the inverter station was not running at its capacity. The reactive power at G1 is shown in figure F.13 in the Appendix. The excess reactive power came from the capacitor banks which injects a relatively fixed amount of reactive power into the system.

8.2.1.2 Case 2: Hybrid HVAC- HVDC Transmission Line

The simulation results obtained in this case are shown in figure 8.11 to figure 8.18.

Figures 8.11 to 8.14 show the results obtained from generator G3. The effect of both rectifier and inverter faults on the rotor angle of G3 is shown in figure 8.11. The rotor angle of G3 before the fault in case two is -44^0. Furthermore with the hybrid HVAC-HVDC scheme, the time taken for G3's rotor angle oscillations to stabilize has decreased by 25 seconds.

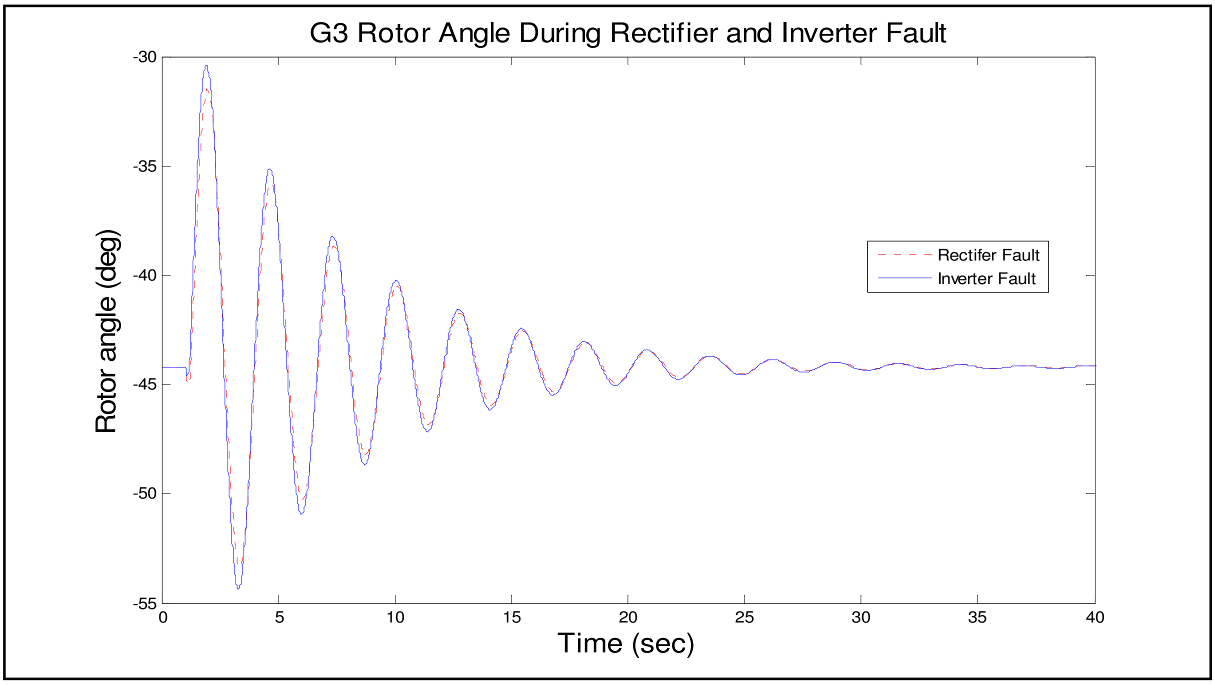

Figure 8.11 Case 2: Effects of Converter Fault on the Rotor Angle of G3

As in case one, the effect of the rectifier fault is greater on the terminal voltage of G3 as compared with that of the inverter fault, as shown in figure 8.12. During inverter and rectifier faults the terminal voltage of generator G3 decreased to 0.8 pu and 0.65 pu respectively before increasing to the pre-fault voltage of 1.0 pu.

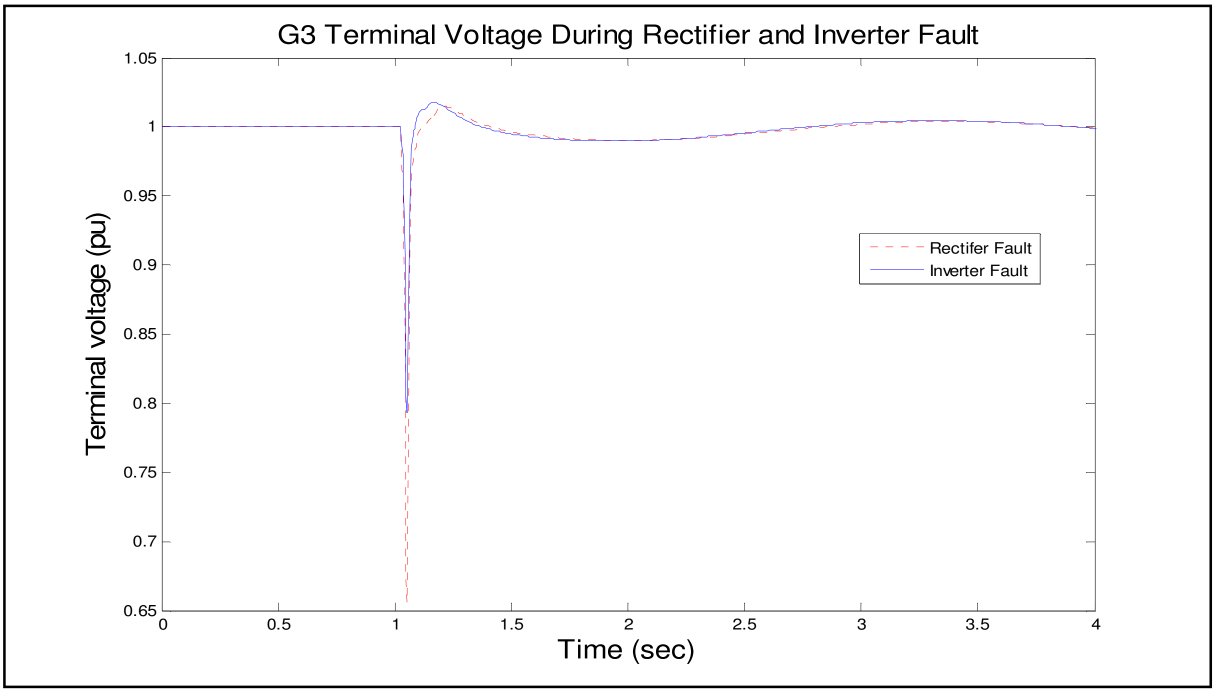

Figure 8.12 Case 2: Effects of Converter Fault on the Terminal Voltage at G3

Figure 8.13 shows the active power generation at G3. It can be seen that the active power generation of G3 during both faults is very similar to that of case one, in that the active power increased from 1000 MW to 3050 MW during the fault. The major difference, however, is that the post-fault waveform in case (figure 8.6) is smoother when compared with case two. This means that with the HVAC line in transmission in parallel to the HVDC line, the active power restoration of G3 has more oscillations and takes 15 seconds longer to settle down than in case one. Figure F.7 in Appendix F shows the current wave form of G3. From the current waveform, it can be seen that the increase in active power generation is directly proportional to the increase in current output. During the rectifier DC fault, the current increased from 0.6 pu to 2.8 pu, while it increase from 0.6 pu to 2.3 pu during the inverter fault.

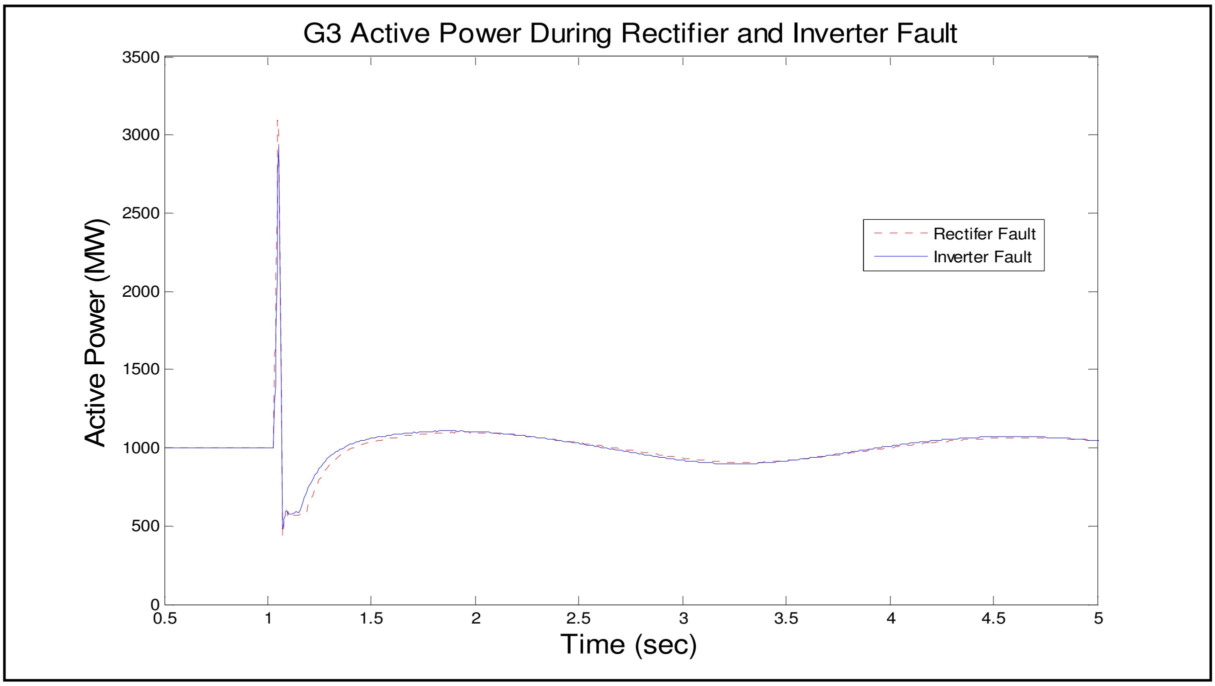

Figure 8.13 Case 2: Effects of Converter Fault on the Active Power of G3

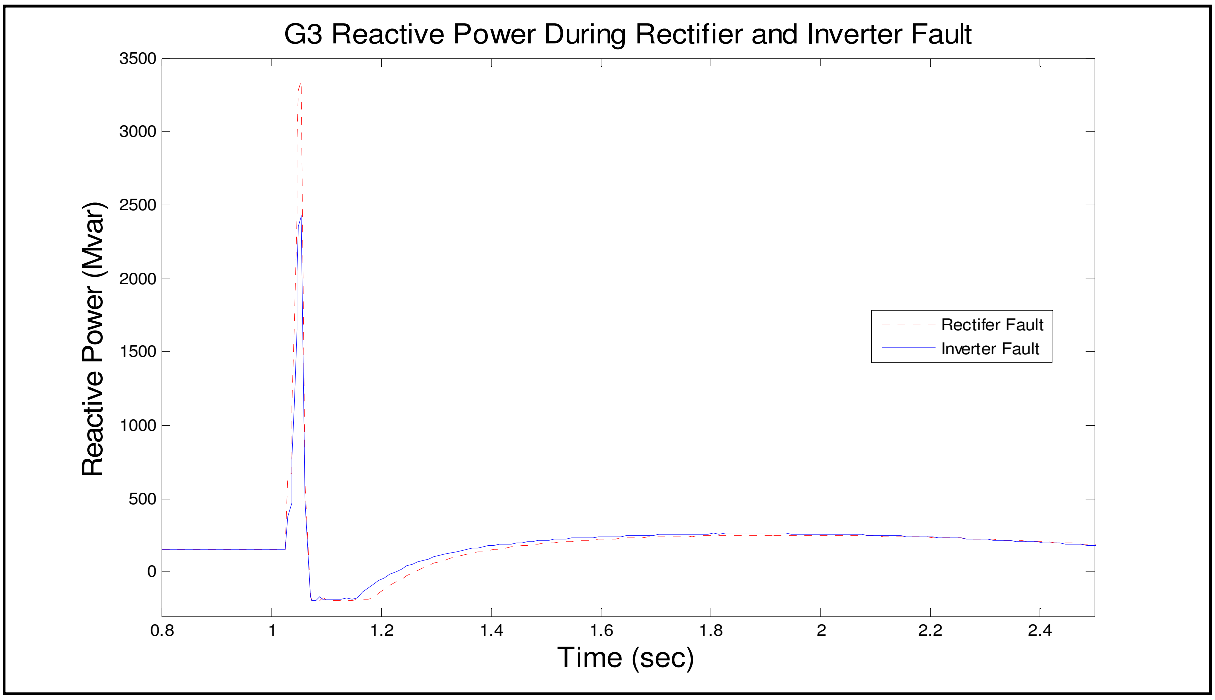

Figure 8.14 Case 2: Effects of Converter Fault on the Reactive Power of G3

Considering the reactive power compensation in area one, G3 had to increase reactive power generation during the DC faults. During the rectifier DC fault G3 generated 800 Mvar more than it did during the inverter fault, as shown in figure 8.14.

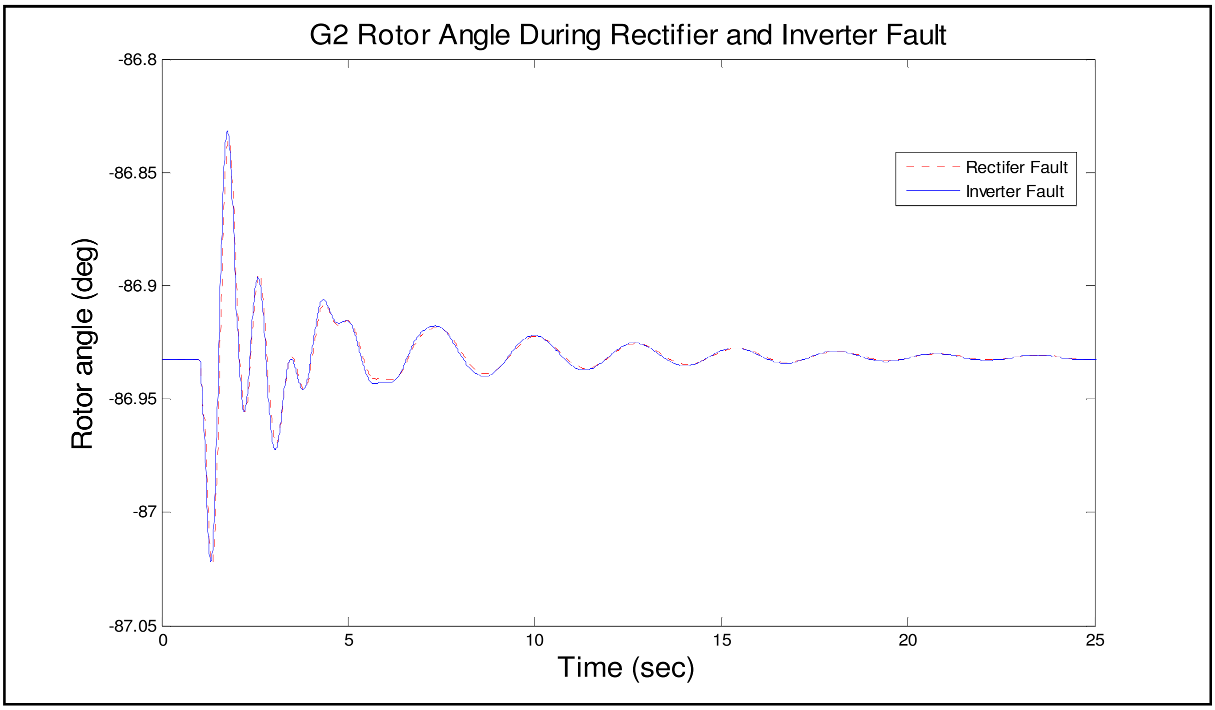

Figure 8.15 Case 2: Effects of Converter Fault on the Rotor Angle of G2

In area one which is close to the distribution centres, the rotor angle of generator G2 had some decaying oscillations with small amplitudes as shown in figure 8.15. The rotor angle oscillated between -86.85^0 and -87.01^0 which is a relatively small range as compared to case one (figure 8.7). However, it took about fifteen seconds longer than in case one (figure 8.7) to stabilise.

Figure 8.16 shows the increase in G2 terminal voltage during both inverter and rectifier faults. After the fault was removed the terminal voltage decreased to 0.99 pu as it oscillated with decreasing amplitudes until it reached the pre-fault value of 1.0 pu. Figure 8.16 also shows that the impact of both rectifier and inverter DC fault on the terminal voltage of G2 is almost the same. The terminal voltage of G2 reached its pre-fault value in 30 seconds.

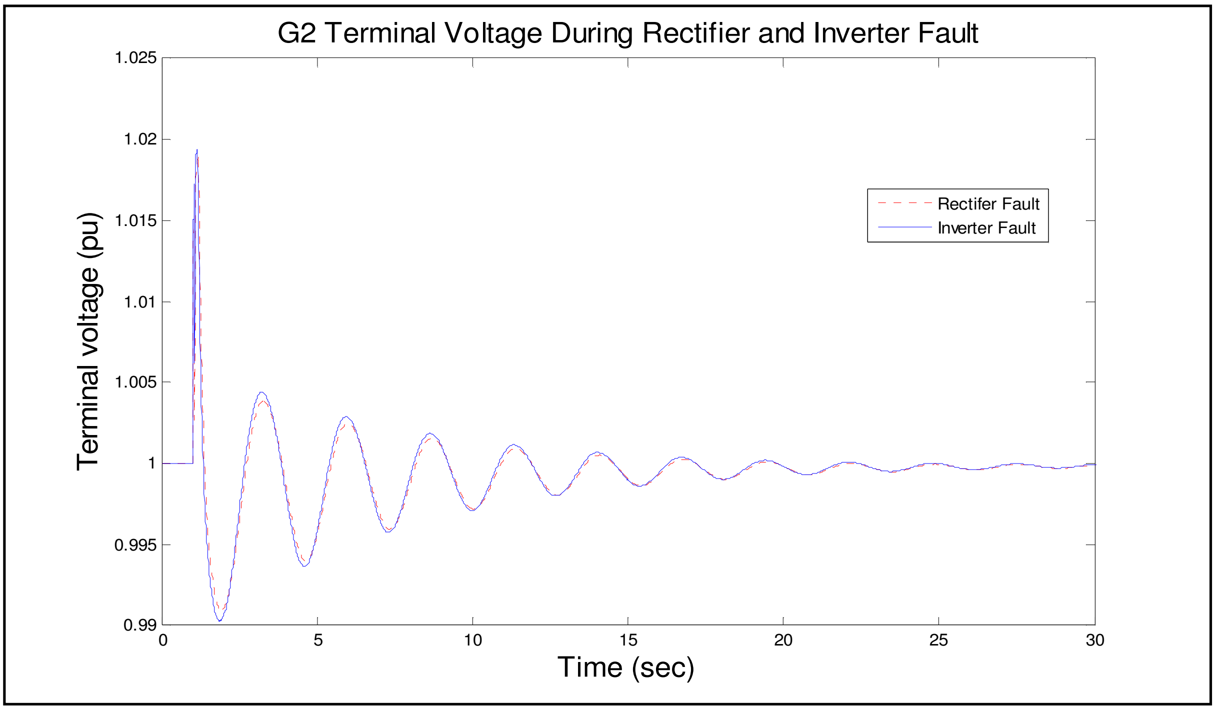

Figure 8.16 Case 2: Effects of Converter Fault on the Terminal Voltage at G2

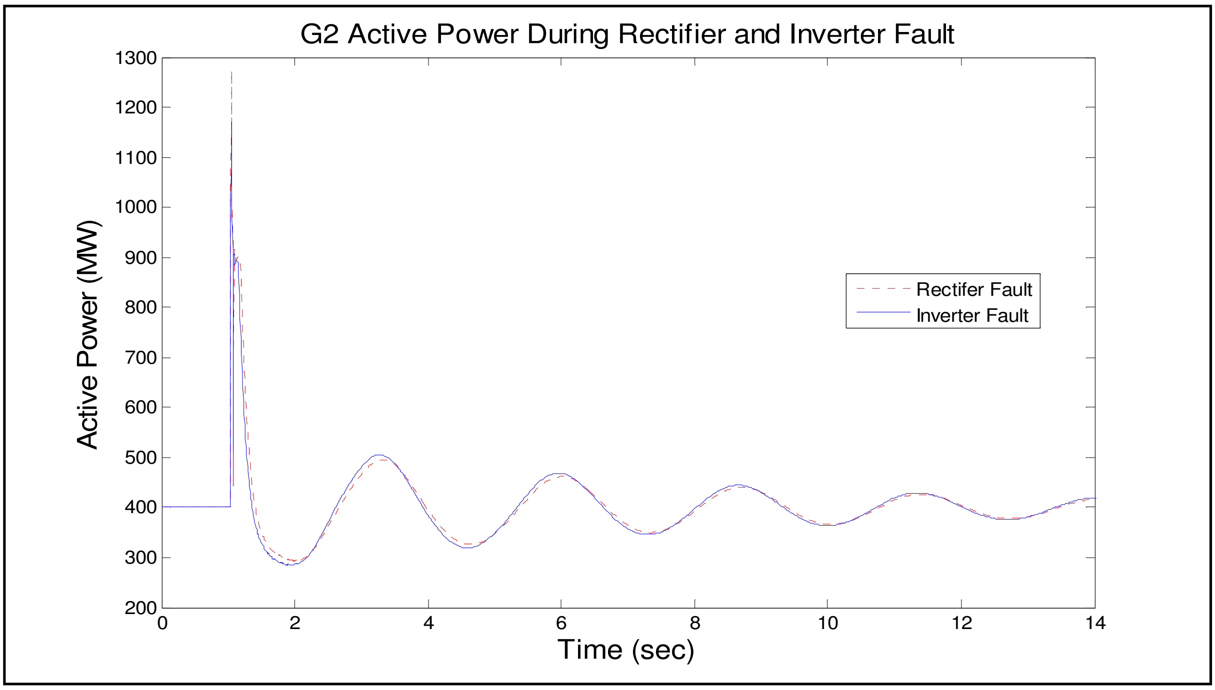

Figure 8.17 Case 2: Effects of Converter Fault on the Active Power of G2

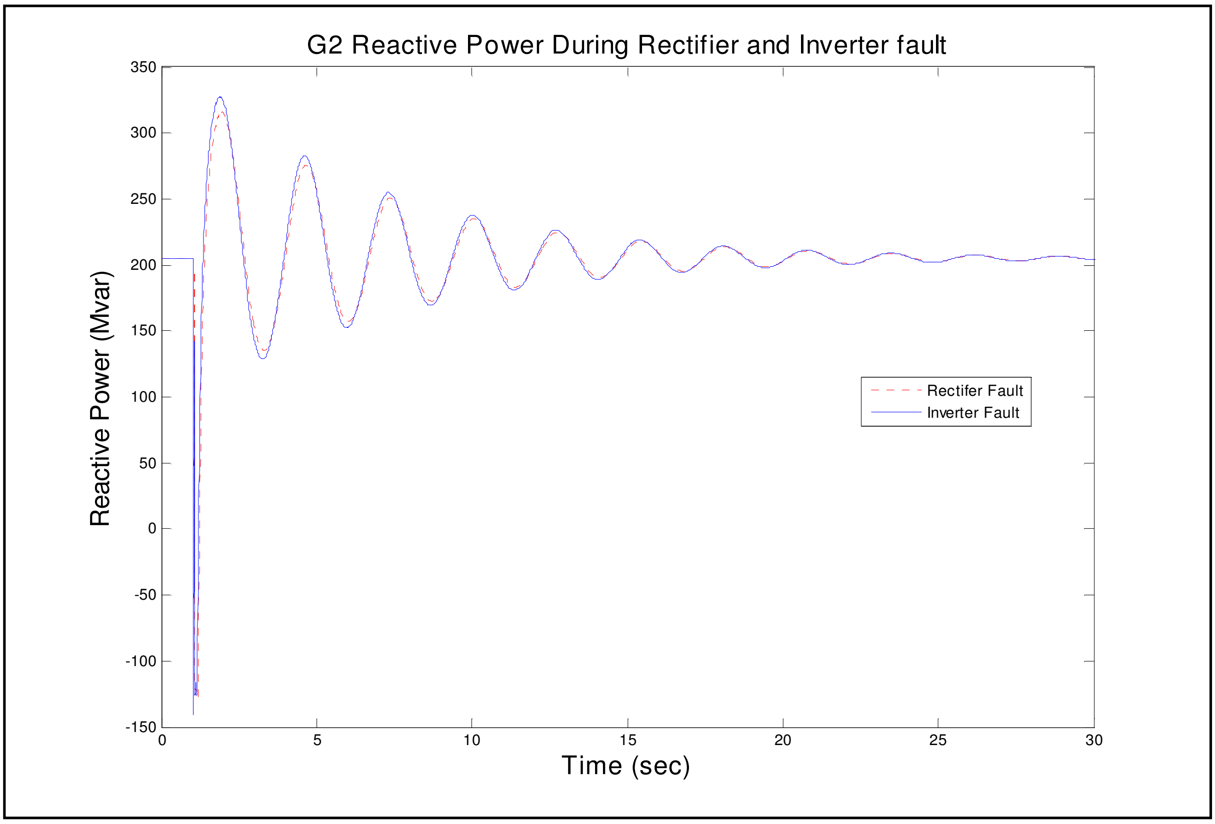

Figure 8.18 Case 2: Effects of Converter Fault on the Reactive Power of G2

Figure 8.17 shows that during the fault more active power is supplied by both G2 and G1 to meet the demands of the distribution centres. The active power supplied by G2 increased from 400 MW to 1190 MW during the inverter fault and from 400 MW to 1260 MW during the rectifier fault. In other words, during the rectifier and inverter faults the generator G2 output power increased by 215% and 197.5% respectively. Figure F.6 in Appendix F shows the current waveform of G2. The current increased from 0.25 pu to 0.78 pu during the rectifier fault and from 0.25 pu to 0.7 pu during the inverter fault. This indicates that the capacity of G2 was not exceeded during the both rectifier and inverter DC faults while using the hybrid HVAC-HVDC transmission line.

8.2.2 Effects of 3-phase fault on Transient Stability

The system configuration in this section was explained at the beginning of section 8.2. At one second into the simulation, a three-phase fault was applied at generator G4 terminals for 50 ms. The effects of the three-phase to ground fault at the terminals of G4 on two generating stations (G2 and G3) under both transmission configurations are investigated.

8.2.2.1 Case 1: HVDC Transmission Line

The simulation results obtained in this case are given in figures 8.19 to 8.26. The current waveforms are given in Appendix F:2.

Before the three-phase fault at G4, the rotor angle of G2 was at -87.01°. During the fault, the imbalance of the electrical power in the system led to the oscillation of the rotor angle. After the fault was cleared, it took about thirteen seconds for the rotor angle of G2 to stabilise. The magnitude of the oscillations were between a small range [-87.2^0, -86.9^0], as shown in figure 8.19.

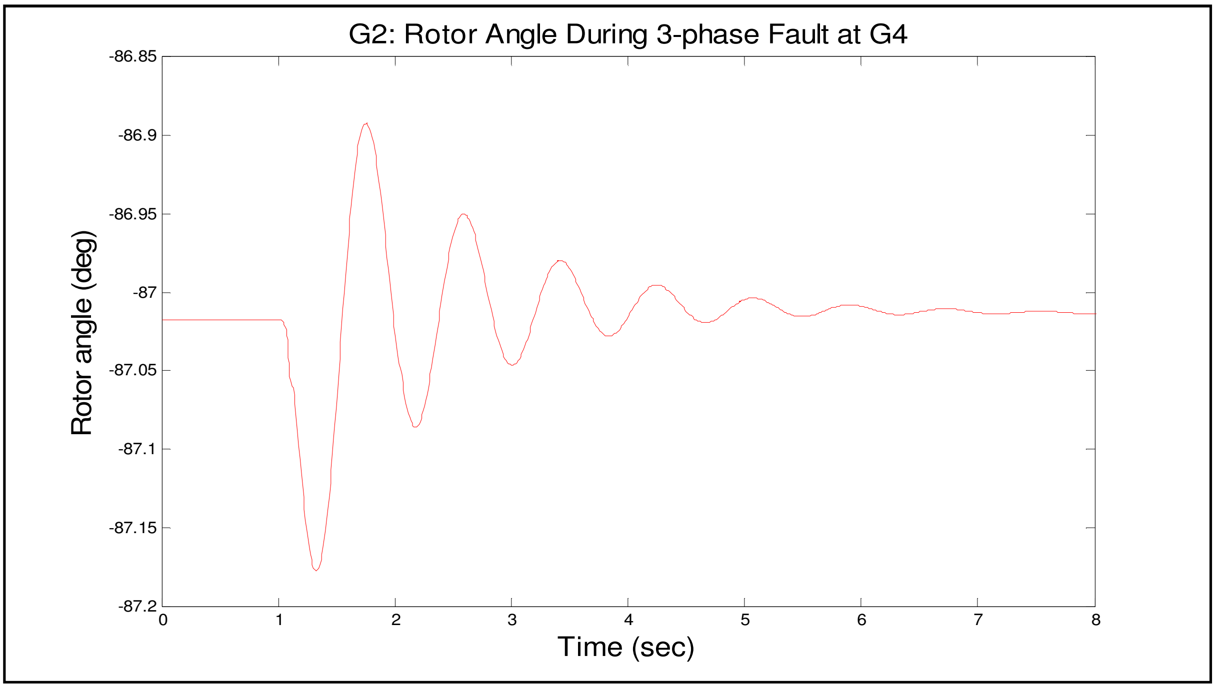

Figure 8.19 Case 1: Effect of G4 3-Phase Fault on the Rotor Angle of G2

Figure 8.20 shows that the terminal voltage of G2 increased slightly from its pre-fault value of 1.0 pu to 1.035 pu for a short time during the fault before reducing to 0.998 pu and finally to its pre-fault value of 1.0 pu in about seventeen seconds.

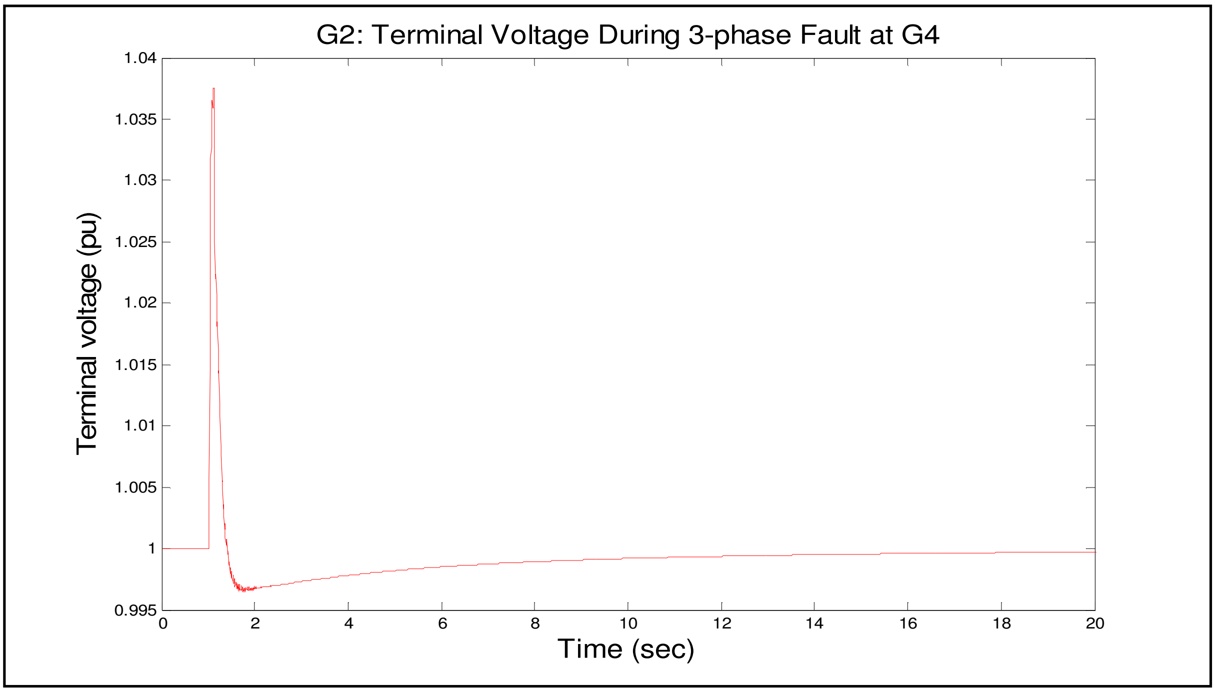

Figure 8.20 Case 1: Effect of G4 3-Phase Fault on the Terminal Voltage at G2

Figure 8.21 shows the active power generation at G2. The active power generated by G2 increased from 400 MW to 1490 MW (i.e., a 275% increase) during the fault. At four seconds into the simulation, the active power generation reduced to 380 MW which is below the pre-fault value before reaching the pre-fault steady state value at twelve seconds. The reason for the active power increase to 1490 MW is because the HVDC was not transmitting at its rated capacity during the fault and power had to be supplied to the distribution centre by G1 and G2. The current waveform given in figure F.10, in the Appendix, shows that the generator current increased from 0.354 pu to 0.85 pu. Hence, with regards to the maximum current of 1.0 pu, the capacity of G2 was not exceeded.

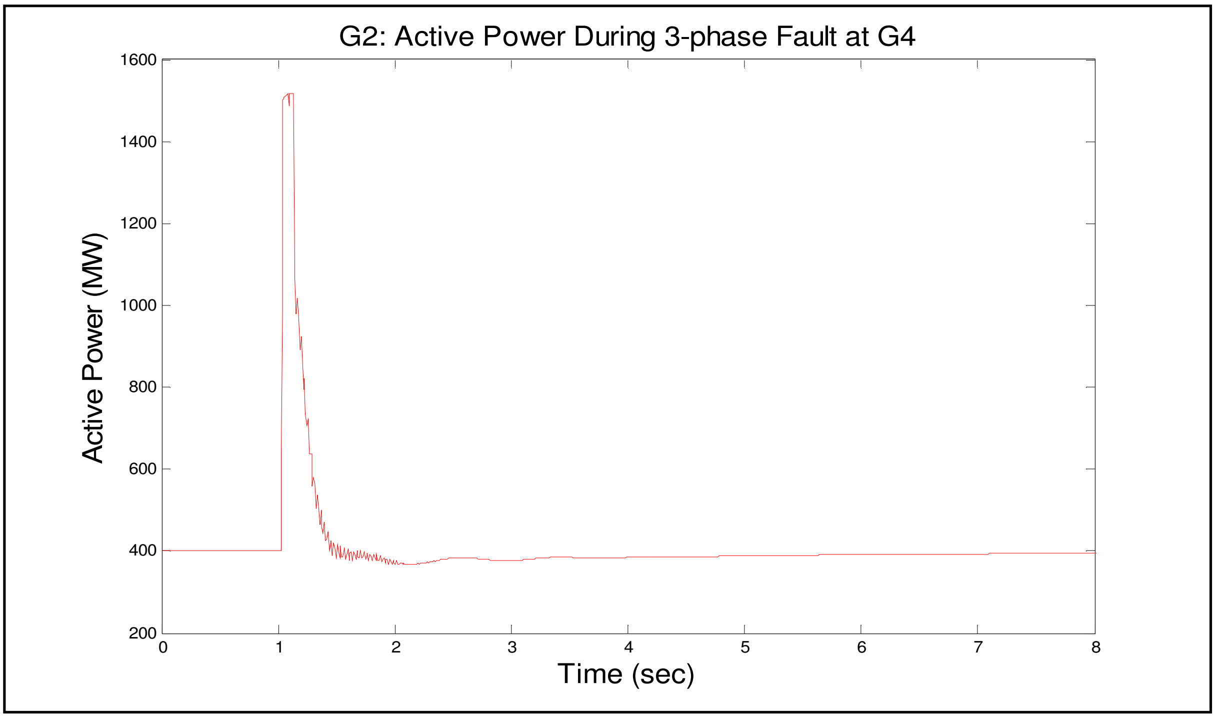

Figure 8.21 Case 1: Effect of G4 3-Phase Fault on the Active Power at G2

Figure 8.22, shows G2 reactive power variations during the fault. It can be seen that the reactive power at G2 decreased during the fault. This is because the reactive power compensation was in excess during the time of the fault as the inverter was not running at rated capacity (2500 MW). This result is similar to the effect of the effect of converter DC on the reactive power profile at G2, as seen in figure 8.10.

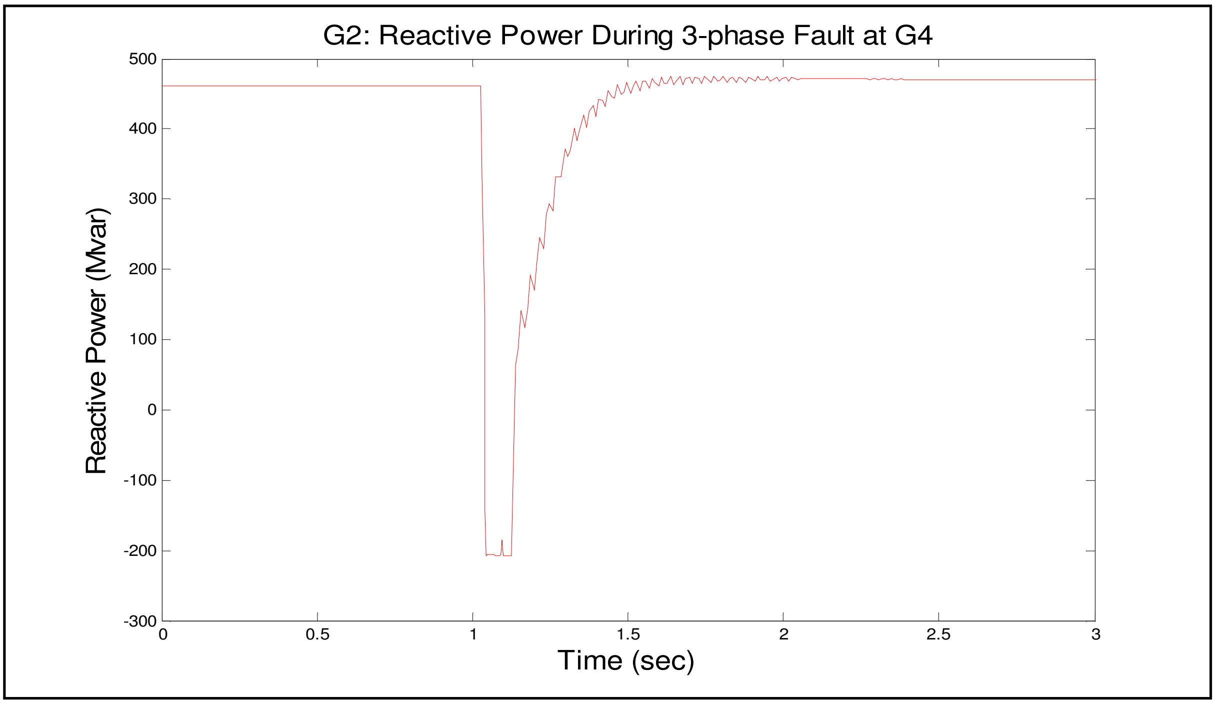

Figure 8.22 Case 1: Effect of G4 3-Phase Fault on the Reactive Power at G2

The fault at G4 had a larger impact on G3 than on G2. The loss of 1000 MW from G4 led to the large swings in the rotor angle of G3 between +160^0 and -160^0, as seen in figure 8.23.

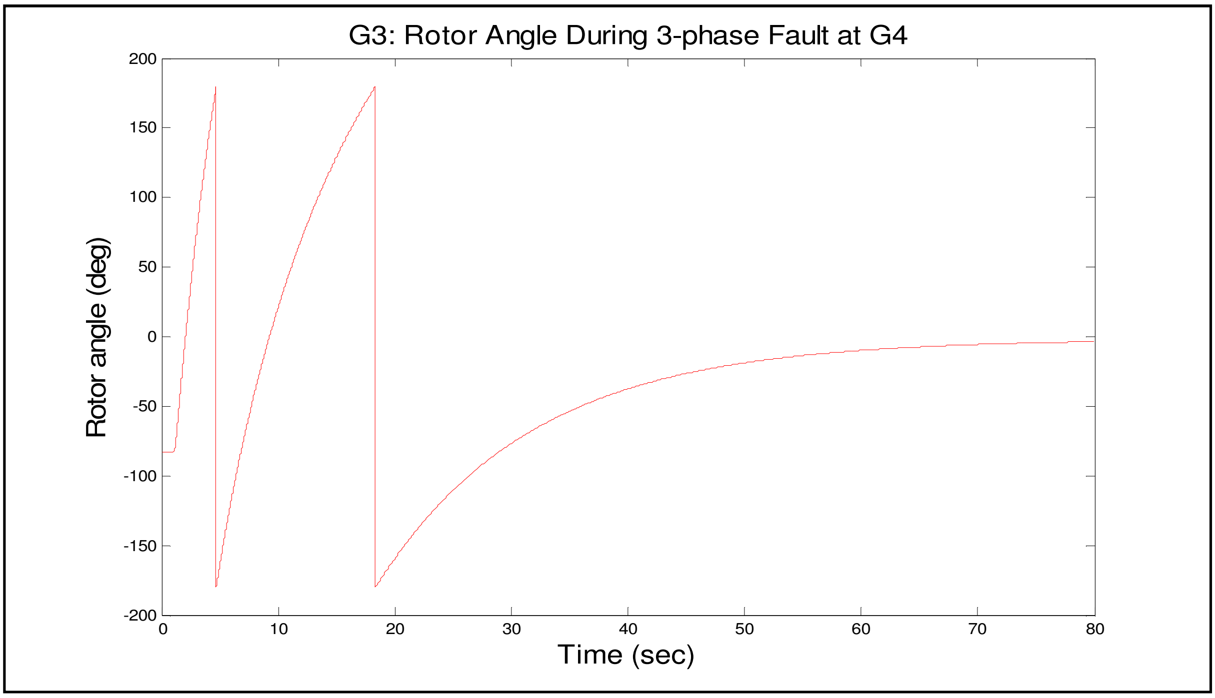

Figure 8.23 Case 1: Effect of G4 3-Phase Fault on the Rotor Angle of G3

It can be seen from figure 8.24 that during the three-phase fault at G4, which led to the loss of 1000 MW (half of the HVDC line capacity), generator G3 reached a very low voltage level of 0.4 pu but stabilised very fast in less than one second.

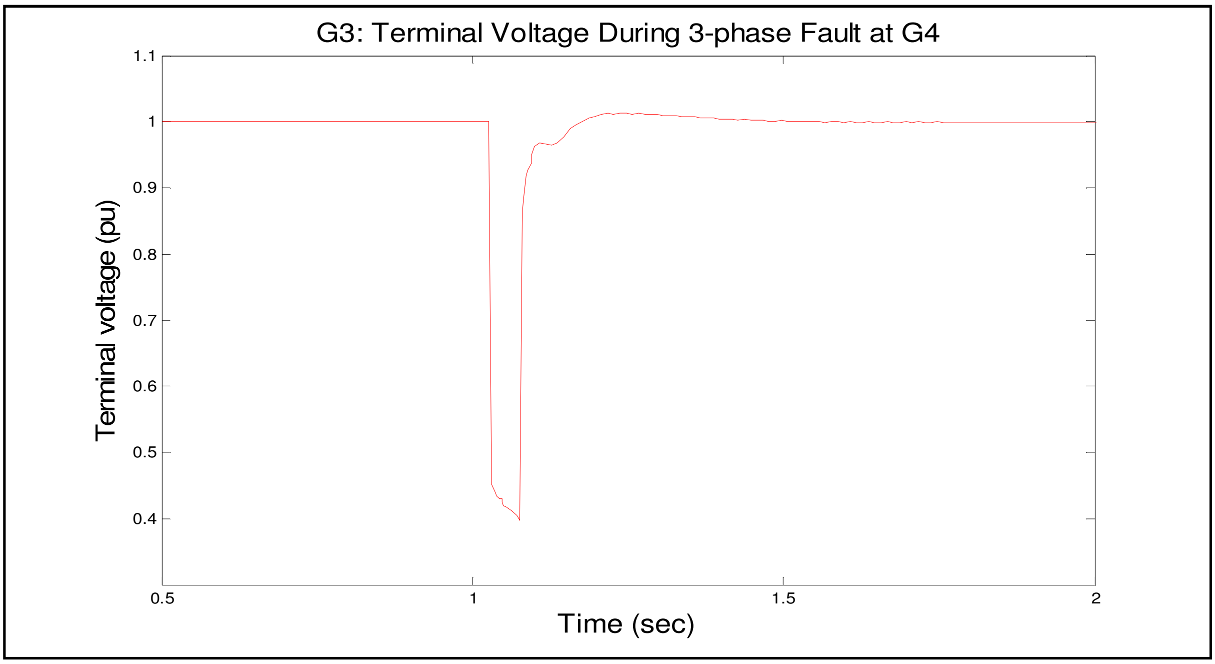

Figure 8.24 Case 1: Effect of G4 3-Phase Fault on the Terminal Voltage at G3

The drop in the voltage level at G3 led to the drop of the active power generation at G3 which is shown in figure 8.25. However, a steady state was reached in seven seconds. In response to the decrease in the active power of G3 during the fault, the active power of G2 was increased to meet the power demand of the distribution centre.

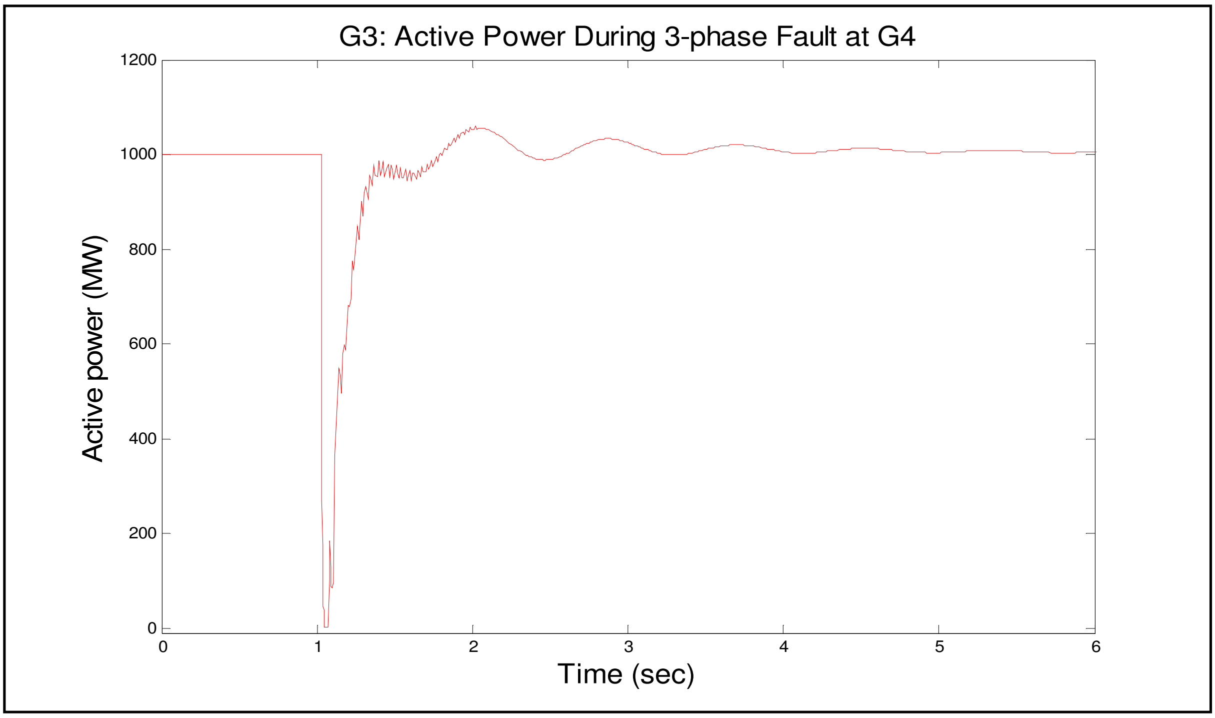

Figure 8.25 Case 1: Effect of G4 3-Phase Fault on the Active Power at G3

Figure 8.26 shows the reactive power generation at G3. The reactive power supplied by G3 increased from 435 Mvar at pre-fault condition to 1800 Mvar during the fault. Figure F.11 in Appendix F shows the current waveform of G3. The current output of G3 increased from, 0.6 pu to 3.6 pu during the 3-phase fault at G4, exceeding the maximum current output of 1.0 pu. To prevent this, G3 has to be cut off immediately to avoid the excess generation of reactive power. Otherwise dynamic reactive power compensation will be needed in area one, in order to supply the needed reactive power. The excess reactive power that was generated by G3 was absorbed by G4 during the fault.

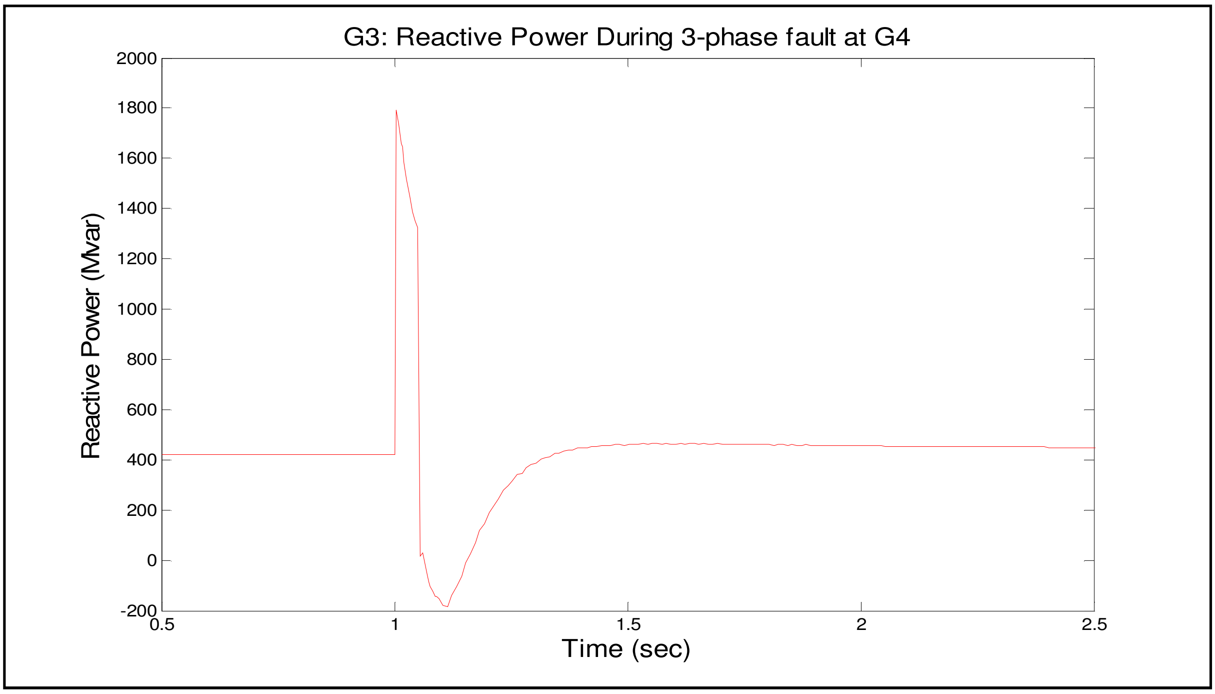

Figure 8.26 Case 1: Effect of G4 3-Phase Fault on the Reactive Power at G3

8.2.2.2 Case 2: Hybrid HVAC-HVDC Transmission Line

The simulation results obtained in this case are given in figures 8.27 to 8.34.

Figure 8.27 shows the rotor angle oscillation during the perturbation in the power system which was caused by the three-phase fault at the terminals of G4. The amplitude of these oscillations is very similar to that of case one in figure 8.19 when only HVDC was used for transmission. However, the major difference is the settling time of the system. In this case (hybrid transmission), it took about 40 seconds for the rotor angle to stabilise as opposed to case one where the rotor angle stabilised in about nine seconds. This operation is not ideal, as power systems are expected to have faster settling times, as is the case in figure 8.19.

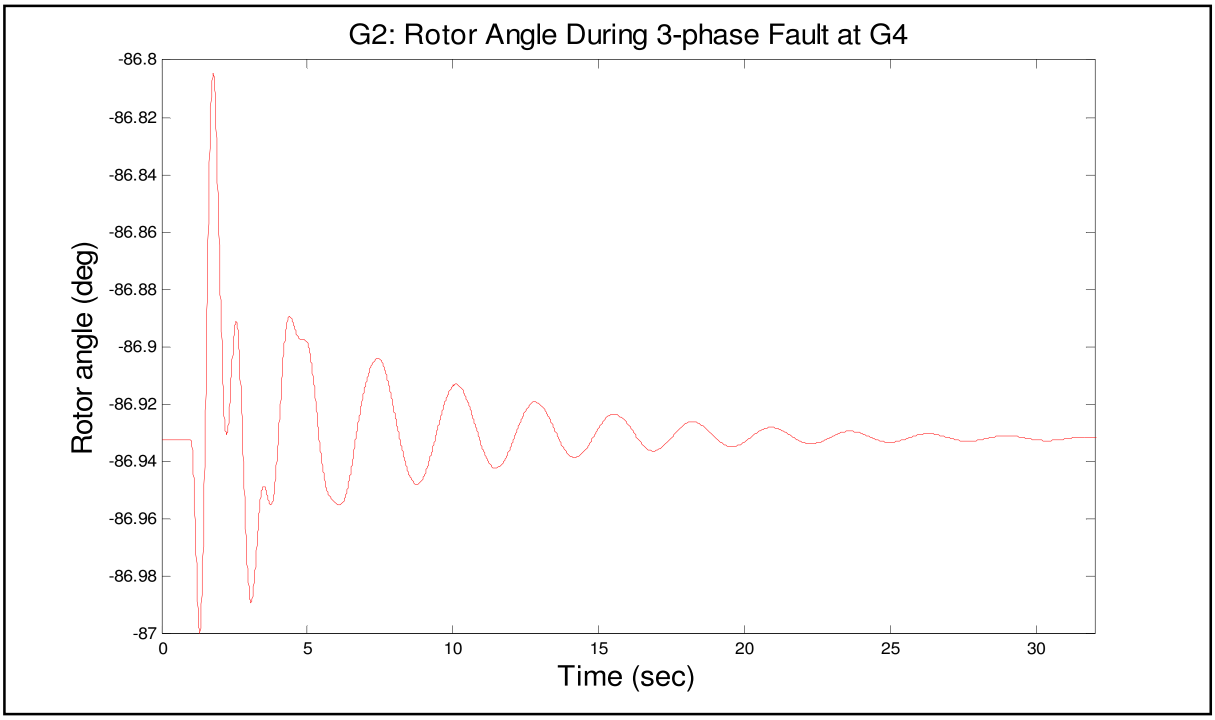

Figure 8.27 Case 2: Effect of G4 3-Phase Fault on the Rotor Angle of G2

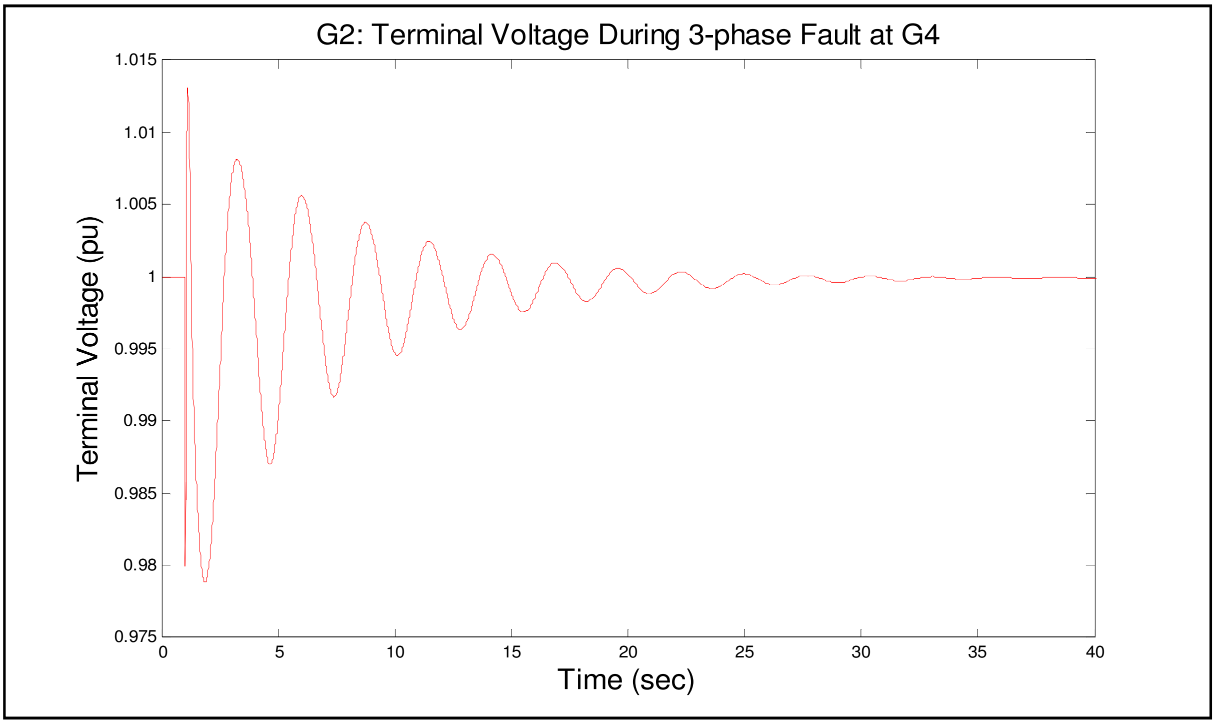

Figure 8.28 Case 2: Effect of G4 3-Phase Fault on the Terminal Voltage of G2

Figure 8.28 shows the terminal voltage at G2. Before the fault the terminal voltage of G2 was 1.0 pu. During the fault the terminal voltage oscillated between 1.013 pu and 0.98 pu. After the fault the terminal voltage returned to its pre-fault value of 1.0 pu at about 35 seconds into the simulation. The difference between the terminal voltage in case one (Figure 8.20) and that of case one is that in case 2 more oscillations are experienced as the voltage returns to its pre-fault value. Also, in case 1, the voltage increased during the fault but in this case the voltage decreased first before increasing during the fault. The increase in the rotor angle oscillations in this case is due to the HVAC transmission line between the two areas of the power system. This also led to the increase in settling time.

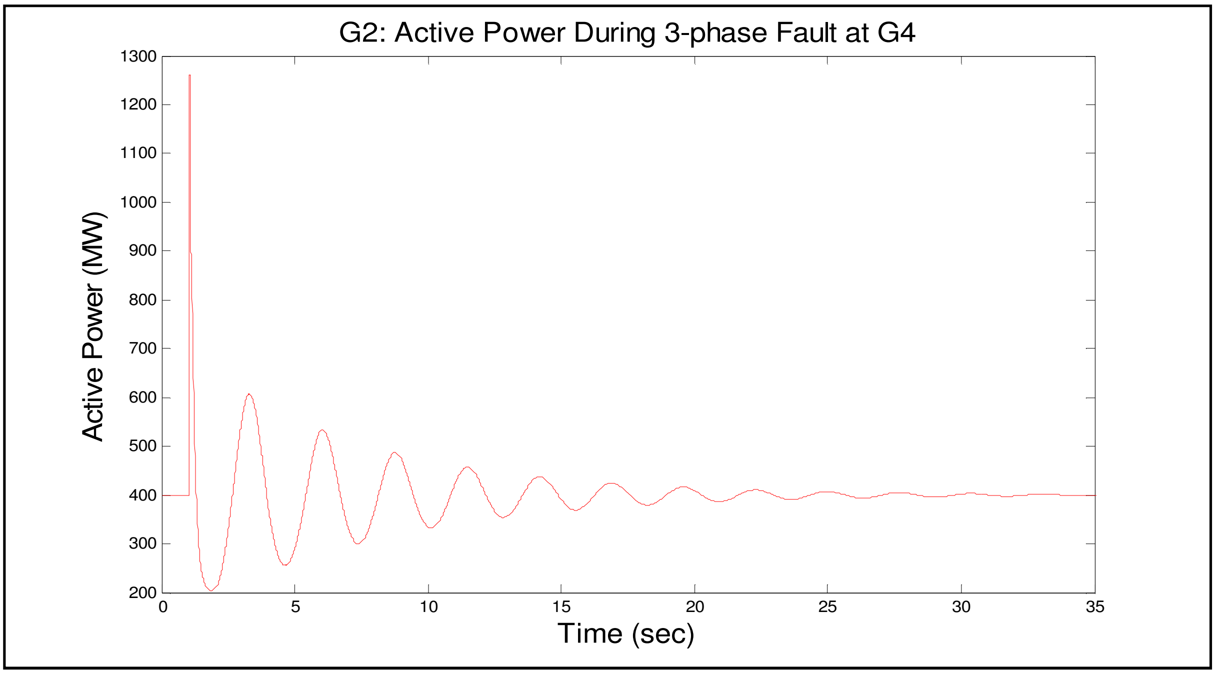

Figure 8.29 Case 2: Effect of G4 3-Phase Fault on the Active Power at G2

Figure 8.29 shows the active power generation at G2. The active power increased to 1300 MW during the fault, before decreasing to its pre-fault value of 1000 MW with decaying oscillations. The active power increase at G2 is about 100 MW less than the active power increase in case one (figure 8.21) during the fault. This means that the impact of the three-phase fault at G4 on the active power generation at G2 was reduced when the hybrid HVAC-HVDC transmission line was used.

Figure 8.30 shows the reactive power generation at G2. It can be seen from figure 8.30 that G2 increased its reactive power generation from 210 Mvar to 510 Mvar during the fault and absorbed about 50 Mvar shortly after. After the fault was cleared the reactive power oscillated between 380 Mvar and -60 Mvar before settling down to its pre-fault value. This is seen to be different from case one (figure 8.22), where G2 was absorbing reactive power during the fault. Before the fault in case one generator G2 was generating 470 Mvar while in this case, it was generating 210 Mvar. This is the reason why G2, in this case, absorbed less reactive power when compared with what happened in case one.

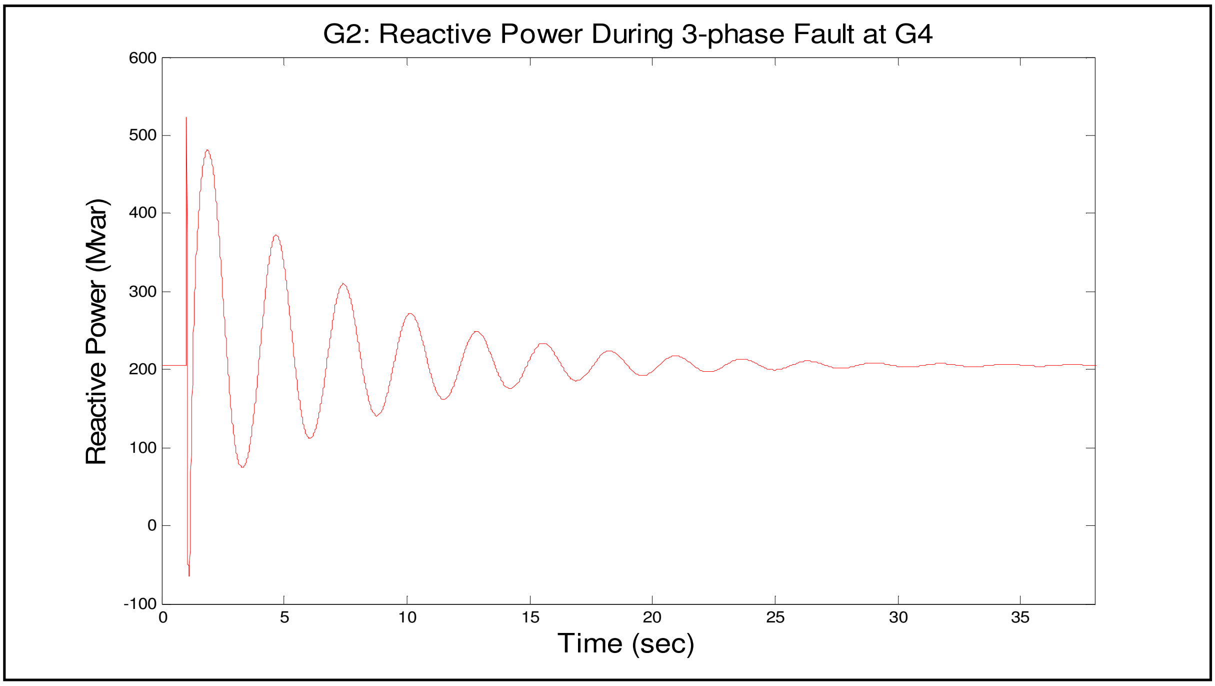

Figure 8.30 Case 2: Effect of G4 3-Phase Fault on the Reactive Power at G2

The results presented in figures 8.31 to 8.34 are taken from G3. Figure 8.31 shows the rotor angle of G3. In figure 8.32, it can be seen that the amplitudes of the rotor angle oscillation ranged from -25^0 to -57^0 and settled in about 33 seconds. Hence, under the hybrid transmission, the impact of the three-phase fault at the terminals of G4 on the rotor angle of G3 is lower than in case 1 (figure 8.23). Although the oscillations in case two are more than the rotor angle oscillations in case one, the amplitudes of the oscillations are smaller and damped out in about 45 seconds faster than in case one.

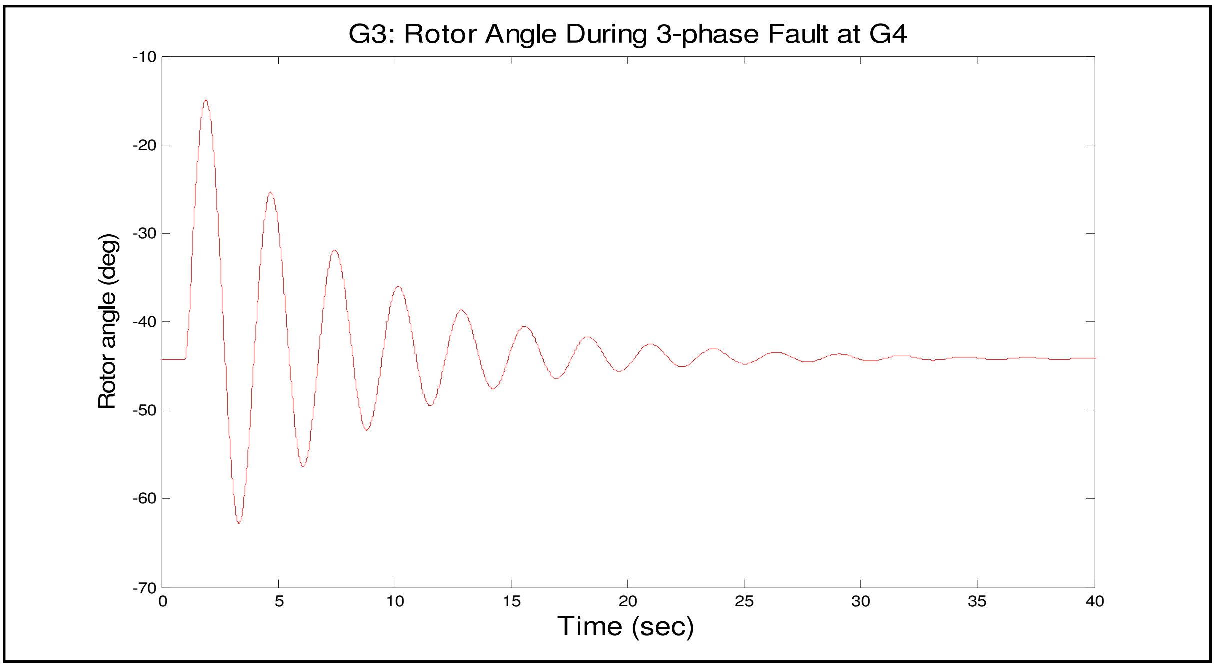

Figure 8.31 Case 2: Effect of G4 3-Phase Fault on the Rotor Angle at G3

It can be seen from figure 8.32 that the terminal voltage at G3 has no significant difference between that of cases one and two. In both cases, the terminal voltage at G3 dipped to a very low potential of 0.4 pu. There are, however, more oscillations in Figure 8.32 than in case one Figure 8.24. In other words, the system settles faster in case one than in case two.

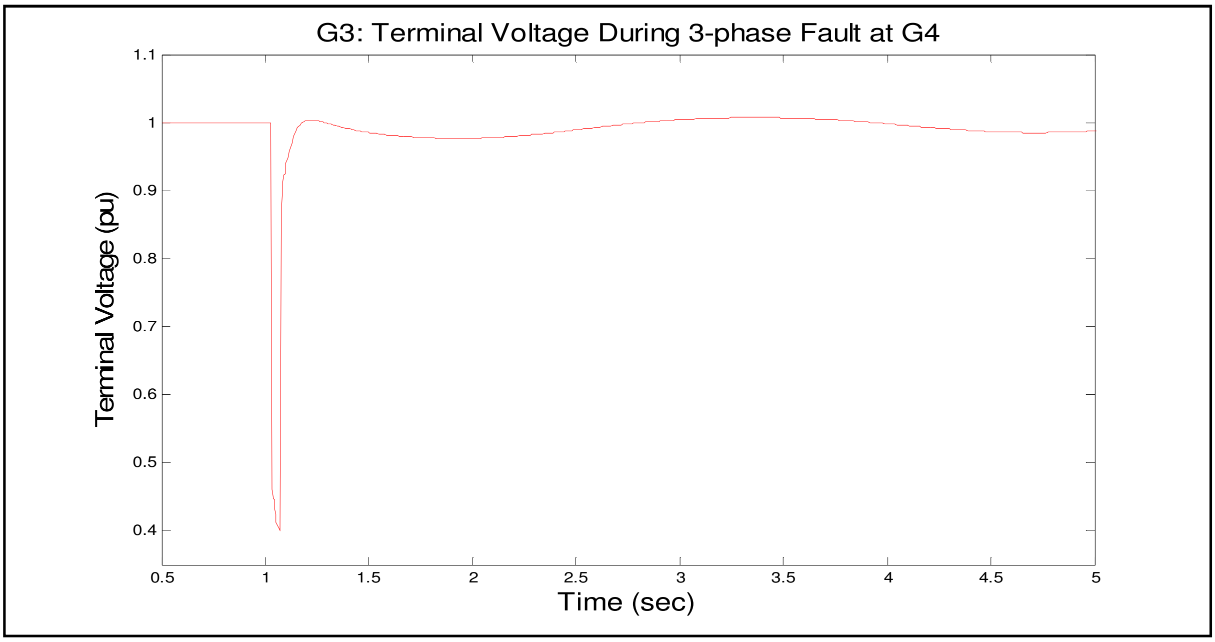

Figure 8.32 Case 2: Effect of G4 3-Phase Fault on the Terminal Voltage of G3

Figure 8.33 shows the active power generation at G3. It can be seen that the active power generation dropped to 200 MW following the low voltage dip during the fault. The major difference between case one and case two is that the active power generation at G3 dropped to 0 MW in case one (figure 8.25), while it dropped to 200 MW in case two. As a result the active power generated by G2 during the fault to meet the load demand is lower than that in case one.

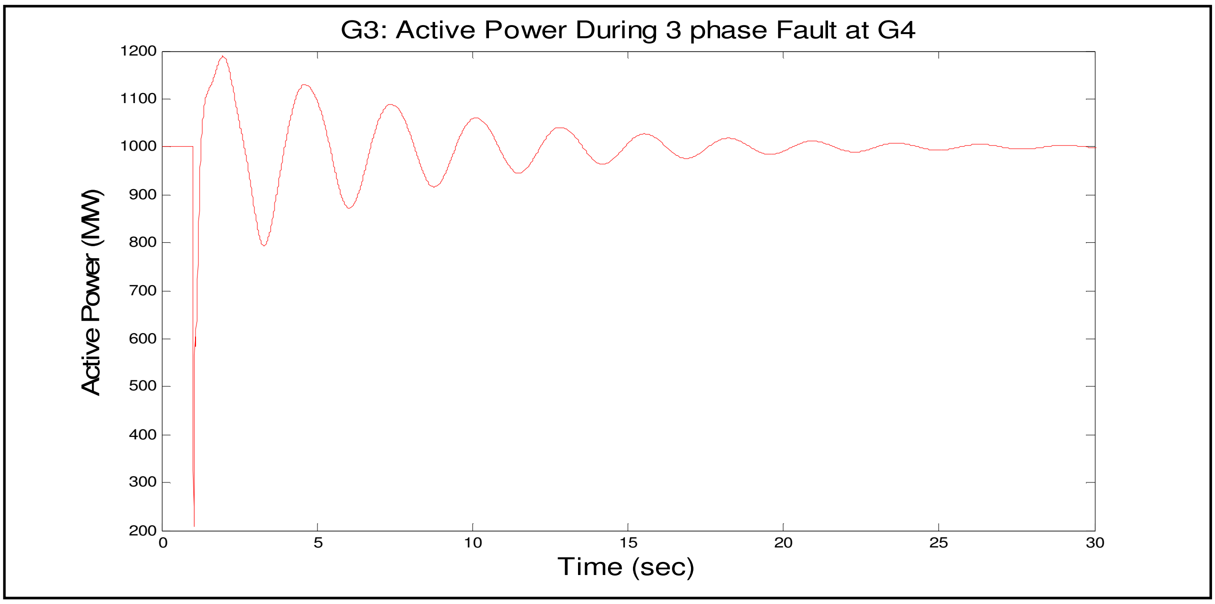

Figure 8.33 Case 2: Effect of G4 3-Phase Fault on the Active Power at G3

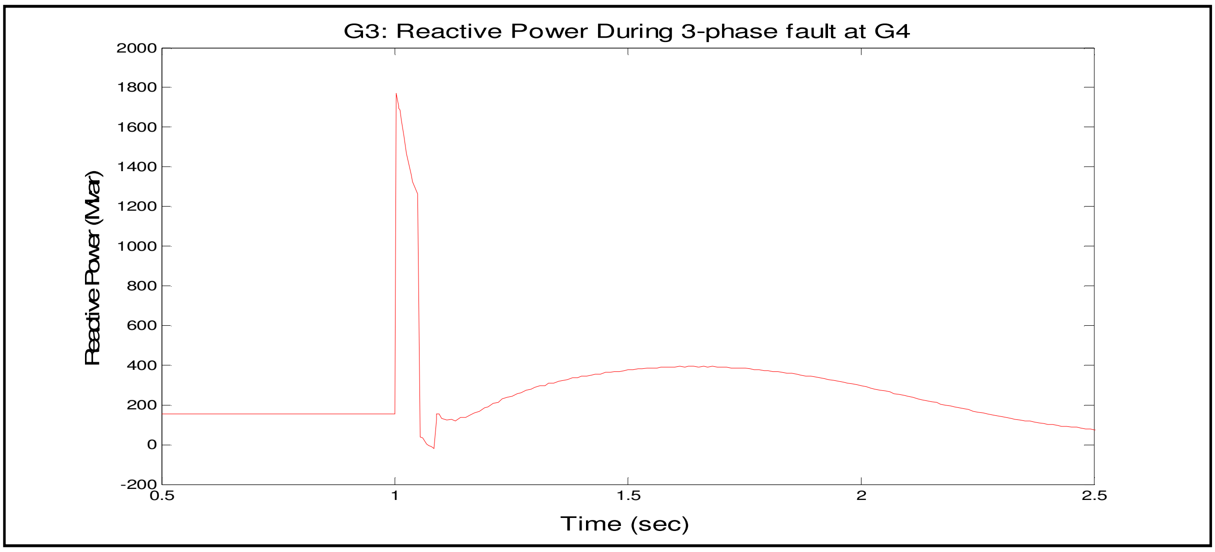

Figure 8.34 Case 2: Effect of G4 3-Phase Fault on the Reactive Power at G3

Figure 8.34 shows the excessive increase in reactive power generation at G3 which is the same across all the simulations that were conducted on the TAMM power system. In this case the excess reactive power that was generated by G3 was absorbed by G4 (where the 3-phase to ground fault occurred). The major setback in both cases is that the effect of G4 three-phase fault on the reactive power generation at G3 is very stringent. The normal capacity of G3 was exceeded during both cases. Although the time during which the reactive power increased to about 4600 Mvar in figure 8.34 (case two) and figure 8.26 (case one) are very short, the generator alone cannot cope with this demand and there is a need for (dynamic) reactive compensation. Otherwise the generators would be disconnected.

8.3 SMALL SIGNAL STABILITY

As in the case of the SMIB simulations, the DigSILENT round rotor synchronous generator model was used in the simulation. This generator is modelled as a 5^{th} order generator [37]. Hence 5 modes are expected from each of the generator in the result of the modal analysis of the small signal stability. The IEEET1 AVR and IEEEST PSS controllers were added to the model of generator G2. The function of the PSS is to add damping to the generator oscillations by controlling its excitation using stabilizing signal(s). The AVR has four state variables in its model which is expected to yield four modes while the PSS has 8 state variables in its model which should give eight modes. Therefore the total number of modes expected from the modal analysis is 32 since the controllers were only added to one of the machines, G2. The parameters of these controllers are given in Appendix D.

Tables 8.5 and 8.6 show the modes in case one (HVDC transmission) and in case two (Hybrid HVAC-HVDC transmission) respectively.

Table 8-5 Eigenvalues for the TAMM Power System Model in Case 1: HVDC Transmission

Name	Real Part	Imaginary Part	Magnitude	Damped Frequency	Damping Ratio
	1/s	rad/s	1/s	Hz	
Mode 02	-30.02882	0	30.02882	0	1
Mode 03 & 04	-24.30482	1.960208	24.38374	0.3119768	0.9967635
Mode 05	-17.16799	0	17.16799	0	1
Mode 06 & 07	-0.8587247	7.546915	7.595613	1.201129	0.1130554
Mode 08	-13.783	0	13.783	0	1
Mode 09	-13.76398	0	13.76398	0	1
Mode 10	-1.521529	0	1.521529	0	1
Mode 11	-1.432745	0	1.432745	0	1
Mode 12	-1.47445	0	1.47445	0	1
Mode 13	-0.6308175	0	0.6308175	0	1
Mode 14	-0.07187722	0	0.07187722	0	1
Mode 15	-0.112776	0	0.112776	0	1
Mode 16	-0.09747365	0	0.09747365	0	1
Mode 17	-0.09108192	0	0.09108192	0	1
Mode 18	-0.00000017	0	0.00000017	0	1
Mode 01, 19, 20, 21, 22, 23 & 24	0	0	0	0	0

In table 8.5, two sets of oscillatory modes exist. These are modes 03 & 04, 06 & 07. Mode 03 & 04 is an inter-area mode, which is critically damped with a damping ration of 0.99. Mode 06 & 07 is a local mode, whose damping ratio is 0.11. Modes 02, 05 and 08 to 18 are critically damped and stable as their eigenvalues have negative real parts. Figure 8.35 to 8.36 shows the only two states (speed and excitation flux.) and their participation factor to modes (3 & 4) and (6 & 7).

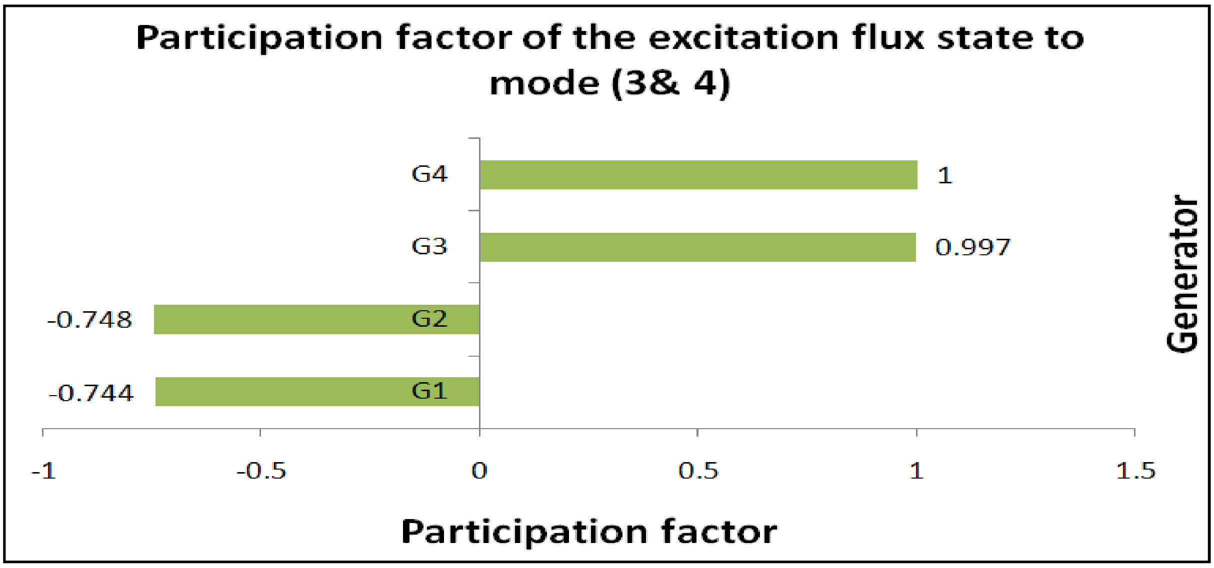

Figure 8.35 Excitation flux participation factor to mode 3 & 4

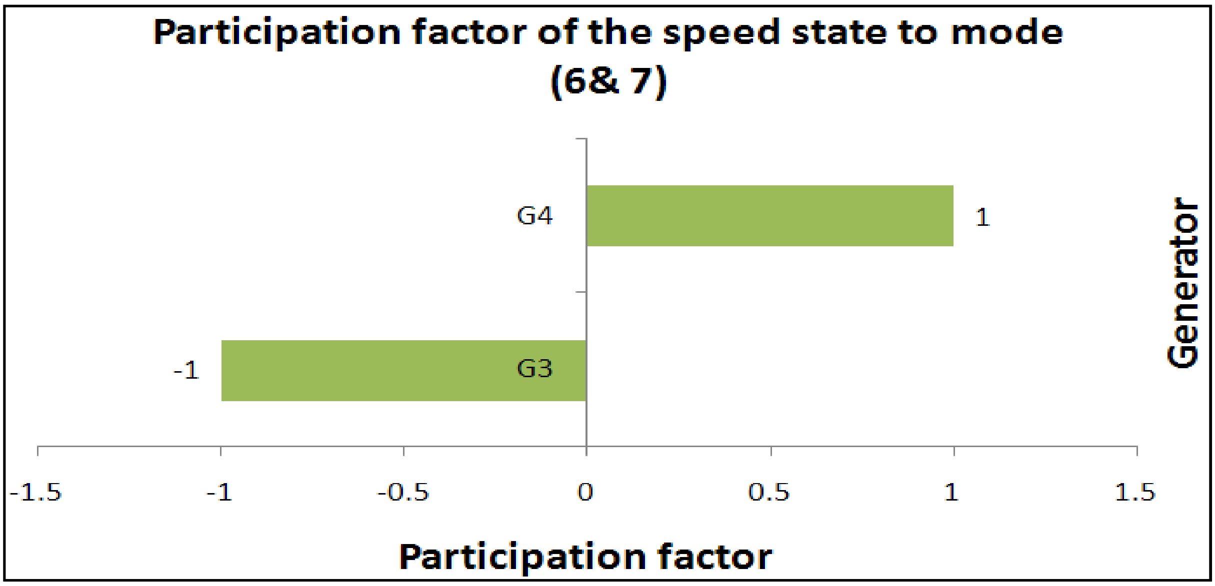

Figure 8.36 Speed participation factor to mode 6 & 7

Figure 8.35 shows the excitation flux participation to mode 3 &4. From the results obtained, it is only the excitation flux that contributed to mode 3 & 4, with G3 and G4 as the highest contributor. Other states like the speed and rotor angle did not contribute to this mode. In mode 6 & 7, the only state that contributed to this mode is the speed from G3 and G4.

For case two, with the hybrid HVAC-HVDC transmission line, the eigenvalues obtained from the system are presented in table 8.6.

Table 8-6 Eigenvalues for the TAMM Power System in Case 2: Hybrid HVAC-HVDC Transmission

Name	Real part	Imaginary part	Magnitude	Damped Frequency	Damping Ratio
	1/s	rad/s	1/s	Hz	
Mode 02	-30.02915	0	30.02915	0	1
Mode 03 & 04	-24.19782	1.780552	24.26325	0.2833836	0.9973037
Mode 05	-17.16492	0	17.16492	0	1
Mode 06	-13.77991	0	13.77991	0	1
Mode 07	-14.19595	0	14.19595	0	1
Mode 08 & 09	-0.8622598	7.536616	7.585781	1.19949	0.1136679
Mode 10 & 11	-0.231039	2.901493	2.910677	0.4617869	0.07937639
Mode 12	-1.480148	0	1.480148	0	1
Mode 13	-1.516516	0	1.516516	0	1
Mode 14	-1.498707	0	1.498707	0	1
Mode 15	-0.07239681	0	0.07239681	0	1
Mode 16	-0.1128598	0	0.1128598	0	1
Mode 17	-0.09141712	0	0.09141712	0	1
Mode 18	-0.1021724	0	0.1021724	0	1
Mode 19	0	0	0	0	1
Mode 01, 20, 21, 22, 23 & 24	0	0	0	0	0

In table 8.6, three sets of oscillatory modes exist. These are modes 03 & 04, 08 & 09 and 10 & 11. Among these oscillatory modes, only mode 03 & 04 is critically damped with a damping ratio of 0.99. Mode 08 & 09 (a local mode) has an acceptable damping ratio of 0.11, while mode 10 & 11 (an inter-area mode) is poorly damped with a damping ratio of 0.08. All the other modes are critically damped with a damping ratio of one, excluding modes 01 and 20 to 24. Figure 8.37 to 8.39 shows the only state (speed) and its participation factor to modes (3 & 4), (8 & 9) and (10 &11). These states are speed and excitation flux.

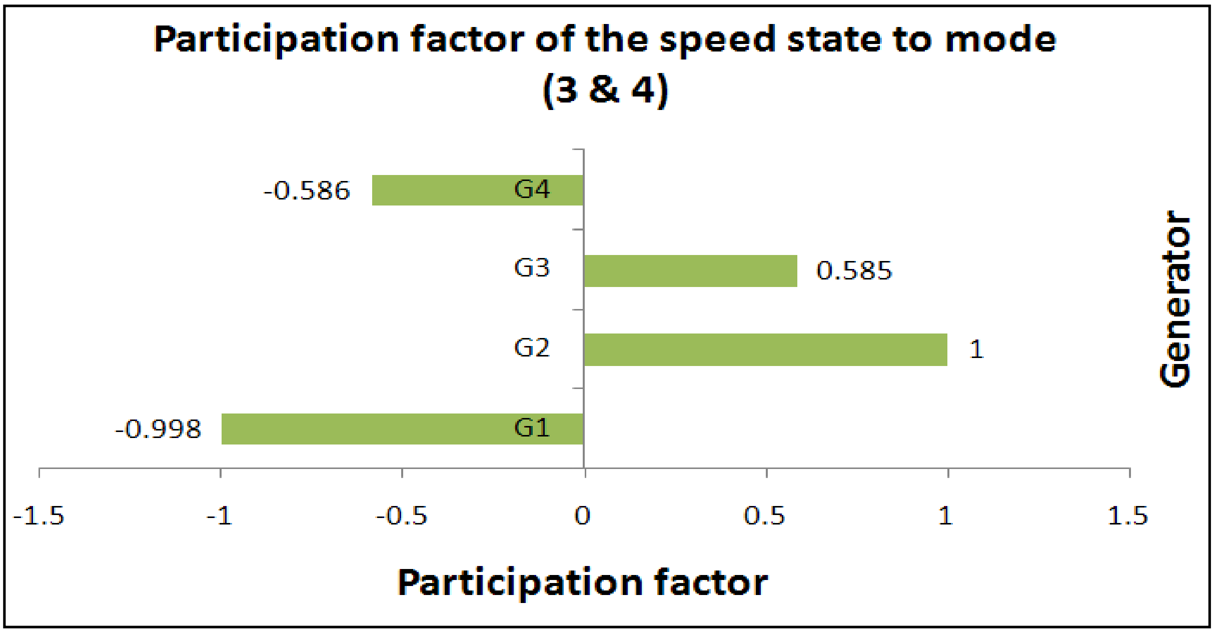

Figure 8.37 Speed participation factor to mode 3 & 4

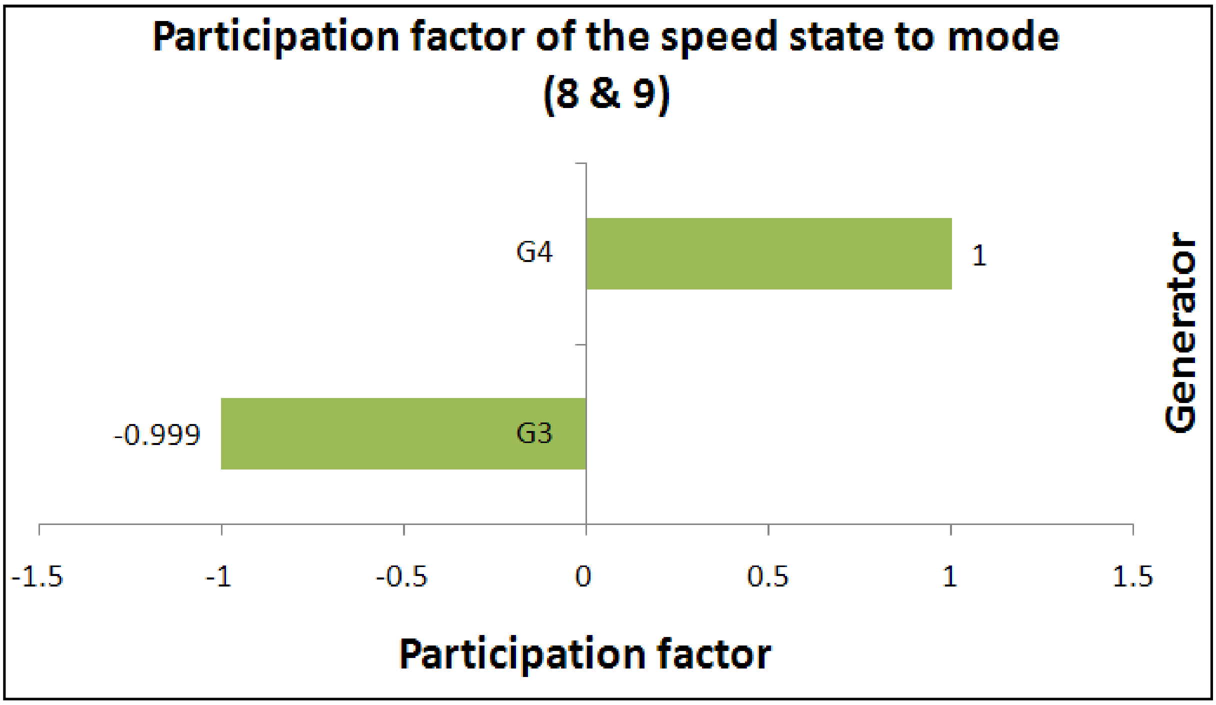

Figure 8.38 Speed participation factor to mode 8 & 9

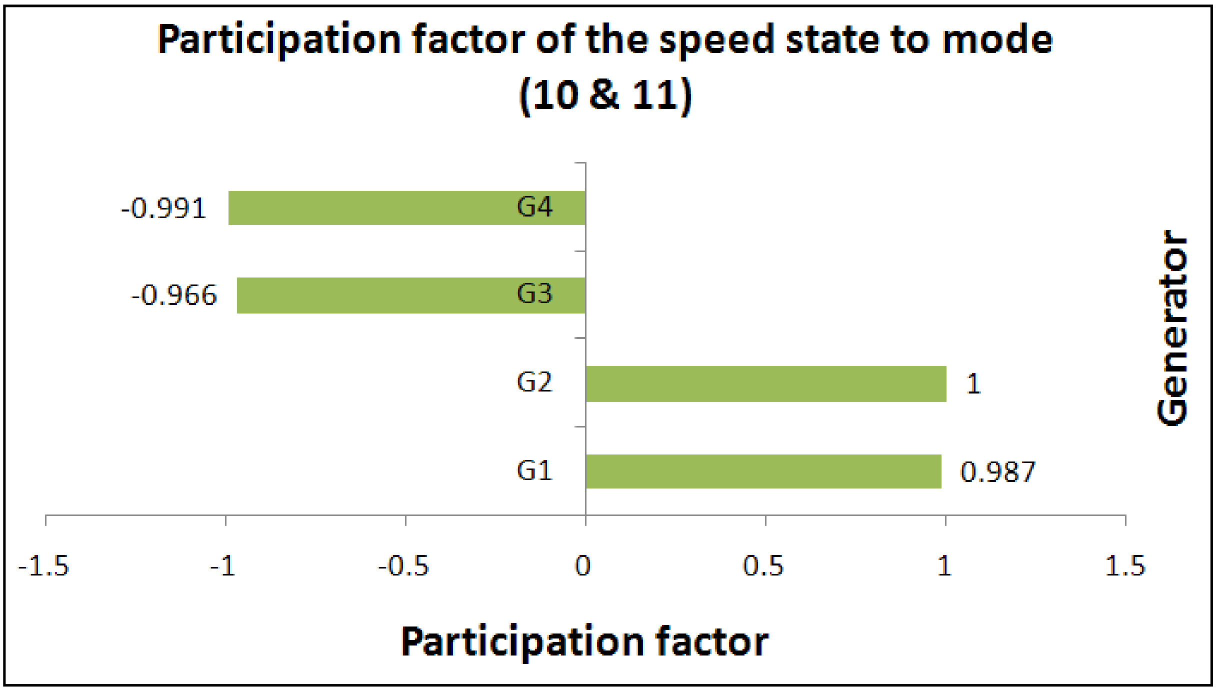

Figure 8.39 Speed participation factor to mode 10 & 11

From the results shown in figure 8.37 to 8.39, mode 10 & 11 had the highest speed participation factor from all four generators at approximately 1 each. In mode 3 & 4, the highest speed participation factor came from G1 and G2, each at approximately 1, while G3 and G4 had a lower participation of about 0.585 each. In mode 8 & 9, only G3 and G4 contributed each with a participation of approximately 1. Figure 8.40 shows the combined eigenvalue plot from both case one and case two. From figure 8.40, it can be concluded that all the eigenvalues of from case one and case two are highly correlated except for the additional inter-area mode in case two which has no corresponding mode in case one.

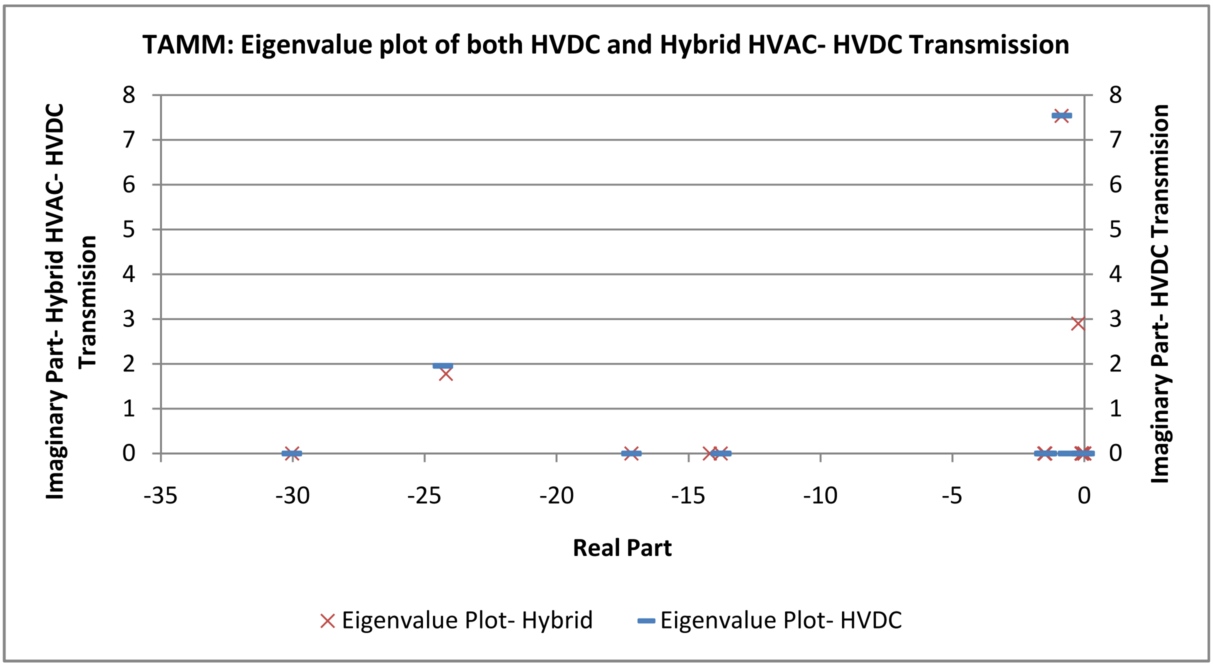

Figure 8.40 TAMM Eigenvalue Plot from HVDC Transmission and Hybrid HVAC-HVDC Transmission

Based on the findings above, it can be concluded that the HVDC transmission scheme has less inter-area oscillations when compared to the hybrid HVAC-HVDC transmission scheme. The hybrid HVAC-HVDC transmission scheme introduced an additional inter-area mode. Hence, the hybrid HVAC-HVDC scheme is relatively less stable and more susceptible to small signal instability when compared to the HVDC scheme. For the Hybrid HVAC-HVDC transmission scheme, only state that contributed to the oscillatory modes, is the speed. While the excitation flux contributed to one of the modes for the HVDC transmission scheme.

CHAPTER 9

Conclusions and Recommendations

Conclusions:

From the reviewed literature, it is concluded that relatively little published work was done in the field of parallel hybrid HVAC- HVDC transmission when compared to HVDC transmission. Hence, this thesis has made some significant contributions to the available literature on hybrid parallel HVAC-HVDC power system interconnections. From the simulation results on load flow and rotor angle stability using the SMIB and TAMM power system models, the following conclusions were reached:

The load flow analysis conducted on the SMIB power system indicated that the voltage drop across the HVDC transmission line for both transmission configurations was 0.03 pu. There was a 42.8 % decrease in the amount of reactive power demand by the converter stations with the hybrid HVAC-HVDC transmission. For both transmission schemes, the delivered real power to the distribution centre was the same at 1942 MW. Given that the transmission line losses in the two cases are different, the transmitted power in each case was different.

The loss in the HVDC transmission scheme was 28 MW lower than the loss in the hybrid HVAC-HVDC transmission line. Nevertheless, the hybrid HVAC-HVDC transmission scheme provided a solution for reducing the voltage angle difference between the terminating AC busbar on the HVAC and HVDC transmission line, while keeping the total amount of power transmitted constant. Consequently, the steady state stability margin is increased. This seems to be one of the major advantages in terms of load flow, for the hybrid HVAC-HVDC transmission line configuration.

The transient simulation results indicated that the SMIB power system regained stability faster when the HVDC line alone is used for transmission. This is due to the reduced number of post fault rotor angle oscillations in the power system. The generators exceeded their maximum capacity due to reactive power generation during the transients, hence, there is a need for (dynamic) reactive compensation, or the generators which exceeded their maximum reactive power generation would have to be disconnected during the fault.

Small signal stability analysis conducted on the SMIB power system showed that the HVDC transmission scheme is less susceptible to small signal instability when compared to the hybrid HVAC-HVDC transmission scheme.

The load flow analysis conducted on the TAMM power system indicated that, the voltage drop across the HVDC transmission line was 0.03 pu when HVDC transmission was used, and 0.02 pu using the hybrid HVAC-HVDC transmission line. There was a 57.2 % decrease in the amount of reactive power demand by the converter stations with the hybrid HVAC-HVDC transmission line. The power loss in transmission using HVDC was 29 MW lower than the power loss on the hybrid HVAC-HVDC transmission line.

The transient simulation results showed that, the rotor angle response of the generators in each area of the power system are similar, during the converter DC fault at G3. Nevertheless, the rectifier fault was found to be more severe on the rotor angle stability when compared to the inverter fault for the HVDC transmission scheme. The terminal voltage dip at G3 during the rectifier DC fault was larger than the terminal voltage dip at G3 during the inverter fault across both transmission schemes. This dip however, was found to be reduced with the hybrid HVAC-HVDC transmission scheme.

G2's active power increase during both converter faults was reduced with the hybrid HVAC-HVDC transmission line. Similarly, the reactive power drawn by G2 during the converter faults was reduced with using the hybrid-HVAC-HVDC transmission line.

Only G3 exceeded its capacity during the converter fault due to the additional active and reactive power it had to provide. To prevent this, there is a need for (dynamic) reactive compensation, or G3 would be disconnected during the converter fault. Similar to the SMIB power system, the TAMM power system regained stability faster when the HVDC line alone is used for transmission. This is due to the reduced number of post fault rotor angle oscillations in the power system.

From the small signal stability analysis, it can be concluded that the hybrid HVAC-HVDC scheme is relatively less stable and more susceptible to small signal instability when compared to the HVDC scheme. For the Hybrid HVAC-HVDC transmission scheme, the only state that contributed to the oscillatory mode is the speed. While the excitation flux contributed to one of the modes in the HVDC transmission scheme.

Recommendations:

Based on the work that was carried out in this thesis, the following recommendations are made:

The hybrid HVAC-HVDC transmission scheme is recommended for power transmission between areas of a network. Nevertheless, it is recommended that this work should be carried out in other simulation packages for validation. Localised application of DC faults within the converter station and along different segments of the HVDC line can also be carried out in further studies. This will enhance a more robust analysis of the interrelations of DC faults on the entire power system.

Furthermore, a study on the presence of AC and DC harmonics in the power system using both HVDC and hybrid parallel HVAC-HVDC transmission can be carried out to determine the adequate filters that should be adopted. Further research should be carried out to reduce the post fault oscillations in the hybrid HVAC-HVDC transmission scheme. An investigation needs to be carried out to explain why the active power momentarily increases at G3 and G4 when a DC fault occurs at both the rectifier and the inverter station. And finally, more research needs to be carried out to explain why the post fault rotor angles in most cases are different from the pre-fault rotor angle.

References

1. Kundur, P., Paserba, J., Ajjiarapu, V., Andersson, G., Bose, A., Canizares, C., Hatziargyriou, N., Hill, D., Stankovic, A., Taylor, C., Van Cutsem, T. and Vittal, V., "Definition and classification of power system stability - IEEE/CIGRE Joint Task Force on Stability Terms and Definitions, " *IEEE Trans. on Power Systems*, Vol.19, No. 2, pp. 1381 -1397, May, 2004.
2. Fischer de Toledo, P., Bergdahl, B. and Asplund, G., "Multiple infeed short circuit ratio-aspects related to Multiple HVDC into one AC network. Sweden", ABB Power Systems, HVDC Division, 2005.
3. Li Gengyin, Li Guangkai, Liang, H., Zhao, C. and Yin, M., "Research on Hybrid HVDC," *2004 International Conference on Power System Technology, POWERCON.* Singapore, 21-24 November, 2004.
4. Tuson, P., "HVDC strengthening in Southern Africa", *IEEE PES Power Africa 2007 Conference and Exposition*, Johannesburg, South Africa, 16-20 July, 2007.
5. Eskom Holdings Limited, South Africa, *New Build News*, Issue 7, http://www.eskom.co.za/content/NBMar09.pdf, 15th September, 2009.
6. Husain, Ashraq , "*Electrical Power Systems*", 5th Edition, New Delhi: CBS Publishers & Distributors, 2007.
7. Hausler, M. "Multi terminal HVDC for high power transmission in Europe",presented at *CWPEX99*, Pozan, Poland, March 1999.
8. Bozhko, S.V., Blasco-Gimenez, R. and Li, R., "Control of offshore DFIG-based wind farm grid with line-commutated HVDC connection," *IEEE Transactions on Energy Conversion*, vol 22, No. 1, pp. 71- 78, March 2007.
9. Hammad A., Koelsch, H. and Daehler, P., "Active and reactive power controls for the GEZHOUBA-SHANGHAI HVDC transmission scheme", *6th International Conference on AC and DC Transmission, IEE*. May, 1997.

10. Perez de Andres, J., Muhlenkamp, M., Retzmann, D. and Walz, R., "Prospects for HVDC:getting more power out of the grid, "*Jornadas Tecnicas sobre la "Sesion Plenaria Cigre 2006"*, , 29-30 November, 2006.
11. Bresesti P., Kling, W.L. and Hendriks, R.L., "HVDC Connection of Offshore Wind Farms to the Transmission System," *IEEE Transactions on Energy Conversion*, Vol 22, No. 1, pp. 37-43, March 2007.
12. Wu, F. F., " Technical Considerations for Power Grid Interconnections in Northeast Asia," University of Hong Kong and University of California at Berkeley, http://www.nautilus.org/archives/energy/grid/abstracts/wu_technical.pdf, April 27th , 2009.
13. Woodford, D. A., *HVDC transmission*. Canada: Manitoba HVDC Research Center, pp. 1-25, 1998.
14. Hingorani, N. G., "HVDC transmission: a power electronic workhorse", *IEEE Spectrum*, pp. 63-72, April, 1996.
15. Oyedokun, D. T. , "Using DigSILENT and PSCAD for planning and operation of HVAC-HVDC interconnections". Bsc (Elec Eng) thesis, University of Cape Town , 2007.
16. Folly, K. A., "EEE4090F transfer of power between active sources: class notes", UCT, Cape Town, 2007.
17. Bahrman, M. P., "The ABCs of HVDC transmission technologies", IEEE *Power and Energy Magazine*, pp. 33-44, March/April 2007.
18. Ijumba, Katrine, "Effect of AC line length on the stability of the AC/DC interconnection". Bsc (Elec Eng) thesis, University of Cape Town, 2005.
19. Kundur, P., *Power system stability and control,* New York: McGraw-Hill, 1993.
20. Arrillaga , J. *High Voltage Direct Current Transmission*, London: Peter Peregrinus 1983, pp. 149-151.
21. Padiyar, K.R., *Analysis of subsynchronous resonance in power systems*, Boston: Kluwer Academic Publishers 1999, pp. 181.

22. Dash, P.K., Routry, A. and Liew, A. C., "Design of an energy function based fuzzy tuning controller for HVDC Links," *Electrical Power and Energy Systems,* pp. 337 -347, No. 21, 1999.

23. Gao, D., "AC transmission lines and underground cables", Tennessee Tech University, 2008.

24. Szechtman ,M., Woss, T. and Thio, C.V., "A benchmark model for HVDC system studies," *5th International conference on AC and DC Transmission, IEE*. May, 1996.

25. Dash, P.K., Routray A., Panda, S.K. and Liew, A.C., "A fuzzy self-tuning PI controller for HVDC links", *IEEE Transactions on Power Electronics*, Vol 11, No.5, pp. 669 -679, Sept, 1996.

26. Glover, J. D. and Sarma, M. S., Power System Analysis and Design, 3rd ed, Califonia: Brooks/ Cole, pp. 208-221, 2002.

27. Padiyar, K.R., *HVDC Power Transmission Systems: Technology and system interactions*. England: Willey, pp. 84-90, 1990.

28. Mohanty, K.B., "Development of neuro-fuzzy controller for a two-terminal HVDC link," *Journal of Systems Science & Engineering,* Vol.9 No.1, pp. 8-15, June 2004.

29. Kanngiesser, .W., Ring, H., and Wess,T., "Simulator study on line fault clearing by DC circuit breakers in a meshed MTDC system, "*5th International Conference on AC and DC Transmission, IEE*, pp. 102-107, 1996.

30. Joetten, R., Wess, T. and Woodford, D., "On the fault recovery of HVDC systems," *European Conference on Power Electronics and Its Applications (EPE)* Aachen, 1989.

31. Schmitt, H., Christil, N., Gampenrieder, R., Leigl, K., and Gartmair, H., "System performance and basics design aspects for the Etzenricht 600MW Back-to-Back HVDC Converter Station," *5th International conference on AC and DC Transmission, IEE,* May, 1996.

32. Arrillaga, J. and Smith, B., "AC - DC power system analysis, "*IEE Power and Energy Series* 27, pp. 51-125, 1998.

33. Ambriz-Perez, H., Acha, E., and Fuerte-Esquvel, C.R., “High voltage direct current modelling in optimal power flows”, J*ournal of Electrical Power and Energy Systems*, vol. 30, 2008, pp.157-168.

34. Alfuhaid, A.S., Mahmoud M.S. and El-Sayed, M.A., “Modelling and control of *High Voltage AC- DC Power Systems”,* Journal of the Franklin Institute, no 336, pp 767-781, 1999.

35. Aik, D.L., and Andersson, G. “Voltage and power stability of HVDC aystems: emerging issues and new analytical methodologies,” *VII SEPOPE,* Curtiba, Brazil, 23-28 May, 2000.

36. Liu, G., Z.Xu and Huang, Y., “ Analysis of Inter-area oscillations in the South China Interconnected Power System, ”*Journal of Electrical Power Systems Research*, vol. 70, pp. 38-45, 2004.

37. DigSILENT, *Technical Reference V-14.0.513*.DigSILENT GmbH (C), 2009.

38. Khatir, M., Zidi, S. A., Hadjeri, S., Fellah, M. K. and Amiri, R., “Performance evaluation of line CCC-based HVDC system in Simulink environment, ”*Journal of Electrical and Electronics Engineering*, Vol 8,No.1, pp. 481- 490, 2008.

39. Hume, D., “*Technical notes on transpowers HVDC upgrade-final.* System Studies Group NZ Ltd”, New Zealand, July, 2008.

40. Taylor, C. W., “Power system voltage stability”, New York: McGraw-Hill, pp. 181-190, 1994.

41. Zhang, L. and Harnefors, L., “ Power system reliability and transfer capability improvement by VSC-HVDC (HVDC Light©), ” *Security and Reliability of Electrical Power Systems CIGRE Regional Meeting*, Tallinn, Estonia, June 18-20, 2007.

42. Senthil, J. and Padiyar, K.R. , “A simulator study of Recovery of HVDC Links following AC system fault, ” *5th International Conference on AC and DC Transmission, IEE*,May, 1996.

43. Jeunehomme, A., Charles, P. J. and Roguin J., “Numerical simulation of the cross channel HVDC link during AC system faults: comparison with site results,” *5th International Conference on AC and DC Transmission,* IEE. May, 1996.

44. Kumar, A., Lagerskvist, M., Eklund, M. and QingYun, Y. , “Three Gorges-Changzhou HVDC: ready to bring bulk power to East”*, 4th International Conference on Power Transmission and Distribution Technology 2003*, Changsha, 14-16 October, 2003.

45. Kimbark, E. W. “*Direct Current Transmission”,* Wiley-Interscience, New York, 1971.

46. WG 14.02, “The Cigre HVDC benchmark model: a new proposal with revised parameters” *Electra,* No. 157, December 1994.

47. EPRI Report EL-3004, “*Methodology for Intergration of HVDC Links in Large AC Systems-Phase 1: Reference Manua”,* New York: Ebasco Services, 1983.

48. To, K. W., V., David, A. K., Hammad, A. E., “A Robust Co-ordinated Scheme for HVDC Transmission with Parallel AC Systems”, IEEE Transactions on Power Delevery, Vol. 9, No. 3, pp. 1710-1716, July 1994.

49. Ekstrom, A. and Liss, G., “A Refined HVDC Control System”, IEEE Transactions on Power Apparatus and systems, Vol. 89, No. 5/6, pp. 723-732, May/June 1970.

50. Gan, D., Thomas, R. J. and Zimmerman, R. D., “Stability- constrained optimal Power flow”, IEEE Transactions on Power Systems, Vol. 15, No. 2, pp. 535-540, May 2000.

Published research papers

1. Oyedokun, D.T. and Folly, K.A., , ”Power flow studies in HVAC and HVDC transmission lines*, ”, IASTED African Conference on Power and Energy Systems-AfricaPES*, September 8-10, 2008, Gaborone, Botswana.

2. Oyedokun, D.T. and Folly K.A, “Power flow analysis on a Multi-Machine Power System with HVDC transmission link” , *18th Southern African University’s Power Engineering Conference (SAUPEC)*, January 28 -29, 2009, Stellenbosch, South Africa.

3. Oyedokun, D.T., Folly, K.A. and ,Chowdhury, S.P.,“Rotor Angle Stability of a Multi-Machine Power System interconnected with HVDC transmission”, *44th International Universities’ Power Engineering Conference (UPEC 2009)*, 1- 4 September, 2009, Glasgow, Scotland.

4. Sheetekela, S.P., Folly, K.A., Oyedokun, D. T., “ Multi-machine power system stabilizer design based on Evolutionary Algorithms”,44th International Universities’ Power Engineering Conference (UPEC 2009), 1st to 4th September, 20009, Glasgow, Scotland.

5. Kaur, K., Chowdhury, S., Chowdhury, S.P, Gaunt, C.T., Oyedokun, D. T., “Fuzzy logic based power optimization of variable speed, variable pitch wind power generation systems”, 44th International Universities’ Power Engineering Conference (UPEC 2009), 1st to 4th September, 20009, Glasgow, Scotland.

6. Oyedokun, D.T., Folly, K.A ., and Chowdhury, S.P., “Effect of converter DC fault on the transient stability of a Multi-Machine Power System with HVDC transmission lines”, *9th IEEE Africon*, 23- 25 September, 2009, Nairobi, Kenya.

7. Azimoh, L. C., Folly, K.A., Chowdhury, S.P. and Oyedokun, D.T., “Transient and small signal stability of a two-area HVAC power network Interconnected with a HVDC

link", 9th *IASTED European Conference on Power and Energy Systems-EuroPES*, September 7-9, 2009, Palma de Mallorca, Spain.

8. Oyedokun, D.T. and Folly K.A., Sheetekela, S.P., Azimoh, L.C., Ubisse, A.V., "Impact of integrated HVAC-HVDC transmission on the rotor angle stability of a power system network" , *19th Southern African University's Power Engineering Conference (SAUPEC)*, January 28 -29, 2010, Johannesburg, South Africa.

9. Azimoh, L.C., Folly, K.A., Chowdhury, S.P., Oyedokun, D.T., Sheetekela, S.P., Ubisse, A.V., "Enhancement of power systems stability of a HVAC network using HVDC and VSC- HVDC links" , *19th Southern African University's Power Engineering Conference (SAUPEC)*, January 28 -29, 2010, Johannesburg, South Africa.

10. Ubisse, A.V., Folly, K.A., Awodele, K.A., Azimoh, L.C., Oyedokun, D.T., Sheetekela, S.P., "Comparison Matlab PST, PSAT and DigSILENT for load flow studies on parallel HVAC-HVDC transmission lines" , *19th Southern African University's Power Engineering Conference (SAUPEC)*, January 28 -29, 2010, Johannesburg, South Africa.

11. Sheetekela, S.P., Folly, K.A., Ubisse, Oyedokun, D.T., Azimoh, L.C., "Power system stabiliser design based on Evolutionary Algorithm techniques" , *19th Southern African University's Power Engineering Conference (SAUPEC)*, January 28 -29, 2010, Johannesburg, South Africa.

APPENDIX A:

Short Circuit Ratio

For transmission systems that have HVDC transmission lines, the short circuit ratio (SCR) is defined as the ratio of the short circuit MVA rating of the AC system and the rated MW of the DC converter as seen in equation A.1 [19].

$$SCR = \frac{\text{Short - Circuit level of AC system (MVA)}}{\text{DC rating at the converter terminals (MW)}} \tag{A.1}$$

The short-circuit level in MVA of the AC system is given by the ratio of the commutation bus voltage at the rated DC power and the Thevenin equivalent impedance of the AC system as seen in equation A.2 [19].

$$\mathrm{S}C_{MVA} = \frac{E_{ac}{}^{2}}{Z_{TH}} \tag{A.2}$$

Where E_{ac}= Commutation AC bus voltage at rated DC Power

Z_{TH} = Thevenin equivalent impedance of the AC system

$$SC_{MVA} = \text{Short Circuit Level(MVA)}$$

When the AC side components such as filters and shunt capacitors are taken into account in order to obtain the total system strength which will reflects the new system impedance, the SCR is called an effective short circuit ratio (ESCR) which is a better indication of the strength of the AC system [38]. The ESCR is given in equation A.3.

$$ESCR = \frac{(\mathrm{SC}_{\mathrm{MVA}} - \mathrm{Q}_{\mathrm{C}})}{(\mathrm{Converter}\ \mathrm{P}_{\mathrm{DC}}\ \mathrm{rating})} \tag{A.3}$$

When STATCOMS are added to the AC side, the Mvar injection of the STATCOM, Q_S is added to the SC_{MVA} of the AC side and hence the ESCR evaluation in equation A.3 will now be modified and defined as seen in equation A.4 [2, 39, 40].

$$ESCR = \frac{SC_{MVA} - (Q_C - Q_S)}{(\mathrm{Converter}\ \mathrm{P}_{\mathrm{DC}}\ \mathrm{rating})} \tag{A.4}$$

In practice, the SCR is not a constant value due to changes in the AC system impedance configuration as well as the amount of DC power transferred via the HVDC transmission link. Therefore a new definition is formulated, namely, the Operating Effective Short Circuit Ration (OESCR) [26].

The OESCR reflects the exact amount of P_{DC} transmitted and the online system impedance as indicated in equation A.5.

$$OESCR = \frac{\frac{\mathrm{E}_{\mathrm{AC}}^{2}}{\mathrm{Z}_{\mathrm{TH(REAL)}}} - [\mathrm{Q}_{\mathrm{C}} - \mathrm{Q}_{\mathrm{S}}]}{\mathrm{P}_{\mathrm{DC(REAL)}}} \tag{A.5}$$

Finally, when the OESCR is calculated, the following parameters must be stated as the OESCR takes them into account: the firing angle, commutation reactance X_C, extinction angle (γ) and the control scheme such as adopted by the HVDC converters [32, 39].

The strength classification of AC systems according to the ESCR is as follows: [19].

$0 < ESCR < 2 \rightarrow$ Very Low

$2 < ESCR < 3 \rightarrow$ Low

$ESCR > 3 \rightarrow$ High

APPENDIX B:

HV Transmission lines, Transformers and Synchronous Machines

Table B1: Transmission Line Parameters [46]

Parameter	HVDC-Line	HVAC Line
Susceptance, B (uS/Km)	4.35	0.45
Rated Voltage (kV)	500	500
Rated Current (kA)	3	3
System Type	DC	AC
Cable/OHL	OHL	OHL
1,2 Sequence Resistance (R')	0.015	0.028
1,2 sequence Resistance (X')	0.025	0.325
Length (km)	500	500

Table B2: Transformer Parameters

Parameter	TR1,TR2, TR3, TR4	TR5, TR6	TR7,TR8	T9,TR10
Rated Voltage (kV)	22/500	500/11	500/230	230/500
Rated Power (MVA)	2000	1500	1400	1400
Zero Sequ Leakage Impedance, HV side (z,HV)	0.51	0.51	0.51	0.51
Zero Sequ Leakage Impedance, LV side z,LV	0.49	0.49	0.49	0.49
Zero Sequ Impedance, Short-circuit Voltage uK0 (10%)	10	10	10	10
No Load Current (%)	1	1	1	1
No Load Losses (Kw)	0	0	0	0

Table B3: Generator Parameters

Parameter	G1, G2	G3, G4
Reactive Power Limits (Mvar)	-100, 900	-500, 1200
Nominal App. Power (MVA)	1900	2700
Nominal Voltage (kV)	22	22
Power Factor (pf)	0.8	0.8
Inertia (H)	7.6	7.6
Vector Group	YN	YN
Stator Resistance (rstr)	0.01	0.01
d-axis Synchronous Reactance (Xd)	0.09	0.09

Parameter	**G1, G2**	**G3, G4**
q-axis Synchronous Reactance (Xq)	0.09	0.09
Transient Time Constant (Td')	8	8
Transient Reactance (xd')	0.3	0.3
d-axis Sub Transient Reactance (xd'')	0.2	0.2
d-axis Sub Transient Reactance (xq'')	0.2	0.2

APPENDIX C:

Transmission Line and Voltage Level Calculation

This was approached by calculating the Surge Impedance Loading (SIL) of HVAC transmission lines at different voltage levels. The equations below show how the SIL was calculated

The Surge impedance Loading of a HVAC transmission line is defined as the real power a transmission lines delivers when it is terminated by its surge impedance.

This power is the ratio of the rated line-line voltage of the transmission line to the surge impedance of the transmission line as given in equation C.1.

$$SIL = \frac{V_L{}^2}{Z_{SI}}[W] \qquad \text{(C.1)}$$

Where V_L = Sending end line-line Voltage

Z_{SI} = Surge impedance of the transmission line

Equation C.2 shows the characteristic impedance of a transmission line

$$Z_C = \sqrt{\frac{R + j\omega L}{j\omega C}} \qquad \text{(C.2)}$$

Where R = Line Resistance

L = Line Inductance

C = Line Capacitance

When the transmission line is considered lossless i.e., G is negligible and $R <<< \omega L$, the characteristic impedance of the line Z_C can be redefined as the surge impedance Z_{SI} of the transmission line in equation C.3.

When $R <<< \omega L$ and R is neglected

$$Z_{SI} = \sqrt{\frac{j\omega L}{j\omega C}} = \sqrt{\frac{L}{C}} \tag{C.3}$$

When a lossless transmission line is terminated by its SIL, it is expected that the reactive power generated by the capacitance of the transmission line is equal to the reactive power absorbed by the transmission line [26].

For the following line parameters;

$X_L = 0.2708\Omega / km$, $B_C = 4.3333 \text{ e}10^{-6} \ S / km$

$V_L = 500\text{k}V$

$R = 0.028 \ \Omega / km$ (has been already neglected)

$$\omega = 2\pi F = 314.159 \quad \text{@ F= 50 Hz} \tag{C.4}$$

$$L = \frac{X_L}{\omega} = 0.8619e10^{-3} \ H \tag{C.5}$$

$$C = \frac{B_C}{\omega} = 0.013e10^{-6} \ F \tag{C.6}$$

Hence for a single circuit HVAC transmission line,

$$Z_{SI} = \sqrt{\frac{L}{C}} = 257.5\,\Omega \qquad \text{(C.7)}$$

$$SIL = \frac{{V_L}^2}{Z_{IS}} = 971\,MW \qquad \text{(C.8)}$$

Hence, from equation C.8, the SIL for the HVAC transmission line is 971 MW at 500 kV.

From this result, it was determined that one HVAC line would transmit 1000MW while the HVDC line would also transmit 1000 MW. Therefore in case one, two HVDC lines would transmit 2000 MW while in case two, the hybrid HVAC and HVDC line would each transmit 1000 MW. The rest of the 442 MW required by the distribution centre will be provided by local generation close to the distribution centre.

APPENDIX D:

Appendix D contains the parameters and block diagram for the AVR and PSS that was used in the simulations.

Table D.1 IEEET1 AVR Parameters [37]

Parameter	**Value**
Tr: Measurement Delay (s)	0.02
Ka: Controller Gain (pu)	0.5
Ta: Controller Time Constant (s)	0.03
Ke: Exciter Constant (pu)	1
Te: Exciter Time Constant (s)	0.2
Kf: Stabilization Path Gain (pu)	0.05
Tf: Stabilization Path Time Constant (s)	1.5
E1: Saturation Factor 1 (pu)	3.9
E2: Saturation Factor 3 (pu)	0.1
Se1 :Saturation Factor 2 (pu)	5.2
Se2: Saturation Factor 4 (pu)	0.5
Vrmin: Controller Output (pu)	-10
Vrmax: Controller Output (pu)	10

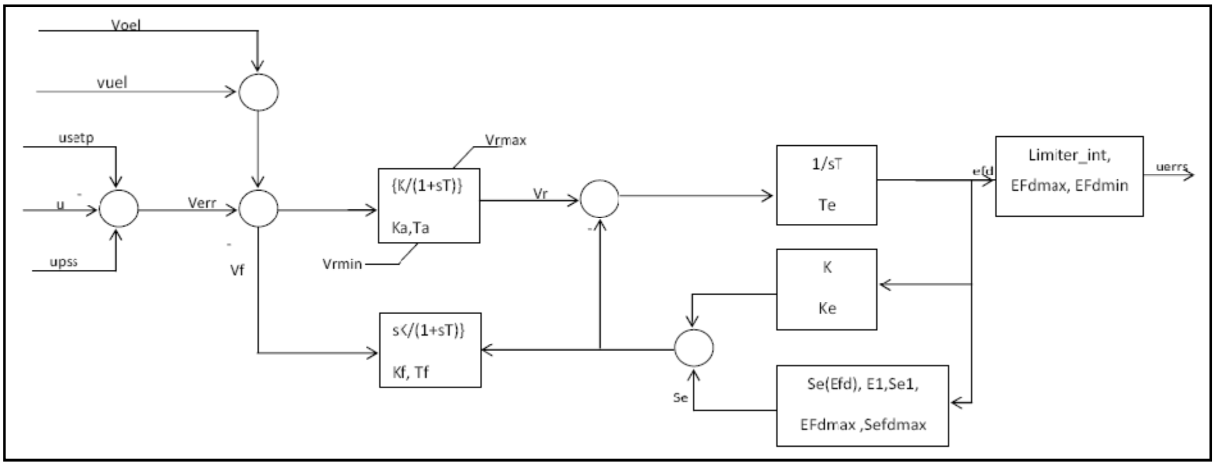

Figure D. 1 IEEET1 AVR Block Diagram

Table D.2 IEEEST PSS Parameters [37]

Parameter	Value
Input Selector [1-6]	2
T1 Lead- lag 1st Derivative Time Constant [s]	0.05
T2 Lead- lag 2nd Delay Time Constant [s]	0.3
T3 Lead- lag 3rd Derivative Time Constant [s]	1.2
T4 Lead- lag 4th Delay Time Constant [s]	1
T5: Stabilizer Derivative Time Constant [s]	1
T6: Stabilizer Time Constant [s]	1
Ks: Stabilizer Gain [pu]	-1
Kd: Derivatitor Factor [pu]	0.01
A1: Filter 1th Time Constant [s]	0
A2: Filter 2nd Time Constant [s]	0
A3: Filter 3rd Time Constant [s]	0.5
A4: Filter 4th Time Constant [s]	1
A5: Filter 5th Time Constant [s]	2
A6: Filter 6th Time Constant [s]	1
Lsmin: Controller Minimum Output [pu]	-0.1
Vcl: Controller Minimum Limit [pu]	0.8
Lsmax: Controller Maximum Output [pu]	0.1
Vcu: Controller Maximum Limit [pu]	1.1

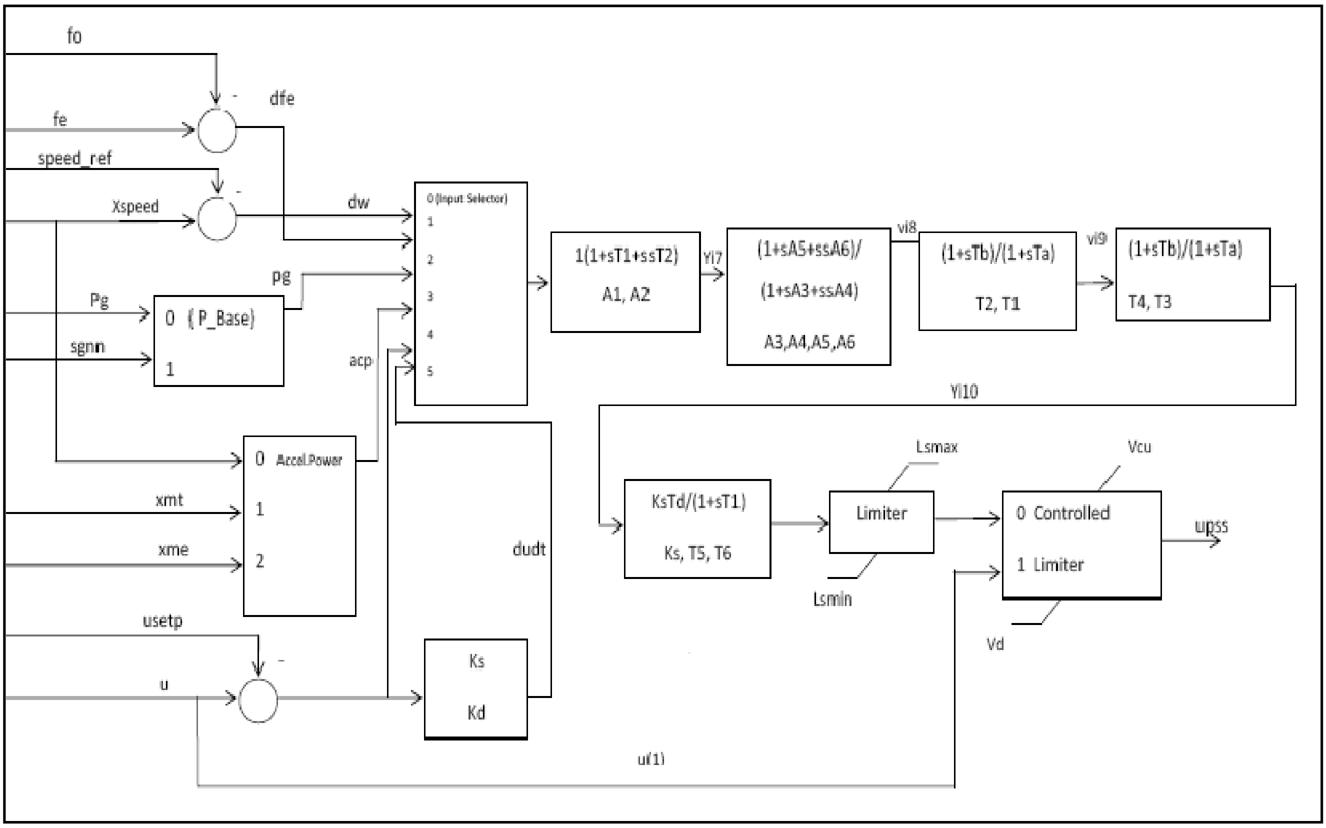

Figure D. 2 IEEEST PSS Block Diagram

APPENDIX E:

Rectifier and inverter Data per six pulse converter

Table E.1 Rectifier data

Parameter	**Value**
Rated Voltage DC (kV)	500
Rated Power (MW)	1000
Minimum Firing Angel (Deg)	15
Maximum Firing Angel (Deg)	80
Commutation Reactance	3
Automatic Firing	Y
Current Set Point (kA)	2
Controller	Current Control

Table E.2 Rectifier data

Parameter	**Value**
Rated Voltage DC (kV)	500
Rated Power (MW)	1000
Extinction Angle (Deg)	37
Minimum Firing Angel (Deg)	120
Maximum Firing Angel (Deg)	160
Commutation Reactance	3
Control	CEA
Automatic Firing	Y

APPENDIX F:

Figures F.1 to F.12 in Appendix F, shows the generator current graphs for the TAMM power system models during the converter DC faults and the 3-phase to ground fault at G4.

Appendix F:1 Converter DC fault with HVDC transmission line

Generator current graphs, during the converter DC fault while using the HVDC transmission line.

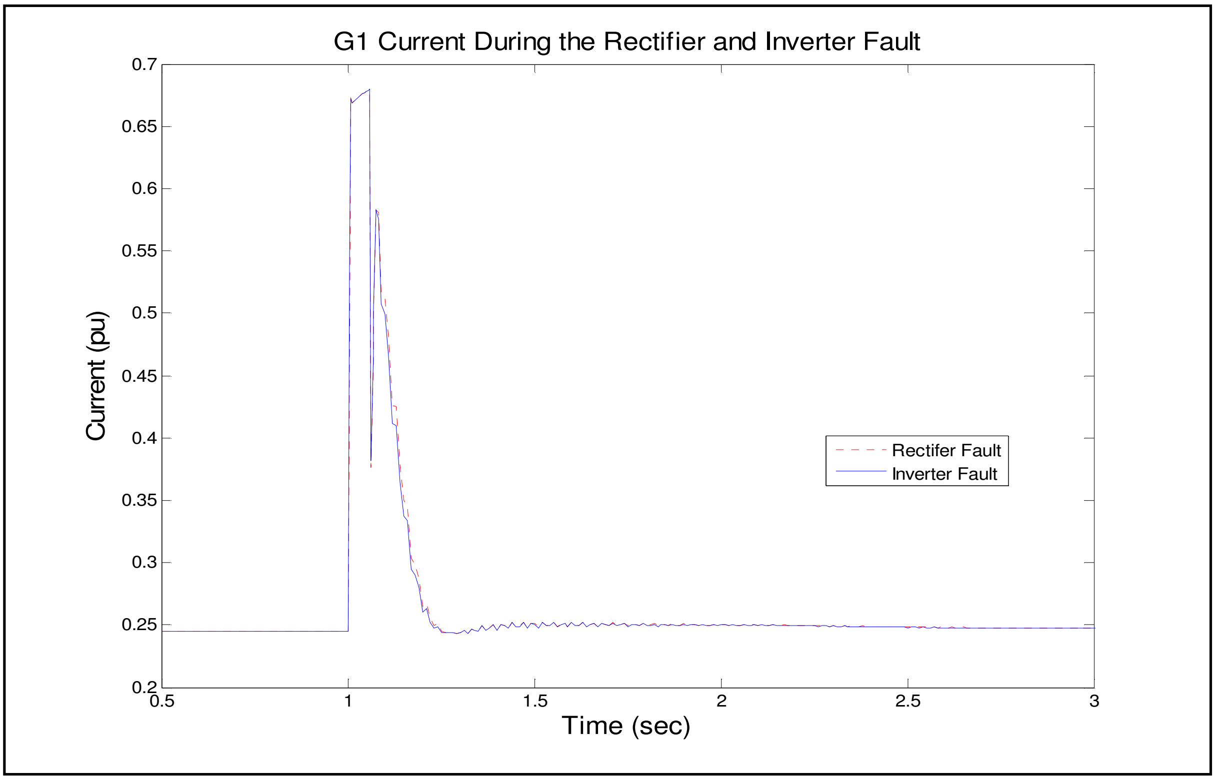

Figure F. 1 G1: Current during Rectifier and Inverter DC Fault

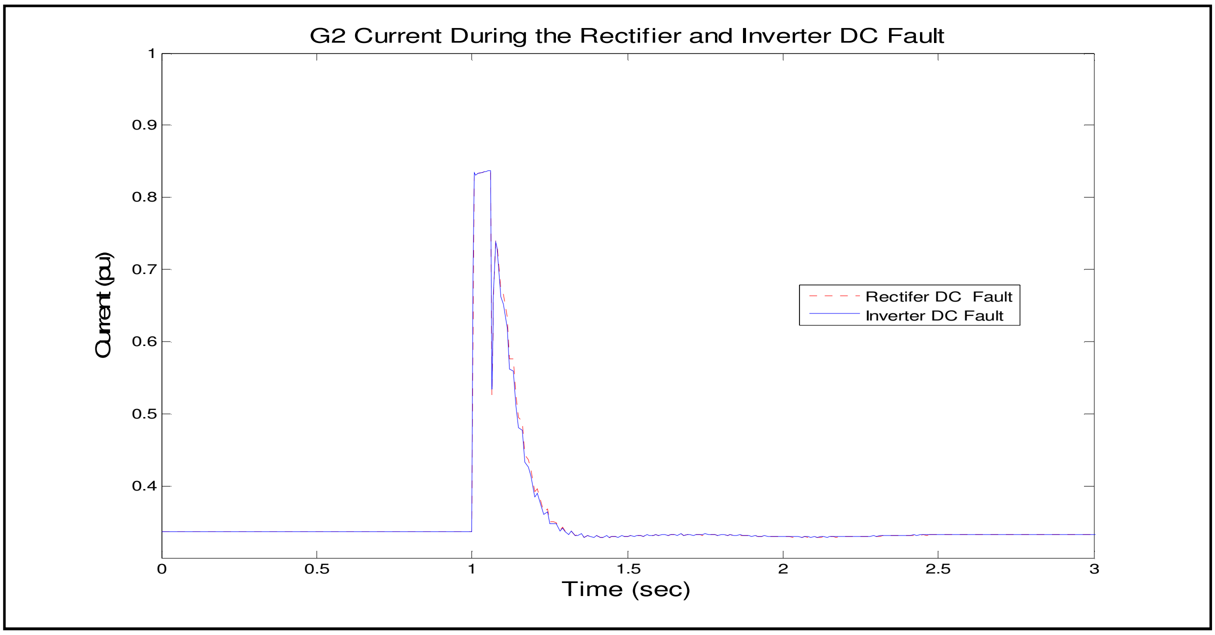

Figure F. 2 G2: Current during Rectifier and Inverter DC Fault

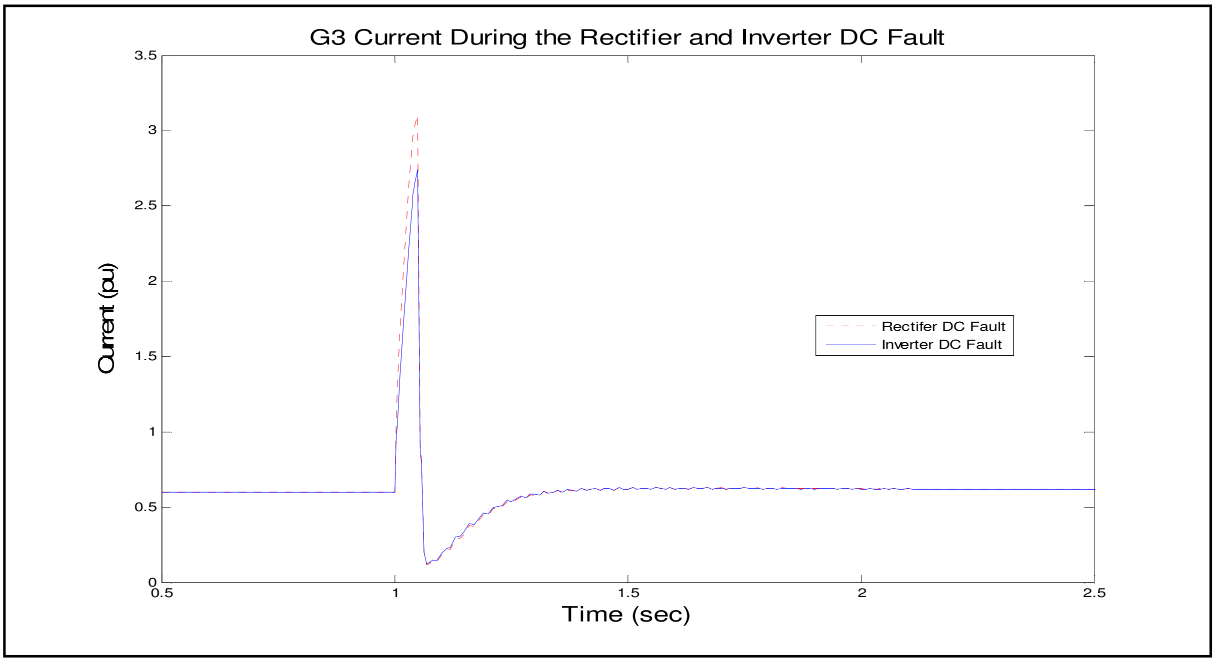

Figure F. 3 G3: Current during Rectifier and Inverter DC Fault

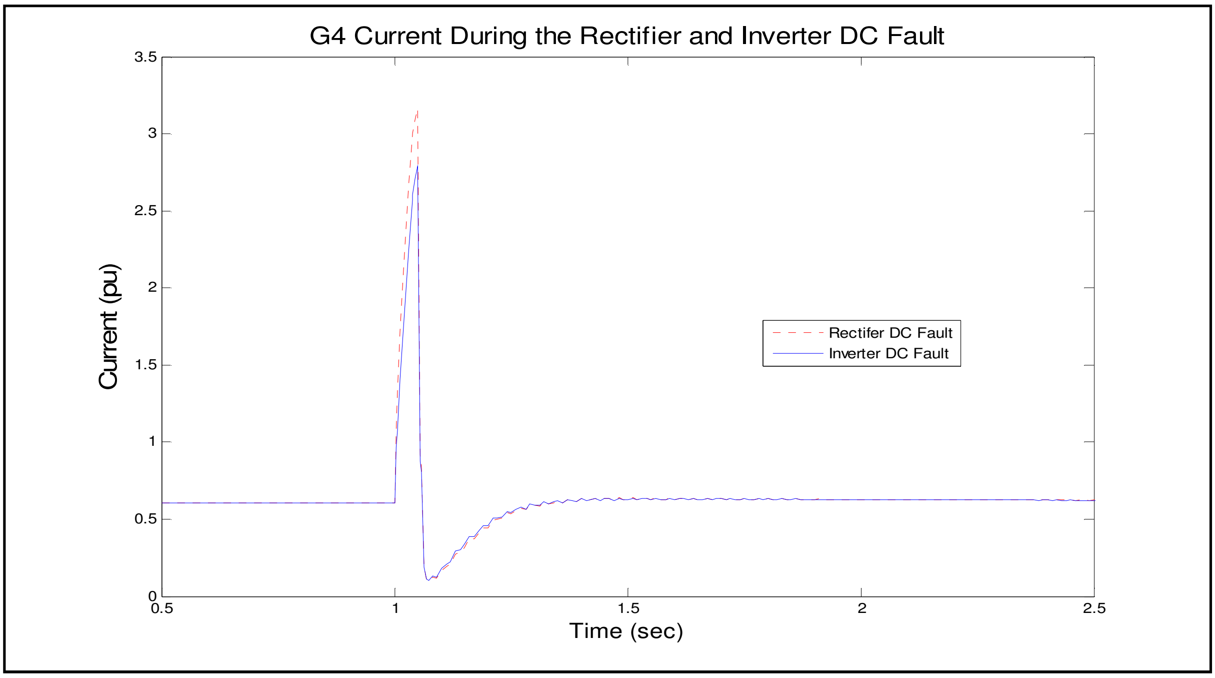

Figure F. 4 G4: Current during Rectifier and Inverter DC Fault

Appendix F:2 Converter DC fault with hybrid HVAC-HVDC transmission line

Generator current graphs, during the converter DC fault while using the hybrid HVAC-HVDC transmission line.

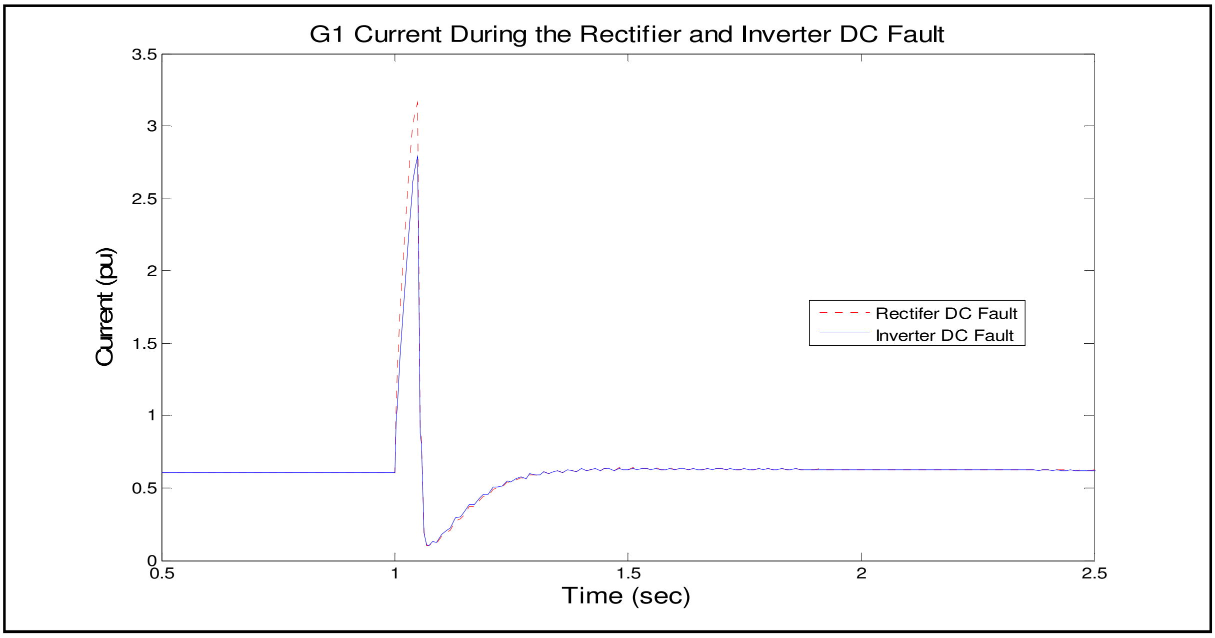

Figure F. 5 G1: Current during Rectifier and Inverter DC Fault

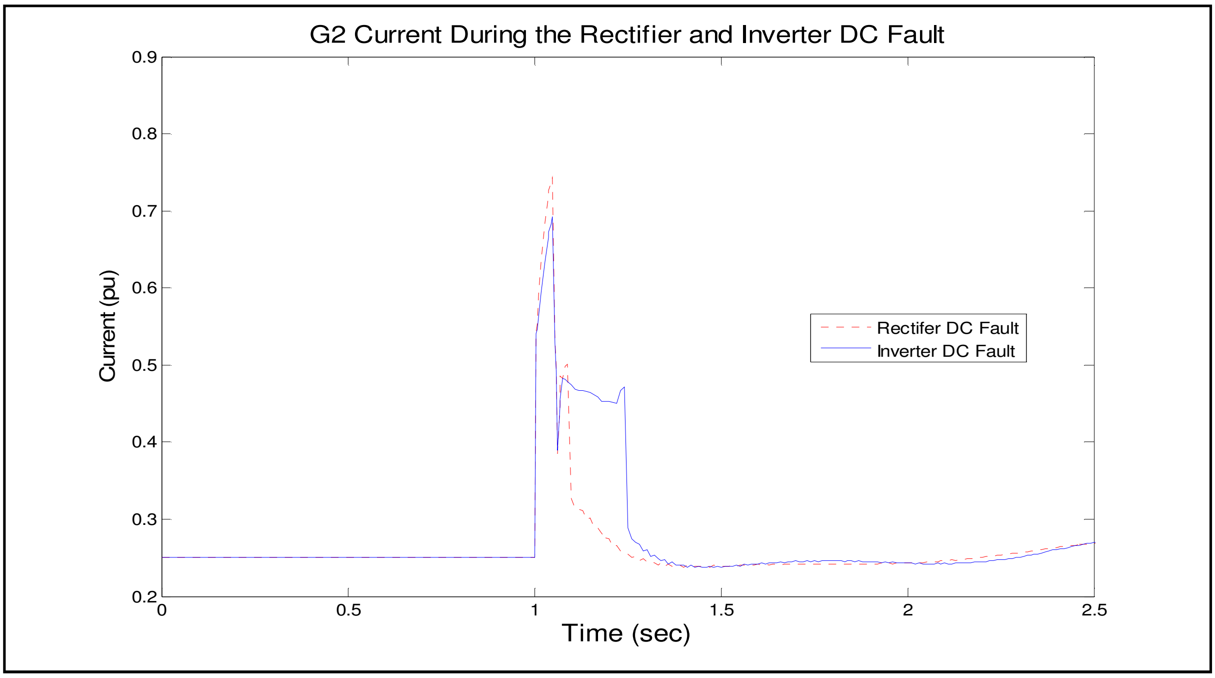

Figure F. 6 G2: Current during Rectifier and Inverter DC Fault

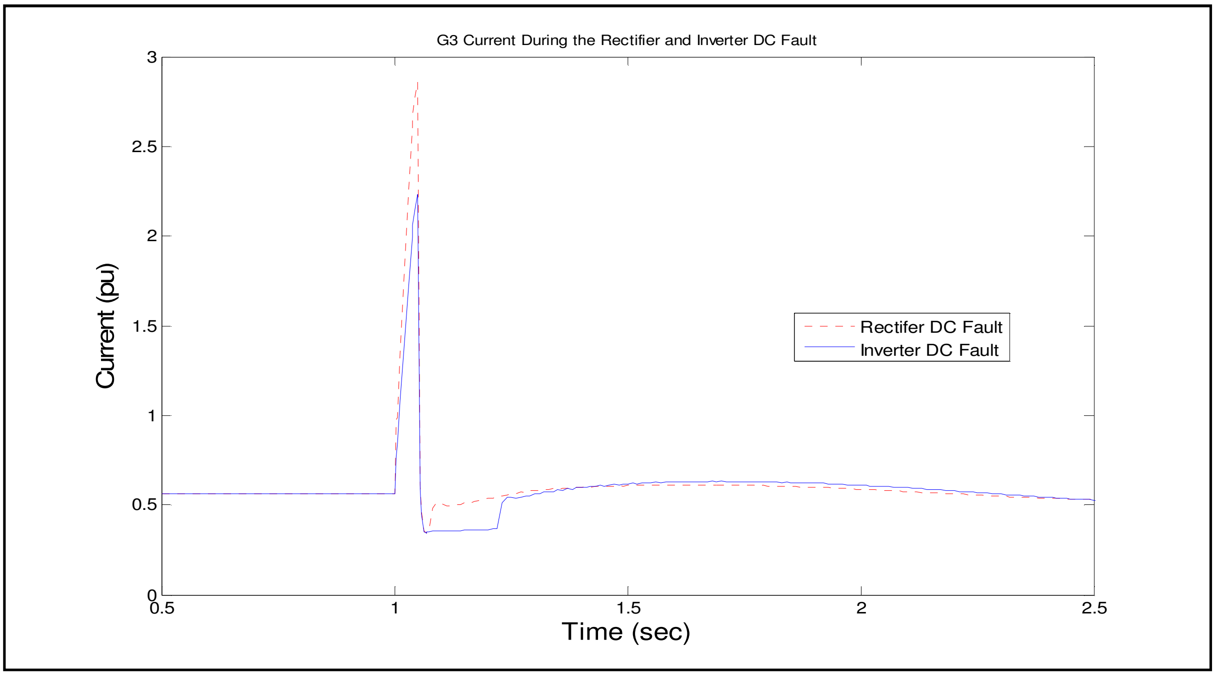

Figure F. 7 G3: Current during Rectifier and Inverter DC Fault

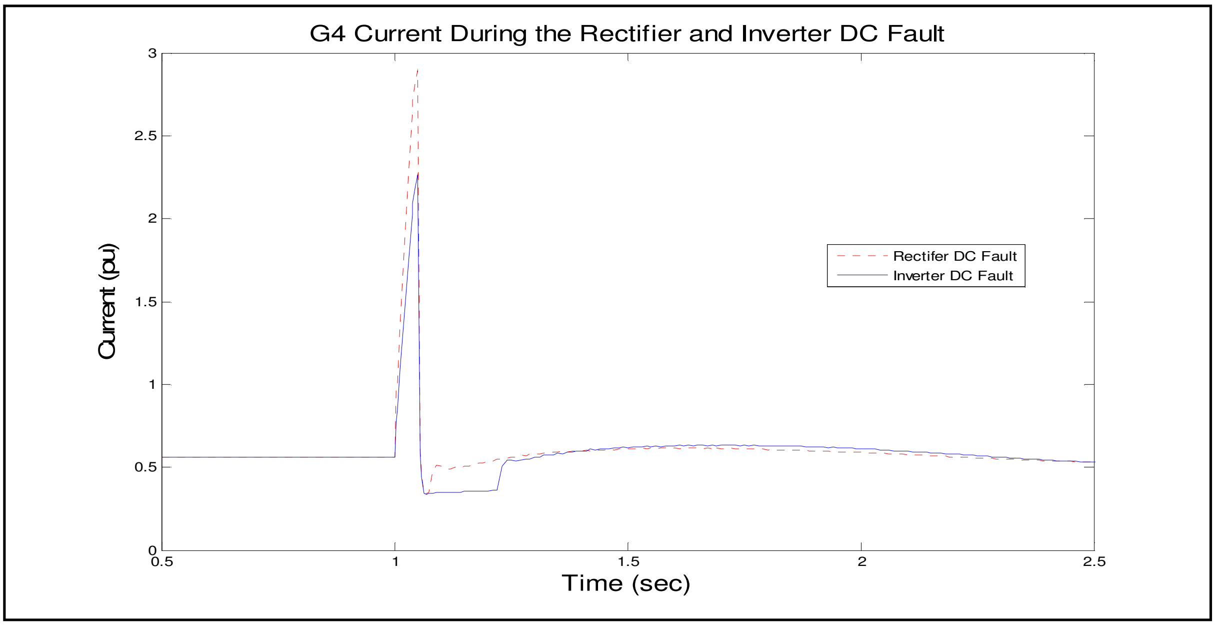

Figure F. 8 G4: Current during Rectifier and Inverter DC Fault

Appendix F:3

Generator Current graphs, during the 3-phase to ground fault at G4 while using the HVDC and the hybrid HVAC-HVDC transmission lines

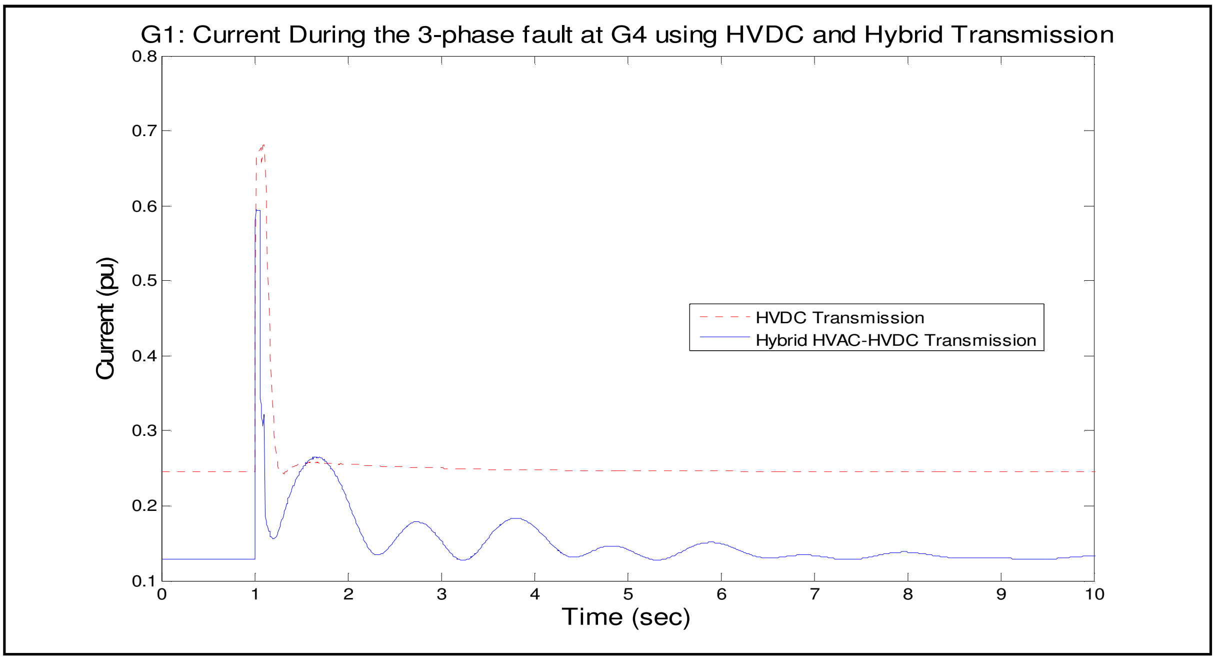

Figure F. 9 G1: Current during 3-phase fault at G4

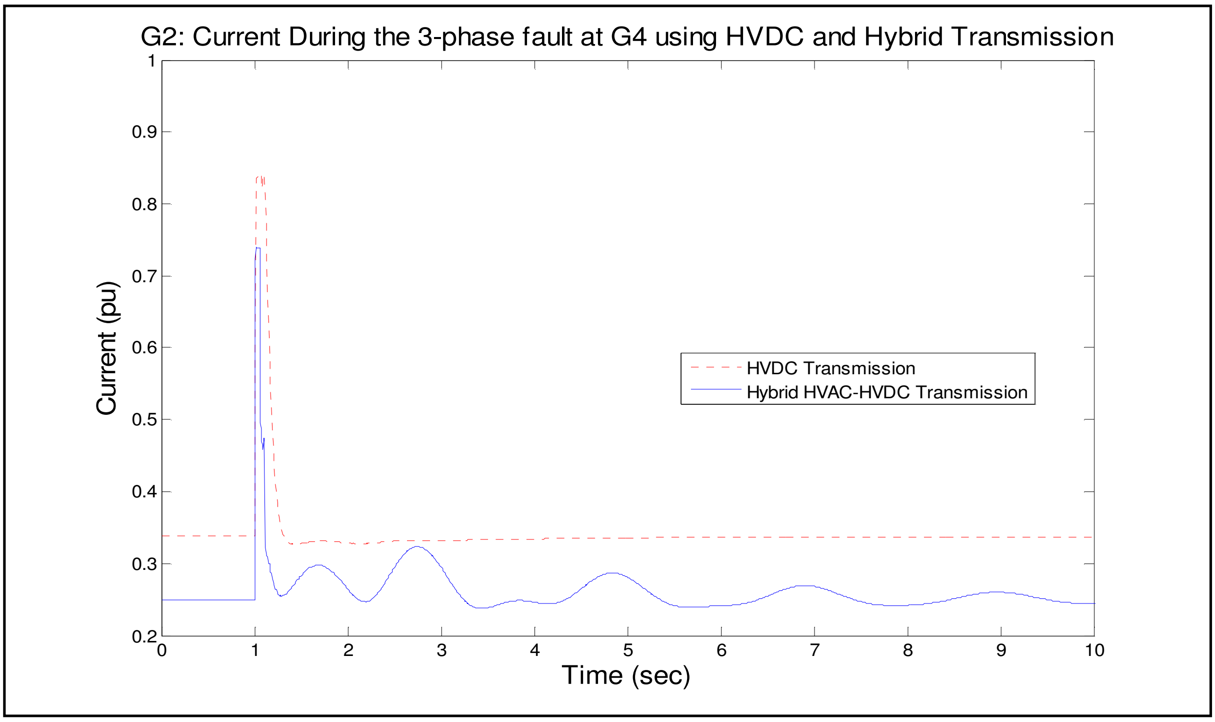

Figure F. 10 G2: Current during 3-phase fault at G4

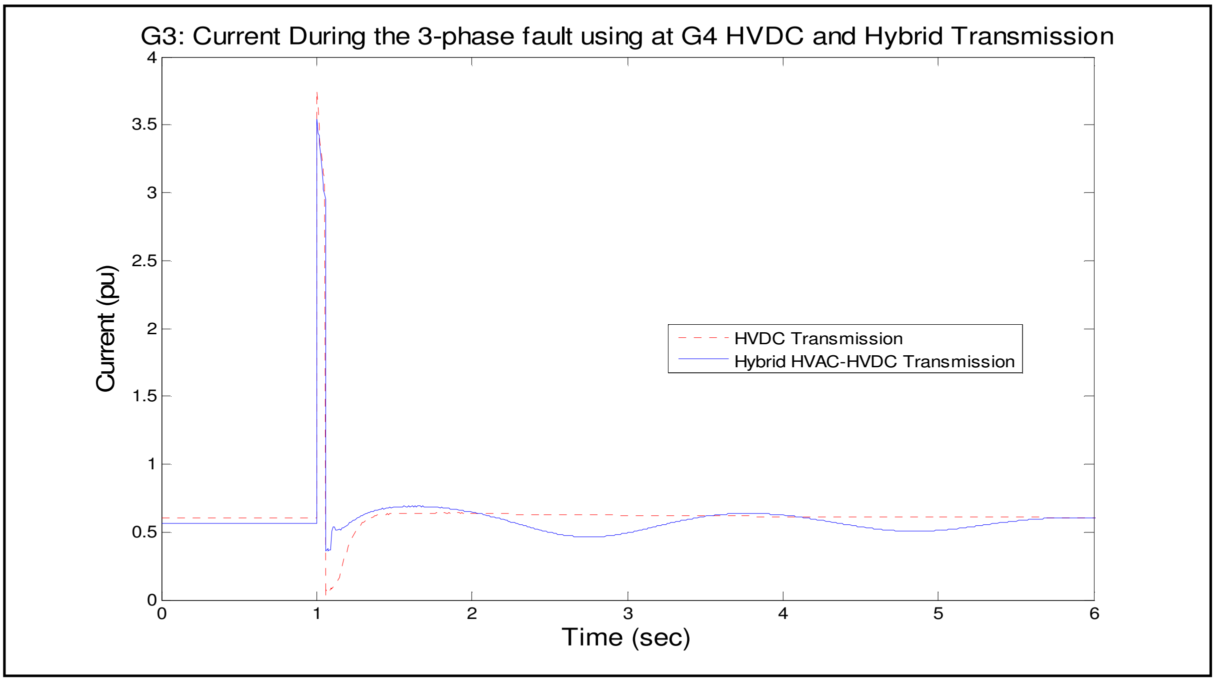

Figure F. 11 G3: Current during 3-phase fault at G4

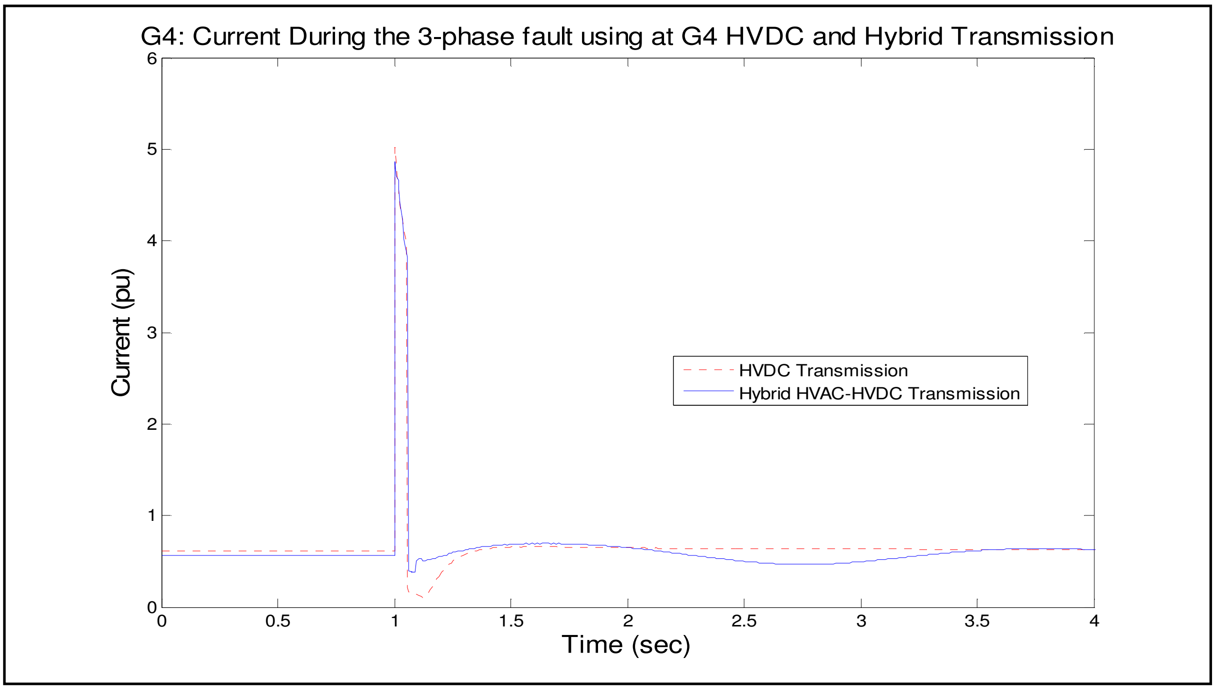

Figure F. 12 G4: Current during 3-phase fault at G4

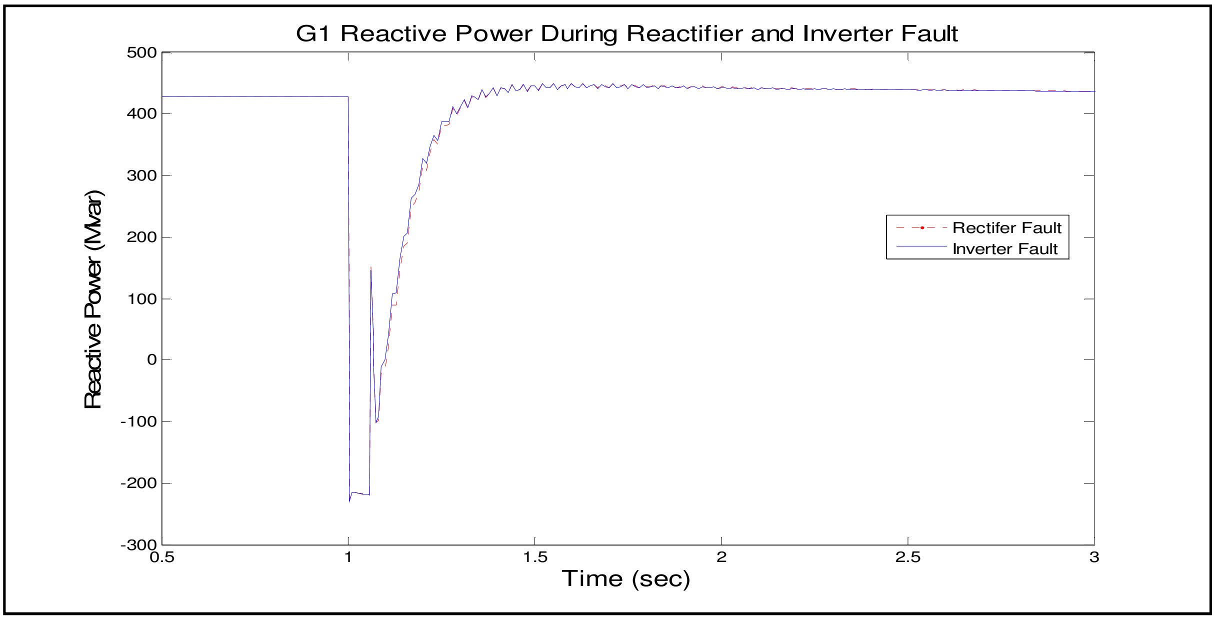

Figure F. 13 G3 Reactive power during the DC fault at the converter station using the HVDC transmission scheme with the TAMM power system.